July 2016

# Synthesis and Characterization of Polymeric Anion Exchange Membranes

WENXU ZHANG
*University of Massachusetts Amherst*

# SYNTHESIS AND CHARACTERIZATION OF POLYMERIC ANION EXCHANGE MEMBRANES

A Dissertation Presented

by

Wenxu Zhang

Submitted to the Graduate School of the

University of Massachusetts Amherst in partial fulfillment

of the requirements for the degree of

DOCTOR OF PHILOSOPHY

May 2016

Polymer Science and Engineering

**SYNTHESIS AND CHARACTERIZATION OF POLYMERIC ANION EXCHANGE MEMBRANES**

A Dissertation Presented

by

Wenxu Zhang

Approved as to style and content by:

_____

E. Bryan Coughlin, Chair

_____

Ryan C. Hayward, Member

_____

Dhandapani Venkataraman, Member

_____

David A. Hoagland, Department Head

Polymer Science and Engineering

## DEDICATION

This dissertation is dedicated to my dear friends all over the world, who have been generously sharing the life of both happiness and sorrow, and helping me to become a better person.

Most importantly, this dissertation is dedicated to my family and Dr. Dong “Michelle” Li, who have always supported me with their persistent love as well as respects on my hobbies, decisions, and enthusiasm towards scientific research, especially my Grandfather, who initiated my interests in science but is sadly no longer with us to see me finishing the Ph.D. degree.

## ACKNOWLEDGMENTS

Firstly, I would like to express my sincere gratitude to my advisor Prof. E. Bryan Coughlin for his continuous support and patience during my Ph.D. study, as well as his immense knowledge. His guidance helped me in all the time of reading literature, conducting experiments, and writing papers in addition to professional developments. I could not have imagined having a better advisor.

Also, I thank Prof. Ryan Hayward and Prof. Dhandapani Venkataraman for being my committee members and providing guidance and helpful suggestions in designing experiments and analyzing data.

I give my thanks to all the PSE faculty members for giving inspiring lectures and cumulative exams. I would like to thank Dr. Weiguo Hu for NMR training and assistances. I would like to thank Dr. Stephen Eyles and Dr. Rinat Abzalimov for performing mass spectroscopy experiments. Thanks to Lisa Groth and Maria Farrington for help in processing my documents and payrolls.

Thanks to Zhiwei Sun for being such a wonderful collaborator and many exciting brainstorms. I would like to thank Dr. Himanshu Sarode, Ye Liu, Dr. Aaron Jackson, Dr. Fredrick Beyer, and other collaborators for their patient help.

I genuinely thank all the past and present members of Coughlin group. Dr. Shilpi Sanghi and Dr. Elizabeth Sterner taught me basic experimental skills. Dr. Hui Zhao has always been sharing research ideas with me. Thanks to Dr. Tsung-Han Tsai, Dr. Xiaohui Liu, Dr. Huseyin Tas, Dr. Chya-Yan Liaw, Piril Ertem, Haomiao Yuan, Rohit Gupta, Chinomso Nowsu, and Deborah Ehrlich for so many enlightening discussions. Many thanks to Katherine Williams, Patrick Homyak, Brian Cromer, Josh Enokida, Christian Steinmetz, and John Epling for sharing laboratory and fun.

Last but not least, I gratefully acknowledge financial support from the Army Research Office through a MURI award, W911NF-10-1-0520, and the analytical facilities were supported by the NSF-Sponsored MRSEC at UMass Amherst.

**ABSTRACT**

SYNTHESIS AND CHARACTERIZATION OF POLYMERIC ANION EXCHANGE MEMBRANES

MAY 2016

WENXU ZHANG

B.S., ZHEJIANG UNIVERSITY

M.S., UNIVERSITY OF MASSACHUSETTS AMHERST

Ph.D., UNIVERSITY OF MASSACHUSETTS AMHERST

Directed by: Professor E. Bryan Coughlin

As alkaline anion exchange membrane fuel cells (AAEMFC) are regarded as promising and important energy devices, the development of high performance anion exchange membranes are in urgent need, as well as fundamental investigation on the structure-property relationship, which are the motivation of this dissertation. Three different polymer systems are presented and focused on polymer synthesis, material morphology, and ion transport phenomena.

Crosslinked membranes are promising as practical materials, however, the understanding and further improvement of its performance is hindered by the lack of an ordered morphology or well-defined chemical structure. In Chapter 2, a series of crosslinked membranes were design to bear cationic groups organized via covalent linkages, which were synthesized by sequential reversible addition-fragmentation chain transfer radical polymerization (RAFT), “click” chemistry,

cast/crosslinking process, and solid state quaternization. Significant enhancement in conductivities was observed and presumably attributed to the formation of ion transport channels directed by polycation chains. Excellent membrane performance were observed, including conductivities, water diffusivities, and fuel cell power densities.

In Chapter 3, phosphonium containing block copolymers were synthesized and subjected to morphology characterization. Using Small Angle X-ray Scattering (SAXS) and Transmission Electron Microscopy (TEM), it was observed that these materials form well-ordered morphologies upon solvent casting, and the ionic block preferred to form a continuous phase. By comparing the anion conductivities, the matrix in a hexagonal phase was proved to be more efficient in ion transport than lamellae.

Polycyclooctene (PCOE) based triblock copolymers were synthesized in Chapter 4, by using a special chain transfer agent (CTA) to mediate Ring-Opening Metathesis Polymerization (ROMP) and reversible addition-fragmentation chain transfer radical polymerization (RAFT). The well-defined melting transition (~50 $^{o}$C) of PCOE enabled the investigation of the thermal transition in hydrophobic block affecting ionic domain behavior.

Then metal ion doped star block copolymers were investigated in bulk and thin film forms to demonstrate that the star block copolymer architecture can facilitate microphase separation and thus the preparation of smaller features. Using an *ortho*-nitrobenzyl ester junction, triblock copolymers based on PEO and PSt were synthesized and applied to hierarchical pattern fabrication in self-assembled thin films.

During these studies, the single monomer insertion methodology was developed for high efficiency synthesis of (multi)functional RAFT CTAs. The molecular characterization and controlled polymerization results were documented in Chapter 7.

The last chapter contains outlooks based on the research in this dissertation. Methods to improve the previously presented materials were listed. Also, fundamental questions were raised on ion transport membranes, and possible ways to answer them were provided. In addition, potential research directions are proposed.

**TABLE OF CONTENTS**

Page

## LIST OF TABLES

Table Page

## LIST OF FIGURES

Figure Page

## LIST OF ABBREVIATIONS

| | |
|---|---|
| $^{o}C$ | degree Celsius |
| Đ | Molecular Weight Dispersity, $M_w/M_n$ |
| δ | Chemical shift |
| χ | Flory-Huggins Parameter |
| λ | number of water molecules absorbed per cation |
| σ | Conductivity |
| μL | microliter |
| μm | micromoeter |
| 2VP | 2-Vinylpyridine |
| 4CMS | 4-Chloromethylstyrene |
| 4VPO | 4-Vinylphenyloxirane |
| AAEMFC | Alkaline Anion Exchange Membrane Fuel Cell |
| ACBN | 1,1'-Azobis(cyclohexanecarbonitrile) |
| AEM | Anion Exchange Membrane |
| AFM | Atomic Force Microscopy |
| AIBN | 2,2′-Azobis(2-methylpropionitrile) |
| Ar | Aromatic Ring |

| | |
|---|---|
| $Ar_3P$ | Tris(2,4,6-trimethoxyphenyl)phosphine |
| ATRP | Atom Transfer Radical Polymerization |
| AzCOE | 5-Azido-cis-cyclooctene |
| BCP | Block Copolymer |
| BES | Broadband Electrical Spectroscopy |
| BrCOE | 5-Bromo-cis-cyclooctene |
| Bz-CTA | Benzyl *n*-butyl trithiocarbonate |
| $BzAr_3P^+$ | Benzyl Tris(2,4,6-trimethoxyphenyl) Phosphonium |
| BzCl | Benzyl Chloride |
| $C_{12}$COOH-CTA | 2-(Dodecylthiocarbonothioylthio)-2-methylpropionic acid |
| ClBz | Chlorobenzene |
| cm | centimeter |
| CMS | Chloromethylstyrene |
| conv. | conversion |
| CT-ROMP | Chain Transfer Ring-opening Metathesis Polymerization |
| CTA | Chain Transfer Agent |
| COE | Cis-cyclooctene |
| COE-CTA | Chain transfer agent containing a StCOE unit |
| COE-Xan | Cyclooctene connected to O-ethyl carbonodithioate via a triazole ring |

| | |
|---|---|
| COOH-CTA | 4-Cyano-4-[(butylsulfanylthiocarbonyl)sulfanyl]pentanoic acid |
| COSY | Correlation Spectroscopy (NMR) |
| Cl-CTA | Chain transfer agent containing one 4CMS unit |
| $Cl_2$-$MI_2$-$TTC_2$ | Chain transfer agent containing two benzyl chloride groups and a bismaleimide |
| $Cl_3$-$TTC_3$ | Chain transfer agent containing 3 benzyl chloride and 3 trithiocarbonate groups |
| CT-ROMP | Chain Transfer Ring-Opening Metathesis Polymerization |
| CXCAm | Cyclooctene Crosslinked Membranes with Connected Ammonium Ions |
| d-spacing | Domain Spacing |
| DCC | N,N'-Dicyclohexylcarbodiimide |
| DCM | Dichloromethane |
| DCPD | Dicyclopentadiene |
| DEPT135 | Distortionless Enhancement by Polarization Transfer at 135$^{o}$ Angle (NMR) |
| DMAP | 4-Dimethylaminopyridine |
| DMF | N,N-Dimethylformamide |
| DMSO | Dimethylsulfoxide |
| DP | Degree of Polymerization |
| DSC | Differential Scanning Calorimetry |

| | |
|---|---|
| DVB | Divinylbenzene |
| DVB-CTA | Divinylbenzene based chain transfer agent |
| DVS | Dynamic Vapor Sorption |
| DXB | α,α'-Dibromo-*p*-xylene |
| DXB-CTA | 1,4-Bis(*n*-butyl sulfanylthiocarbonyl sulfanyl methyl)benzene |
| DXCAm | Dicyclopentadiene Crosslinked Membrane with Connected Ammonium Ions |
| EI-MS | Electron Impact Mass Spectrometry |
| EO-*hv*-SEO | Poly(ethylene oxide)-ONB-polystyrene-*b*-poly(ethylene oxide) |
| ER | End-group Removal |
| EtOH | Ethanol |
| equiv. | molar equivalent |
| ESI-MS | Electrospray Ionization Mass Spectroscopy |
| F5-CTA | Chain transfer agent containing a StF5 unit |
| FAB-MS | Fast Atom Bombardment Mass Spectroscopy |
| faf | free arm fraction in star (co)polymer product |
| g | gram |
| G2 | Grubbs 2$^{nd}$ Generation Catalyst |
| G3 | Grubbs 3$^{rd}$ Generation Catalyst |
| GPC | Gel Permeation Chromatography |

| | |
|---|---|
| HMBC | Heteronuclear Multiple-bond Correlation Spectroscopy (NMR) |
| HMQC | Heteronuclear Multiple Quantum Coherence (NMR) |
| *hv* | Photocleavable Junction |
| IEC | Ion Exchange Capacity |
| Ip | Isoprene |
| kg | kilogram |
| M | Molecular Mass |
| MADIX | Macromolecular Design by Interchange of Xanthate |
| MeOH | Methanol |
| mg | milligram |
| MI-Yne | Prop-2-yn-1-yl 6-(2,5-dioxo-2,5-dihydro-1*H*-pyrrol-1-yl)hexanoate |
| MI-$C_4$-Yne | But-3-yn-1-yl 6-(2,5-dioxo-2,5-dihydro-1*H*-pyrrol-1-yl)hexanoate |
| mL | milliliter |
| $M_n$ | Number average molecular weight |
| MM | Macromonomer |
| mmol | millimole |
| mol | mole |
| MS | Mass Spectroscopy |
| mS/cm | millisiemens per centimeter |

| | |
|---|---|
| MW | (Number Average) Molecular Weight |
| $M_w$ | Weight average molecular weight |
| $mW/cm^2$ | milliwatts per centimeter square |
| N | Number of Monomers per Arm in a Star Polymer |
| nBA | *n*-Butyl Acrylate |
| NBE | Norbornene |
| NBE-CTA | Chain transfer agent containing a StNBE unit |
| nm | nanometer |
| NIPAAm | N-Isopropyl Acrylamide |
| NMR | Nuclear Magnetic Resonance Spectroscopy |
| NMP | Nitroxide Mediated Polymerization |
| O-CTA | 2-Cyano-2-propyl butyl trithiocarbonate |
| ODT | Order-Disorder Transition |
| OH-CTA | Chain transfer agent containing one hydroxyl group |
| ONB | *ortho*-Nitrobenzyl junction |
| PEM | Proton Exchange Membrane |
| PEMFC | Proton Exchange Membrane Fuel Cell |
| PEO | Poly(Ethylene Oxide) |
| PMDETA | N,N,N’,N”,N”-Pentamethyldiethylenetriamine |

| | |
|---|---|
| PMMA | Poly(Methyl Methacrylate) |
| POSS | Polyhedral Oligomeric Silsesquioxane |
| ppm | parts per million |
| PSt | Polystyrene |
| PTFE | Polytetrafluoroethylene |
| q | Scattering wave factor |
| $R_2$-CTA | Chain transfer agent for mediating RAFT and ROMP polymerizations |
| RAFT | Reversible Addition-Fragmentation Chain Transfer Radical Polymerization |
| RH | Relative Humidity |
| RIE | Reactive ion etching |
| ROMP | Ring-Opening Metathesis Polymerization |
| S/cm | Simerns per centimenter |
| SAXS | Small Angle X-ray Scattering |
| St | Styrene |
| StCOE | (1Z)-5-[(4-Ethenylphenyl)methoxy]cyclooct-1-ene |
| StEneSt | 1,1'-[(2Z)-But-2-ene-1,4-diylbis(oxymethylene)]bis(4-ethenylbenzene) |
| StF5 | Pentafluorophenyl vinylbenzyl ether |
| StNBE | 5-{[(4-Ethenylphenyl)methoxy]methyl}bicyclo[2.2.1]hept-2-ene |
| StTCOE | Cyclooctene connected to styrene via a triazole link |

| | |
|---|---|
| StYne | Propargyl *para*-Vinylbenzyl Ether |
| SVA | Solvent Vapor Annealing |
| TAEM | Triblock Copolymer Based Anion Exchange Membrane |
| tBS | *t*-Butyl Styrene |
| TEM | Transmission Electron Microscopy |
| $TTC_2$ | Chain transfer agent with two trithiocarbonate groups |
| $TTC_3$ | Chain transfer agent with three trithiocarbonate groups |
| $T_g$ | Glass transition temperature |
| $T_m$ | Melting transition temperature |
| THF | Tetrahydrofuran |
| UV | Ultraviolet |
| v:v | Volume Ratio |
| VAc | Vinyl Acetate |
| WU | Water-uptake |
| Yne | Alkyne functionality |
| Yne-Cl-CTA | Chain transfer agent containing an alkyne and a benzyl chloride group |
| Yne-CTA | Chain transfer agent containing a StYne unit |
| Yne-Ester-CTA | Prop-2-yn-1-yl 4-{[(butylsulfanyl)carbonothioyl]sulfanyl}-4-cyanopentanoate |
| Yne-ONB-OH | 5-Propargylether-2-nitrobenzyl Alcohol |

| | |
|---|---|
| Yne-ONB-Yne-CTA | Chain transfer agent based on Yne-ONB-OH containg an extra alkyne |
| $Yne_2TTC_2$ | Chain transfer agent containing two alkyne and two trithiocarbonate groups |

# CHAPTER 1

# INTRODUCTION

## 1.1 Fuel Cells

Today the energy sources of our world are based primarily on fossil fuels such as oil, gas, and coal, which have limited reserves and are being consumed at a very fast rate. At the recent consumption rates, it is estimated that the reserves of gas and oil will be depleted within this century, while coal will be exhausted in the next century.[1] The consumption of fossil fuels also leads to the enormous emission of greenhouse gases, which are known to cause degeneration of the earth's climate. It is urgent to reduce the usage of fossil fuels to meet the target of limiting global warming below 2 $^{o}$C in this century.[2] To obtain new sources of energy and reduce the release of carbon dioxide, one alternative method of energy production is to use a fuel cell. It is an environment-friendly electrochemical device, which could be used to supply energy for mobile devices, such as cellphones, and vehicles.[3]

There are many varieties of fuel cells, all of which are comprised of three major components: the anode, the electrolyte, and the cathode. The oxidation of fuels is assisted by a catalyst at the anode, while the oxidant is reduced at the cathode, and a current is produced as electrons move from the anode to the cathode through the closed circuitry (Figure 1). The electrolyte is a special substance which transports ions while prevents the passage of electrons. Hydrogen is often used as the fuel, while in some cases, methanol and even longer-chain alcohols can also be used.[4]

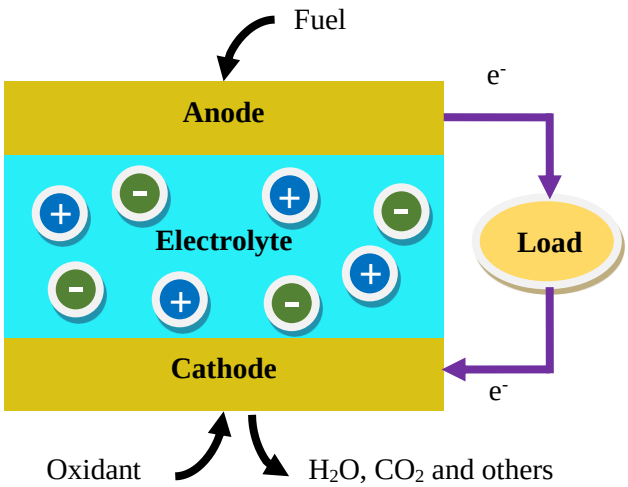


**Figure 1: Scheme of a Fuel Cell.**

### 1.2 Proton exchange membrane fuel cells (PEMFCs)

Among all of the membrane fuel cells, PEMFCs are the most developed.[5] The specially designed membranes in which strong acid groups are usually installed separating the two electrodes. Hydration of the membranes yields ion dissociation and solvation of the proton of the acid groups present on the polymer. The solvated protons are mobile within the polymer matrix and provide electrolyte conductivity. The ideal membrane should have low permeability to oxygen and fuel to prevent efficiency losses. This kind of fuel cell was used in the NASA Gemini series of spacecraft.[6] A typical PEMFC is shown in Figure 2.

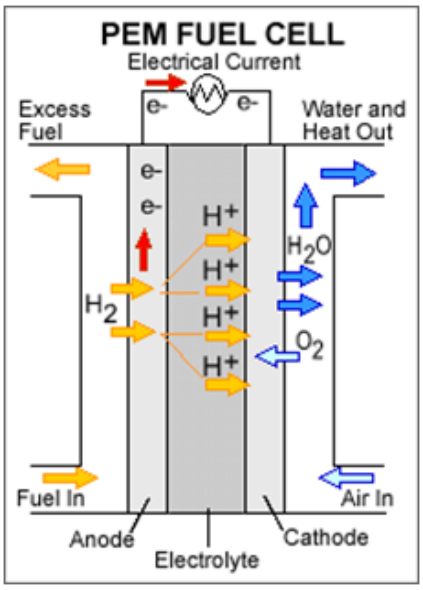


**Figure 2: Schematic of a PEMFC.**

**Figure adapted from http://en.wikipedia.org/wiki/Fuel_cell.**

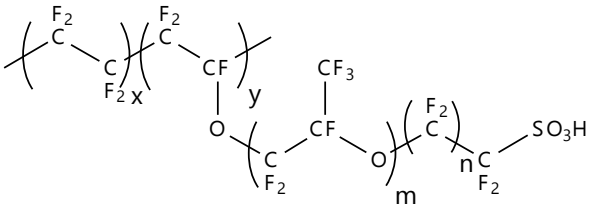

Nafion®: m≥1, n=2, x=5-13.5, y=1000

Aciplex® : m=0-3, n=2-5, x=1.5-14

Flemion® : m=0 or 1, n=1-5

**Figure 3: Structures of Nafion® and Other Commercially Available Poly(perfluorosulfonic acid) Copolymers.**

Nafion®, synthesized by conventional free radical copolymerization of tetrafluoroethylene and a perfluorinated alkyl vinyl ether bearing a sulfonyl acid fluoride group, is the most successful commercial proton exchange membrane. It has a polytetrafluoroethylene backbone which provides excellent chemical, thermal and, mechanical stability, and pendent sulfonic acid groups (Figure 3). The molecular weight (MW) can only be estimated to be between $10^5$ and $10^6$ Da, since accurate values cannot be determined by light scattering or size exclusion chromatography due to solubility limitations.[7,8] The copolymer morphology is complicated because of several factors: the

architecture is a random copolymer and thus possesses no ordered structures; the polytetrafluoroethylene backbone is semicrystalline; the perflurosulfonic acid groups self-assemble to form nanostructures. Several models have been proposed to describe the morphology. For example, the "cluster model" was proposed by Gierke et al., based on small angle X-ray scattering (SAXS) data, in which the sulfonic acid groups self-organize into reverse micelles which are clusters as large as about 4 nm, interconnected by pores or channels with a diameter of around 1 nm (Figure 4).[9]

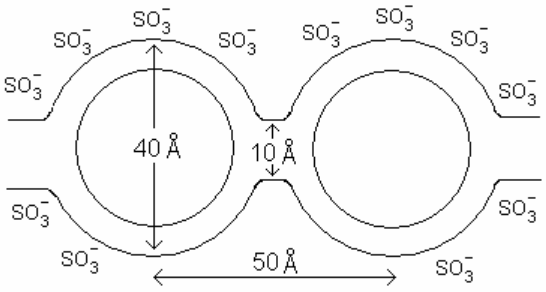


**Figure 4: Schematic of the Cluster Model.**

**Figure reprinted from Ref 9.**

Another more recent model named the water channel model, describes the morphology of Nafion® as arrays of parallel water channels surrounded by sulfonic acid groups, where ion transport is facilitated.[10] Despite the fact that no model can be proved to perfectly simulate Nafion®, it has been agreed that the presence of ion transporting channels is critical for ionic conductivity.[8] Other similar ionomers are also produced by the Asahi Chemical Company (Aciplex®), the Asahi Glass Company (Flemion®), and 3M Company.

### 1.3 Alkaline Fuel Cells

Alkaline fuel cells are among the most efficient fuel cells, which can reach efficiencies as high as 70%.[11] The two electrodes are separated by an aqueous alkaline solution of potassium hydroxide

(KOH). However, the electrolyte is subject to poisoning by carbon dioxide ($CO_2$), since the formed carbonate precipitates at the electrode, lowering the conductivity and blocking the catalyst surface. Thus, only hydrogen can be used as fuel and pure oxygen as the oxidant. The strongly alkaline liquid electrolyte corrodes the device surface, and is hazardous if there is a leak in the system.

An attractive alternative design is to use a polymeric electrolyte membrane, in which the cations are fixed charge carriers and thus carbonate will not form insoluble crystallites. Therefore, methanol and higher carbon number alcohols, which are easily transported and have high energy density, can be used directly in Alkaline Anion Exchange Membrane Fuel Cells (AAEMFCs).[3,12,13] Compared to PEMFCs, in alkaline media, the oxidation of methanol is known to be more facile and carbon monoxide poisoning of the catalysts is less pronouced. Even more encouragingly, non-noble metal catalyst, such as nickel for the fuel electrode and silver, iron phthalocyanines for the oxygen electrode have been reported in AAEMFCs, to replace platinum or platinum alloys, which are the limited options being used in PEMFCs. Another advantage of AAEMFCs is the suppression of fuel crossover when methanol is used, since the anion transport direction is from cathode to anode (Figure 5), which is in the opposite direction with methanol diffusion. Finally, oxidative radical degradation, a significant problem in PEMFCs, has been shown to be prevented in highly alkaline environments due to much more rapid oxygen reduction reactions. This facilitates the long-term stability of the polymer membrane and thus enables the usage of non-fluorinated polymers, such as polysulfone, polyethylene, and polystyrene, which can be synthesized via a variety of polymerization techniques. The wide range of possible polymer backbones provides great opportunities to reduce the cost of the electrolyte membrane, and, maybe more importantly, to systematic tune the chemical, mechanical, and electrochemical properties of the polymer matrix. Since tremendously versatile chemical reactions have been demonstrated efficient and convenient on these polymers, it is also now possible to carefully investigate how the polymer architecture as

well as subtle chemical structure, such as the linkage between the ionic group and backbone, can affect the stability, conductivity, water sorption, and morphologies.

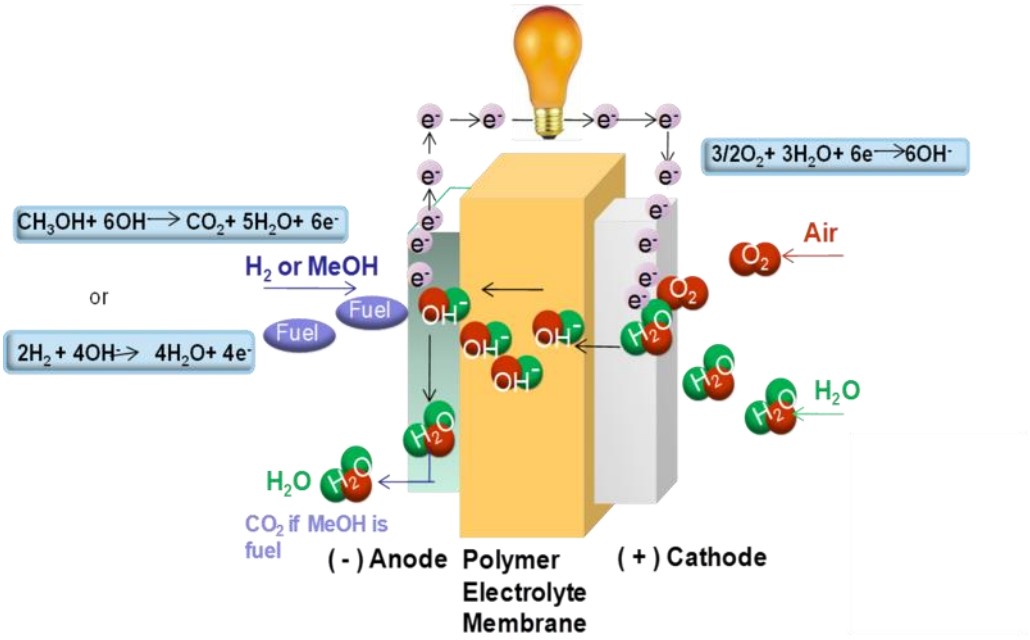


**Figure 5: Alkaline Anion Exchange Membrane Fuel Cell.**

**Figure adapted from**

**http://en.wikipedia.org/wiki/Alkaline_anion_exchange_membrane_fuel_cells.**

One of the most widely quoted concerns with anion exchange membranes (AEMs) is the lack of chemical stability. The hydroxide anion ($OH^-$) is a strong nucleophile at elevated temperature, which may lead to direct $S_N2$ substitution reaction as shown. More importantly, Hofmann elimination dominates in many cases of ammonium degradation (Figure 6). Currently, most stable ammonium ions described in the literature were designed with the absence of $\beta$-hydrogens.[14,15]

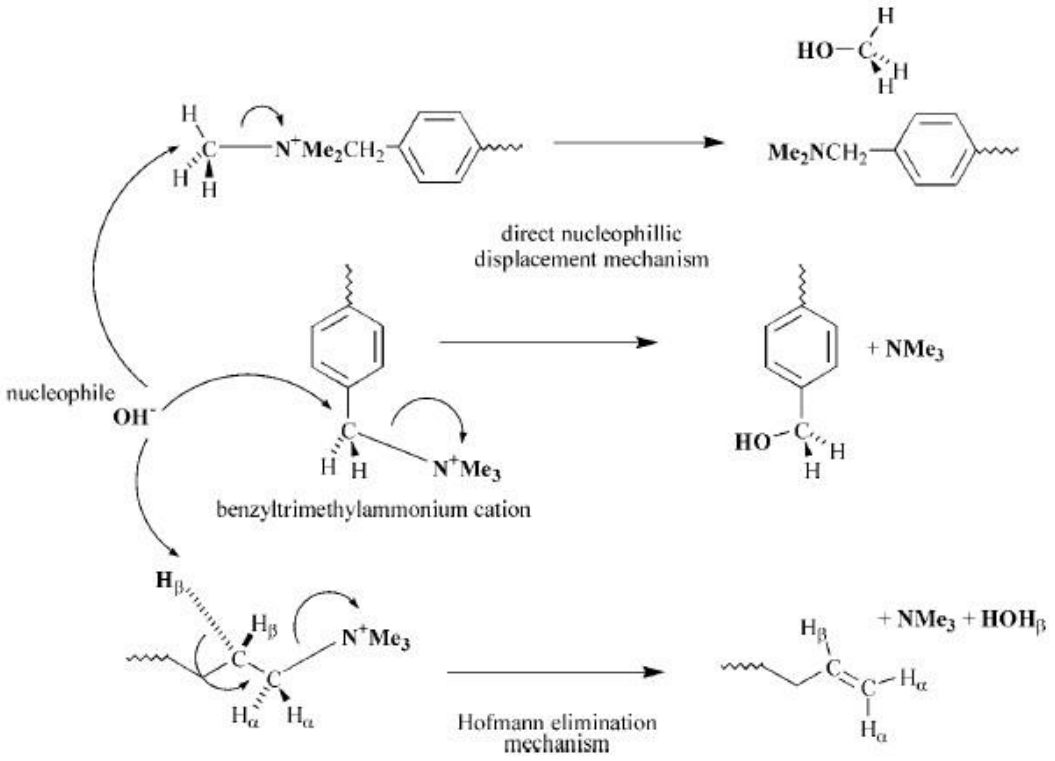


**Figure 6: Degradation Mechanism of Ammonium Groups by $OH^-$.**

**Figure adapted from Ref 4.**

Specially designed phosphonium cations have also been reported, with bulky side groups which not only sterically hinder nucleophilic attack, but also strongly donate electron density to stabilize the positively charged center.[16,17]

### 1.4 Synthetic Anion Exchange Membrane (AEMs)

#### 1.4.1 Anion Exchange Resins

Many reported anion exchange resins are based on copolymers of styrene and divinylbezene.[18] Chloromethylation chemistry was applied to produce benzyl chloride groups, which were quaternized afterward. The polystyrene backbone is believed to be chemically stable, however, they may not provide good mechanical properties when serving as membranes. The work by Tomoi et al. should be noted, since it carefully investigated the stability of different

ammoniums.[14] It was found that a long alkyl spacer between the ammonium ion and phenyl ring can further enhance alkaline stability. This was attributed to the elimination of a benzylic carbon attached directly to the onium ion which is susceptible toward nucleophilic attack.

### 1.4.2 Polysulfones & Polyethersulfones Random Copolymers

Polysulfones and polyethersulfones are thermoplastic materials with high toughness and good chemical stability, and dimensional integrity at elevated temperature. These are the most widely investigated polymer backbone used for AEMs. These polymers are amorphous membranes with incorporated guanidinium,[19] ammonium,[20–22] imidazolium,[23] and phosphonium ions.[17] The incorporation of cations onto the polymer scaffold can be achieved by a number of synthetic methods. The functionalization of the polymer precursors used a Friedel-Crafts reaction of chloromethylation with chloromethyl methyl ether catalyzed by Zn(II). Quaternization of the benzyl chloride with either an amine, guanidine or imidazole was performed to yield polymers A,[20] B,[19] and C[17] shown below in Figure 7). Suzuki coupling was also reported as a synthetic to install the ionic groups.[24]

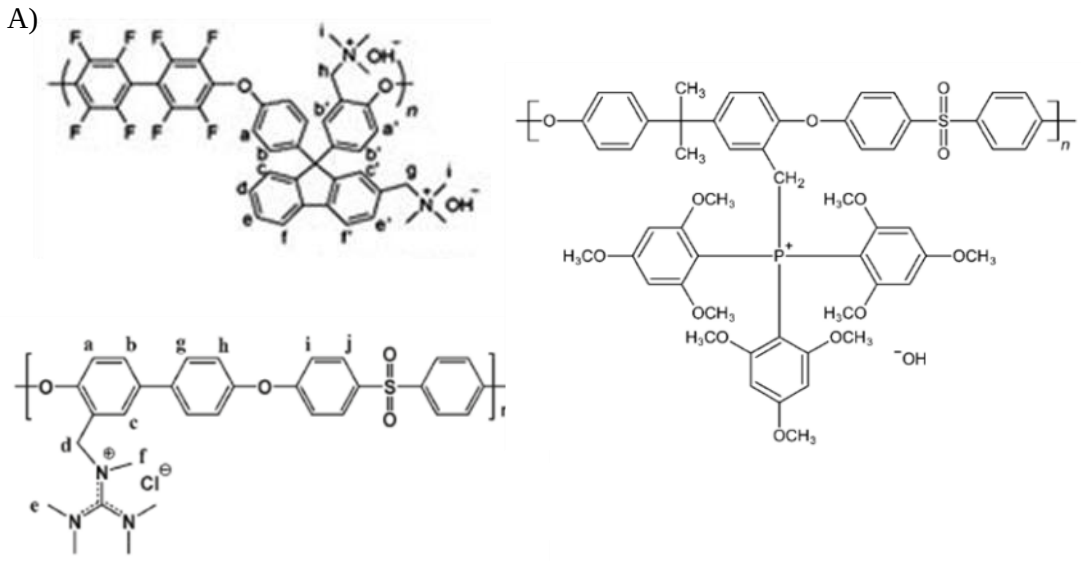


**Figure 7: Quaternized Poly(ether)sulfones.**

**A) Poly(arylene ether sulfone) with ammonium substituted fluorenyl groups;[20] B) poly(arylene ether sulfone) with pendant guanidinium;[19] C) polysulfone with pendent phosphonium.[17] Figures adapted from Ref 20, Ref 19, and Ref 17, respectively.**

A second preparative strategy can be applied to polymers with tolyl functionality present in the precursor polymer. Random bromination of the Ph-$CH_3$ units can be achieved by reaction with NBS or $Br_2$.[25] Quaternization with a tertiary amine again results in the ammonium ion form of the polymer for example, the polymer in Figure 8.

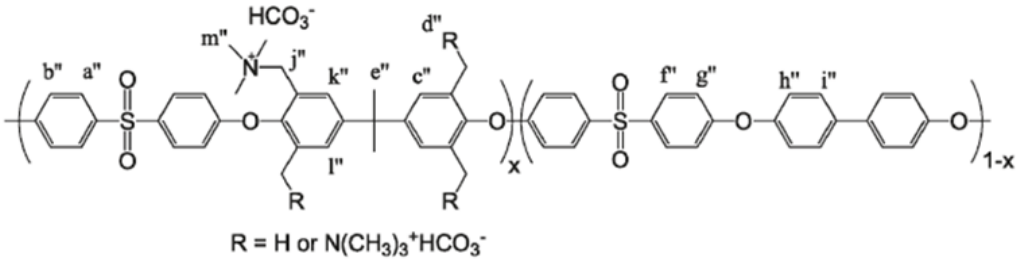


**Figure 8: Benzyltrimethylammonium Decorated Polysulfone.**

**Figure adapted from Ref 25.**

The direct polymerization of monomers with tertiary amines, which can subsequently be quaternized with iodomethane, is displayed in Figure 9.[26]

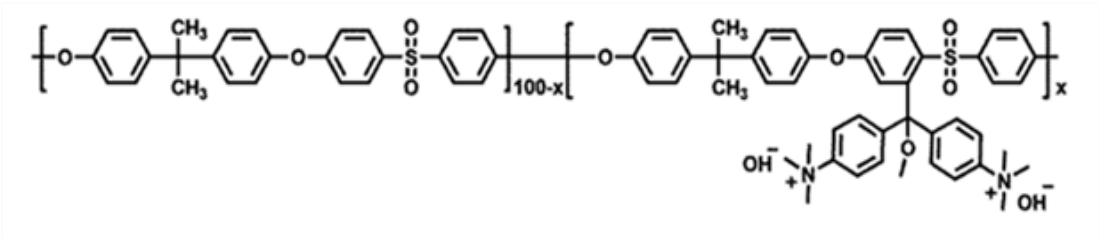


**Figure 9: Phenyltrimethylammonium Functionalized Polysulfone.**

**Figure adapted from Ref 26.**

Cationic monomer was directly polymerized (Figure 10). The poly(fluorene ether sulfone) based material showed impressive hydroxide conductivity (42 mS/cm at 60 $^{o}$C), which may be partly due to the relatively high water uptake, which not only give the anions better mobility but also the chance to form ion transport channels.[27]

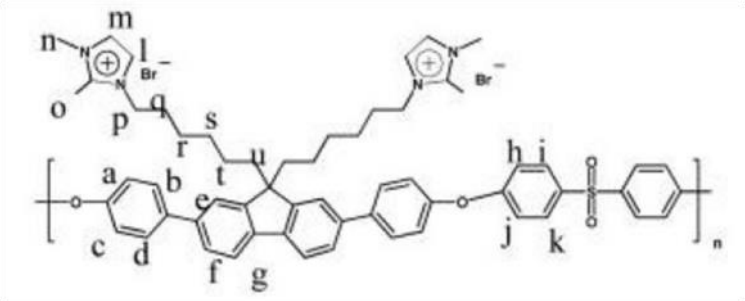


**Figure 10: Poly(fluorene ether sulfone) Containing Imidalozium.**

**Figure adapted from Ref 27.**

The robust modification reactions and polymer stability endows poly(ether)sulfone great potential in AEMFC application. However, the random copolymer nature limits the possibility in adjusting the polymer architecture for investigation of structure-property relationship, and tunability of the morphology, water management, and mechanical properties.

### 1.4.3 Polyethylene Based Random Copolymers

Polyethylene based materials exhibit excellent electrochemical and alkaline stability. Their semi-crystalline nature affords them good mechanical properties. One preparative strategy is to utilize coordination insertion polymerization, while another strategy requires post-polymerization hydrogenation on precursor polymers prepared from Ring-Opening Metathesis Polymerization (ROMP). Due to the hydrophobicity of the polyethylene backbone, these membranes were insoluble in water or aqueous methanol. In regards to anion transport, linear polyethylene materials with pendant ammonium (A in Figure 11) and phosphonium (B in Figure 11) cations showed $OH^-$ conductivities of 22 mS/cm at 22 °C and 65 mS/cm at 50 °C, respectively.[16,28] These materials were reported to be highly stable and processable, however, also their preparation protocol suffered from multistep synthetic procedure.

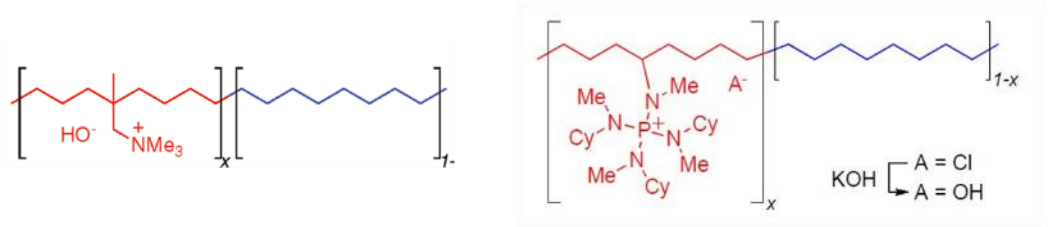


**Figure 11: Polyethylene Based AEMs.**

**The backbones were anchored with A) ammonium and B) phosphonium cations. Figures adapted from Ref 28 and Ref 16, respectively.**

### 1.4.4 Other Non-crosslinked Amorphous Membranes

Polyphenylene precursors, which are prepared by Diels-Alder polymerization and subsequent bromination, can be cast as membranes from chloroform solution and then quaternized with aqueous trimethylamine solutions to install benzyltrimethylammonium groups.[29] The water uptake was high (<130%) and hydroxide conductivity values as high as 86 mS/cm were achieved at 80 °C. Poly(phenylene oxide), which is another high performance thermoplastic, was brominated,

quaternized with imidazole and cast to form a membrane.[30] The conductivity achieved with this backbone was reported to be 70 mS/cm at 60 °C, close to the conductivity values reported for polysulfone materials. These two materials are displayed in Figure 12. Chu et al. reported a quaternized material derived from the terpolymer of methyl methacrylate, butyl acrylate and vinylbenzyl choride.[31] However, the longer term stability of acrylate polymers in a caustic environment will be problematic. Blends of polycation and polyanion have also been reported, where both ionomers dissolve in water while the blends after removal of excess base were insoluble, displayed hydroxide conductivities between 9 and 13 mS/cm at 21 °C.[32]

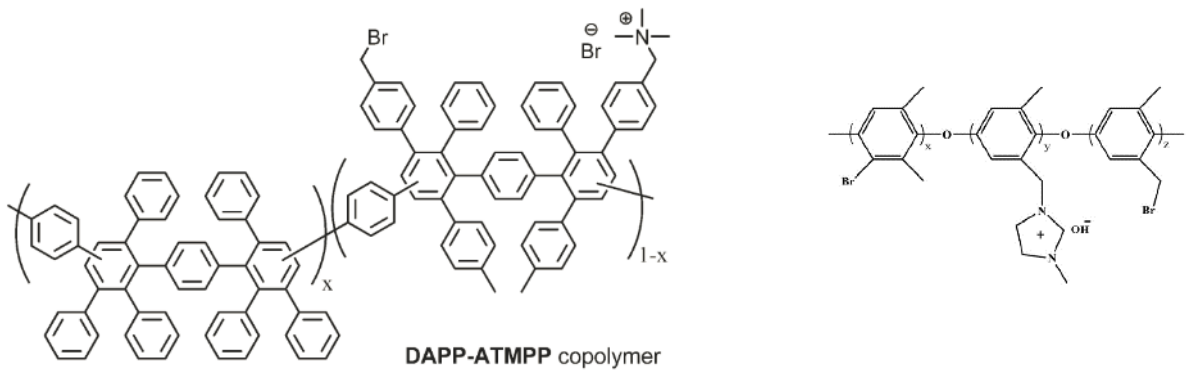


**Figure 12: Polyphenylene and Poly(phenylene oxide) Based AEMs.**

**A) Polyphenylene with ammonium and B) Polyphenylene oxide with imidazolium.**

**Figures adapted from Ref 29 and Ref 30, respectively.**

### 1.4.5 Crosslinked Amorphous Membranes

In order to achieve suitable ion conductivity, a high ion exchange capacity (IEC) is important. However, this often brings several problems. First, the high hydrophilicity due to ionic groups often makes the membrane dimensionally unstable in water. Second, it lowers solvent resistance, especially in aqueous methanol, which may cause extensive membrane swelling, suffers from severe methanol crossover. Chemical crosslinking is one method to solve these problems.[33]

In some cases, the crosslinking take place within the hydrophobic segment. A typical method is to use dicyclopentadiene (DCPD) as the comonomer in ROMP based membranes, which serves as a crosslinker. With this methodology, reasonable conductivity was achieved, as high as 14 mS/cm for $HCO_3^-$ conductivity with a Ruthenium based cation at 70 °C (A in Figure 13),[34] and 28 mS/cm for $OH^-$ conductivity with an ammonium cation at 50 °C (B in Figure 13).[35] In other cases, the membranes were crosslinked at the ionic site, with dual- or multi-functional cations often involved. A cyclooctene (COE) based membrane (C in Figure 13) reported by Coates et al. showed an excellent $OH^-$ conductivity as high as about 140 mS/cm at 70 °C.[36]

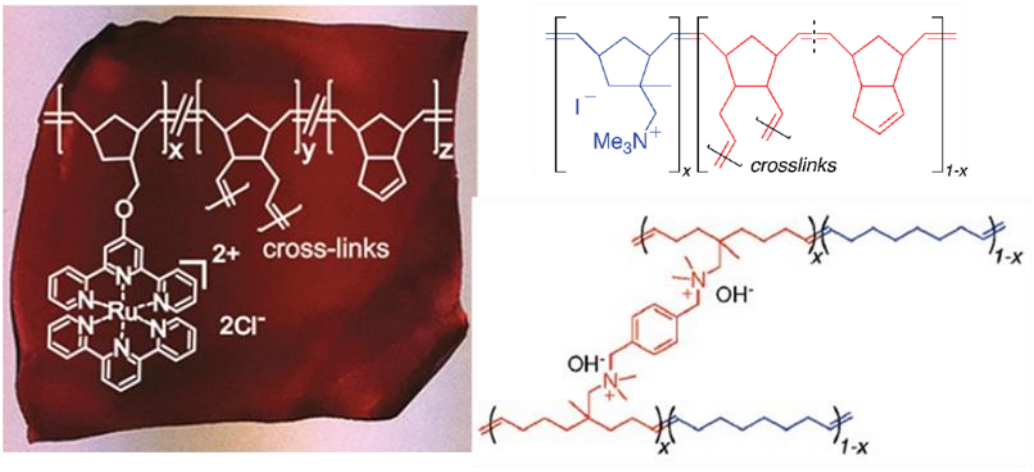


**Figure 13: Crosslinked AEMs Based on PolyDCPD.**

**AEMs with A) Ruthenium and B) ammonium cations; C) crosslinkable ammonium monomer. Figures adapted from Ref 34, Ref 35, and Ref 36, respectively.**

A special case of crosslinked AEMs is benzyltris(2,4,6-trimethoxyphenyl)phosphonium, where the phenyl rings are electron-rich, although they are adjacent to the positively charge center and thus provided the chance to use Friedel-Crafts reaction in membrane self-crosslinking. In the report by Yan et al.,[37] a crosslinked phosphonium membrane showed largely decreased swelling and increased conductivities. Photocrosslinking was also reported to result in membranes with reasonable conductivities.[38]

These membranes usually provide good mechanical integrity and controlled water sorption, which are extremely important from the practical viewpoints of AEMs. However, since the processability is sacrificed, the membrane processing is limited, which is important to achieve different thickness, shapes, and alignment and tune the mechanical and electrochemical properties. It also leads to loss of the possibility of using the membrane as a catalyst ink, which is important to improve the contact between the electrodes and electrolyte membrane and thus the overall device performance.[39] Moreover, the crosslinked membranes usually provides limited information on the structure-property correlation, and thus it has been difficult to understand the transport of ions in a crosslinked membrane. One specially designed crosslinked membrane will be presented in Chapter 2, in which the effect of ion arrangements on conductivities are investigated.

### 1.4.6 Block copolymers (BCPs)

In BCPs for PEMs have been explored extensively, however in AEMs there have been only a few reports of BCPs. These BCP have all been synthesized by controlled radical polymerization. Most of the reports were based on polystyrene as the hydrophobic block, while poly(hexylmethacrylate) was reported by Hickner and coworkers, the long term alkaline stability of which, however, is suspect.[40] In Elabd's work, surprisingly, conductivity achieved with block copolymers was reported to be even higher than that for the corresponding homopolymer, which was ascribed to a nano-confinement.[41] In previous work in the Coughlin research group, polymethylbutylene block copolymers were synthesized via nitroxide mediated polymerization and multi-step modification. This study provided one efficient method to avoid the use of a rigid polystyrene matrix while still retaining good chemical stability (A in Figure 14). Multiblock copolymers based on polycondensation were reported as well (for example, B in Figure 14).[42] The highest hydroxide conductivity was 150 mS/cm at 60$^{o}$C, which was attributed, in part, to a microphase separated morphology. The BCP systems provide the characteristics to investigate how

the material morphology affects the membrane performance, including conductivities, water diffusion, and mechanical properties. More discussion on BCPs will be in Chapter 3 and 4.

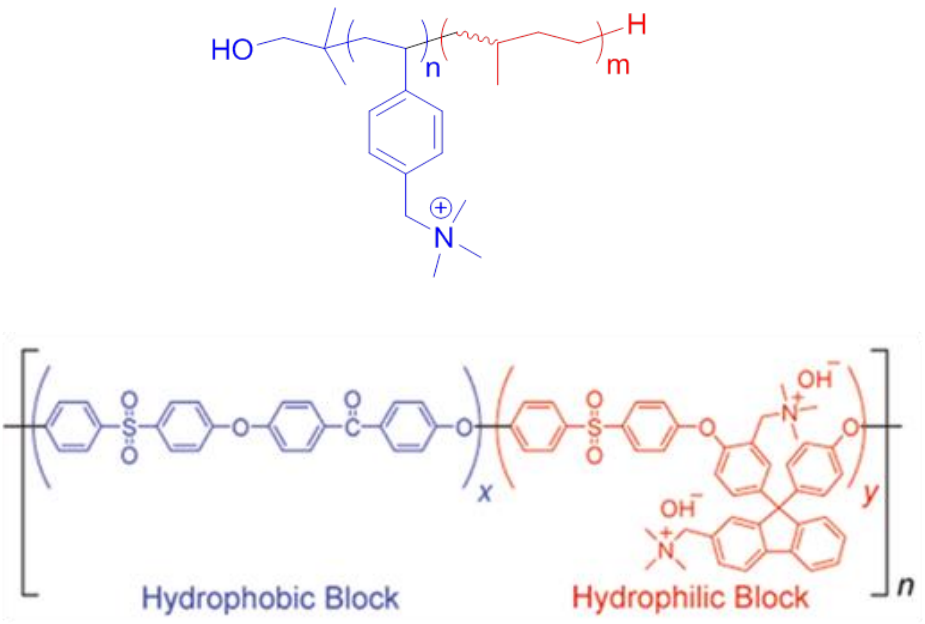


**Figure 14: Examples of BCP Based AEMs.**

**A) polymetylbutylene based diblock copolymer containing ammonium cations; B) Multiblock polysulfone based AEM.**

**Figures adapted from Tsung-Han Tsai's dissertation and Ref 42, respectively.**

### 1.5 Outline of the Dissertation

Conductivity is the most important property of AEMs, while reasonable water uptake, chemical stability and mechanical property should also be taken into consideration. In this dissertation, polymer materials with different architectures will be synthesized to explore structure-property relationships with a goal being to enhance conductivity. One method for conductivity enhancement is to pre-organize the ions in a crosslinked membrane, which can assist the formation of ion transporting pathways. This method will be described in Chapter 2, where the synthetic

protocol and structure-property characterization are presented. In Chapter 3, a series of block copolymers containing phosphonium ions are documented, with which ordered morphologies were achieved and are significantly affected by the bulky size and charged density of the charged block. This provides the chance to investigate the effect of various morphologies on ion conduction. Chapter 4 is focused on the synthesis and characterization of triblock copolymers with poly(vinylbenzyltrimethylammonium) outerblocks and polycyclooctene (PCOE) midblocks. The melting point of PCOE is around 50 $^{o}$C, which enables the direct comparison of semicrystalline and amorphous hydrophobic block on membrane performance. Beside polycation block copolymers, Chapter 5 documents the morphology of salt doped star block copolymers, synthesized by controlled radical polymerization, and demonstrates that the polymer architecture facilitates microphase separation. A major work in the former chapters is to characterize the morphology in bulk materials, while thin film morphology is investigated in Chapter 6 as well. The synthesis of photo-cleavable block copolymers is reported and thin films of these were applied to regional UV exposure to achieve multi-pattern on a single wafer. From the synthesis of block copolymers mentioned above, a synthetic methodology by single unit insertion technique was developed, and is discussed in Chapter 7 to provide a feasible pathway towards high efficiency functionalization of reversible fragmentation-addition chain transfer radical polymerization (RAFT) chain transfer agents (CTAs).

# CHAPTER 2

# CROSSLINKED ANION EXCHANGE MEMBRANES WITH PRE-ORGANIZED CATIONS

## 2.1 Polyelectrolyte Materials

Polyelectrolytes, polyelectrolyte hydrogels, and ion exchange membranes all have mobile counter ions in an aqueous environment. The diffusion of the counter ions depends on numerous factors such as hydration and ion organization that are, in turn, influenced by the nature of the oppositely charged polymer. Selective ion transport materials are required for a number of advanced devices such as, fuel cells,[4] electrolyzers,[43] rechargeable batteries,[44] and water purification membranes.[45] Polyelectrolytes are ionizable polymers, which not only possess some key properties of but also differ from neutral polymers and salts. Polyelectrolytes have been studied in dilute solution,[46] and also in assembled nanostructures i.e. micelles (particles and layer by layer thin films).[47–49] Due to their dynamic nature polyelectrolytes find applications in drug and gene delivery, or as surfactants for latex stabilization. However, a lack of dimensional stability limits their applicability for use in selective ion transport. Dimensionally stable polyelectrolyte hydrogels can be prepared by either chemical or physical crosslinking to form macroscopic hydrogels.[50,51] The polyelectrolyte network in a hydrogel provides controlled diffusivity by electrostatic interactions, while the major component, i.e. water imparts high mobility for soluble molecules as well as ions.[52,53] However, these hydrogels are limited in applications requiring transport/separation, at least in part due to a lack of mechanical toughness caused by high water content.

Ion exchange membranes are polyelectrolytes that are designed to exhibit reduced water sorption to suppress the tendency to form gels or dissolve. Practical strategies include preparing random copolymer or block copolymer architectures to reduce water sorption thus confining the polyelectrolyte to the solid state. The ionic groups generally possess strong immiscibility with

hydrophobic matrix. The strong segregation strength and Columbic interactions drive the ionic segments to self-assemble into micro-domains that is separated from the hydrophobic phase. In a random copolymer, such as Nafion®, the ions form clusters, between which the percolation was demonstrated to be critical for fast ion transport.[8,10,54] In a typical block copolymer system, the ionic block aggregates into microdomains. The nanophases can facilitate anion conduction, while it also suffers from alignment and grain boundary conditions.[55,56] In both cases, the installation of the hydrophobic segments confined the polyelectrolyte/water phase into isolated nano-domains. This is a result from the absence of the polyion chain network in a polyelectrolyte hydrogel. Thus, it is necessary to explore a methodology to bridge polyelectrolyte hydrogels and ion exchange membranes, in other words, to maintain the polyelectrolyte network while improving the mechanical integrity.

In this chapter, we demonstrate that enhanced ion conductivities by designing a material that contains a connected ion networks to direct counterion transport. A versatile method was devised to organize the ionic groups in the material. Crosslink density and the degree of connectivity are prescribed by the synthesis of a precursor polymer. A one-step ring-opening olefin metathesis casting/crosslinking method employing the precursor polymer and a cyclic olefin was utilized to lock the network structure. Quaternization of the latent functionality on the precursor polymer installs the ionic species with a pre-determined ion exchange capacity, and controllable water distribution.

## 2.2 Experimental Section

### 2.2.1 Materials

Propargyl *para*-vinylbenzyl ether (StYne),[57] 5-azidocyclooctene (AzCOE),[16] and 2-cyano-2-propyl butyl trithiocarbonate (O-CTA)[58] were synthesized via literature reported methods. 4-Chloromethylstyrene (4CMS) was purchased from Sigma Aldrich and passed through a basic $Al_2O_3$

column to remove inhibitors. Azobisisobutyronitrile (AIBN) was recrystallized from methanol and stored at 0 °C before use. Other reagents were used as received without further purification.

### 2.2.2 Precursor Copolymer Synthesis

First, the random copolymers of 4CMS and StYne were synthesized. A representative process is as following. 1.51 g 4CMS (9.89 mmol), 0.71g StYne (4.11 mmol), 76 mg O-CTA (0.34 mmol) and 6 mg AIBN (0.037 mmol) were added into a reaction vial with a magnetic stirrer bar. The mixture was degassed by purging with nitrogen flow for at least 15 minutes and then the vial was sealed with a rubber septum. The vial was placed into an oil bath at 70 °C. After reacting for 17 hours, the reaction was quenched to 0°C and opened. After precipitation twice into hexanes, the copolymers poly(4CMS-*ran*-StYne) were dried in vacuum for 2 days. $^1$H NMR shows the compositon to be poly(4CMS$_{22.6}$-*ran*-StYne$_{8.1}$). The MW and Đ determined by GPC against polystyrene standards are 4.4 kg/mol and 1.14, respectively.

In the second step, poly(4CMS-*ran*-StTCOE) was synthesized. Into a two-necked flask, 570mg poly(4CMS$_{22.6}$-*ran*-StYne$_{8.1}$) (0.95 mmol alkyne groups), 171 mg AzCOE (1.12 mmol) and 77mg bipyridine (0.49 mmol), 4 mL toluene was charged with a magnetic stirrer bar. Sealed with rubber septums, a long needle with nitrogen penetrating the septum was used to purge the mixture for 10 minutes. The septum without needle was removed and 20 mg Cu(I)Cl (0.20 mmol) was added with nitrogen flow. After the flask being sealed again and purged with nitrogen for another 10 minute, the needles were removed and the reaction mixture was stirred at room temperature in darkness for 2 days. Finally, the mixture was passed through basic $Al_2O_3$ to remove copper catalyst and precipitated into hexanes twice to yield the product. $^1$H NMR confirmed quantitative conversion of alkyne groups. The MW and Đ determined by GPC against polystyrene standards were 5.1 kg/mol and 1.21, respectively.

### 2.2.3 Membrane Preparation

At 0 °C, 150 mg poly(4CMS$_{239}$-*ran*-StTCOE$_{12}$) and 150 mg DCPD was dissolve in 5mL chloroform. 4 mg Grubbs' 2$^{nd}$ generation catalyst (G2) in 1 mL chloroform was transferred into the polymer solution and stirred violentaly for 30 seconds. The solution was quickly cast onto a clean Teflon® sheet at 20 °C and covered by a glass petri dish to reduce solvent evaporation rate. After 12 hours, the film was carefully peeled off and dipped into 45 wt% $Me_3N$ aqueous solution for quaternization. After reacting at room temperature for 2 days and 40 °C for 24 hours, the membrane was washed with pure water and annealed in water at 60 °C for 24 hours. Transmission IR shows the benzyl chloride positions were quantitatively converted.

### 2.2.4 Ion Conductivity Measurement

The in-plane conductivity of the membranes was calculated using electrochemical impedance spectroscopy to measure membrane resistance as given by the equation below.

$$\sigma = l/(R*w*t)$$

Where R is the membrane resistance, l is the distance between the electrodes, w is the width of the membrane samples, and t is the thickness of the sample. Impedance spectra were obtained over a frequency range of 1 to $10^6$ Hz using a four-electrode test cell connected to a BioLogic VMP3 multi-channel Potentiostat. The measurements were made in a TestEquity environmental chamber to control sample temperature and humidity. The resistance of the membrane was determined from the low frequency intercept of the Nyquist impedance plot. Experiments were performed at constant 95% RH, varying temperature from 30-90 °C.

For $OH^-$ tests, to ensure that we were measuring the real $OH^-$ conductivties instead of carbonate/bicarbonate, sophisticated exchange/protection procedure was designed. First, the membrane was ion exchanged into $OH^-$ form by immersing in KOH aqueous solution and then mounted to the testing cell after washing with de-ionized water. After the installation, the AEM

was the AEM was ion exchanged further into $OH^-$ form with KOH aqueous solution to exclude the as-formed carbonate/bicarbonate, and finally washed thoroughly inside the chamber.

### 2.2.5 Small Angle X-ray Scattering (SAXS)

The experiments were performed at The Basic Energy Sciences Synchrotron Radiation Center (BESSRC) at the Advanced Photon Source at Argonne National Lab on beamline 12 ID-B. A Pliatus 2M SAXS detector was used to collect scattering data with an exposure time of 1 s. The X-ray beam had a wavelength of 1 Å and power of 12 keV. The intensity (I) is a radial integration of the 2D scattering pattern with respect to the scattering vector (q).

Temperature and humidity were controlled within a custom sample oven as described previously. The humidity of the sample environment was controlled by mixing heated streams of saturated and dry nitrogen. Sample holders were inserted into an oven environment of 60 $^oC$ and <10% relative humidity. The samples were allowed to dry for 40 minutes before X-ray spectra were taken. Relative humidity was then ramped to 25%, 50%, 75% and 95% while the temperature was maintained at 60 $^oC$. The equilibrium time before taking an X-ray spectrum was 20 minutes between dry, 25% and 50% and increased to 40 minutes between 50%, 75% and 95%.

### 2.2.6 Membrane Degradation Test

A piece of membrane was cut into several pieces of 5~10 $cm^2$. One cut piece was ion exchange thoroughly with $NaNO_3$ solution and then the solution was titrated with standard $AgNO_3$ aqueous solution. The rest of the cut pieces were immersed into 1 mol/L KOH aqueous solution and heated to 80$^oC$. After a certain time period, a piece was taken out and washed three times with deionized water before applied to ion exchange in KCl aqueous solution. After ion exchange, the solution was titrated with standard HCl solution. And the membrane in $Cl^-$ form was ion exchanged to extract the $Cl^-$ with $NaNO_3$ solution. The $NaNO_3$ solution was titrated with $AgNO_3$ solution.

## 2.3 Results and Discussions

### 2.3.1 Synthesis

To prepare crosslinked membranes with connected ammonium cations, a neutral precursor copolymer was designed. The "clickable" monomer, StYne, was copolymerized with the quaternizable monomer, 4CMS, mediated by RAFT polymerization to synthesize poly(StYne-*ran*-4CMS). Due to the relative inertness in radical polymerization, the alkyne groups were preserved. After polymerization and purification, Cu(I) catalyzed Huisgen [3+2] cycloaddition was used to "click" AzCOE to the StYne units (Figure 15 and 16). By adjusting the ratio of StYne in the random copolymers, various extents of connectivity between 4CMS and density of crosslinkable units were achieved.

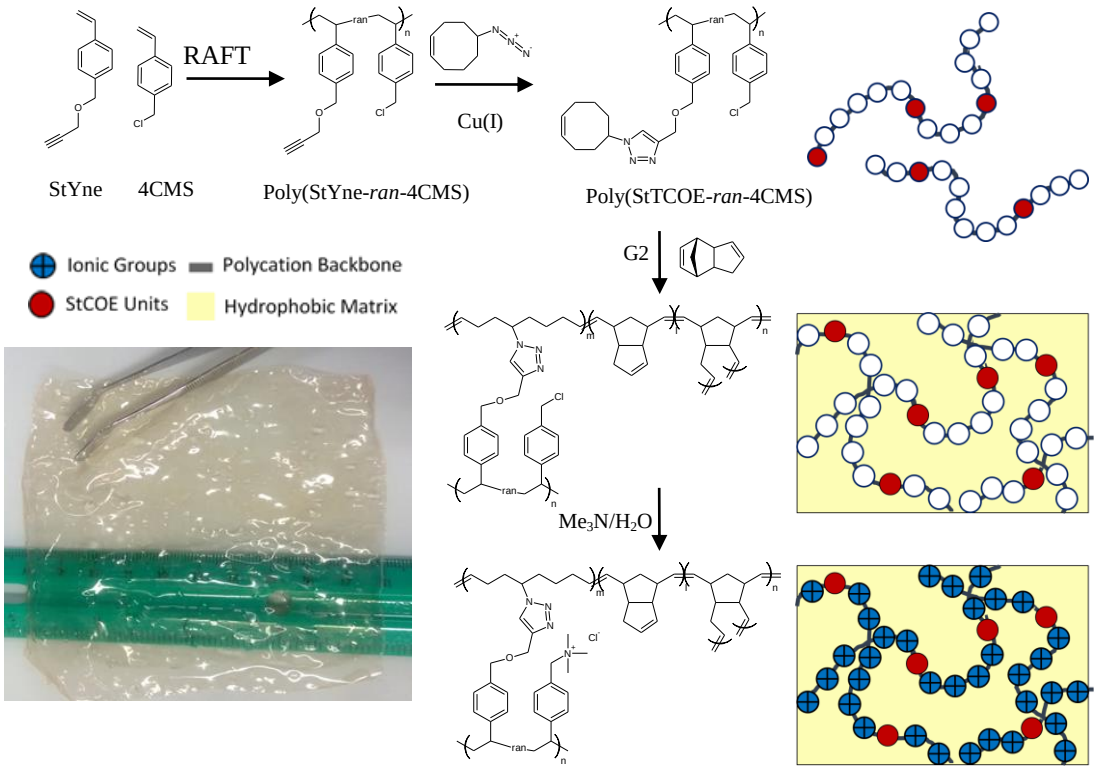


**Figure 15: Synthetic Scheme of DXCAm Membranes.**

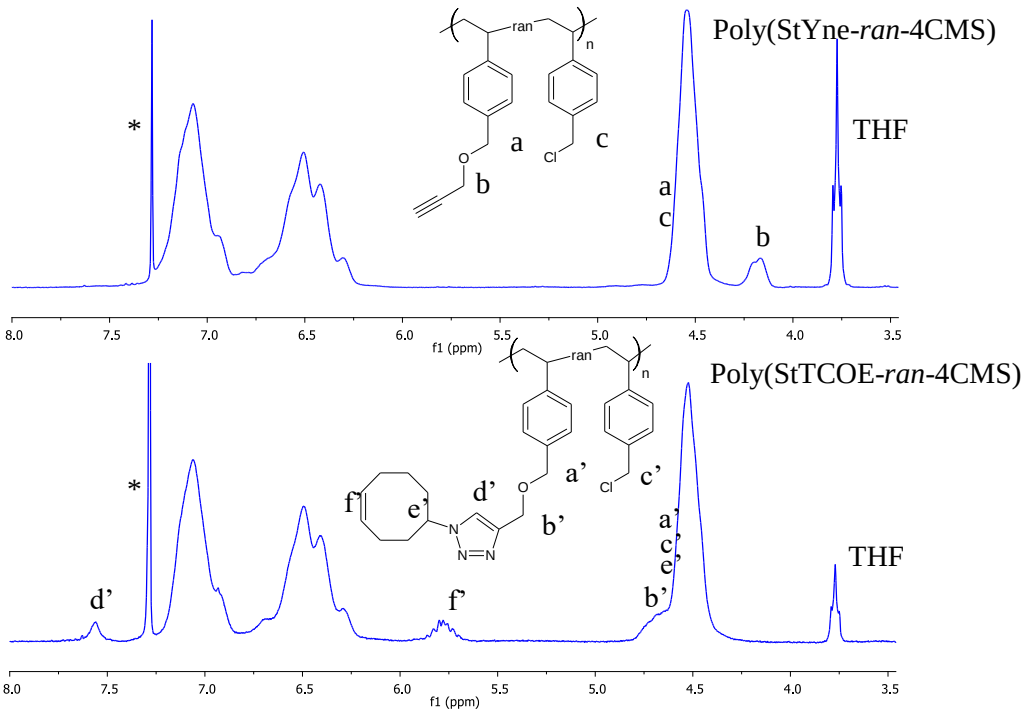


**Figure 16: $^{1}$H NMR of Poly(StYne-*ran*-4CMS) and Poly(StTCOE-*ran*-4CMS).**

In the membrane casting/crosslinking, Grubbs' 2$^{nd}$ generation catalyst (G2) was used, because of its air stability, excellent tolerance to functional groups and high reactivity. The amount of G2 was typically at a mole ratio of [G2] to [StTCOE] = 1:10. Dicyclopentadiene (DCPD) was chosen as the comonomer to form a crosslinked network. A solution of G2 was added to a chloroform solution of DCPD and poly(4CMS-*ran*-StTCOE) at 0 $^{o}$C. After stirring vigorously for 1 minute, the homogeneous solution was cast onto a clean PTFE sheet. Covered by a glass dish, the solvent evaporation was decelerated and the polymer network slowly solidified at 20 $^{o}$C. The neutral precursor polymer was used instead of the quaternized counterpart for solubility and minimization of phase separation during film formation. After 12 hours, the film was peeled off from the polytetrafluoroethylene sheet and immersed into aqueous $Me_3N$ solution (50 wt%) for complete quaternization of 4CMS units. Finally, the quaternized membrane was soaked in deionized water at 60 $^{o}$C for 24 h to achieve a DCPD crosslinked membrane with connected ammonium cations (DXCAm). The theoretical IEC can be systematically tuned by varying the ratio of DCPD to neutral precursor. The highly efficient crosslinking chemistry by ROMP allows for

preparation of membranes with IEC as high as 3.2 mmol/g. Membranes with higher IECs swelled excessively in water and lost mechanical integrity. Listed in Table 1 are the membranes which were synthesized and characterized in this work. The water-uptake (WU) was measured at room temperature and 100% RH, unless specifically stated.

**Table 1: Summary of DXCAm Membranes.**

| Membrane # | mol% of StTCOE in Precursor | IEC (mmol/g) | WU (wt%) |
|---|---|---|---|
| DXCAm-7%-3.0 | 7 | 3.0 | 70[a] |
| DXCAm-26%-2.0 | 26 | 2.0 | 50 |
| DXCAm-5%-1.5 | 5 | 1.5 | 40 |
| DXCAm-5%-2.0 | 5 | 2.0 | 55 |
| DXCAm-5%-2.5 | 5 | 2.5 | 85 |
| DXCAm-5%-2.9 | 5 | 2.9 | 116 |
| DXCAm-5%-3.2 | 5 | 3.2 | 447 |

[a]Measured in water vapor at 95%RH and 60 $^{o}$C.

### 2.3.2 Characterization

The DXCAm membranes are dual networks, a hydrophobic network formed by polyDCPD, and the other network is overlapping hydrophilic polycation. The networks are linked together by covalent bonds between the polyDCPD and StTCOE. This crosslinking is necessary in order to suppress phase separation (Figure 17A). Despite the limited chain mobility, the incompatibility between the two components provided the driving force for partial microphase separation. For example, membrane DXCAm-7%-3.0 was synthesized from a precursor with 7 mol% StTCOE and had an IEC of 3.0 g/mol. Figure 17B shows the small angle X-ray scattering (SAXS) pattern of it at 60 $^{o}$C and varied hydration conditions. In dry state, a shallow peak was observed in SAXS profiles at medium q range. The width of the peak indicated the lack of order in the self-assembled structure. The d-spacing was on the scale of 20 nm, which was comparable with other DXCAm

membranes. Considering the large spacing, the feature was likely due to microphase separation instead of ion clustering. The low peak intensity was a result of the lack of well-defined boundary between the ionic domain, if any, and hydrophobic matrix. When the membrane was treated with water vapor, the peak intensity decreased, which was partly attributed to more uniform distribution of ionic groups. However, the decrease in scattering contrast due to the absorption of water should be noted. At high q regime (~0.3 $Å^{-1}$), a broad shallow peak raised upon water swelling and it was assigned to the water domain[59,60].

The $Cl^-$ conductivities were measured by impedance spectroscopy. The conductivity values were 59, 71 and 79 mS/cm at 65, 80 and 90 $^oC$, respectively, with RH fixed at 95% (Figure 17C). The conductivities were higher than any halide conductivities previously reported and thus strongly suggested that the ion network design facilitated efficient anion transport.

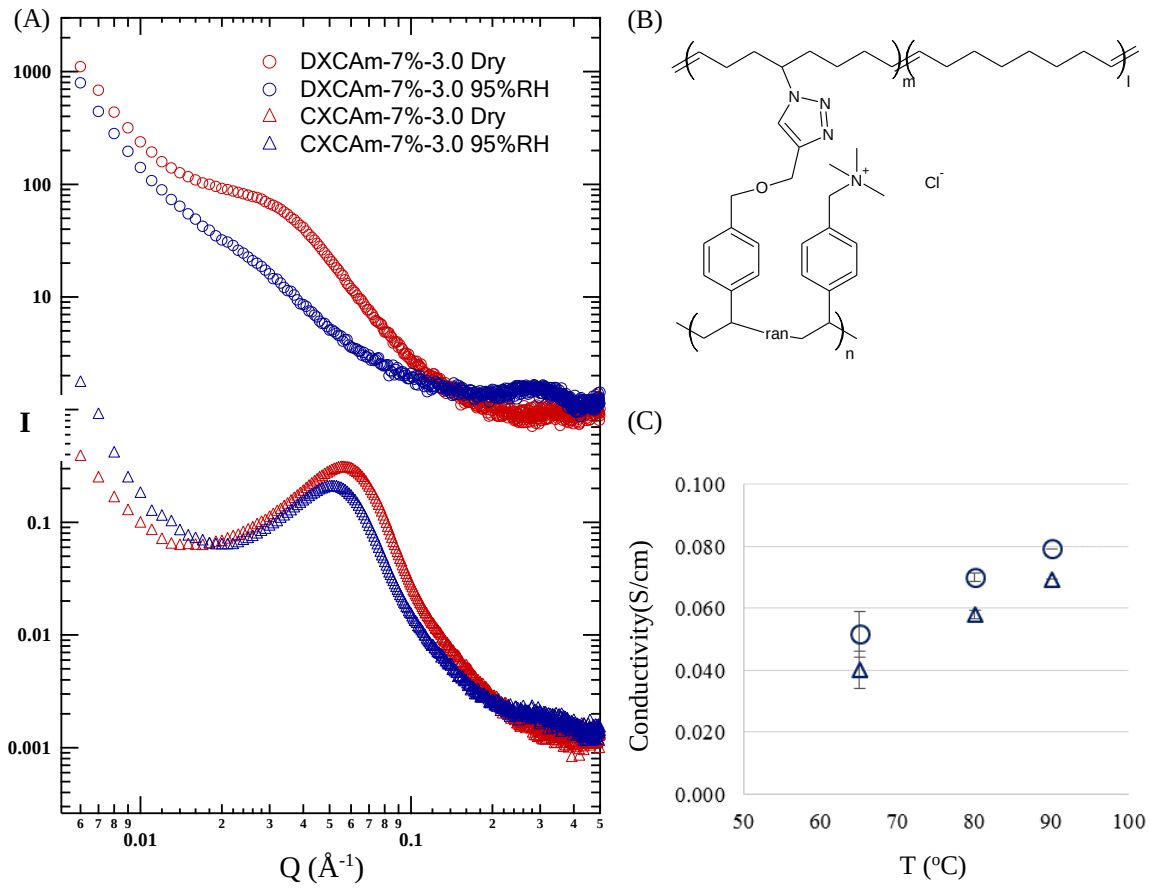


**Figure 17: Characterization of DXCAm-7%-3.0 and CXCAm-7%-3.0. A) SAXS profiles of DXCAm-7%-3.0 (circle) and CXCAm-7%-3.0 (triangle) at 60oC; B) the chemical structure of CXCAm-7%-3.0; C) Cl- conductivities of DXCAm-7%-3.0 (circle) and CXCAm-7%-3.0 (triangle) plotted against temperature.**

### 2.3.3 Effect of Polymer Structure

To demonstrate the effect of the polyDCPD network, a comparison membrane CXCAm-7%-3.0 (Figure 17B) with an IEC being 3.0 mmol/g was synthesized. Utilizing the same precursor as that in DXCAm-7%-3.0 ensured the formation of an analogous polycation network. The hydrophobic matrix consisted of a rubbery polyCOE, which showed no crystallization or melting transition in differential scanning calorimetry (Figure 18) due to the random copolymer structure,

instead of the thermosetting polyDCPD. For CXCAm-7%-3.0, a strong peak was detected by SAXS at controlled environmental conditions (Figure 17A). The spacing was determined to be 11.2 nm at dry conditions, indicating that the polycations were able to microphase separate with polyCOE. Being treated in humid air (>90% RH), the peak intensity slightly decreased. The d-spacing increased to 12.1 nm, which was attributed to the swelling of ion-rich domain. Interestingly, at 95% RH and 60 $^{o}$C water sorption was measured to be 66 wt%, similar to that in DXCAm-7%-3.0 (70 wt%). We attributed it to the fact that water was absorbed primarily within the ion rich domain of CXCAm-7%-3.0. The conductivities were measured to be 40, 58, and 69 mS/cm, at 65, 80, and 90$^{o}$C respectively (plotted in Figure 17C), slightly lower than those of DXCAm-7%-3.0 at similar testing conditions. It was explained by the constrained ion transport within the ion rich domains, since ion diffusion through hydrophobic polyolefin domain was extremely slow. However, membrane CXCAm-7%-3.0 still displayed comparable anions conductivities with DXCAm-7%-3.0. This suggested that in this system, microphase separation had only minor effect on anion transport. Despite strong segregation, the connected cation network still existed in this material. Upon water sorption, the polycation segments could act as anion transport tunnels to facilitate percolation.[61] The comparison between DXCAm-7%-3.0 and CXCAm-7%-3.0 demonstrated the effect of matrix on microphase separation and water distribution. However, the morphology had only a minor effect on anion conductivities, at least in these materials.

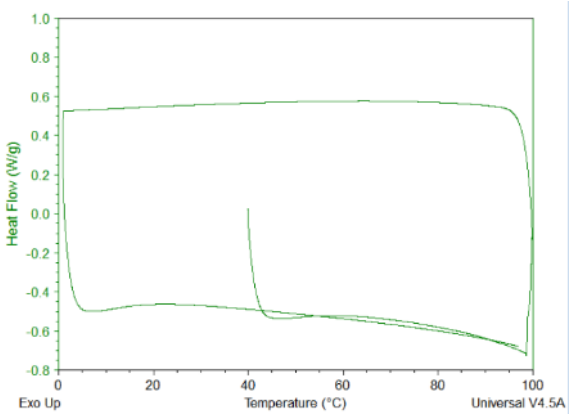


**Figure 18: DSC of CXCAm-7%-3.0.**

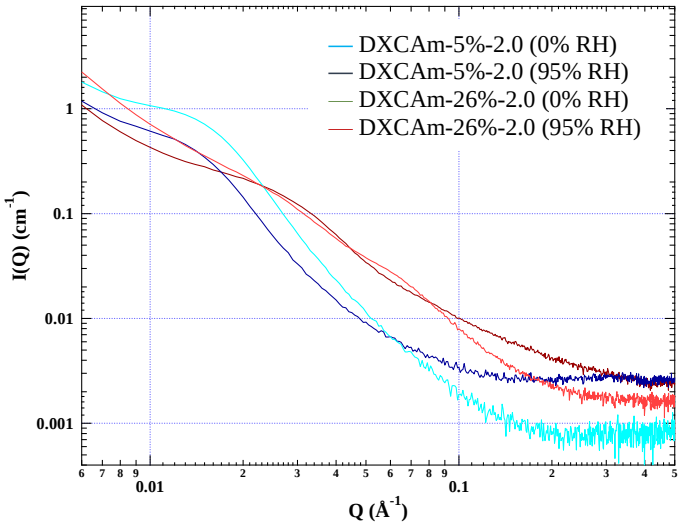


**Figure 19: SAXS Profiles of DXCAm-5%-2.0 and DXCAm-26%-2.0.**

The most important feature of DXCAm membranes was the covalent connectivity between cations. Two membranes with IEC values of 2.0 mmol/g were synthesized for comparison (SAXS profiles in Figure 19). In DXCAm-5%-2.0, the precursor has 5 mol% StTCOE and the membrane was crosslinked by DCPD. In this membrane, ~20 cations on average were directly connected, while membrane DXCAm-26%-2.0, prepared from a precursor with 26 mol% StTCOE, had on average ~3 cations directly connected along the polymer chain. Similar amounts of water were absorbed (55% vs 50%) in those two membranes, which was because of the identical IECs. The

conductivities of DXCAm-5%-2.0 were more than twice as high as those of DXCAm-26%-2.0 at all temperatures measured (Figure 21A). This could not be ascribed to difference in morphology as mentioned above, or crosslinking density (Figure 20 shows the crosslinking density, tuned by varying the ration between G2 and StTCOE, did not affect the membrane wateruptake and performance), and our explanation was that the organization of cations was critical for the ion transport. Since most anions reside close to cationic groups due to strong electrostatic interaction, the anions would replicate the cation distribution. Water molecules, absorbed by the ionic species, are similarly distributed primarily along the polyelectrolyte chain. When cations were isolated by StTCOE units, the counter ions were separated as well and at the same time hydration shell surrounding the ions were relatively discontinuous. The conduction was then limited by the absence of well-defined percolation pathways.[62] On the contrary, when the cationic sites were persistent along the polymer chain, the anion and water were both organized along the polymer backbone. It had been found that the anion transport can be accelerated when the motion was directed by the polycation chain with or without hydration.[61,63] It was postulated that the anion diffusion in DXCAm-5%-2.0 was significantly less retarded by the hydrophobic segments, with the longer persistent cationic monomer sequence than that in DXCAm-26%-2.0. In addition, the interchain exchange of anions, assisted by water, provided a percolation pathway for anion motion along the polyelectrolyte chain. This process was facilitated by the overlap of connected cations acting as 'network junctions', which should be more frequent in DXCAm-5%-2.0 with the longer connected cation sequence than in DXCAm-26%-2.0. Both of the anion transport mechanisms, i.e. motion along the polymer chain and interchain exchange, were faster than the diffusion in the absence of well-defined percolation channels. More importantly, they formed the three dimensionally continuous network of anion transport pathways in DXCAm-5%-2.0, and thus endowed the high conductivities. This experiment demonstrated that linking the ionic groups together improved both intra- and interchain ion motion, and we hypothesize that this strategy can also be applied to other transport/separation materials.

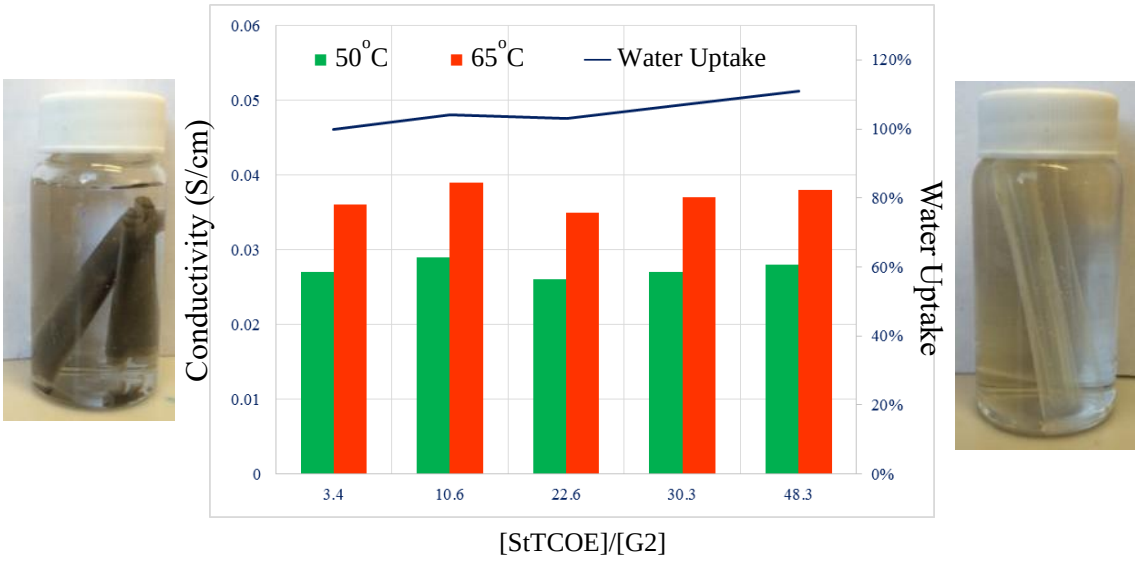


**Figure 20: Effect of Crosslinking Density.**

**The pictures on the left and right side show the appearance of membrane prepared with [StTCOE]/[G2] being 3.4 and 48.3, respectively.**

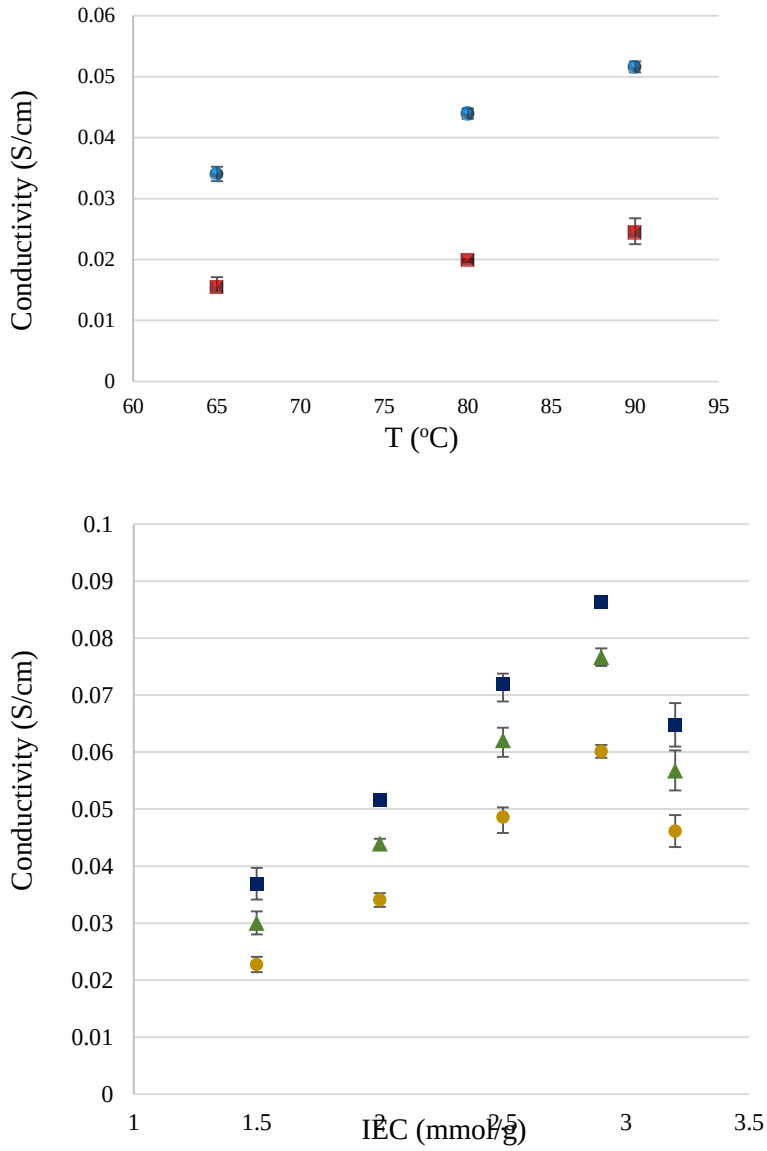


**Figure 21: $Cl^-$ Conductivities Affected by Cation Connectivity and Temperature.**

**$Cl^-$ conductivities of A) DXCAm-5%-2.0 (●) and DXCAm-26%-2.0 (■) plotted versus temperature and B) DXCAm-5% membrane series plotted against IECs at 65 ºC (●), 80 ºC (▲), and 90 ºC (■).**

### 2.3.4 Effect of IEC

Beside high conductivity, this approach was promising for various applications due to its tunability. As mentioned above, the mechanical properties and water distribution can be tuned by changing the identity of ROMP comonomer and the neutral precursor composition. Moreover, starting from the same precursor copolymer, by simply changing the feeding ratio of the precursor polymer and DCPD, membranes with different IECs were prepared. The conductivities of these membranes were plotted against IECs in Figure 21B. When the IEC was below 3.0mmol/g, the conductivity increased monotonically with IEC, due to two reasons: firstly, there were more ions in high IEC membranes; secondly, ion mobility was raised by increased water uptake. However, when IEC reaches higher value, in this case, 3.2mmol/g, a drop in conductivities was observed across all temperatures and the membrane softened, both of which were assigned to overswelling.[34]

### 2.3.5 Membrane Performance

The membrane stability was evaluated by degradation experiment in 1M KOH aqueous solution at 80°C. It was found that the IEC remained stable for at least 24 hours, which indicated relative stability of these membranes (Figure 22), which was attributed to the absence of β-H in benzyltrimethylammonium cations avoiding the Hoffmann elimination mechanism.[4,64]

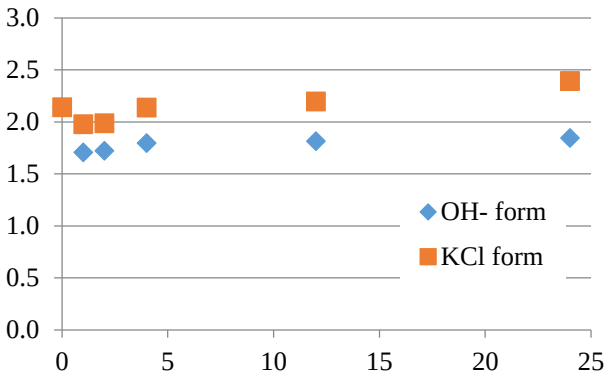


**Figure 22: Alkaline Degradation Test of a Representative Membrane.**

Having established the alkaline stability, the membranes were evaluated for $OH^-$ conductivities (Figure 23). Similar to $Cl^-$ conductivities, the $OH^-$ conductivities were significantly dependent on the testing temperatures. These conductivity values were much higher than $Cl^-$ values, because Grotthuss hopping mechanism largely facilitated $OH^-$ transport under hydrated conditions. The $OH^-$ conductivity of the optimized membrane was higher than 200 mS/cm at 80°C, which was comparable with the proton conductivity of Nafion®, especially when considering the lower diffusion coefficient of $OH^-$ than $H^+$. As the most important properties of ion exchange membranes, some $OH^-$ conductivities of synthetic membranes, based on either crosslinked[34–38,65–69] or block copolymers[41,42,56,70–72], were plotted in Figure 23, along with commercial membrane Tokuyama[24] for comparison. The $OH^-$ conductivities detected on our materials were among the highest. It was noticed that most crosslinked materials were with moderate anion conductivities due to the lack of continuous conduction pathways. However, the material reported by Beyer exhibited promising anion conductivities, and it was due to the bicontinuous microphase separated morphology.[65] Block copolymers were more scattered in the plot, which was attributed to uncontrolled alignment and grain boundary conditions.

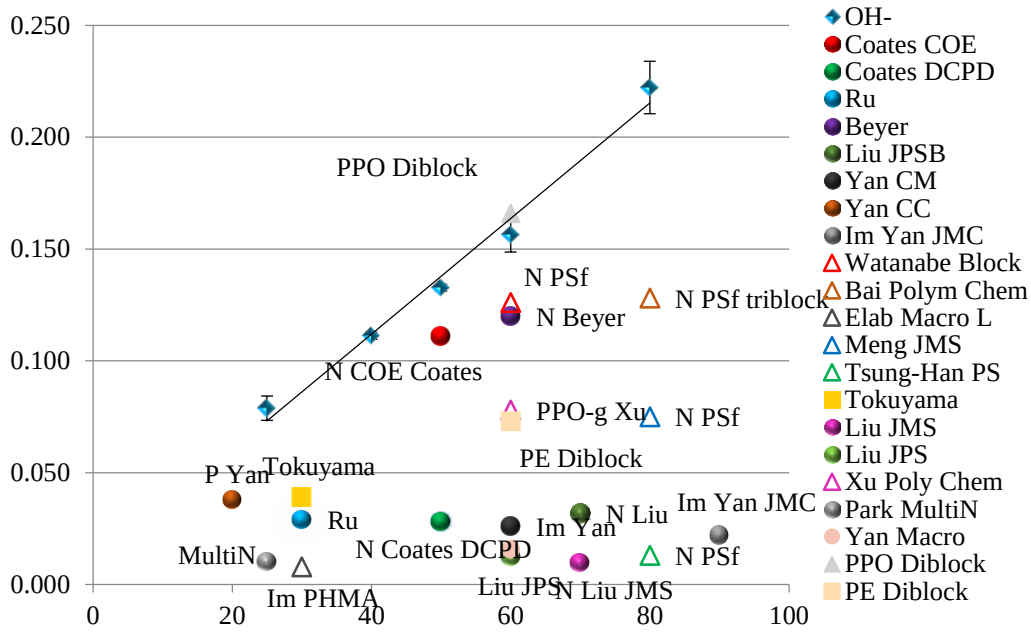


**Figure 23: Hydroxide Conductivities.**

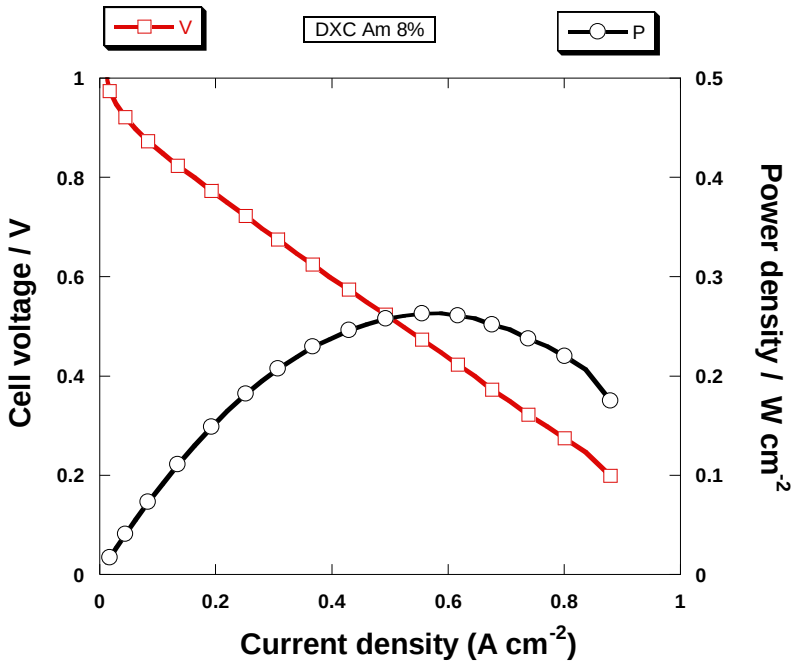


**Figure 24: Fuel Cell Test.**

Membrane DXCAm-8%-2.5, with a thickness of 61 μm, was then applied to fuel cell performance at U.S. Army Research Laboratory. At 55 ºC, the opening circuit voltage was 1.056

V and the peak power density was as high as 260 $mW/cm^2$ (Figure 24). These results were extremely promising, when compared with the Tokuyama A901 membrane, which had a thickness of 10 μm and displayed a peak power density of 215 $mW/cm^2$. This was due to the extremely low cell resistance, 0.15 $\Omega * cm^2$, in DXCAm-8%-2.5 (compared with 0.11 $\Omega * cm^2$ in Tokuyama A901). It is expected that decreasing the thickness in our membranes can further improve the fuel cell performance.

To testify the potential of these membranes in a wide range of applications, water permeation was tested. The water vapor flux was detected to be $9.4 * 10^5$ $g*\mu m/m^2*day$ on membrane DXCAm-8%-2.5 in $Cl^-$ form (conditions: 0.8 vapor activity, 500 ccm flow, 35 $^oC$), 30% higher than that of Nexar®. It was also found that by varying the anion in the membrane, the water diffusivity can be carefully tuned.

**2.4 Conclusions**

A crosslinked anion exchange membrane with connected cations was presented in this work. The membrane was prepared by one-step casting/crosslinking method using a neutral precursor and a ROMP-active comonomer. By comparing membranes with varied structures, it was demonstrated that the long range crosslinking of the hydrophobic polyDCPD network locked the cations into uniform distribution and controlled the morphology, though this did not affect the conductivities significantly. The connectivity between cations was essentially important for fast anion conduction, because it provided a directed pathway for ion transport, together with which the overlap between gave the conduction network. The organization of charge carrier sites may be a general method applicable to many materials for transport applications. The highest conductivity was achieved with IEC being around 3.0 mmol/g because of its balanced ion mobility and water swelling. This method may be a general platform for the design of polymer materials for the transport/separation of small molecules/ions.

# CHAPTER 3

# ANION EXCHANGE MEMBRANES WITH ORDERED MORPHOLOGIES FROM SOLVENT PROCESSABLE BLOCK COPOLYMERS CONTAINING PHOSPHONIUM IONS

## 3.1 Introduction

### 3.1.1 RAFT Polymerization

Reversible addition-fragmentation chain transfer (RAFT) polymerization is a type of controlled/living radical polymerization. The general mechanism is shown in Figure 25.[73,74] In a RAFT polymerization, often a very small amount of initiator is used to provide radical input, and due to the fast, reversible chain transfer the length of every polymer chain is averaged. Since there is only a very low concentration of radical in the system, chain termination is largely suppressed and most of the chain-ends (typically > 90%) can preserve a RAFT end-group for further chain extension. In this technique, to ensure fast reversible chain transfer, the RAFT chain transfer agent (CTA) needs to be carefully selected with a high chain transfer coefficient ($C_{tr} = k_{tr}/k_p >> 1$). Most of the CTAs are a family of chemicals named thiocarbonylthio, as in the general structure shown below (Figure 25), which includes dithiocarbomate, dithiobenzoate, xanthate, and trithiocarbonate. Among these reagents, trithiocarbonate is a popular CTA, which is suitable for a wide range of monomers, including styrenes, methacrylates, acrylates, and even certain dienes, which cannot be readily controlled by other CTAs. [74–78]

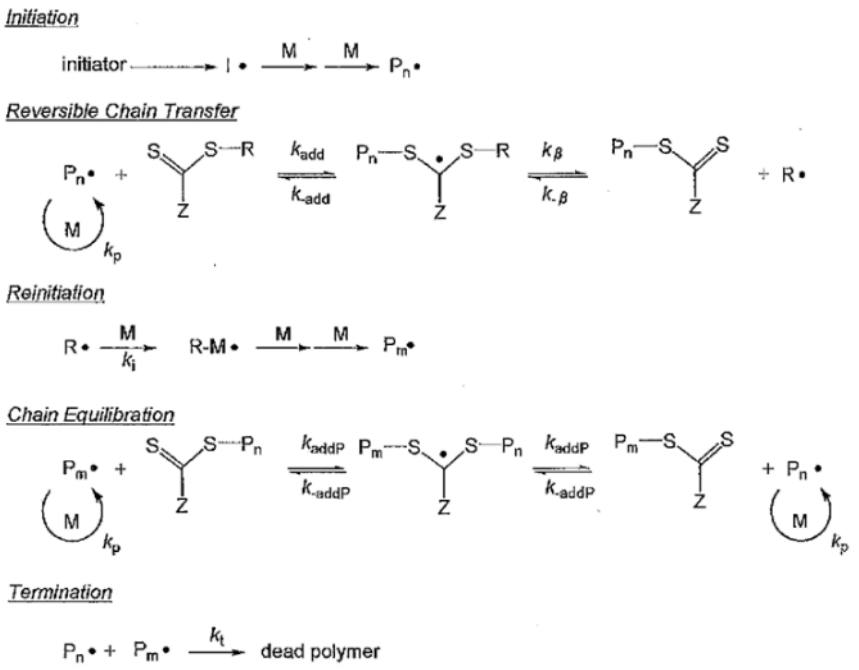


**Figure 25: Mechanism of RAFT Polymerization.**

**Figure adapted from Ref 73.**

### 3.1.2 Block Copolymer Microphase Separation

Microphase separation is a common phenomenon when the block segments in a polymer chain are immiscible with each other. Depending on the segregation strength ($\chi$), the degree of polymerization (N) and relative volume fraction of the blocks (f), ordered morphologies are observed in diblock copolymers, where closely packed spheres, hexagonally packed cylinders, lamella and gyroid are the most common and accessible morphologies (Figure 26).[79,80] The morphologies are also affected by other factors, such as conformational asymmetry,[81,82] polymer architecture,[83,84] MW distribution,[85] and electrostatic interactions.[86] This provides a versatile platform for the investigating the structure-property relationships of polymer materials. It also provides opportunities to enhance material performance, since functionalities can be incorporated by introducing different polymer blocks.

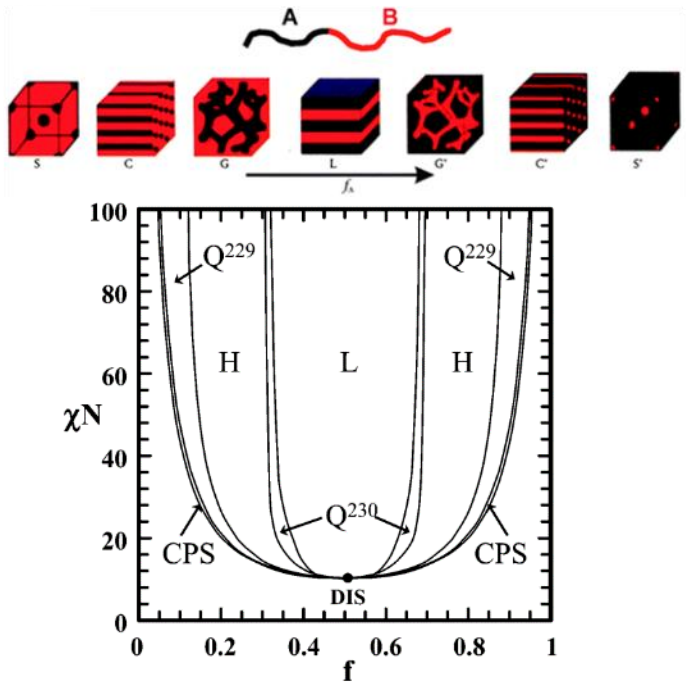


**Figure 26: Microphase Separation of Diblock Copolymers.**

**A) Topological structure of the microphases; B) The theoretical phase diagram of a symmetric diblock copolymer. Figures adapted from Ref 79 and Ref 80, respectively.**

### 3.1.3 Block Copolymers for AEMs

Compared to the extensive studies on proton exchange membranes (PEMs),[87] fundamental understanding of the structure-performance relationship in anion exchange membranes (AEMs) is urgently needed. This requires well-defined ionic polymers for AEM preparation and investigation. The most widely used strategy of AEMs synthesis is through chemical modification of engineering polymers, such as polysulfone,[17,19,22,24–27,88–92] poly(ether ether ketone),[33] polyphenylene,[15,29,93] and poly(phenylene oxide).[30,94–98] Other strategies include direct polymerization to synthesize homopolymers[99] or random copolymers.[16,28,31,100,101] In addition, crosslinked materials have also

been reported, where better mechanical properties, higher ion content, controlled water sorption and reduced fuel crossover could be achieved.[34,35,38,67,69,102–105] However, although good membrane performance has been achieved, the disordered nature of these materials still hinders developing a more complete understanding of the anion transport.

As demonstrated in PEMs, microphase separation can promote ion transport and water diffusion.[106,107] Recent research has discovered similar effects in AEMs. A few examples of multiblock poly(arylene ether)s were prepared by polycondensation.[42,72,108,109] Faster anion transport was observed in ordered structures compared to random copolymer counterparts. Similarly, triblock copolymers with polysulfone as the midblocks were prepared by polymer coupling and displayed improved anion conductivities.[70] Modifying precursor block copolymers, via chloromethylation or bromination and subsequent quaternization resulted in ionic copolymers with promising conductivities.[40,110,111] Knauss et al.[112] and Xu et al.[71] reported block and graft copolymers from end-functionalized poly(phenylene oxide), and good mechanical strengths were achieved together with remarkable anion conductivities. Direct polymerization was utilized to synthesize poly(methyl methacrylate) block copolymers containing polymerized ionic liquids.[41,62] It was found that in weakly segregated block copolymers, nano-confinement significantly enhanced anion transport. Strongly segregating block copolymers were crosslinked via ring-opening metathesis polymerization to provide disordered bicontinuous morphologies.[65] Excellent anion conductivities were achieved, despite the fact that these materials were no longer processable. In the materials discussed above, it was difficult to directly correlate the nanostructure with the ion transport behavior because of the lack of long range order.

Well-defined morphologies were observed in a few reports. Polystyrene (PSt) based imidazolium and ammonium block copolymers were synthesized by controlled polymerization and quaternization reactions.[113] Investigation under anhydrous conditions demonstrated that the

morphologies, including the connectivity and long-range order, significantly affected the conductivity. However, these materials showed limited solution processability. Balsara et al.[114,115] synthesized PSt block copolymers using controlled polymerizations, where the bound ion effect was investigated in lamellar morphologies. An interesting PSt block copolymer carrying cyclopropenium was reported, where the ionic block with 50% weight fraction formed the matrix in the hexagonal phase.[116] However, there was no detailed discussion on morphological effect on conductivities. Coughlin et al.[117] used atom transfer radical polymerization (ATRP) to chain extend PSt macro-initiator with vinylbenzyltrimethylammonium and observed ordered lamellar and hexagonal morphologies. It was found that at low humidities the lamellae forming polymer showed a sudden conductivity increase when raising the temperature. It appeared that most ordered morphologies were achieved on PSt block copolymers, as a consequence of multiple reasons. First, common solvents are available for PSt and certain polyions, such as DMF and DMAc. In addition, the versatility in polymerization methods facilitates the synthesis of well-defined block copolymers. Moreover, the segregation strength is high between polycations and PSt, which induces microphase separation.

In anhydrous ion transport materials, it has been shown that 3-D continuous ionic domain can provide higher conductivity values than 1-D and 2-D channels.[118,119] However, on water-assisted ion transport materials, experimental comparison has been conducted on spherical, cylindrical, and lamellar morphologies, while the matrix of cylindrical and spherical phases were scarcely investigated. This was likely due to the fact that the formation of matrices require a high volume fraction of the ionic block, and can lead to excessive hydration and loss of mechanical integrity upon water sorption. The over-swelling effect can possibly be suppressed by using a less hydrophilic ionic species. At the same time, introducing appropriate Columbic interactions[86,120–122] and conformational asymmetry[81,123] were demonstrated to effectively shift the morphological behavior, using both theoretical and experimental methods.

In addition, solvent processability could possibly introduce ease in membrane fabrication, domain alignment, and catalyst/electrode assembly. This had been emphasized in tuning the performance of proton exchange membrane devices.[124–127] A key to unlocking the ionic copolymer solubility challenge might be the identity of the cation. Random copolymers containing phosphonium ions were processed in the solution state and showed moderate to excellent alkaline stabilities.[16,100,101,128] Homopolymer and block copolymers containing benzyl trioctyl phosphonium was discovered to be soluble in THF.[129] As reported by Yan et al., polysulfone and polyphenylene oxide with a pendant benzyl tris(2,4,6-trimethoxyphenyl) phosphonium ($BzAr_3P^+$) could be solution processed both as a membrane and as a high performance catalyst ink.[17,98,130] The promising solubilities of phosphonium cations in various organic solvents, enables the usage of other hydrophobic blocks to replace the brittleness of PSt. Promising stability and conductivity were found on the polysulfone containg $BzAr_3P^+$, which were attributed to the strong electron donating effect of the methoxy groups. Based on this robust cation, we devised an efficient synthetic route to prepare block copolymers containing $BzAr_3P^+$ ions and have demonstrated solution processing to obtain ordered morphologies. Isoprene was used as the hydrophobic block because of the potential strong phase separation with polyions and attendant mechanical flexibility.

## 3.2 Experimental Section

### 3.2.1 Materials

Isoprene was distilled and stored under -30 $^oC$ before use. St and CMS (mixture of *para*- and *meta*- isomers) were passed through basic alumina and stored at -30 $^oC$ before use. Thermal initiators, 2,2'-Azobis(2-methylpropionitrile) (AIBN) and 1,1'-Azobis(cyclohexanecarbonitrile) (ACBN) were recrystallized from methanol (MeOH) and stored at -30 °C. Other chemicals were used as received. 1,4-bis(*n*-butyl sulfanylthiocarbonyl sulfanyl methyl)benzene (DXB-CTA), 2-

cyano-2-propyl butyl trithiocarbonate (O-CTA), and S-benzyl-S'-butyl trithiocarbonate (Bz-CTA) were synthesized using previously reported methods.[58,131,132]

### 3.2.2 Synthesis of Phosphonium Monomer

In 25 mL ethyl acetate/THF (4:1 = v:v), 1.992 g tris(2,4,6-trimethoxyphenyl)phosphine ($Ar_3P$, 3.74 mmol) was dissolved. At room temperature, 640 mg 4CMS (4.19 mmol) was added dropwise and precipitates formed slowly. The mixture was stirred overnight. The precipitates were collected and dried in vacuum as 2.338 g white solid (3.41 mmol, 91%) as vinylbenzyl tris(2,4,6-trimethoxyphenyl) phosphonium chloride. ESI-MS found 649.1 m/z (M-Cl, theo. 649.3). The chemical structure and NMR results are shown in Figure 27.

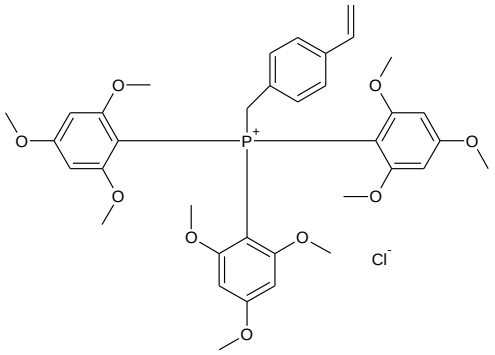

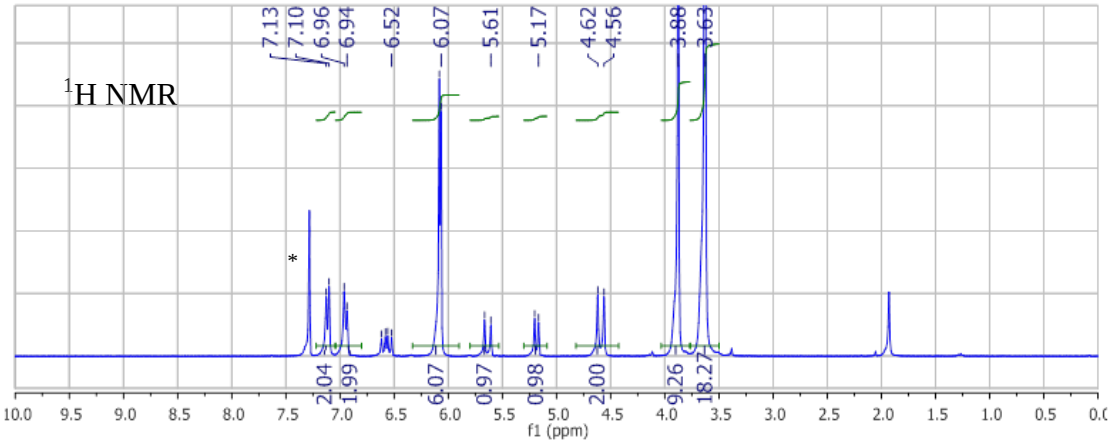
$^{1}$H NMR
7.13
7.10
6.96
6.94
6.52
6.07
5.61
5.17
4.62
4.56
3.88
3.63
2.04
1.99
6.07
0.97
0.98
2.00
9.26
18.27
f1 (ppm)

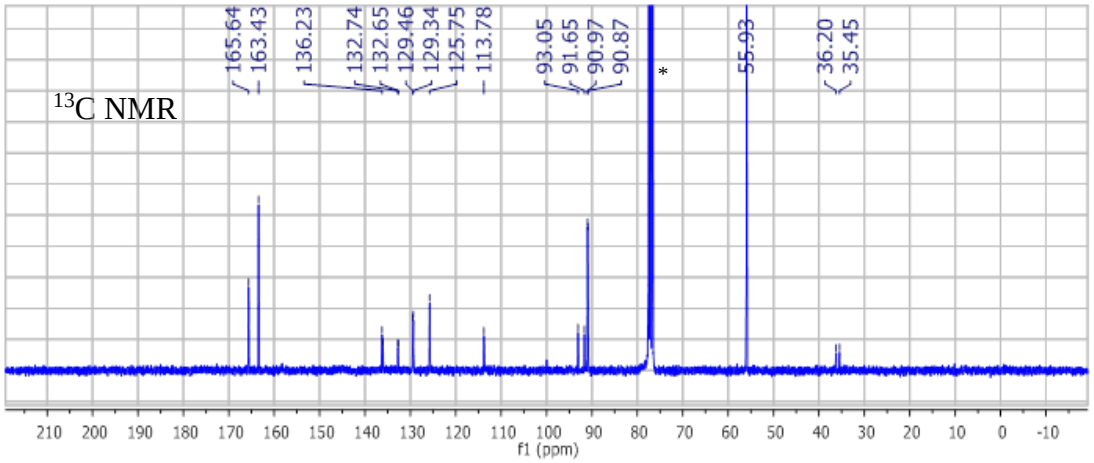
$^{13}$C NMR
165.64
163.43
136.23
132.74
132.65
129.46
129.34
125.75
113.78
93.05
91.65
90.97
90.87
55.93
36.20
35.45
f1 (ppm)

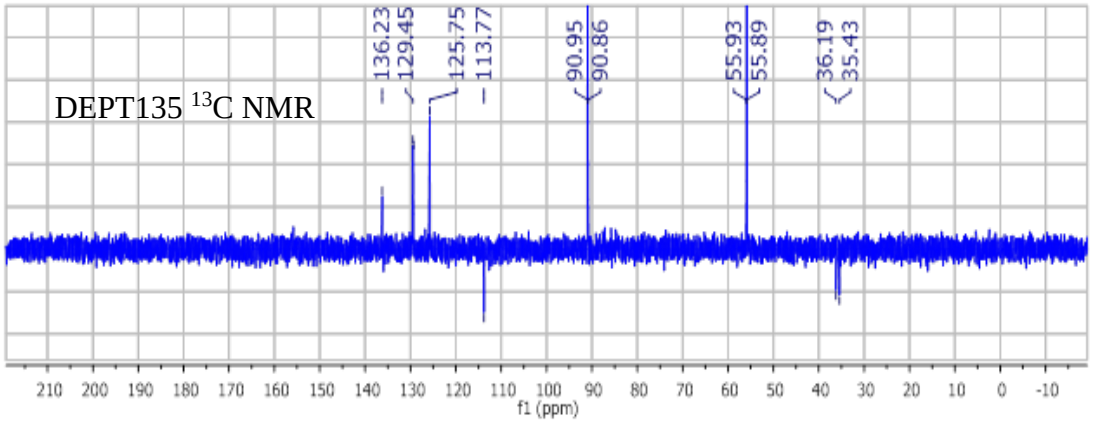
DEPT135 $^{13}$C NMR
136.23
129.45
125.75
113.77
90.95
90.86
55.93
55.89
36.19
35.43
f1 (ppm)

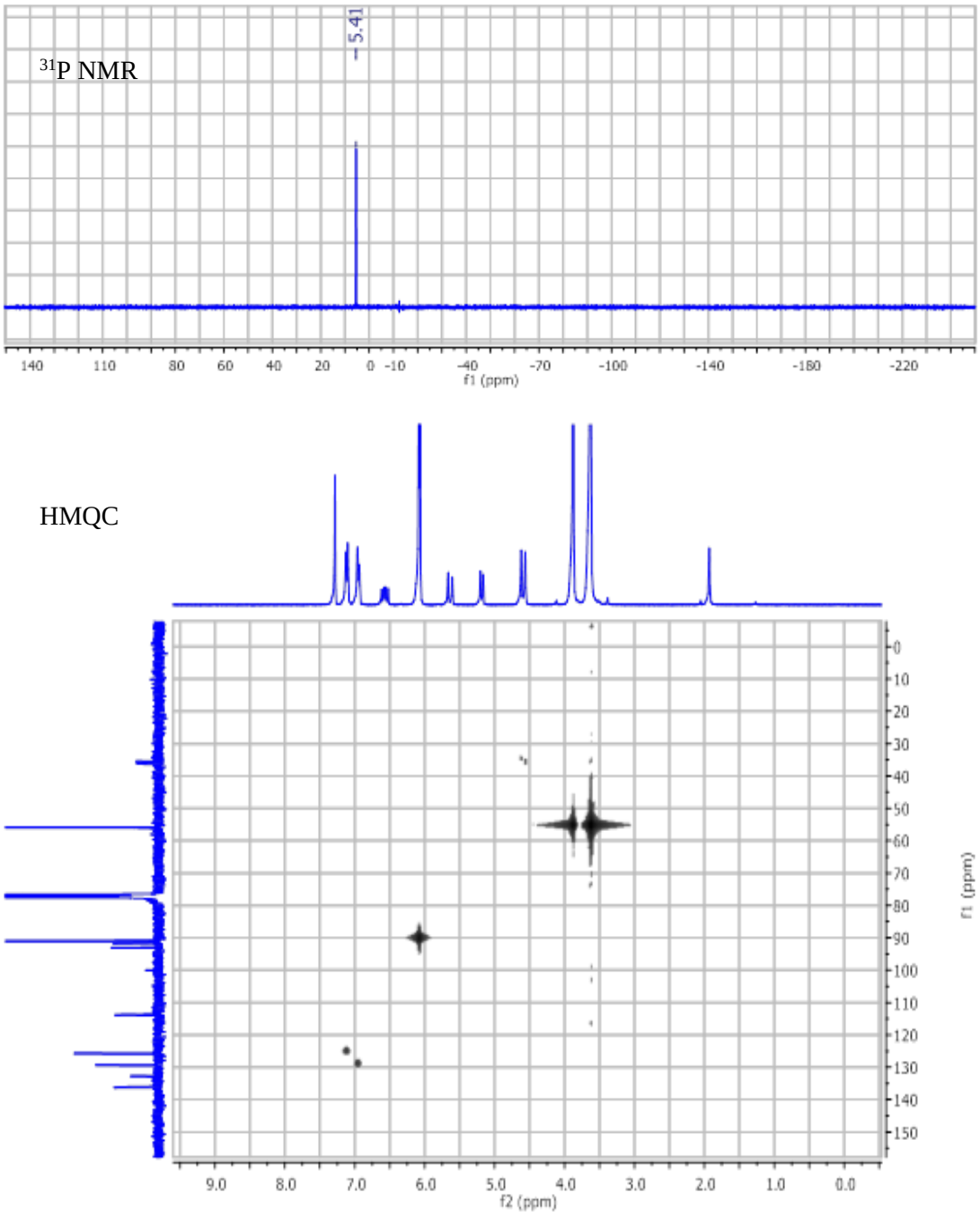


**Figure 27: Chemical Structure and NMR Characterization of Styrenic Phosphonium Monomer.**

### 3.2.3 Free Radical Polymerization of Phosphonium Monomer

Phosphonium monomer (679 mg) and 4.0 mg AIBN was dissolved in 7.184 g of DMF. The mixture was divided into 4 test tubes. Each tube was degassed by purging with nitrogen for 0.5 hour and then sealed. The reaction was started by immersing the test tubes in an oil bath preheated to 60 $^{o}$C. Each tube was quenched in ice bath at pre-determined times. By running $^{1}$H NMR on the reaction mixtures, the conversions were calculated (Table 2).

**Table 2: Free Radical Polymerization of Phosphonium Monomer.**

| # | $[M_0]$: $[I_0]$: [DMF][a] | T(°C) | time(hours) | conversion |
|---|---|---|---|---|
| 1 | 41: 1: 4035 | 60 | 3.5 | 4% |
| 2 | 41: 1: 4035 | 60 | 10 | 26% |
| 3 | 41: 1: 4035 | 60 | 24 | 29% |
| 4 | 57: 1: 2490 | 90 | 6 | 76% |

[a]AIBN was used as initiator at 60 °C and ACBN at 90 °C.

### 3.2.4 Homopolymerization of CMS

A typical homopolymerization of CMS was as follow; in a tube, CMS (6.05 g, 39.7 mmol) was mixed with Bz-CTA (331 mg, 0.761 mmol) and AIBN (8.3 mg, 0.051 mmol). After purging with dry nitrogen for 20 minutes, the tube was immersed in an oil bath at 70 °C for 16.5 hours and then quench in an ice bath. A small aliquot was removed for determination of percent conversion, and the rest was diluted with THF and then precipitated into hexanes twice to remove residual monomer. After drying in a vacuum oven at room temperature for at least 24 hours, PCMS (4.96 g) was obtained. End-group analysis was used to determine the molecular weight (MW) and the Đ was determined by SEC against PSt standards.

### 3.2.5 Homopolymerization of Ip

O-CTA (191.6 mg, 0.441 mmol) and di-tert-butyl peroxide (dtBP, 10 μL, 0.055 mmol) were mixed with Ip (40 mL, 0.400 mol) in a Schlenk flask. The flask was sealed and stored under -30°C. Part of it (3-5 mL) was transferred to a Schlenk tube. After 5 cycles of freeze-pump-thaw, the reaction was sealed under vacuum and heated to 125 °C for 19 hours. The reaction was quenched in ice bath for 3 minutes and opened to air. Half of the reaction mixture was transferred into a vial and dried directly in vacuum oven for conversion analysis. The other half was precipitated into methanol dropwise and the product was dried under vacuum and subject to measure $DP_{NMR}$. Size exclusion chromatography was performed in THF on a Polymer Laboratories PL-GPC 50 Integrated SEC system to measure the MW and dispersity (Đ) against PSt standards.

### 3.2.6 Synthesis of Block Copolymers

A representative procedure was as follow. Telechelic PCMS precursor (MW=10.5 kg/mol, 1.155 g, 0.11 mmol) and dtBP (5 μL, 0.027 mmol) were dissolved in the mixture of Ip (40 mL, 0.400 mmol) and THF (10 mL). 5 cycles of freeze pump thaw was applied. Then the reaction was tightly sealed under vaccum and then heated to 125 °C for 36 hours. The mixture was diluted with dichloromethane and slowly dropped into methanol. The yellow product (5.88 g) was collected and dried in vacuum for at least 48 hours at room temperature. $^{1}$H NMR was performed to measure DP of Ip and SEC (calibrated against polystyrene standards) to measure Đ.

### 3.2.7 Polymer Quaternization and Membrane Casting

All quaternization reactions were conducted in dark. A typical procedure was simply mixing 202 mg P($CMS_{13.2}$-*ran*-$St_{14.7}$)-*b*-$PIp_{322}$, 60 mg tris(2,4,6-trimethoxyphenyl)phosphine ($Ar_3P$), and 1.5 mL chloroform and stored at ambient temperature for at least 24 hours. A small aliquot was dissolved in chloroform for $^{31}$P NMR analysis. The rest of the solution was casted onto

a clean polytetrafluoroethylene sheet to dry slowly overnight, and the membrane was then peeled off the substrate. The quantitative conversion of phosphine and benzyl chloride was characterized by $^{31}$P NMR and FT-IR (Figure 28).

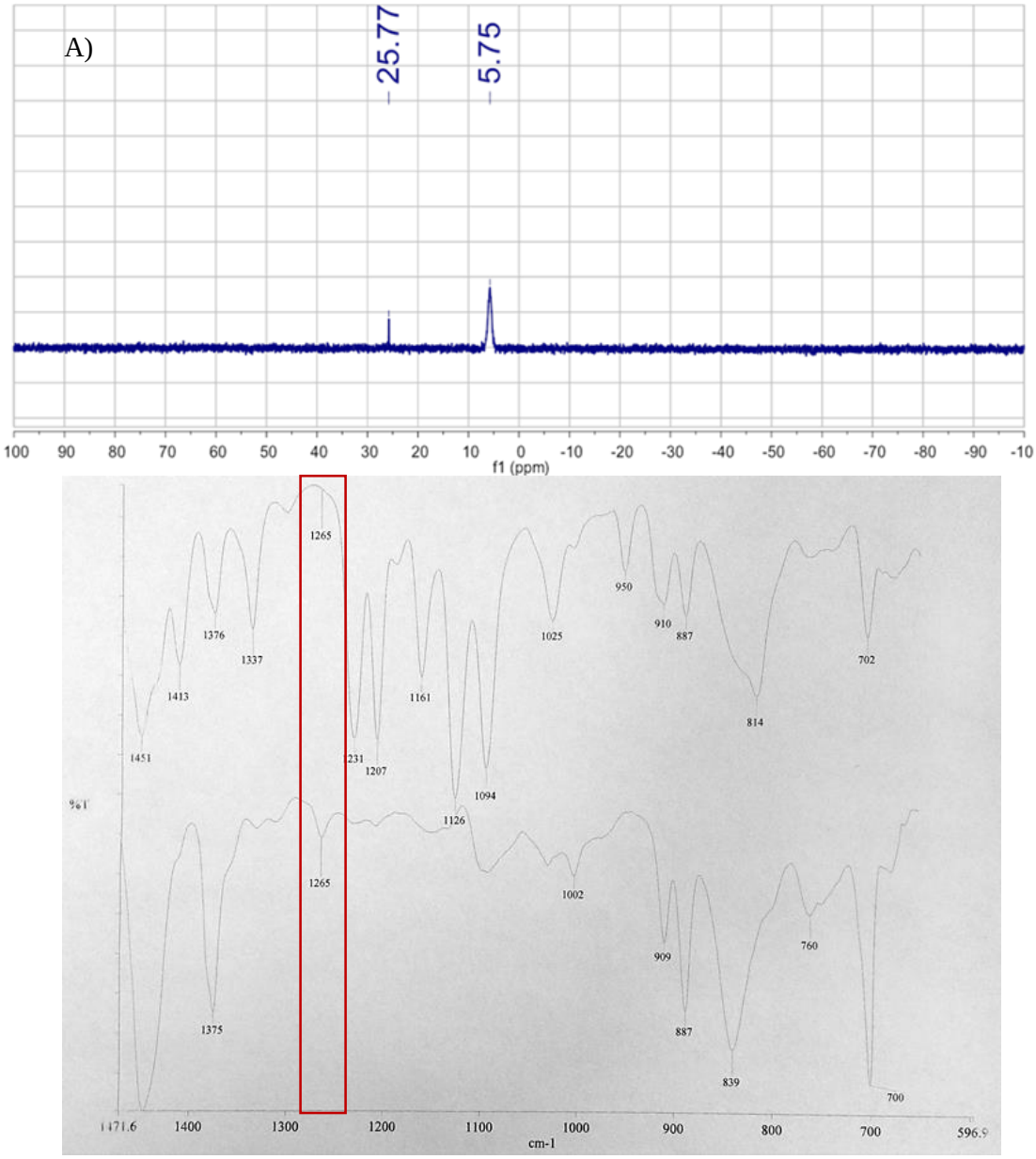


**Figure 28: Characterization of Polymer Quaternization.**

**A) A typical $^{31}$P NMR spectrum of quaternization mixture; B) Representative IR spectra before and after quaternization.**

### 3.2.8 Ion Conductivity Measurement

The in-plane conductivity of the membranes was calculated using electrochemical impedance spectroscopy to measure membrane resistance as given by the equation below,

$$\sigma = l/(R*W*t)$$

where R is the membrane resistance, l is the distance between the electrodes, w is the width of the membrane samples, and t is the thickness of the sample. Impedance spectra were obtained over a frequency range of 1 to $10^6$ Hz using a four-electrode test cell connected to a BioLogic VMP3 multi-channel Potentiostat. The measurements were made in a TestEquity environmental chamber to control sample temperature and humidity. The resistance of the membrane was determined from the low frequency intercept of the Nyquist impedance plot. Experiments were performed at constant relative humidity 95% RH, varying temperature from 30 to 90 °C.[93]

### 3.2.9 Small Angle X-ray Scattering (SAXS)

The testing was performed at The Basic Energy Sciences Synchrotron Radiation Center (BESSRC) at the Advanced Photon Source at Argonne National Lab on beamline 12 ID-B. A Pliatus 2M SAXS detector was used to collect scattering data with an exposure time of 1 s. The X-ray beam had a wavelength of 1 Å and power of 12 keV. The intensity (I) is a radial integration of the 2D scattering pattern with respect to the scattering vector (q).

Temperature and humidity were controlled within a custom sample oven as described previously.[133] Typical experiments studied three membrane samples and one empty window so a background spectrum of the scattering through the Kapton® windows and nitrogen environment could be obtained for each experimental condition. The humidity of the sample environment was controlled by mixing heated streams of water vapor saturated and dry nitrogen. Sample holders were inserted into an oven environment at 60 °C and <10% relative humidity. The samples were

allowed to dry for 40 minutes before X-ray testing was undertaken. Relative humidity was then ramped to 25%, 50%, 75%, and 95% while the temperature was maintained at 60 ºC. The equilibrium time before taking an X-ray spectrum was 20 minutes between dry, 25%, and 50% and increased to 40 minutes between 50%, 75%, and 95%. Soaked membranes were dipped in water for at least 12 hours and quickly mounted to the sample holders at 95% and subjected to SAXS testing.

### 3.2.10 Transmission Electron Microscopy (TEM)

Microscopy was performed on samples prepared using a Leica UCT ultramicrotome equipped with a cryostage. Sections approximately 50 nm in thickness were cut using a Diatome diamond knife. High-angle annular dark field scanning TEM (HAADF STEM) was performed using a JEOL JEM-2100F TEM, operated at 200 kV. A Gatan 806 HAADF STEM detector was used to collect the dark field images. The TEM was operated at 200 kV, with a 40 μm condenser aperture, a HAADF STEM collection angle of 36 to 126 mrad, and spot size of 0.2 nm. Gatan Digital Micrograph was used to collect and analyze the data. In dark field images, high Z regions appear bright and low Z regions are dark. The TEM images were taken in U.S. Army Research Laboratory.

## 3.3 Results and Discussion

### 3.3.1 Polymer Synthesis

Two possible strategies can be adopted to prepare phosphonium based copolymers, direct polymerization of a $BzAr_3P^+$ monomer or post-polymerization modification of a precursor polymer. For the former approach, quaternization of 4CMS with $Ar_3P$ (Ar = 2,4,6-trimethoxyphenyl group) resulted in a 91% yield of styrene based $BzAr_3P^+$ monomer. However, the radical polymerization of this monomer was too sluggish to be a practical preparative method. As an alternative synthetic

approach to prepare the phosphonium homopolymers, we first homopolymerized CMS followed by the quantitative quaternization with $Ar_3P$. The reaction was highly efficient, where all of the chloride positions were substituted, as confirmed by the disappearance $CH_2$ wagging band featuring $CH_2Cl$ at 1265 $cm^{-1}$ in IR spectra.

The fully quaternized homopolymer was soluble in a wide range of solvents: DMF, alcohols, acetone, together with dichloromethane and chloroform/methanol mixtures (Table 3). The solubility suggested the opportunity of synthesizing soluble ionic block copolymers containing phosphonium ions. The density of the fully quaternized phosphonium homopolymer was measured to be $1.20 \pm 0.03$ $g/cm^3$.

The RAFT polymerization technique was chosen for block copolymer synthesis, due to its functionality tolerance and mild reaction conditions.[134] CMS was polymerized as the quaternizable monomer. Isoprene was selected to construct the hydrophobic component, for both the material flexibility and chemical stability. Block copolymers were synthesized by sequential polymerization mediated by trithiocarbonates.[61] In the first step, DXB-CTA was employed for the preparation of telechelic PCMS, while O-CTA was used to synthesize hemitelechlic PCMS. It was noticed that DXB-CTA resulted in broader MW distributions compared to O-CTA (Table 4). This phenomenon was caused by the slow fragmentation to generate a benzylic radical as the new propagating center. Thus, at the early stage of polymerization, there was a slow generation of polymer chains. Though broader dispersities were observed, DXB-CTA was still efficient to synthesize telechelic PCMS chains with trithiocarbonates at each end.

**Table 3: Solubility of Phosphonium Homopolymer.**

| Solvent | Acetone | Hexanes | $CHCl_3$ | $CH_2Cl_2$ |
|---|---|---|---|---|
| Solubility | + | - | ± | + |

| Solvent | MeOH | 2-Propanol | Ethanol | n-Pentanol |
|---|---|---|---|---|
| Solubility | + | + | + | + |

| Solvent | Water | THF | DMF | DMSO |
|---|---|---|---|---|
| Solubility | - | - | + | + |

| Solvent | Acetonitrile | Toluene | Ethyl Acetate | Diethyl Ether |
|---|---|---|---|---|
| Solubility | + | - | - | - |

| Solvent | $CHCl_3$:MeOH =20:1 (v:v) | $CHCl_3$:MeOH =10:1 (v:v) | $CHCl_3$:MeOH =5:1 (v:v) | $CHCl_3$:MeOH =1:1 (v:v) |
|---|---|---|---|---|
| Solubility | + | + | + | + |

+ soluble; -insoluble; ± partially soluble.

**Table 4: Chemical Compositions and Morphologies of AEMs.**

| | AEM # | $DP_{CMS}$[a] | $Đ_{PCMS}$[b] | $DP_{Ip}$[c] | Đ[d] | Q[e] | IEC[f] (mmol/g) | f[g] | Morphology[h] | d-spacing (nm) |
|---|---|---|---|---|---|---|---|---|---|---|
| Triblock copolymers | 1 | 66 | 1.26 | 452*2 | 1.65 | 45% | 0.34 | 24% | Lamellar | 45 |
| | 2 | 66 | 1.26 | 298*2 | 1.55 | 46% | 0.44 | 33% | Lamellar | 37 |
| | 3 | 19(+19) | 1.14 | 305*2 | 1.42 | quantit. | 0.33 | 22% | Lamellar | 27 |
| | 4 | 19(+19) | 1.14 | 257*2 | 1.40 | quantit. | 0.38 | 25% | Lamellar | 26 |
| | 5 | 19(+19) | 1.14 | 232*2 | 1.40 | quantit. | 0.41 | 27% | Lamellar | 25 |
| | 6 | 19(+18) | 1.15 | 192*2 | 1.37 | quantit. | 0.46 | 30% | Hexagonal | 24 |
| | 7 | 19(+19) | 1.14 | 145*2 | 1.30 | quantit. | 0.54 | 37% | Hexagonal | 22 |
| Diblock copolymers | 8 | 36 | 1.12 | 322 | 1.74 | 46% | 0.45 | 33% | Hexagonal | 35 |
| | 9 | 8.8(+8.5) | 1.07 | 516 | 1.44 | quantit. | 0.21 | 13% | Lamellar | 46 |
| | 10 | 13.2(+14.7) | 1.09 | 488 | 1.39 | quantit. | 0.30 | 20% | Lamellar | 42 |
| | 11 | 13.2(+14.7) | 1.09 | 418 | 1.39 | quantit. | 0.34 | 22% | Hexagonal | 38 |
| | 12 | 18(+19.5) | 1.08 | 434 | 1.44 | quantit. | 0.41 | 27% | Hexagonal | 45 |
| | 13 | 18(+19.5) | 1.08 | 385 | 1.45 | quantit. | 0.44 | 30% | Hexagonal | 42 |
| | 14 | 21(+23) | 1.07 | 326 | 1.34 | quantit. | 0.54 | 37% | Hexagonal | 31 |
| | 15 | 21(+23) | 1.07 | 257 | 1.39 | quantit. | 0.61 | 42% | Hexagonal | 29 |

[a]Degrees of polymerization of CMS and (St in parentheses) measured by $^{1}$H NMR end-group analysis. [b]Dispersity index of macro-CTAs determined by SEC in THF using PSt standards. [c]Degree of polymerization of Ip in the block copolymer, measured by $^{1}$H NMR. [d]Dispersity index of block copolymers determined by SEC in THF using PSt standards. [e]Percentage of quaternization in CMS units. [f]Ion exchange capacity. [g]Volume fraction of the ionic block calculated by densities. [h]The morphologies of membranes cast from chloroform solutions.

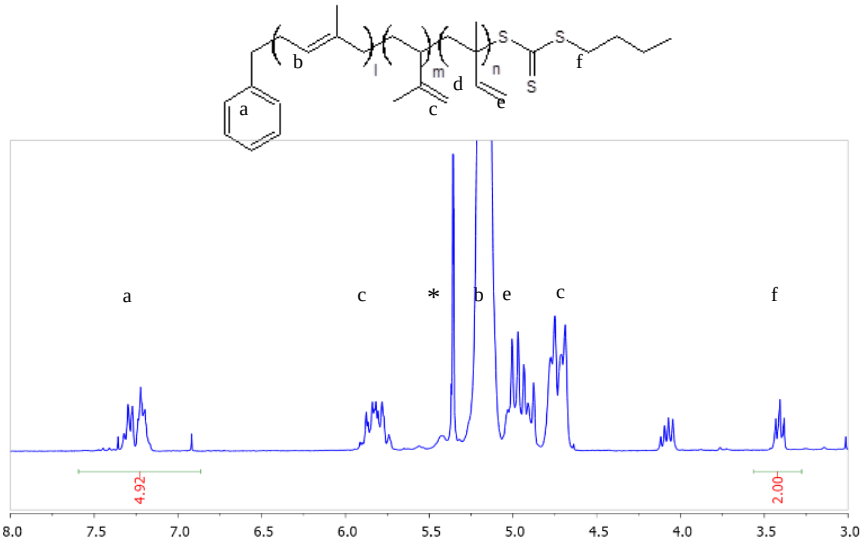


**Figure 29: $^{1}$H NMR of PIp Synthesized in the Presence of BzCl.**

These polymers were then applied to chain extension with isoprene at 125$^{o}$C for fast chain propagation. It was realized that the radical generation rate from thermal initiator intrinsically affected the polymerization control.[76,77,135] To accommodate the polymerization temperature, di-tert-butyl peroxide (dtBP) was chosen for its elongated half-life. In order to confirm that the chain extension with isoprene from PCMS macro-CTA resulted in block copolymer formation, instead of other chemical structures, the irreversible chain transfer to benzyl chloride moieties was investigated. To study this possible chain transfer reaction, Isoprene homopolymerization mediated by Bz-CTA was performed in the presence of benzyl chloride (BzCl, [BzCl]: [Bz-CTA]: [$I_0$] = 108: 1: 0.1) at 125 $^{o}$C. As monitored by $^{1}$H NMR spectroscopy of the resultant polymer, the aromatic region was integrated to be 4.92 when calibrating the end-group methylene as 2.0 (Figure 29), which was very close to the theoretical value 5:2. This indicated that BzCl was barely incorporated into polyisoprene (PIp), which further agreed with the low Đ = 1.34, similar to that in a typical isoprene homopolymerization.[77,135,136] So, it was reasonable to conclude that BzCl sites were inert at isoprene polymerization conditions. On the basis of the above study, diblock copolymers and

symmetric triblock copolymers were synthesized by chain extension with isoprene from PCMS macro-CTAs at 125 °C.

The results are summarized in Table 4. With relatively low MWs, PCMS and P(CMS-*ran*-St) were synthesized, considering that the quaternization reaction with $Ar_3P$ will significantly increase the final MW. The ratio of isoprene to CMS was tuned to cover a range of volume fractions after the quaternization reaction, to enable the investigation of material morphology. It was observed that when the styrenic polymers were chain extended with isoprene, the Đs were raised. It was partly due to the calibration method, which overestimates the MW of PIp.[137] Another contributing factor was that the loading of initiator was relatively high (usually 0.1~0.2 relative to the concentration of trithiocarbonate end-group), which led to biradical termination as well as the formation of extra PIp chains. Finally, the reversible chain transfer rate is slow in isoprene RAFT polymerization, especially when the MW went high, the increased viscosity impeded reversible chain transfer by limiting the chain end diffusion.

The block copolymers were mixed with $Ar_3P$ and stirred in chloroform solution for more than 24 hours. The reaction was conducted in the dark to avoid side reactions. Unfortunately, the fully quaternized copolymers were very brittle after casting, which was possibly due to the bulky size of $BzAr_3P^+$. To prepare membranes with reasonable flexibility, only ~0.5 equivalent (relative to the amount of benzyl chloride moieties) of $Ar_3P$ was added to react with the copolymers. After quaternization, $^{31}P$ NMR analysis of the reaction mixture demonstrated that the conversion of $Ar_3P$ was almost quantitative (Figure 28). The degree of quaternization was estimated by the feed ratio of $Ar_3P$ to benzyl chloride sites and confirmed by $^{31}P$ NMR. The final products of the synthesis described here had a block of CMS and styrenic $BzAr_3P^+$ random copolymer (Figure 30). The resulting ionic copolymers were all soluble in dichloromethane and chloroform, which provided opportunities for solution processing. Another synthetic strategy was to use a random copolymer

of St and CMS as the ionizable block to decrease the density of $BzAr_3P^+$ groups. Similar chain extension reactions were used to synthesize PIp-*b*-P(CMS-*ran*-St)-*b*-PIp and P(CMS-*ran*-St)-*b*-PIp. The quaternization reaction was performed using 1.07~1.10 equivalents of $Ar_3P$ relative to the chlorine atoms to ensure quantitative quaternization.

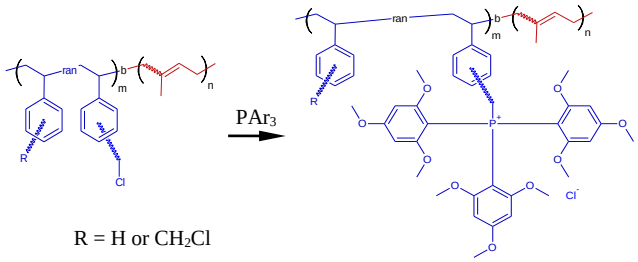


**Figure 30: Synthetic Scheme of Block Copolymers Quaternization.**

### 3.3.2 Morphology Characterization

The quaternization reaction mixtures were directly cast onto clean polytetrafluoroethylene sheets. After drying the films, transparent and uniform AEMs were obtained. The morphologies were analyzed using SAXS. Well-ordered microphase separated morphologies were achieved despite relatively small DPs, suggesting a large $\chi$ parameter between PIp and the ionic block. Although the chloroform evaporation rate was relatively rapid, sharp primary peaks and higher order peaks were observed. For example, AEM 4 displayed a lamellar morphology with the peak position ratios of 1:2:3:4:5:6 (Figure 31). The high order peaks indicate long-range order. This was presumably a result of the fast self-assembly kinetics. The $4^{th}$ order peak was suppressed, due to the form factor cancelling out the structure factor. The d-spacing of AEM 4 was 26.2 nm, which gave a thickness of the ionic domain being 6.6 nm. This thickness was close to the estimated contour length (9.8 nm) of the midblock, indicating the high chain rigidity of the ionic polymer segment. Since solution casting from chloroform was capable of inducing highly ordered

nanophases, these materials are regarded as processable membranes. No sign of ion cluster was observed by SAXS due to the distributed positive charge on the bulky cations, which suppressed the driving force for clustering. It was also found that the membrane morphologies were not impacted by the changes in environmental humidity (red trace for <5%RH and broken blue trace for 95%RH in Figure 31), which could be important for the dimensional stability upon hydration in applications like fuel cells. This was because of the reduced hydrophilicity of the $BzAr_3P^+$ cation with the steric side groups.

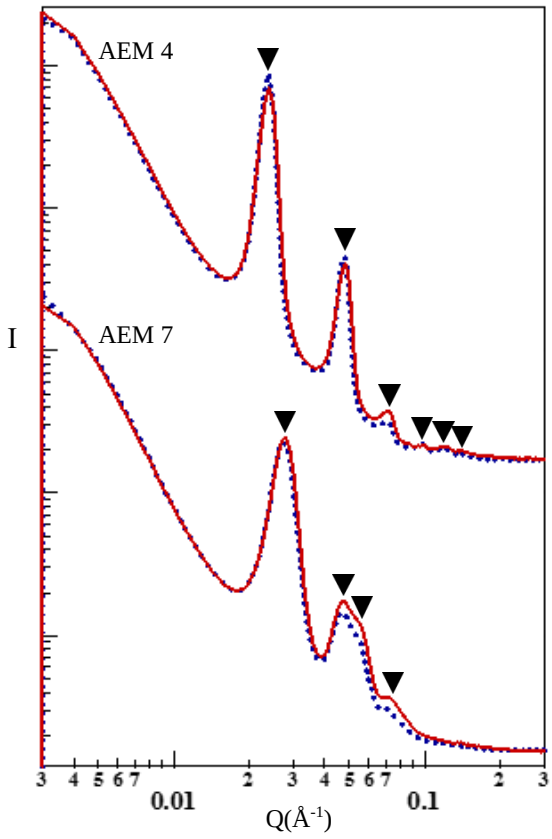


**Figure 31: SAXS Profiles of AEM 4 and 7.**

**The red traces are at dry conditions and the broken blue lines are at 95% RH.**

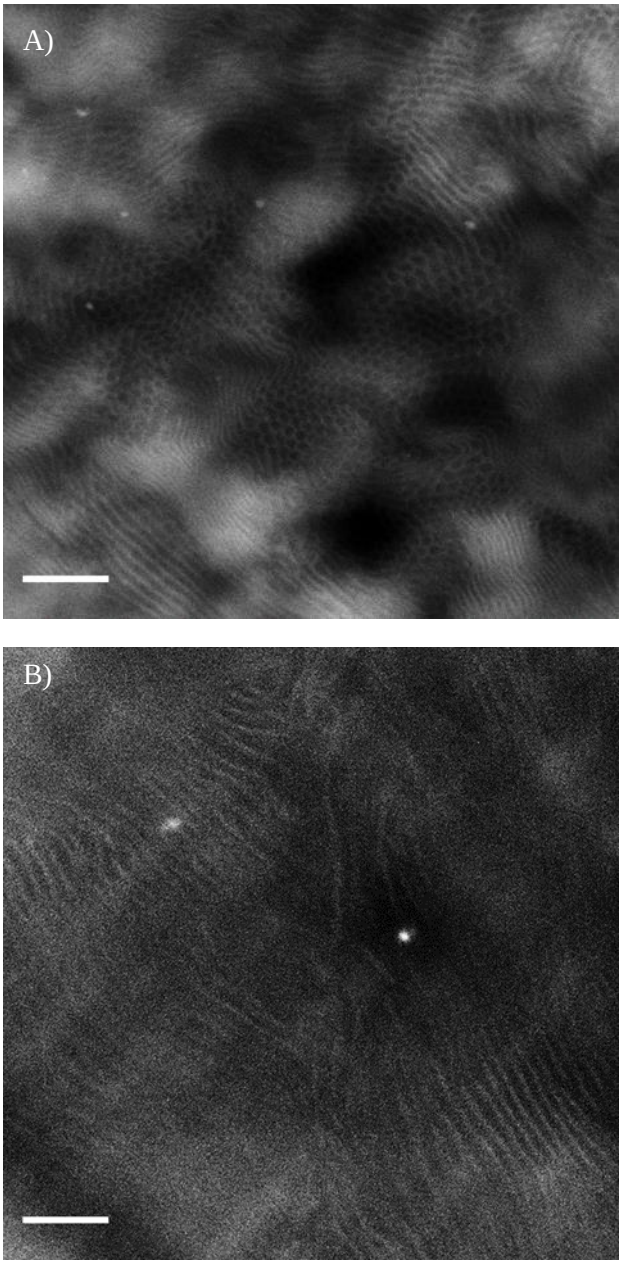


**Figure 32: Dark field TEM images.**

**The scale bars are 200 nm for A) AEM 11 and B) AEM 9.**

Even more interestingly, the morphological results were far from those predicted based simply on volume fractions. The morphologies and volume fractions are listed in Table 4. For a triblock copolymer, lamellar and hexagonal morphologies were observed at low and moderate ionic volume fractions, respectively, with the transition point seeming to be ~30% ionic block volume

fraction. The SAXS profiles of AEM 7 were shown in Figure 31 as an example, where peak position ratios were measured to be 1:√3: √4: √7. Similarly, this membrane showed no obvious response to water vapor treatment. Further evidence of a hexagonal morphology was achieving by dark field imaging TEM (Figure 32A). Both hexagonally packed circles and parallel lines were found, demonstrating the presence of ordered cylindrical domains. In addition, the white contrast of the ionic domain was the continuous matrix despite the much lower volume fraction than that of the PIp. This phenomenon was attributed to two factors. The first one was the conformational asymmetry of the block copolymers, which was caused by the bulky size of the $BzAr_3P^+$ ion. The end-to-end distances of the ionic blocks were calculated to be approximately proportional to the DPs, which indicated that the Kuhn length of the ionic blocks should be larger than the end-to-end distances observed here. The asymmetry ratio $\varepsilon$ was estimated to be >7, which was expected to dramatically shift the phase diagram and introduce similarities to the self-assembly of rod-coil block copolymer.[81,138] Also, important might be the electrostatic interaction between the ionic species. Using a hybrid self-consistent field theory and liquid state theory, it was recently demonstrated that electrostatic forces are able to shift the phase diagram substantially.[86] Experimentally, salt doping has been widely observed to shift block copolymer nanoscale morphologies,[120–122,139,140] and hexagonal phases with ionic matrix were also observed in block copolymers with ionic volume fraction being ~50%.[67,93] However, there have been no experimental reports showing continuous ionic domains at volume fractions as low as those observed in this work.

It was also found that in diblock copolymers the ionic blocks had an even greater tendency to form the continuous phase. Lamellar morphology, evidenced by both multiple peaks in SAXS and imaging by TEM (Figure 32B), was achieved at the ionic volume fraction being just 13%. Similar to triblock copolymers, no ionomer peak and little response to water vapor was detected. However, it seemed that the lamellar/hexagonal transition point shifted to ~21%. This was

attributed to the effect of polymer architecture. As theories suggest, the outer blocks of a symmetric triblock have a larger tendency to form the continuous matrix, compared to a diblock counterpart.[83]

### 3.3.3 Ion Conductivities

Three AEMs were investigated in $Cl^-$ conductivity ($\sigma$) tests at 95% RH by impedance spectroscopy (Table 5). Among them, AEM 1 and 2 were in a lamellar morphology (Figure 33A). It was observed that at all testing temperatures, AEM 2 showed higher conductivities than AEM 1. This was explained by the difference in IECs. AEM 2 possessed a higher IEC, in other words, it had more ions transporting across the material and thus displayed higher conductivities.

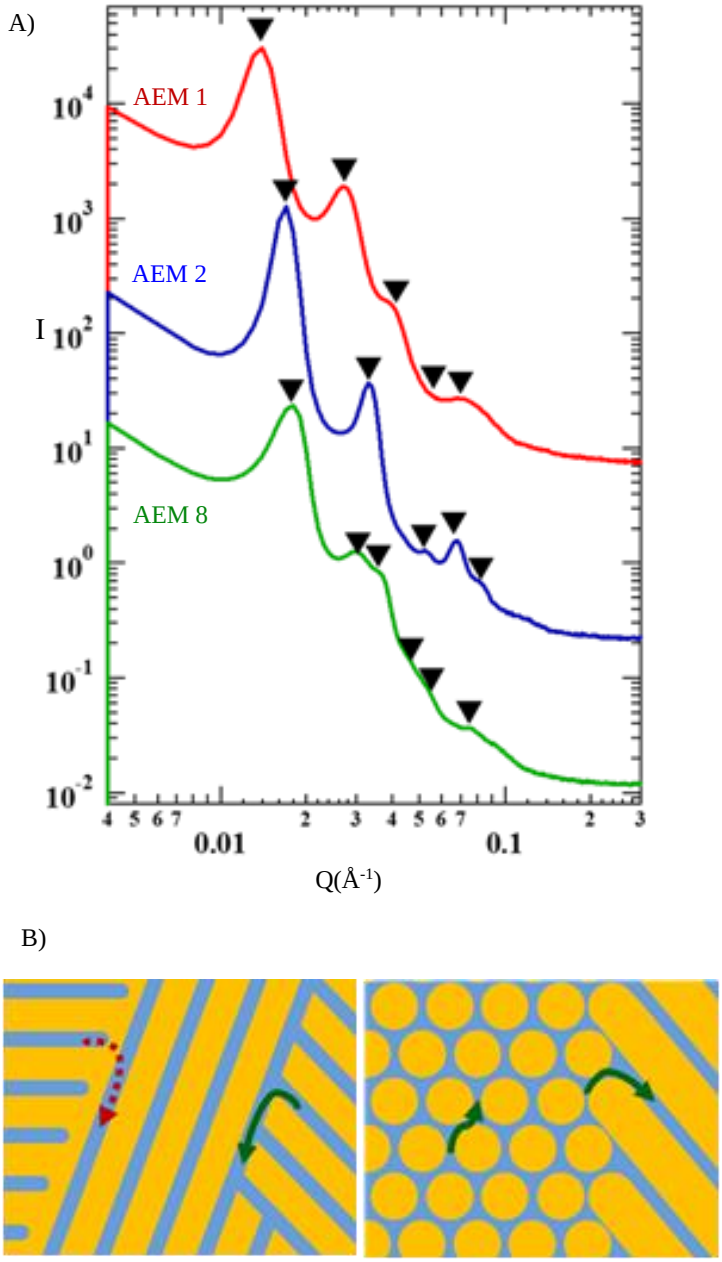


**Figure 33: Morphology and Ion Transport.**

**A) SAXS patterns of AEMs at dry state; B) Scheme of anion transport through lamellar and hexagonal phase, where the light blue domains are the ionic domain.**

**Table 5: Chloride Conductivities of AEMs.**

| AEM | σ(50 ºC) (mS/cm) | σ(65 ºC) (mS/cm) | σ(80 ºC) (mS/cm) | σ(90 ºC) (mS/cm) |
|---|---|---|---|---|
| 1 | 0.4 ± 0.1 | 1.3 ± 0.3 | 3.7 ± 0.9 | -[a] |
| 2 | 0.7 ± 0.0 | 1.9 ± 0.2 | 4.6 ± 0.3 | 6.9 ± 0.6 |
| 8 | 1.0 ± 0.1 | 3.5 ± 0.1 | 10.4 ± 5.3 | 20.6 ± 3.1 |

[a]Inconsistent values were obtained due to membrane failure.

However, AEM 8 seemed to be quite different. It was in a hexagonal phase as shown in Figure 33A, although it had similar ionic volume fraction and IEC with AEM 2. The morphological difference was attributed to the effect of polymer architecture on self-assembly as mentioned above. In addition, AEM 8 possessed a comparable d-spacing, which was a result of its MW being approximately half of that in AEM 2. This facilitated direct comparison between those two materials. It was found that AEM 8 provided much higher conductivities. The difference could not be attributed to the minor difference in the IECs, since the conductivities of AEM 1 and AEM 2 were measured to be of the same order, and thus the morphology was presumably the dominating factor. When $Cl^-$ transported through the hexagonal phase in AEM 8, the continuity of the matrix facilitated the ion motion compared to lamellar phases, due to two factors. First of all, the anion conduction in AEM 1 and AEM 2 is constrained by the orientation of the lamellae, while the hexagonal phase has 3-dimensionally continuous matrix so that the ions can move freely in any direction. Additionally, from the perceptive of the ionic domain shown in Figure 33B, there is either continuous (green arrow) or discontinuous junction (red arrow) across certain grain boundaries in a lamellar phase material, which are ion conductive and non-conductive, respectively, while only the continuous junction exists in a hexagonal phase membrane (Figure 33B). This suggests that the matrix of a hexagonal phase can be a good candidate for unperturbed ion conduction.

The highest conductivity achieved was 20.6 ± 3.1 mS/cm at 90 ºC on AEM 8 (Table 5). This conductivity was comparable with other reported copolymers. A phosphonium ion random copolymer provided 1.3 mS/cm of $Cl^-$ conductivity at room temperature.[101] In ammonium ion containing block copolymers with low $T_g$ hydrophobic blocks, $Cl^-$ conductivity were reported as high as 5 mS/cm at 30 ºC[40] and 13 mS/cm at 80ºC.[111] In the high $T_g$ PSt based materials, both imidazolium and ammonium block copolymers showed similar $Cl^-$ conductivities of ~15 mS/cm at 80ºC,[114] while cyclopropenium polymer provided 4 mS/cm at room temperature.[116] When taking the low IECs into consideration, our material seemed to be superior in anion transport. This was attributed to the continuous morphology and the reduced bounding between phosphonium and $Cl^-$ ions. The activation energy of AEM 1 was calculated to be ~$10^2$ kJ/mol, significantly higher than most AEMs reported.[20,40,72,114,116] This was attributed to the reduced hydrophilicity of the phosphonium cations, to which inadequate water was absorbed. Ion exchanging into other more hydrophilic counter ions, such as hydroxide and fluoride, is expected to enhance the conductivity and decrease the activation energy.

### 3.4 Conclusions

The RAFT synthesis of linear block copolymers based on CMS and Ip are reported. Irreversible chain transfer to BzCl sites was found to be absent. Quaternized block copolymers were cast from chloroform to form AEMs with well-ordered microphase separated morphologies. It was found that the phosphonium cations had unique properties. They imparted the polymers excellent solubility and fast self-assembly behavior, which led to convenient solvent processability. The phosphonium block preferred to form the continuous domain even at low volume fractions. The hexagonal phase with phosphonium matrix transported anions faster than a lamellar morphology. Promising conductivities were achieved at elevated temperatures under hydrated conditions.

# CHAPTER 4

# SYNTHESIS OF IONIC TRIBLOCK COPOLYMERS AND EFFECT OF MELTING TRANSITION IN HYDROPHOBIC BLOCK

## 4.1 Introduction

### 4.1.1 Thermal Transition Effect on Ion Conductivity

In anhydrous polymeric materials, such as salt (lithium salt or ionic liquid) doped polymers and polymerized ionic liquids, the thermal characteristics (i.e. glass transition and crystallization) significantly affect ion transport. Most reports were above the $T_g$ of the ion conducting domain, since the liquid-like material behavior is necessary to provide enough segmental mobility for ion diffusion.[142,143] Often the Vogel-Fulcher-Tammann equation is used to fit the conductivity data, which correlates the ion conductivity with viscosity usually directly affected by the $T_g$.[143–148] The crystallization of the ion conduction domain was also investigated and it was found that the crystallization significantly increased the activation energy, likely due to constrained segmental movement and morphological contribution.[119,149] Surprisingly, the thermal properties of the non-ionic domain in a block copolymer system possesses some non-negligible influence on the ion conduction through the material in a few examples. The transition of the non-ionic domain from a glassy state into the liquid phase increases the ion conductivity, although the mechanism is not yet clear.

In contrast, in water assisted ion transport, the conductivities are usually regressed using Arrhenius-like equations, since the content of water, as a plasticizer, is usually high enough to reduce the $T_g$ to far below the testing temperatures.[20,23,91,93,110,114,116,145] However, behaviors that can be regressed to Vogel-Fulcher-Tammann equation have also been observed, imparted by the high $T_g$ polymer backbone and special morphology.[98,150] Unfortunately, in a microphase separated

material, the effect of hydrophobic block thermal transitions remain challenging to understand. The glass transition of polymethylbutylene (-51 ºC) was found to display a small yet non-negligible effect on the activation energy, as measured by broadband electrical spectroscopy.[63] It was also found that the crystallization of polyethylene block in a proton exchange block copolymer affected the domain interfaces and thus the conductivity.[151] However, this work was based on the comparison between block copolymers with crystalline and amorphous hydrophobic block, where the morphology difference brought by processing conditions could not be excluded.

In this chapter, we will investigate a series of block copolymers with polycyclooctene being the hydrophobic block, which has a melting point of ~50 ºC and thus enables direct observation of the melting transition affecting membrane performance. The block copolymer of PCMS and polycyclooctene (PCOE) can be synthesized by combining ROMP and RAFT polymerizations and transformed into ionic BCPs by quaternization reactions.

### 4.1.2 Ring-Opening Metathesis Polymerization

Ring-Opening Metathesis Polymerization (ROMP) is a high-efficiency polymerization technique for cyclic olefins, where an organometallic catalyst is used to relieve the ring-strain in the monomers as the drive force for polymerization(Figure 34).[152–155] Grubbs' catalysts are the most popular species today, due to the fast propagation rate, mild reaction condition, high stability, and excellent tolerance to a wide range of functionalities.[156–158] Among the reported monomers, norbornene, cyclooctene, cyclooctadiene, and their derivatives are most often used due to fast polymerization kinetics, and availability or ease in synthesis. Functionalized norbornene could be polymerized in a "living" manner with very low dispersity; while polycyclooctene and polycyclooctadiene generally have Đ around 2.0. This is because of slow chain initiation and the presence of secondary metathesis on the C=C double bonds, which gives the polymerization some step-growth characateristics.[159–162] Recently, molecules containing a reactive C=C (for Grubbs

catalysts) or C=O (for Schrock catalysts) bond have been utilized as CTAs to mediate ROMP polymerization the products of which were hemitelechelic or telechelic polymers with the end-functionalities directly from the CTAs.[163–167]

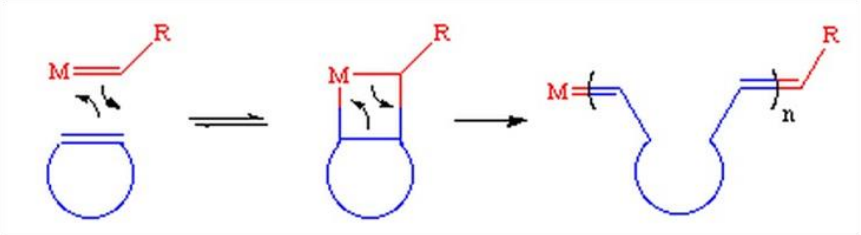


**Figure 34: Mechanism of ROMP.**

**Figure adapted from Ref 152.**

### 4.1.3 Triblock Copolymer with Broad MW Distribution

Using the chain transfer ROMP (CT-ROMP) methodology metioned above, telechelic polycyclooctene and polycycooctadiene (effectively poly(1,4-butadiene)) can be synthesized with Đ being ~2.0. When appropriate functionalites were incorporated at the chain-ends, such as ATRP initiators, nitroxide groups, and hydroxyl groups (initiator for anionic ring-opening polymerization), these polymer can be subjected to chain extension to install outerblocks with narrow MW distributions.[168–170] Using this approach, a series of ABA triblocks were synthesized and applied to bulk morphology investigation. It was found that in the weak segregation regime, a stable disordered bicontinuous morphology was obtained with the volume fraction of B block being ~50%.[171] The critical $\chi N$ value for ordered microphase separation was reduced by >50%, while the lamellar window was shifted to the region with dramatically higher volume fraction of the midblock.[172] This phenomenon was caused by two factors. First, the ABA triblock chains with short midblock acts like dimeric homopolymer and swell the A block domain, which changes the effective volume fraction, and also increases the conformational entropy for microphase separation. At the same time, the B blocks with intermediate and long length distribute differently in its domain,

which increases the entropy of the system as well as forces the interface between A and B domain to buckle towards the B domain.[173–175] However, the effect of Đ on ABA triblock copolymers with intermediate and strong segregation is not entirely clear yet, although phase coexisting and lamellar phase shifting to a regime with lower B block volume fraction have been observed.[176–178]

## 4.2 Experimental Section

### 4.2.1 Materials

Chloromethylstyrene (mixture of *para*- and *meta*-isomers, CMS) and 4-chloromethylstyrene (4CMS) were passed through a short column of basic alumina and stored at -30 °C before use. Thermal initiators, 2,2'-Azobis(2-methylpropionitrile) (AIBN) was recrystallized from MeOH. Using a reported method, 2-cyano-2-propyl butyl trithiocarbonate (O-CTA) was synthesized.[58] Ethyl acetate was dried over magnesium sulfate for at least one day before use. Other chemicals were used as received without further purification.

### 4.2.2 Synthesis of Chain Transfer Agent for ROMP and RAFT

In the first step, 1,1'-[(2Z)-but-2-ene-1,4-diylbis(oxymethylene)]bis(4-ethenylbenzene) (StEneSt) was synthesized by nucleophilic substitution. Sodium hydride (NaH, 60% suspension in oil, 4.12 g) was stirred with hexanes and then quickly filtered before use. Into a conical flask, 4.3 g KI, 11.03 g 4CMS, 3.04 g cis-2-butene-1,4-diol, and 100 mL DMF was charged at 0 °C. While stirring the mixture, NaH was slowly added during a period of 10 minutes. One hour later, the reaction was allowed to warm to room temperature and run overnight. Finally, the reaction was quenched by slowly adding water. The mixture was partitioned between $H_2O$ and diethyl ether. The organic layer was collected and washed with $H_2O$ for 3 times. Finally, the organic layer was concentrated and purified using column chromatography (hexanes: ethyl acetate = 10:1 as the eluent) to yield a colorless oil (8.55 g, yield = 77%) as the product StEneSt. The chemical structure

was confirmed by NMR (Figure 35) and MS (Theoretical 320.2, FAB-MS Found 321.3 for M+H and 319.3 for M-H).

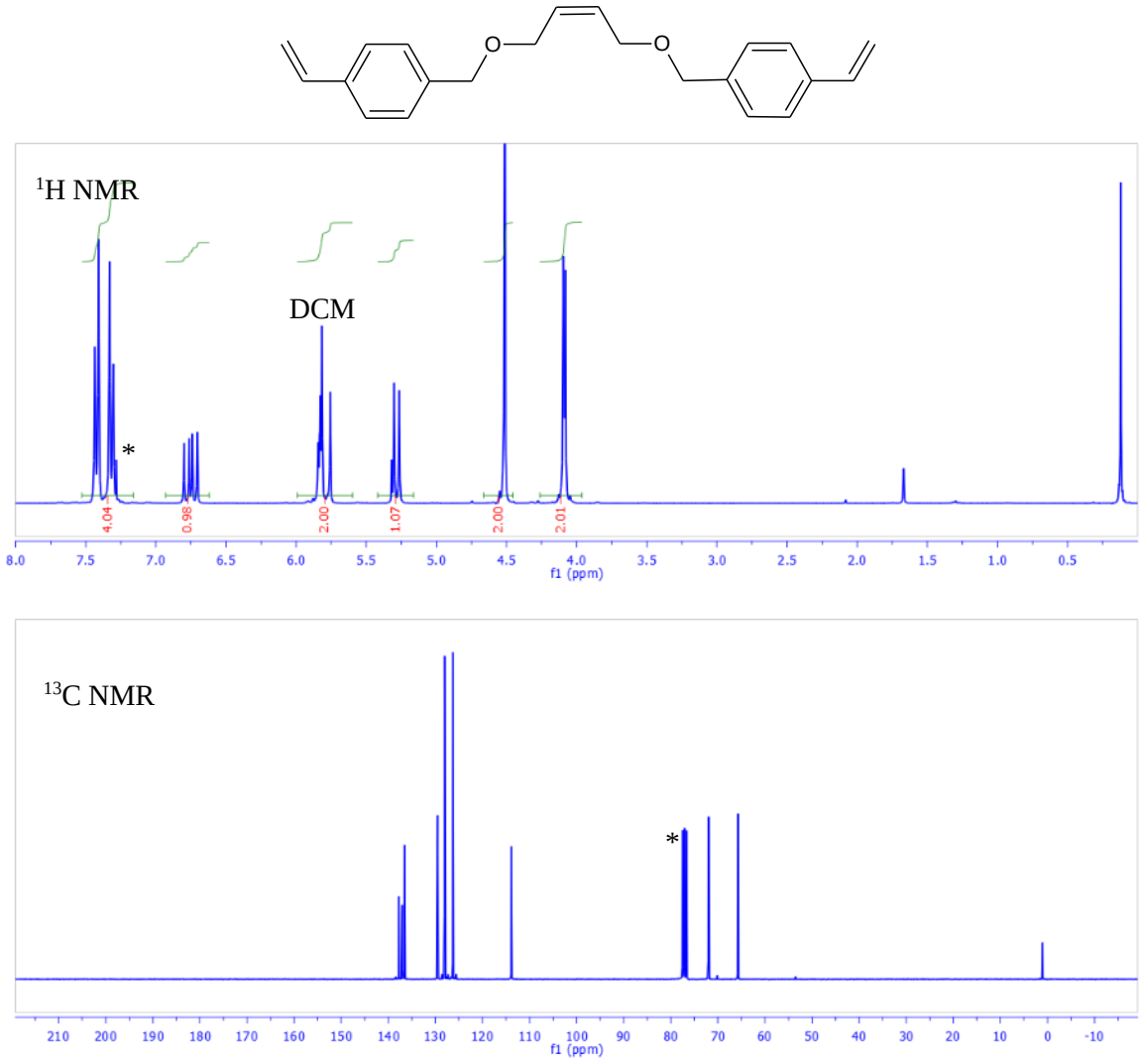


**Figure 35: Chemical Structure and NMR Characterization of StEneSt.**

In the second step, 1.57 g StEneSt was mixed with 2.48 g O-CTA, 305 mg AIBN, and 4 mL ethyl acetate in a Schlenk flask. The yellow reddish solution was degassed by purging with nitrogen for 20 minutes and then sealed before being heated to 70 $^{o}$C. Be careful: a significant amount of nitrogen can be produced and a needle was plugged to balance the pressure. After 48

hours, the solution was concentrated using and subject to column chromatography using hexanes: ethyl acetate = 4:1 (v:v) as the eluent to yield a yellow oil with high viscosity as the product $R_2$-CTA (3.56g, yield = 91%). The structure was confirmed by NMR (Figure 36) and MS (Theoretical 786.25, FAB-MS 785.2 for M-H).

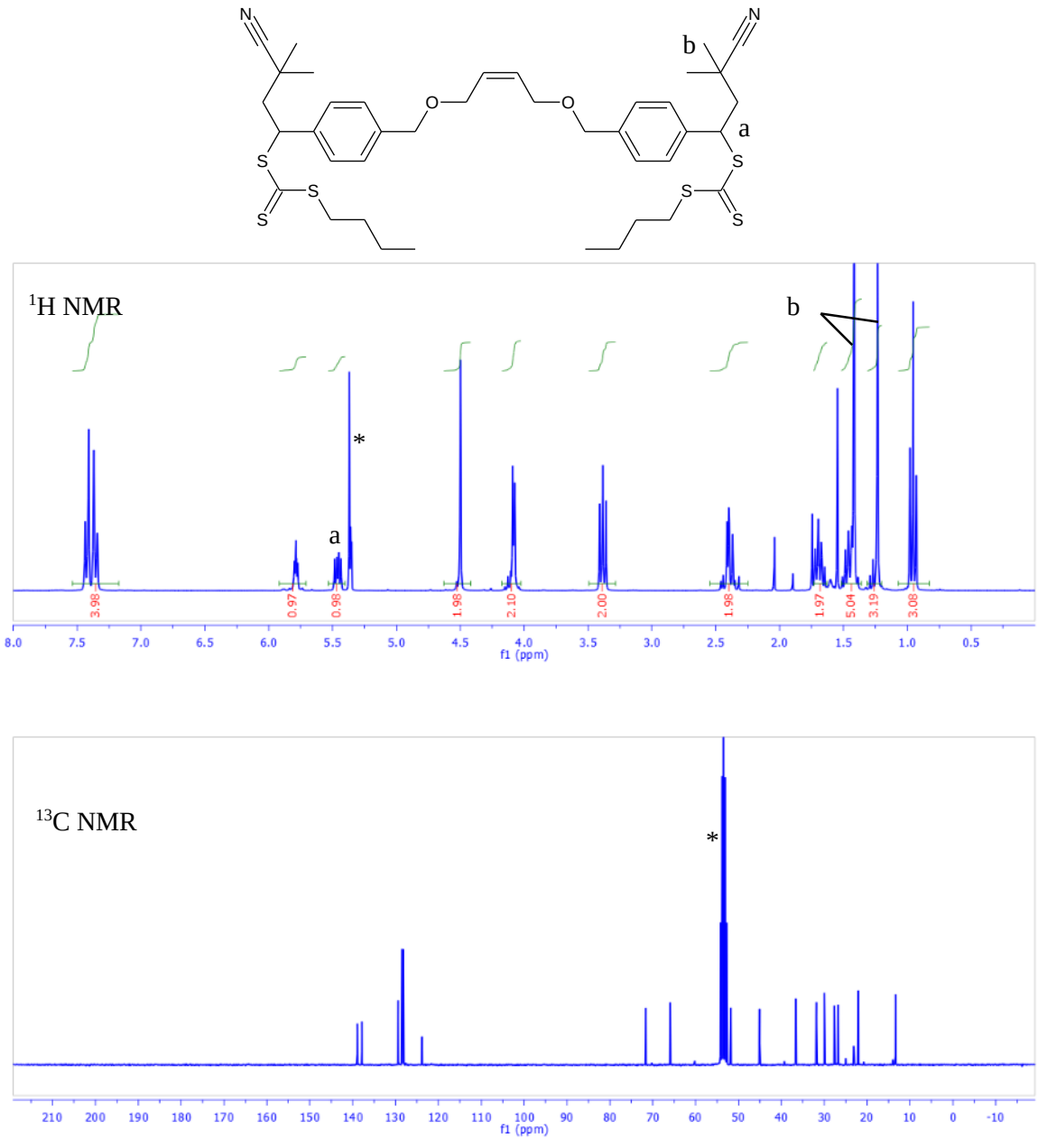

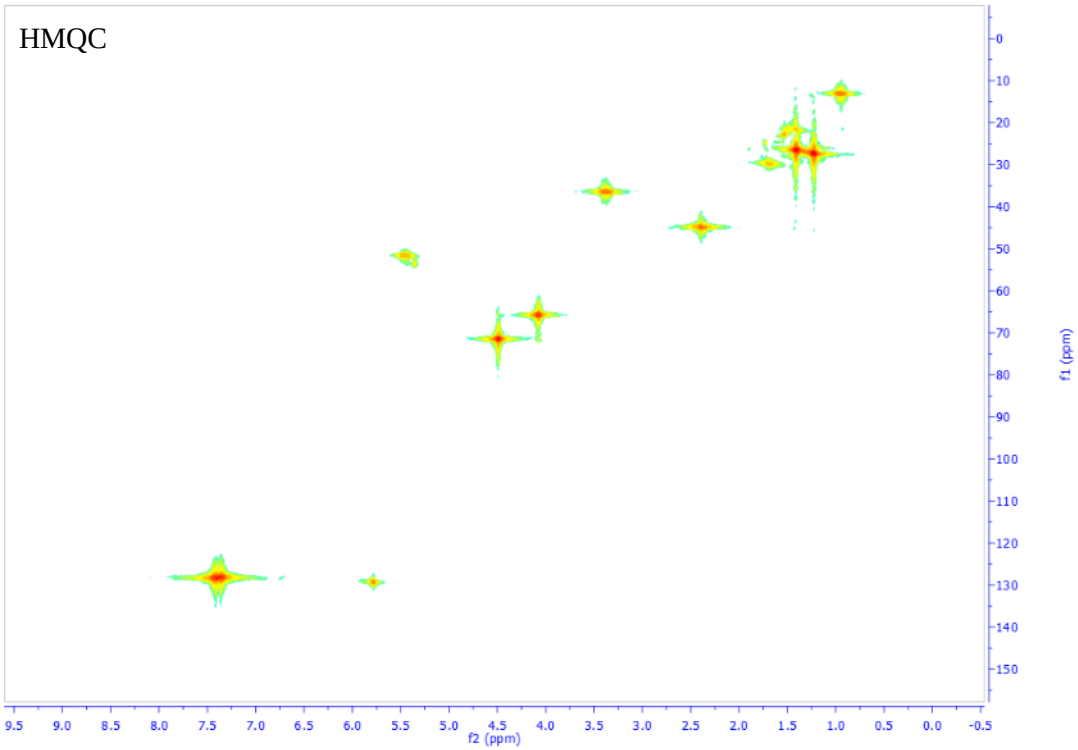


**Figure 36: Chemical Structure and NMR Characterization of $R_2$-CTA.**

### 4.2.3 Synthesis of Cyclooctene Containing RAFT CTA

In the first step, 5-hydroxy-1-cyclooctene was synthesized using a previously reported method.[155,179]

Secondly, sodium hydride (60% suspension in oil, 1.59 g) was stirred with hexanes and then quickly filtered before use. Into a conical flask, 4.62 g KI, 5.02 g 4CMS, 3.41 g 5-hydroxy-1-cyclooctene, and 50 mL DMF was charged at 0 °C. While stirring the mixture, NaH was slowly added during a period of 10 minutes. One hour later, the reaction was allowed to warm to room temperature and run overnight. Finally, the reaction was quenched by slowly adding water. The mixture was partitioned between $H_2O$ and diethyl ether. The organic layer was collected and washed with $H_2O$ for 3 times. Finally, the organic layer was concentrated and purified using column chromatography with hexanes being the eluent to yield a colorless oil (4.80 g, yield = 74%) as the

product, StCOE. The chemical structure was confirmed by NMR (Figure 37) and MS (Theoretical 242.17, FAB-MS Found 243.18 for M+H).

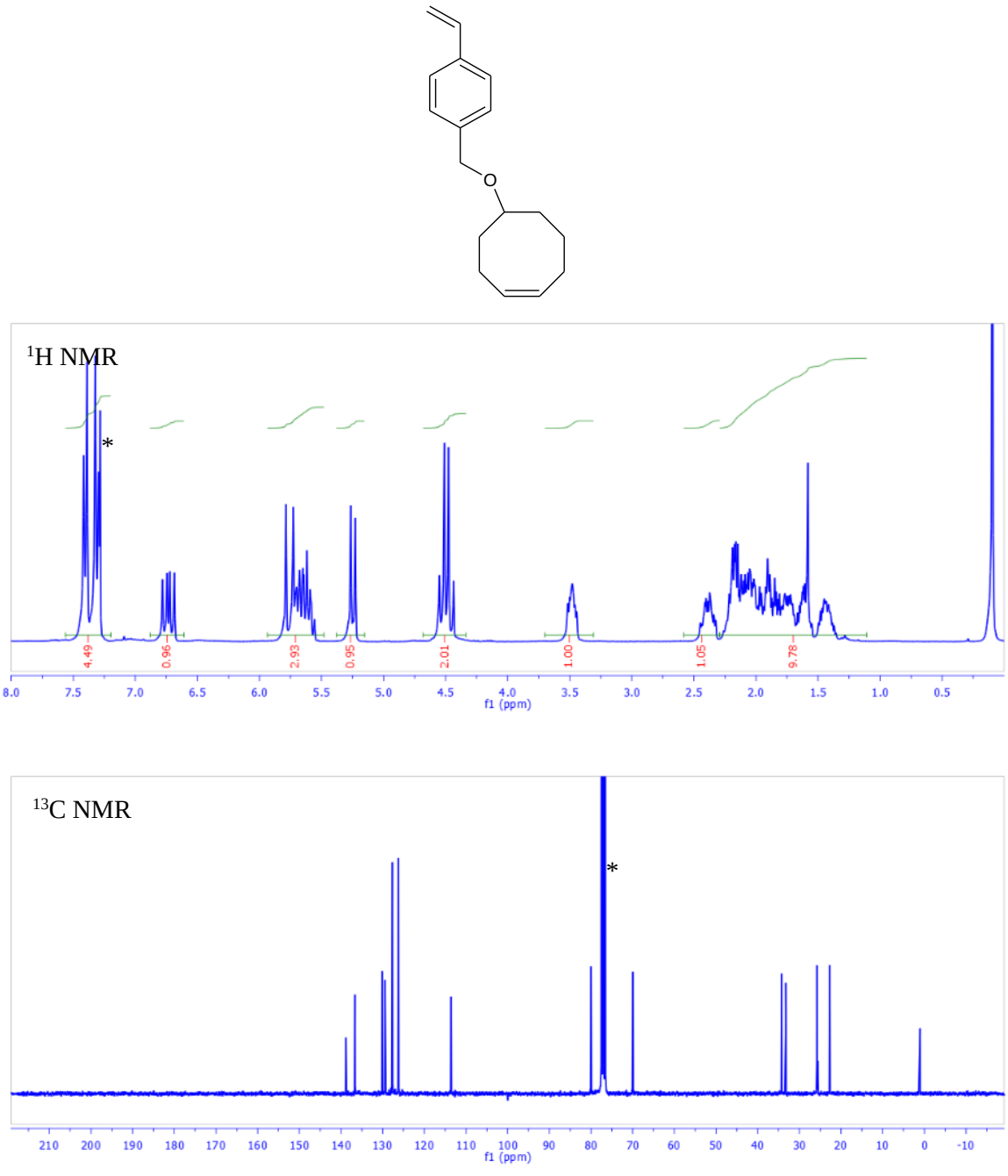


**Figure 37: Chemical Structure and NMR Characterization of StCOE.**

In the third step, 3.75 g StCOE was mixed with 3.90 g O-CTA, 340 mg AIBN, and 9 mL ethyl acetate in a Schlenk flask. The yellow reddish solution was degassed by purging nitrogen for 20 minutes and then sealed before being heated to 70 $^{o}$C. Be careful: a significant amount of nitrogen can be produced and a needle was plugged to balance the pressure. After 48 hours, the solution was concentrated and subject to column chromatography using hexanes: ethyl acetate = 5:1 (v:v) as the eluent to yield a yellow oil with high viscosity as the product COE-CTA (6.28 g, yield = 84%). The structure was confirmed by NMR (Figure 38) and MS (Theoretical 475.2, ESI-MS 498.1 for M+Na).

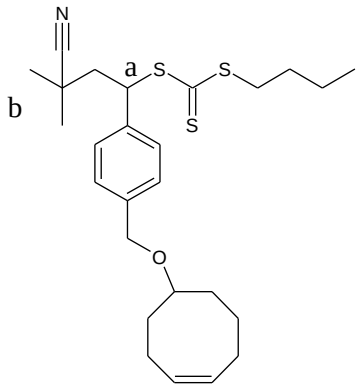

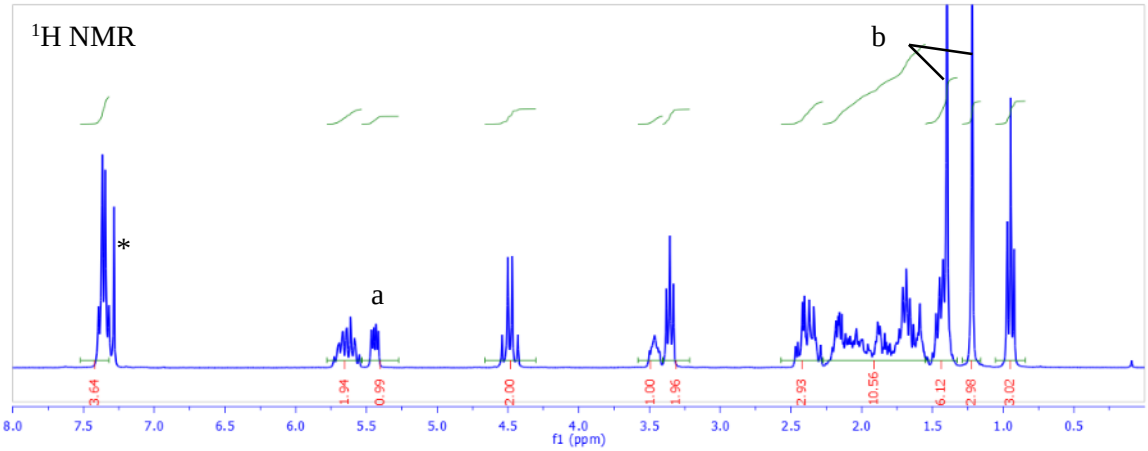
$^{1}$H NMR
b
*
a
3.64
1.94
0.99
2.00
1.00
1.96
2.93
10.56
6.12
2.98
3.02
8.0 7.5 7.0 6.5 6.0 5.5 5.0 4.5 4.0 3.5 3.0 2.5 2.0 1.5 1.0 0.5
f1 (ppm)

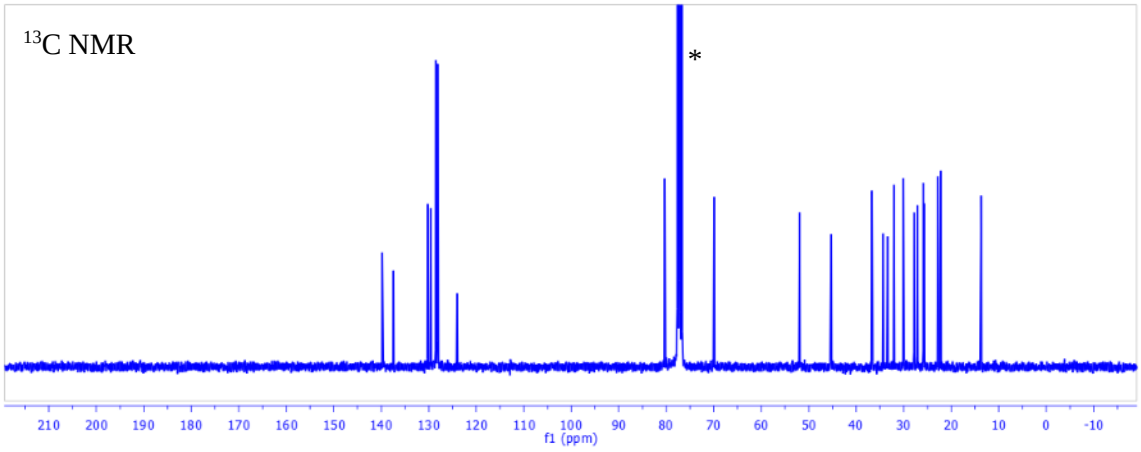
$^{13}$C NMR
*
210 200 190 180 170 160 150 140 130 120 110 100 90 80 70 60 50 40 30 20 10 0 -10
f1 (ppm)

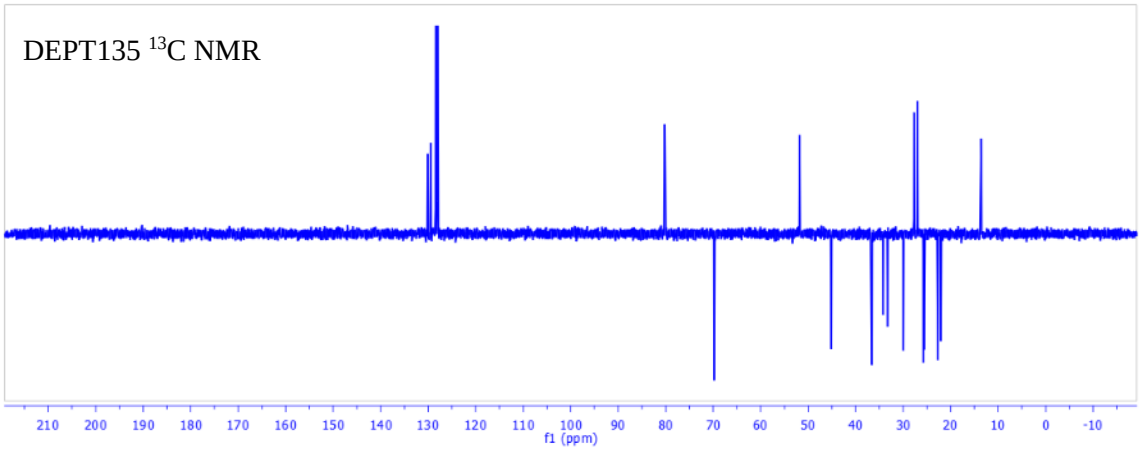
DEPT135 $^{13}$C NMR
210 200 190 180 170 160 150 140 130 120 110 100 90 80 70 60 50 40 30 20 10 0 -10
f1 (ppm)

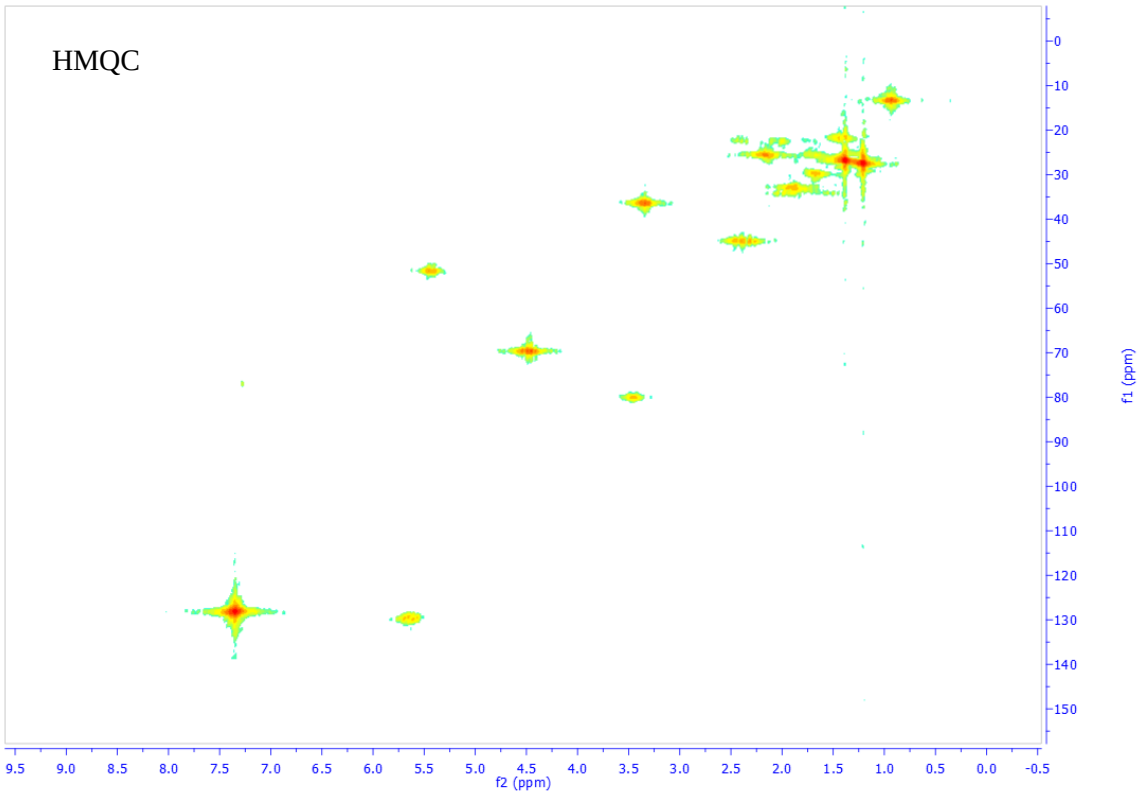


**Figure 38: Chemical Structure and NMR Characterization of COE-CTA.**

### 4.2.4 Synthesis of Telechelic PCOE

Into a reaction vessel was charged 8.5 g COE, 300 mg R2-CTA, and 4.2 g toluene. The mixture degassed by purging with nitrogen for 10 minutes at 0 °C and then sealed before 6.5 mg Grubbs 2nd generation catalyst in 4.3 g toluene was added using a syringe. The solution was subjected to nitrogen purge at 0 °C for another 10 minutes and then sealed. After reacting for 12 hours at 60 °C, the polymer was isolated by precipitating into large excess of MeOH twice. The polymer was tested using GPC against PSt standards.

### 4.2.5 Synthesis of Triblock Copolymer

In a round-bottom flask, 1.8 g PCOE, 5.0 g CMS, and 12.1 g chlorobenzene (ClBz) was charged and heated at 60 °C to fully dissolve. After being cooled to room temperature, to the

solution was added 1.5 mg AIBN. The mixture was degassed by purging with nitrogen for 20 minutes and then sealed before being heated to 60 $^{o}$C to initiate the chain extension reaction. After a certain period of time, the polymerization was quenched to 0 $^{o}$C and precipitated into MeOH three times to remove excess CMS monomer.

To remove PCMS homopolymer, the polymer product was stirred in THF/MeOH (6:5 = v:v, 20 mL for per gram of polymer) for two days. The insoluble part was filtered and washed with more THF/MeOH (40 mL for per gram of polymer). The residual polymer was collected and dried in vacuum. The MW was estimated by NMR end-group analysis, and the molecular weight distribution was measured by GPC using polystyrene calibration.

### 4.2.6 Membrane Fabrication

First, a chloroform solution of the purified triblock copolymer was prepared with a concentration of ~100 mg/mL, where heating may be necessary to ensure full dissolution. When cooled to room temperature, the solution was cast onto a clean polytetrafluoroethylene sheet and covered with a glass petri dish to decelerate the solvent evaporation. After 12 hours, the as-formed film was carefully peeled off and immersed in a trimethylamine aqueous solution (50 wt%) for at least 3 days for solid state quaternization reaction. The quaternized product, triblock anion exchange membrane (TAEM) was washed with and then annealed in deionized $H_2O$ at 80 $^{o}$C for 24 hours. The membrane was carefully pressed into water by a small piece of glassware to avoid floating, because rapid water evaporation at such temperature can damage the membrane.

### 4.2.7 Small Angle X-ray Scattering (SAXS)

The testing was performed at The Basic Energy Sciences Synchrotron Radiation Center (BESSRC) at the Advanced Photon Source at Argonne National Lab on beamline 12 ID-B. A Pliatus 2M SAXS detector was used to collect scattering data with an exposure time of 1 s. The X-

ray beam had a wavelength of 1 Å and power of 12 keV. The intensity (I) is a radial integration of the 2D scattering pattern with respect to the scattering vector (q).

Temperature and humidity were controlled within a custom sample oven as described previously.[133] Typical experiments studied three membrane samples and one empty window so a background spectrum of the scattering through the Kapton® windows and nitrogen environment could be obtained for each experimental condition. The humidity of the sample environment was controlled by mixing heated streams of saturated and dry nitrogen. Sample holders were inserted into an oven environment of 60 ºC and <10% relative humidity. The samples were allowed to dry for 40 minutes before X-ray testing were taken. Relative humidity was then ramped to 25%, 50%, 75%, and 95% while the temperature was maintained at 60 ºC. The equilibrium time before taking an X-ray spectrum was 20 minutes between dry, 25%, and 50% and increased to 40 minutes between 50%, 75%, and 95%. Soaked membranes were dipped in water for at least 12 hours and quickly mounted to the sample holders at 95% and subjected to SAXS testing.

### 4.2.8 Ion Conductivity Measurement

The in-plane conductivity of the membranes was calculated using electrochemical impedance spectroscopy to measure membrane resistance as given by the equation below,

$$\sigma = l/(R*W*t)$$

where R is the membrane resistance, l is the distance between the electrodes, w is the width of the membrane samples, and t is the thickness of the sample. Impedance spectra were obtained over a frequency range of 1 to $10^6$ Hz using a four-electrode test cell connected to a BioLogic VMP3 multi-channel Potentiostat. The measurements were made in a TestEquity environmental chamber to control sample temperature and humidity. The resistance of the membrane was determined from

the low frequency intercept of the Nyquist impedance plot. Experiments were performed at constant relative humidity 95% RH, varying temperature from 30 to 90 °C.

### 4.2.9 Dynamic Vapor Sorption

A DVS-advantage instrument from Surface Measurement Systems was used to study water uptake of membranes. In a dynamic vapor sorption (DVS) study, measurement of water vapor uptake and loss of vapor by the membrane is examined gravimetrically. First, the membrane is dried for 60 min at 60 °C and 0% RH to obtain the dry mass. Following this, RH is increased gradually in four steps to reach a maximum of 90% RH. At each step, the membrane was allowed to equilibrate at a particular RH for 60 min.

### 4.2.10 Mechanical Characterization

Mechanical testing of samples was performed by extentional rheometer tool. Extensioanl testing was performed on a Sentmanat Extensional Rheometer (SER) (Xpansion Instruments, Tallmadge, OH) fixture on an ARES G2 rheometer (TA Instruments, New Castle, DE). The SER tool consists of 2 counterrotating drums, one of the drums is attached to a motor at the bottom and other drum is attached to a transducer at the top of the instrument. Membrane samples (~ 25mm x 3mm) are clamped to the two drums and tension is applied until the membranes break. SER drums were modified by fitting clamps with silicone rubber to prevent slippage of membranes.83 Films were tested at Hencky strain rates that correspond to ASTM D882–12, for tensile testing of thin plastic sheeting, but rates were modified to account for the constant sample loading distance inherent to the SER fixture. Hencky strain rate is decided based on elongation of the samples, which was more than 100% in this case and thus a Hencky strain rate of 0.33 s-1 was used. All measurements were performed in a custom built humidity oven at 30 and 60°C and 25 and 95% relative humidity conditions, such that we can capture the effect of the transition temperature. The

oven has a swinging door with 2 openings at top and bottom to accommodate the SER tool. Humidity was controlled by supplying a mixture of dry and wet gas which was controlled by 2 mass flow controllers (10,000 SCCM, MKS 1179A, Andover, MA) and heated gas lines. Humidity was measured by a humidity probe (Vaisala HMT 337, Boulder, CO) fitted inside of the custom built oven. Oven, gas transfer lines, and humidity bottle were all temperature controlled by external heaters. All temperature and humidity setpoints were controlled by the LabView software with homebuilt feedback control system. Details about the custom built instrument can be found here.[180]

## 4.3 Results and Discussions

### 4.3.1 CTA Synthesis

To mediate the synthesis of PCMS-*b*-PCOE-*b*-PCMS, a strategy using RAFT and ROMP polymerization techniques was designed, in which the midblock PCOE was synthesized first and chain extended with CMS to give the triblock copolymer. To mediate this protocol, a special molecule, $R_2$-CTA, was designed. As shown in Figure 39, $R_2$-CTA was synthesized in a two-step procedure, consisting of a Williamson ether synthesis and a single unit insertion reaction, which worked efficiently to give a yellow viscous oil as the product in an overall yield of 70%. In the ether formation reaction, iodide anion was used to replace the chloride in CMS (Finkelstein reaction) to accelerate the nucleophilic substitution. The single unit insertion reaction was highly efficient and will be discussed in detail in Chapter 7. The structure of the molecule was carefully chosen to incorporate multiple functionalities. The trithiocarbonate groups (groups in orange in Figure 39) were needed to provide a fast chain transfer rate, while the 1-phenylethyl groups (in blue) was necessary for successful fragmentation step in RAFT polymerization, both of which can together mediate well-controlled RAFT polymerizations of CMS. At the same time, the alkene (green group) can act as a CTA in ROMP polymerization of COE to provide partial MW control and a telechelic structure in the resulting polymer.[181] The ether bond (in purplish red) was selected as the covalent

link between the PCOE and PCMS blocks, which is not easily hydrolyzable. Interestingly, it was observed that the methyl protons in the 1-cyano-isopropyl groups have two distinct peak in $^1$H NMR (δ = 1.2 and 1.4 ppm, respectively, Figure 36). This was due to the fact that they were located close to $C_a$, which is a chiral center, and thus they experience different chemical environments.

Using a similar approach, COE-CTA was synthesized, which could be utilized in graft copolymer synthesis. However, it will not be discussed in this dissertation.

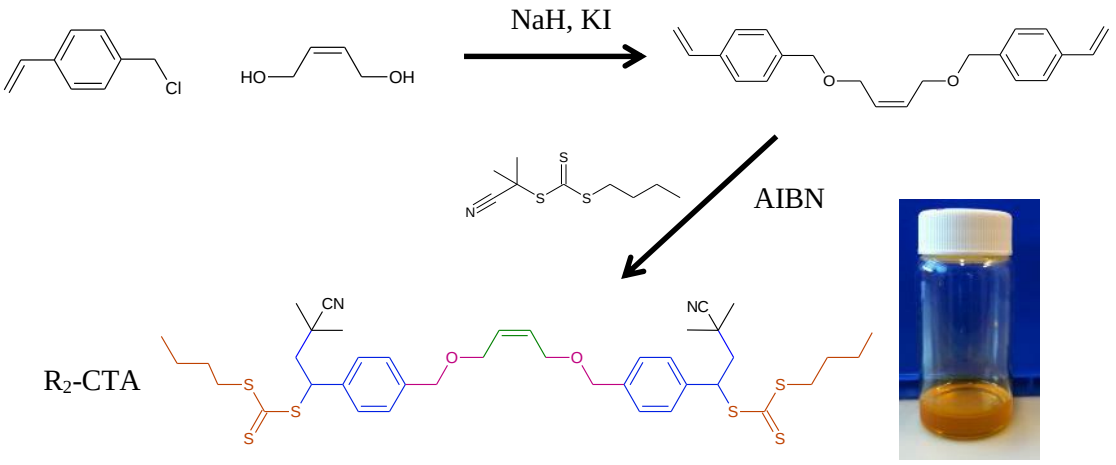


**Figure 39: Synthetic Protocol of $R_2$-CTA.**

### 4.3.2 Triblock Copolymer Synthesis

First, telechelic PCOE was synthesized using chain-transfer ROMP (CT-ROMP) polymerization of COE mediated by $R_2$-CTA. The polymerization proceeded rapidly and the mixture of COE and toluene (~1:1 = v:v) solidified in 15 minutes at 60 °C, which was attributed to the fast polymerization catalyzed by G2 and its excellent tolerance to functionalities, especially trithiocarbonate in this case.[169,182,183] The dispersity was measured to be ~1.7 in the samples synthesized in this chapter, which was in good agreement with literature results, although ROMP is known to proceed in a chain-growth polymerization mechanism.[161,181,184,185] This was mainly due to two reasons. Cis-cyclooctene has a relatively slow initiation rate to be polymerized in a living

manner, when catalyzed by G2.[186] There is frequent secondary olefin metathesis reaction during the reactions, in other words, the C=C bonds in the middle of chains are exchanging with the active Ruthenium center, which gives the reaction some characteristics of step-growth polymerization.[159–162] According to the mechanism of the CT-ROMP, the end-groups of the resulting polymer only comes from two sources, which are the G2 catalyst/initiator and the CTA. Assuming only linear PCOE was generated in the polymerization and considering the feeding ratio of $R_2$-CTA versus G2 being ~50 in this chapter, it was concluded that the majority (>95%) of end-groups were from the $R_2$-CTA and thus most of the resulting PCOE were telechelic with a trithiocarbonate group at each terminus.

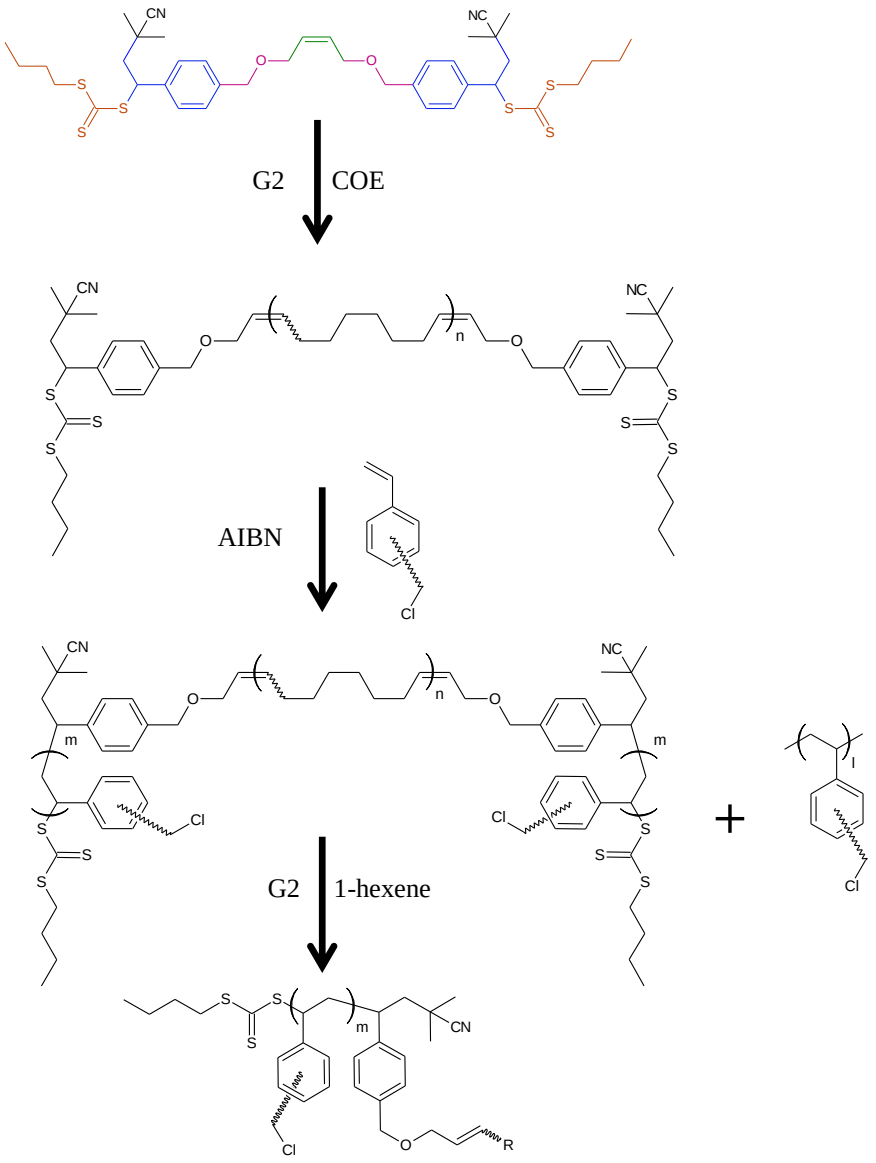


**Figure 40: Synthesis and Degradation of PCMS-*b*-PCOE-*b*-PCMS.**

The slightly yellow (due to the trithiocarbonate end-group) product was chain extended with CMS by RAFT polymerization (Figure 40). A relative low reaction temperature (60 $^{o}$C) was used in this reaction to suppress the irreversible chain transfer or copolymerization of the C=C bonds in PCOE. To demonstrate the well-controlled MW and absence of side reactions, one as-precipitated polymer was reacted with a large excess of 1-hexene and the cross-metathesis reaction was catalyzed by G2 to degrade the PCOE segments. By precipitation into hexanes, the residual

polymer was isolated and identified as PCMS, since proton peak on the C=C disappeared (only end-group C=C proton can be seen by $^1$HNMR in the range of $\delta$ = 5.1 – 5.8 ppm, Figure 41). Narrow MW distribution (Đ = 1.08, $M_p$ = 4.4k) as observed by GPC (Figure 42), which confirmed the side reactions being eliminated, well-controlled polymerization, and thus linear copolymer architecture.

However, it should be noticed that due to the RAFT polymerization mechanism, homopolymer of CMS not attached to PCOE midblock was inevitably generated, which after quaternization could be dissolved in water and detach from the membrane. This can cause errors in membrane composition analysis and thus bias the characterization measurements. To remove the homopolymer fraction, the as-synthesized triblock copolymer was stirred in THF/MeOH (6:5 = v:v), which readily dissolves the homopolymer of CMS but not the block copolymer. The insoluble part was collected and washed to obtain the purified PCMS-*b*-PCOE-*b*-PCMS. The successful removal of CMS homopolymer was proved by the disappearance of low MW shoulder in GPC trace, which was almost overlapping with the peak of isolated PCMS (Figure 42). As a consequence, the composition of CMS was decreased, as observed by $^1$H NMR (Figure 41).

The "soluble" fraction, consisting of the polymer dissolved and suspended during the solid state extraction process, was also analyzed by GPC and NMR. By GPC measurement, it was found to contain homopolymer of CMS as well as a large quantity of polymers with narrow dispersity and higher MW (Figure 42). This fraction had a peak MW $M_p$ = 11.4k in GPC, showing that it is not a dimeric homopolymer of CMS from residual $R_2$-CTA. In the $^1$H NMR spectrum, a small yet non-negligible peak of C=C proton was observed, which indicates that the higher MW fraction was likely triblock copolymer containing only a very short PCOE midblock (DP ~ 22).

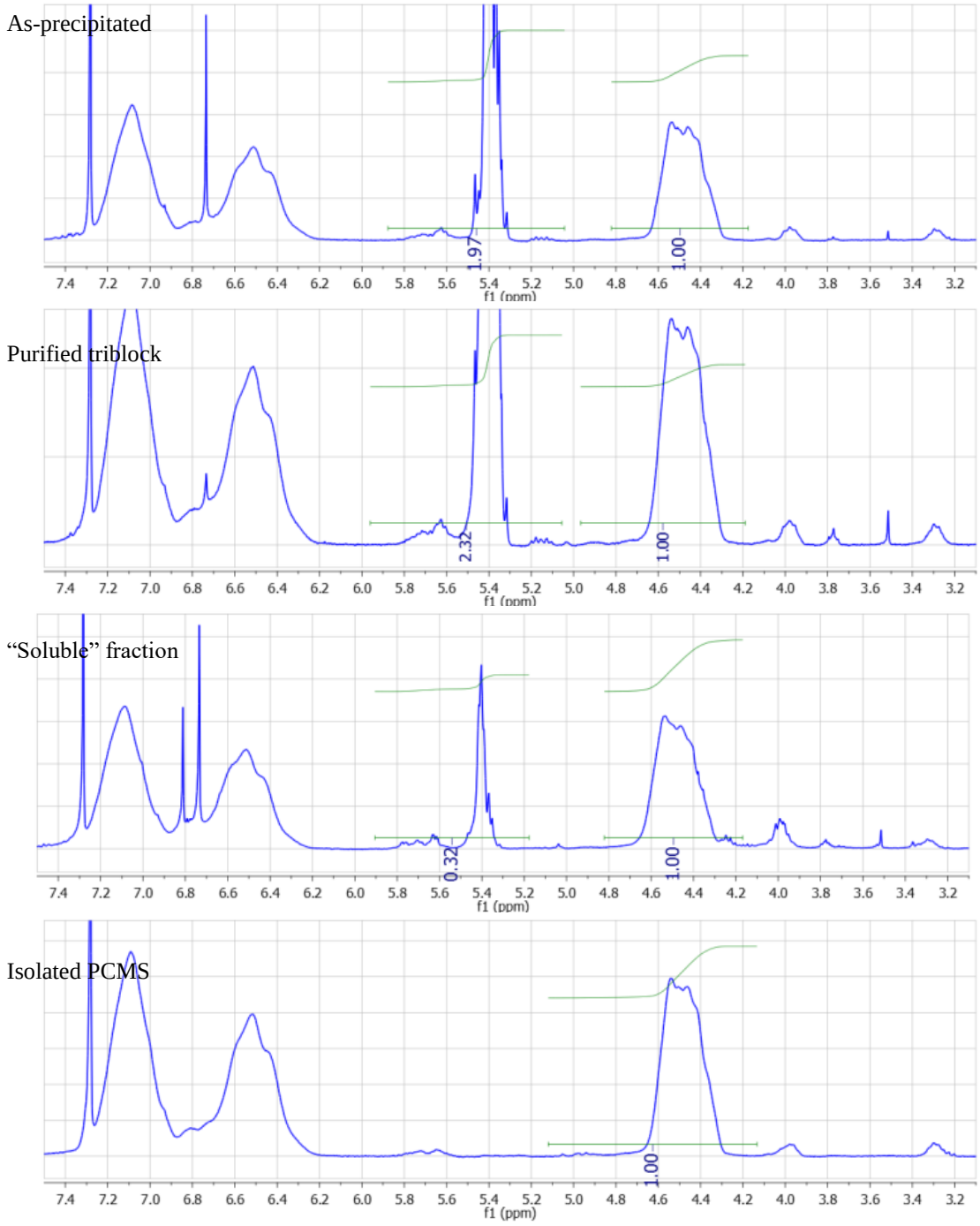


**Figure 41: NMR Characterization of a Representative Triblock Copolymer.**

So far, it is concluded that this synthesis approach can provide well-defined triblock copolymers with a MW distribution of the outer PCMS blocks while having a broad MW

distribution in the midblocks of PCOE. A series of triblock copolymers were synthesized and the MW characterization results were listed in Table 6. The DPs were estimated by end-group analysis using $^{1}$H NMR and the Đs were measured by GPC using polystyrene calibration. It was noticed when the mole percentage of CMS units increased, the Đ decreased, which is attributed to that the PCMS blocks are expected to have narrow MW distribution and reduced the overall dispersity.

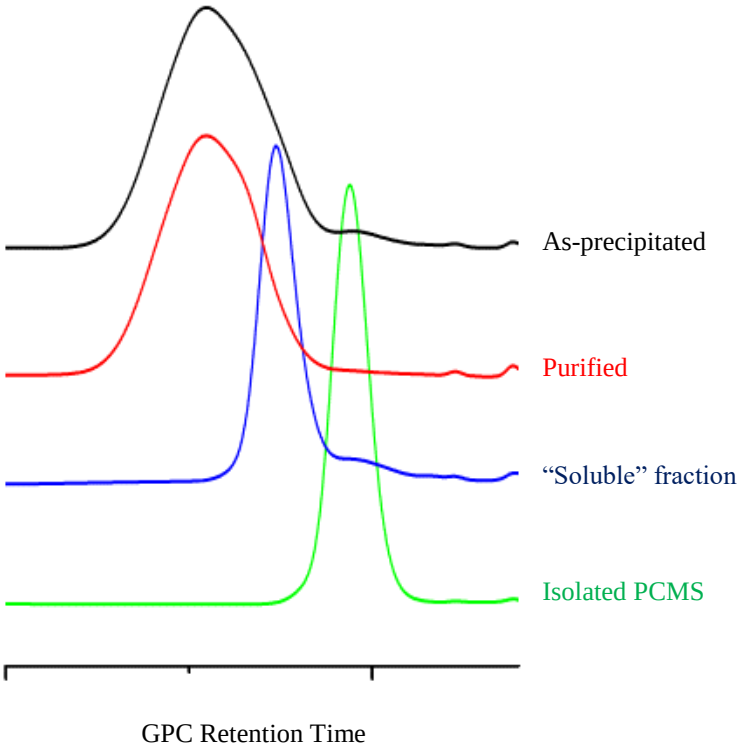


**Figure 42: GPC Characterization of a Representative Triblock Copolymer.**

Since only a very small amount (<20 mg) of $R_2$-CTA is needed to prepare one gram of triblock copolymer, the scalability of this synthetic protocol was demonstrate by running a single batch reaction to yield ~40 grams of PCMS-*b*-PCOE-*b*-PCMS (#12 in Table 6).

**Table 6: Chemical Compositions of TAEMs.**

| TAEM# | $DP_{PCMS}$[a] | $DP_{PCOE}$[a] | $Đ_{GPC}$[b] | IEC(mmol/g) |
|---|---|---|---|---|
| 1 | 13*2 | 237 | 1.68 | 0.9 |
| 2 | 30*2 | 385 | 1.63 | 1.1 |
| 3 | 32*2 | 341 | 1.64 | 1.2 |
| 4 | 68*2 | 367 | 1.57 | 1.7 |
| 5 | 39*2 | 252 | 1.58 | 1.7 |
| 6 | 52*2 | 295 | 1.52 | 1.9 |
| 7 | 57*2 | 292 | 1.52 | 2.0 |
| 8 | 35*2 | 163 | 1.51 | 2.1 |
| 9 | 62*2 | 305 | 1.51 | 2.1 |
| 10 | 60*2 | 288 | 1.50 | 2.1 |
| 11 | 89*2 | 366 | 1.62 | 2.3 |
| 12 | 85*2 | 305 | 1.40 | 2.7 |

[a]Measured by NMR end-group analysis. [b]Measured by GPC using polystyrene calibration.

### 4.3.3 Membrane Preparation

The purified triblock was dissolved in an organic solvent at a concentration of 100 mg/mL and cast onto a clean polytetrafluoroethylene sheet, with the solvent evaporation rate decelerated by a glass petri dish. It was found that using chloroform led to uniform membranes, while casting from THF and toluene resulted in rough surfaces.

The cast polymer film was slowly dried and then peeled off the PTFE sheet. The film was immersed into trimethylamine aqueous solution (50 wt%) for solid state quaternization reaction. The ion exchange capacities (IECs) of these triblock AEMs (TAEMs) in Table 6 were calculated using the chemical compositions of the neutral triblock copolymers. Finally, the membranes were heated in water at 80 $^{o}$C. This thermal/solvent annealing process was adopted due to the high $T_g$ (>200 $^{o}$C) of the ionic block,[114] at which thermal degradation can disintegrate the material, while water can significantly plasticize poly(vinylbenzyl trimethyl ammonium chloride) and thus enable chain mobility. At the same time, this approach mimics the operation conditions in a fuel cell and thus provides a chance to investigate the membrane morphology equilibrated in an environment to what is present in an operating fuel cell device. The chemical structure and the appearance of the resultant membranes are shown in Figure 43. These membranes show a melting transition at ~50 $^{o}$C (Figure 44).

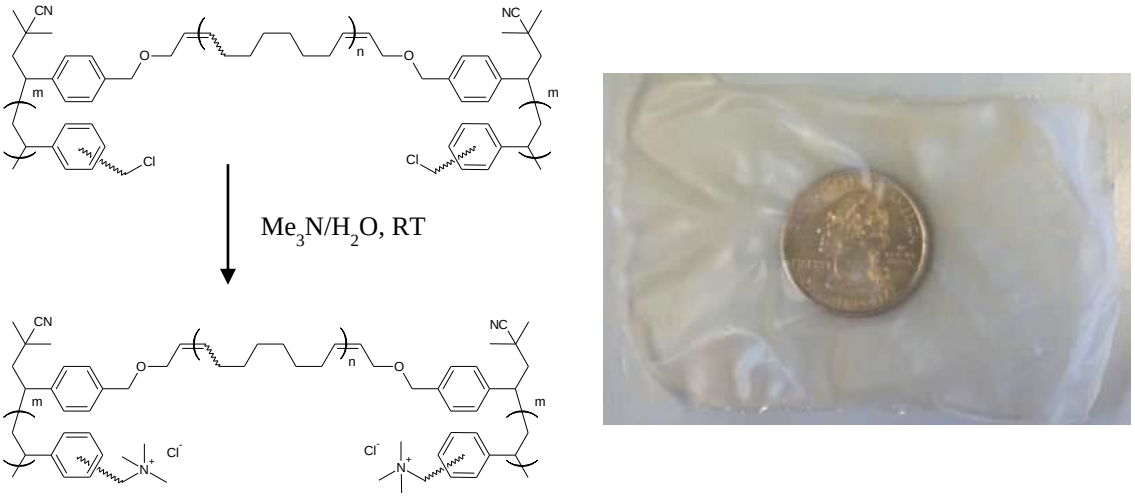


**Figure 43: Chemical Structure and Appearance of a TAEM.**

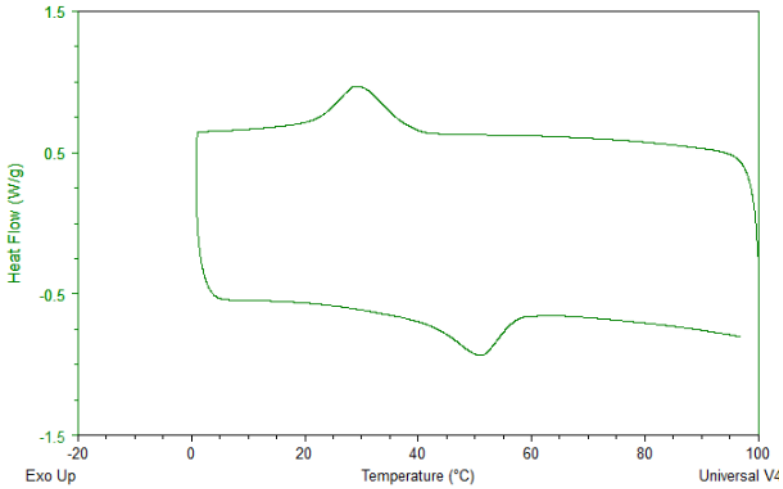


**Figure 44: Differential Scanning Calorimetry of a TAEM.**

### 4.3.4 Morphology Characterization

Small angle X-ray scattering was utilized to characterize the AEMs, however, the peaks were quite broad, which render this data difficult to conclusively identify the morphologies. This was probably due to the broad MW distribution that brought difficulties in efficient chain packing to form ordered morphologies. In the following, two membranes, TAEM 3 and TAEM 9 will be discussed in detail.

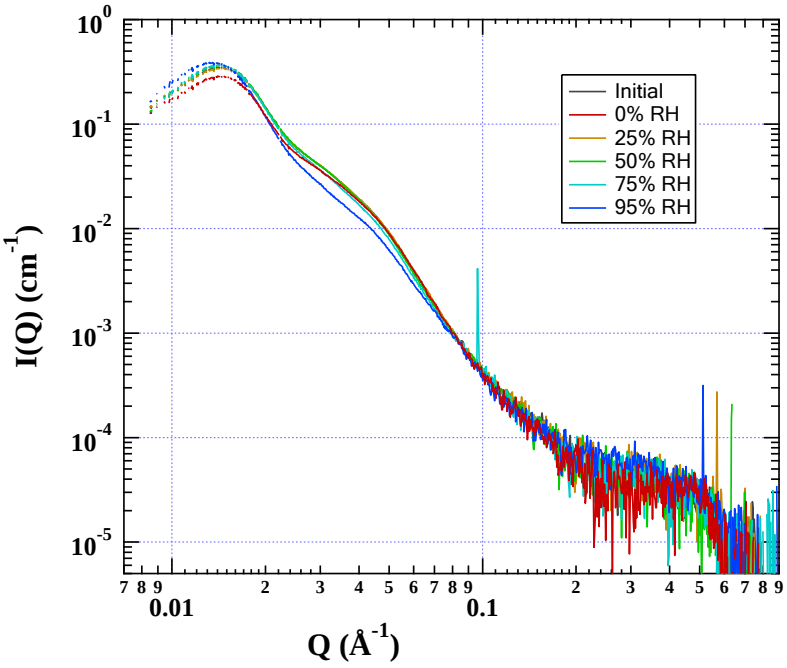


**Figure 45: SAXS Patterns of TAEM 3 at 60 ºC.**

In Figure 45, the SAXS profiles of TAEM 3 at 60 ºC is shown. A broad primary peak was observed at q = 0.0143 Å, corresponding to a d-spacing of 43.9 nm in the dry state. The broad and shallow secondary peak at roughly q = 2q* was seen as well, indicating that the morphology might be poorly ordered lamellar phase, although it is difficult to conclude. No sign of ionic cluster was observed. Response to water vapor treatment was also observed. In Figure 46A, zoomed SAXS patterns are shown for the membrane at 60 ºC. It was found that upon water sorption, the overall d-spacing slowly decreased when the relative humidity (RH) was below 75% (the water sorption is 14.7 wt % by dynamic vapor sorption). Then the d-spacing increased back when the RH was raised to 95% (the water sorption is 20.9 wt %). This phenomenon was due to selective swelling of water molecules inducing contraction of the poorly solvated nanophase.[187–191] When water molecules entered ionic domain, the domain size was increased in all the three dimensions. This resulted in increasing the area of the interface between the ion/water domain and the hydrophobic PCOE domain. However, water barely enters the hydrophobic part, and thus incompressible volume of

the molten PCOE domain required the thickness of this domain to decrease. Using the densities of poly(vinylbenzyl trimethyl ammonium chloride), $H_2O$, and PCOE being roughly 1.3, 1, and 0.9 $g/cm^3$, respectively, it was calculated that the thickness of the PCOE domain decreased from 36.5 nm to 30.3 nm when the RH was increased from 0% to 75%. This resulted in raising the interfacial area by 16.4%, comparing with ~41% increase in the hydrophilic domain thickness. The increase in interfacial energy and loss in PCOE conformational entropy was balanced by the lowered chemical potential of the polyion chains and counterions. However, when the RH was further raised, the hydrophobic domain experience only minor change in thickness (from 30.3 nm to 30.0 nm) and interfacial area (from 16.4% to 17.8%). This indicates that there was no significant further increase in the interfacial area, and thus the hydrophilic domain only expanded in the direction perpendicular to the interface from 12.8 nm to 14.8 nm. We hypothesize that this was an indication of the formation of a water-rich ion-poor domain in the middle of the hydrophilic layer, which was responsible for the d-spacing increase at high humidity. However, this hypothesis still needs more experimental evidence for a clear conclusion. Currently, neutron scattering is being performed for better understanding of the morphology. Assuming lamellar morphology, the proposed d-spacing expansion/contraction mechanism at 60 $^oC$ is shown in Figure 47.

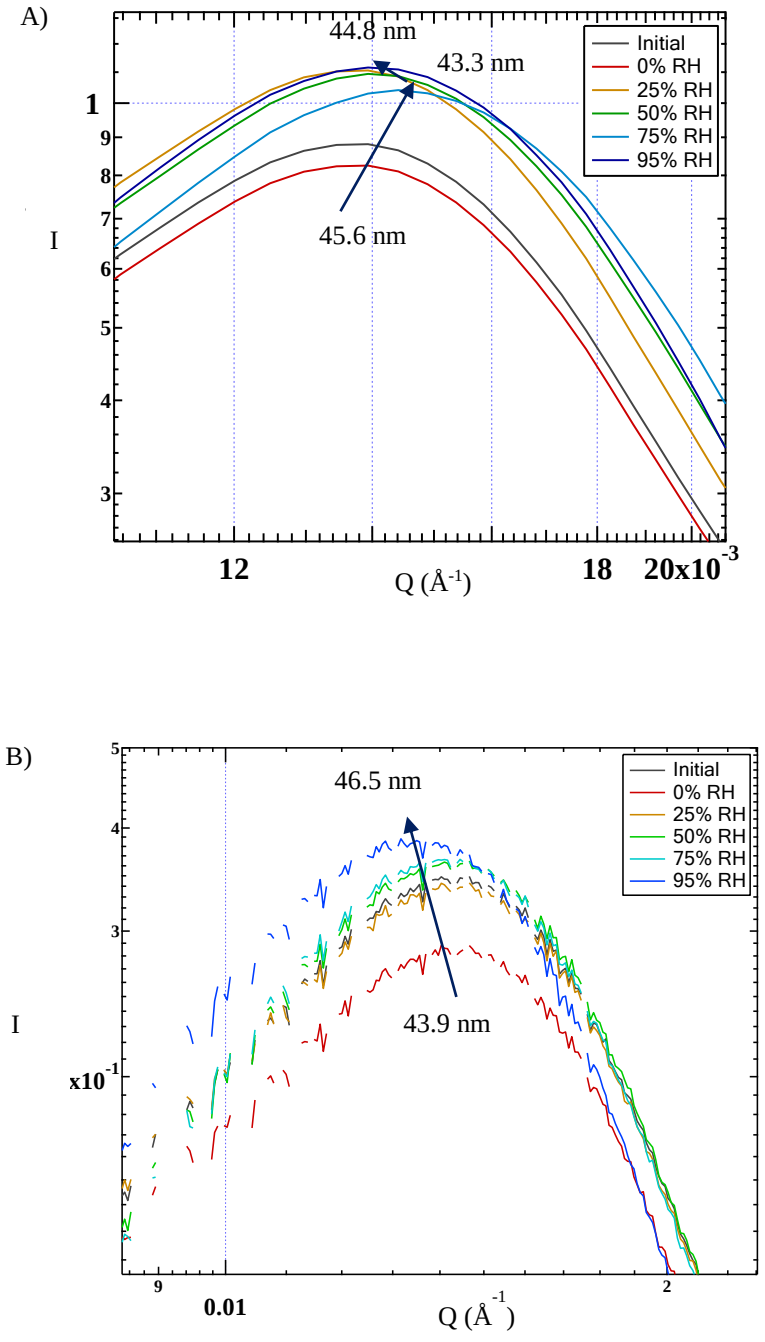


**Figure 46: Zoomed SAXS Patterns of TAEM 3.**

**A) 60 ºC; B) 30 ºC.**

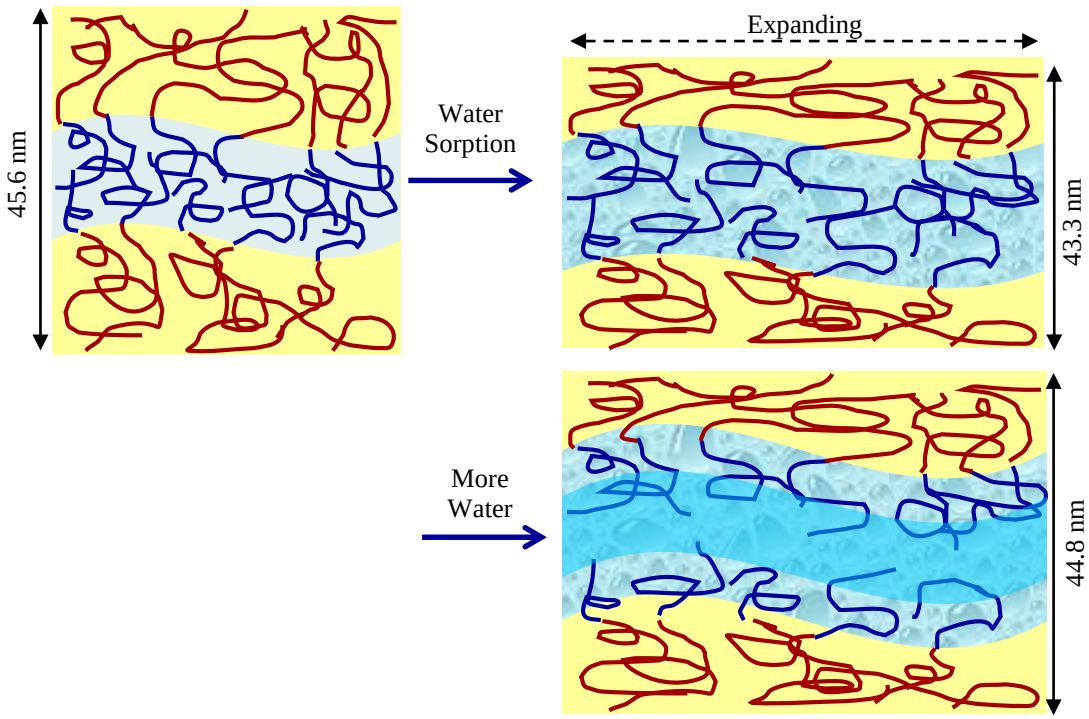


**Figure 47: Spacing Expansion/Contraction Mechanism above $T_m$.**

However, at 30 °C below the $T_m$ of PCOE, the d-spacing only increased in response to raised relative humidity (Figure 46B). This was attributed to the semicrystallinity of the PCOE domain at such a temperature, which acted as physical crosslinkers. Due to the physical crosslinking, the PCOE domain was constrained from deformation, and thus the interfacial area increase was less significant than that above the $T_m$ of PCOE. At RH ≤75%, the thickness increase in the hydrophilic domain (53%) was significant enough to cancel out the decrease in PCOE domain (-16%), so the domain spacing remained almost constant. At higher humidity, the spacing increase was primarily a consequence of polycation block stretching and water-rich ion poor domain formation (Figure 48), while the thickness of PCOE domain remained almost constant (from 31.2 nm to 31.1 nm).

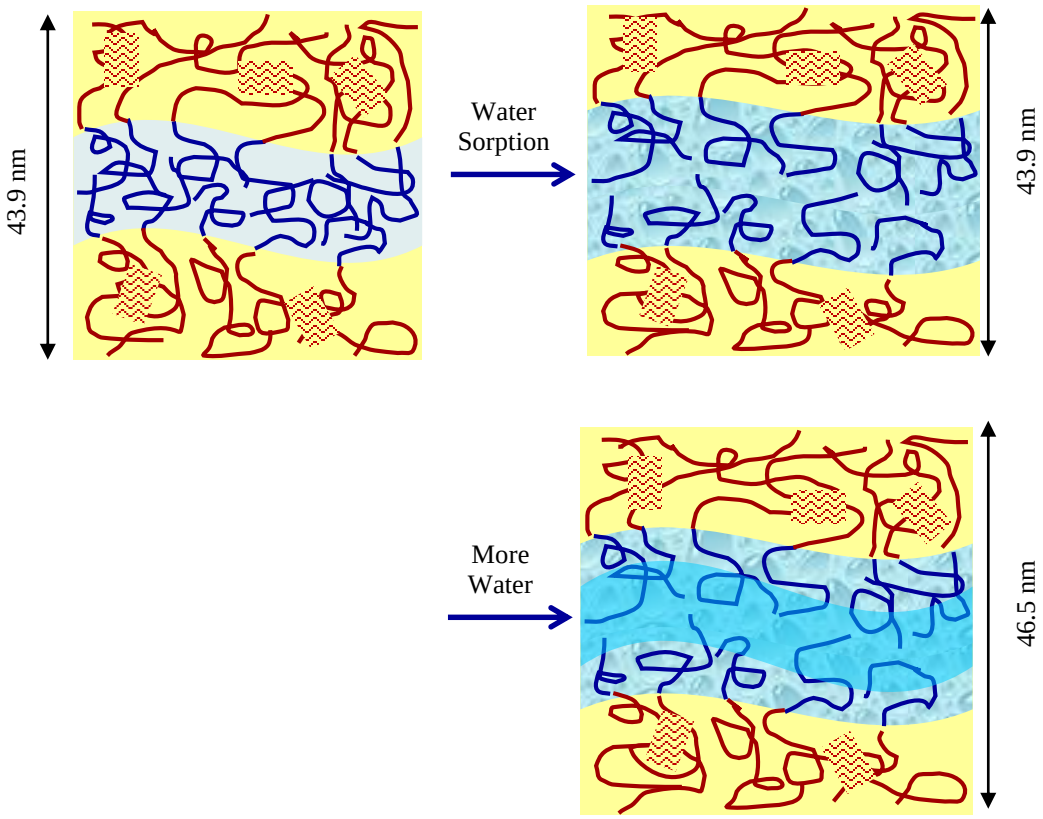


**Figure 48: Spacing Expansion Mechanism below $T_m$.**

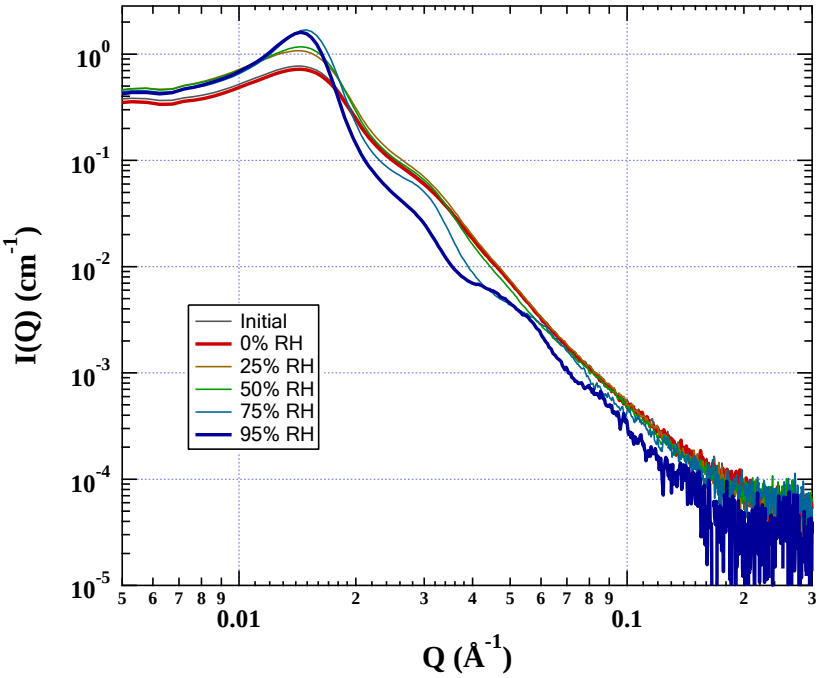


**Figure 49: SAXS Patterns of TAEM 9 at 60 ºC.**

Similar phenomenon was observed on TAEM 9. As shown in Figure 49, the morphology appeared to be lamellar, although high order peaks were weak in scattering intensities. Upon hydration, the primary peak became shaper and more intense, which was possibly due to water plasticizing the polycations chain to form a shaper domain interface (Figure 49). Zoomed SAXS profiles are presented in Figure 50, which focus on the primary peak for spacing expansion/contraction investigation. It was found that when the RH was increased from 0% to 75% and 22 wt% $H_2O$ was absorbed, the thickness of the hydrophobic domain decreased from 28.8 nm to 22.4 nm, while the hydrophilic domain gained a thickness changing from 15.6 nm to 20.1 nm. Further increasing the RH to 95% and water sorption to 33.7 wt% led to the PCOE thickness changing from 22.4 nm to 20.8 nm.

At 30 ºC, the domain spacing expanded from 41.7 nm to 44.3 nm, when the RH was increased from <5% to 95%. The ionic domain thickness increased from 14.6 nm to 23.2 nm, while the interface area was raised by 22%.

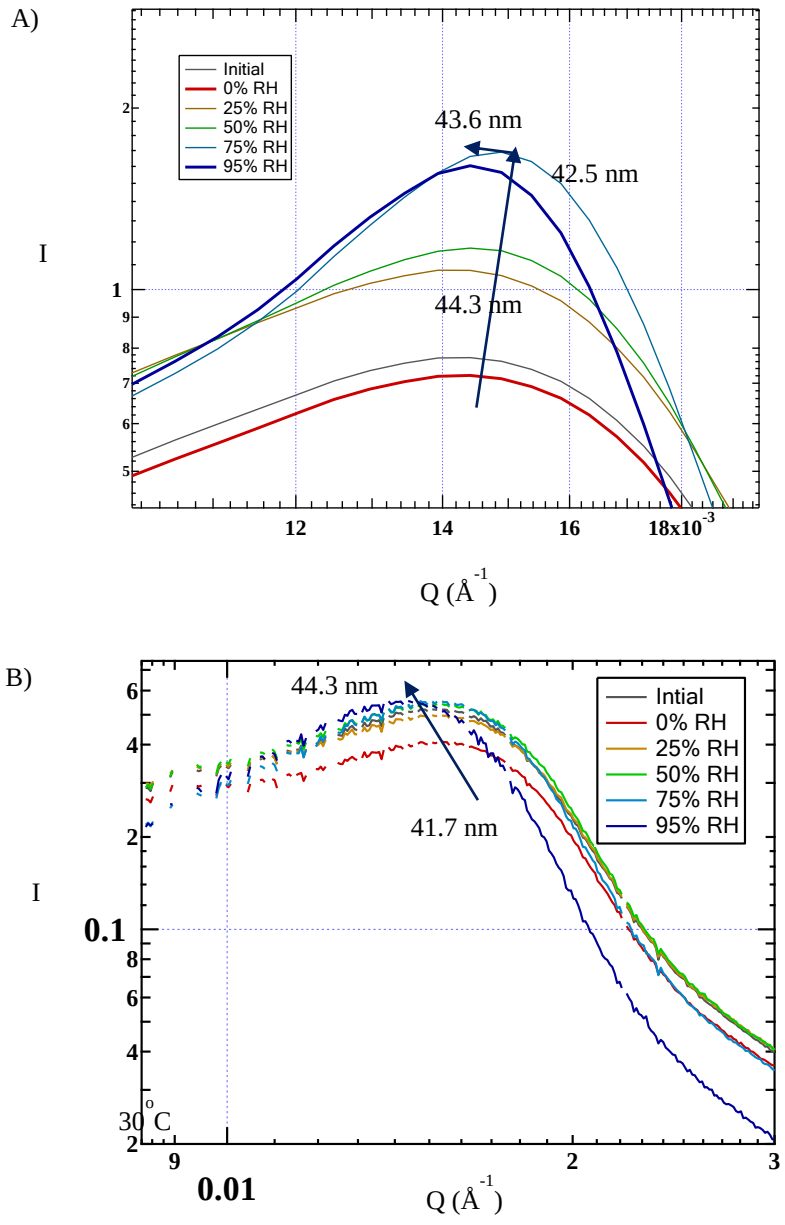


**Figure 50: Zoomed SAXS Patterns of TAEM 9.**

**A) 60 ºC; B) 30 ºC.**

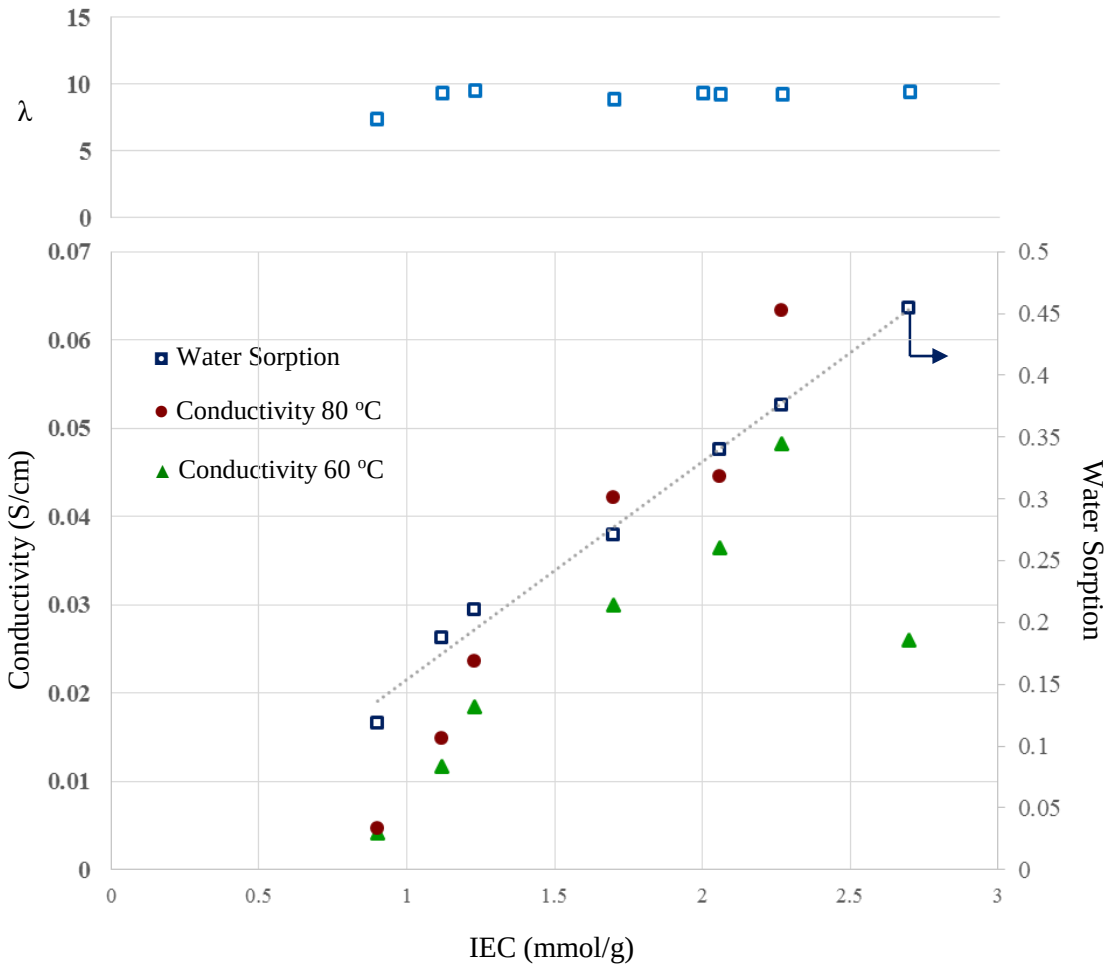


**Figure 51: Water Sorption and Conductivities of TAEMs.**

### 4.3.5 Anion Conductivity

Impedance spectroscopy was used to measure the $Cl^-$ conductivity instead of $OH^-$, due to the high reactivity of $OH^-$ toward $CO_2$ in the air to form $CO_3^{2-}$ or $HCO_3^-$ introducing difficulties in precise measurement. To investigation the effect of IEC on conductivity, a series of TAEMs with similar MWs (45 kg/mol ~ 60 kg/mol) were plot in Figure 51, together with water sorption measured at 60 ºC and 95% RH. The number of water molecules absorbed could be calculated from

the water sorption data, and then it was averaged by the number of ammonium groups to give the λ value.

It was found that most of the conductivities, at both 60 and 80 °C, increased monotonically with IEC except the TAEM with an IEC of 2.7 mmol/g, which was due to the increased concentration of charge carriers. The conductivity of the TAEM with the highest IEC decreased, and this was attributed to membrane failure at such a high temperature. The number of water molecules absorbed per charge was almost constant, which was probably due to the similar morphologies. The highest $Cl^-$ conductivity values achieved at 60 and 80 °C were 48 and 63 mS/cm, which are excellent results, especially when being compared with literature results, which are usually below 15 mS/cm with the highest reported value being 26 mS/cm at 50 °C.[36,40,101,111,114,116]

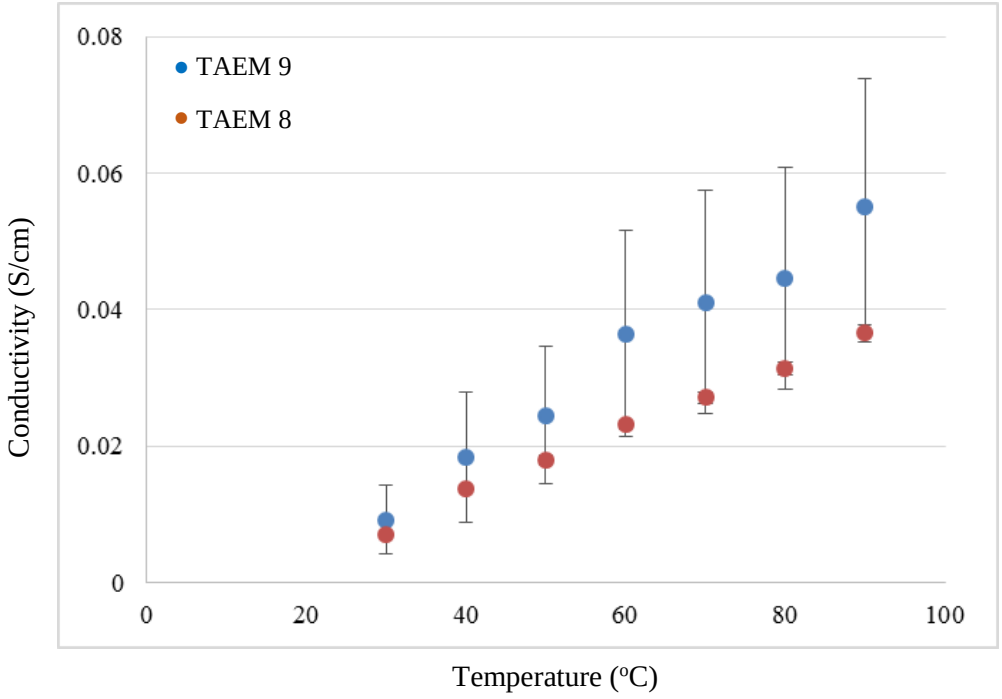


**Figure 52 Conductivity Comparison of TAEM 8 and 9.**

An MW effect on ion conduction was observed. TAEM 8, which had a MW being ~55% of that in TAEM 9, provided much reduced $Cl^-$ conductivities at all temperatures as shown in Figure

52. This was likely due to an interfacial effect. It is estimated that TAEM 8, with a d-spacing of 30.8 nm, displayed an ionic domain thickness of 11.2 nm at 60 ºC in dry state, which was ~28% thinner than that in TAEM 9. Since the strongly segregating polymers have an ~2−3 nm interface,[192] the interfacial layer should be even thicker considering the rough interface caused by the broad MW distribution. Due to partial mixing and the tortuosity in transporting pathway, the interfacial layer does not conduct ions as fast.[151,193]

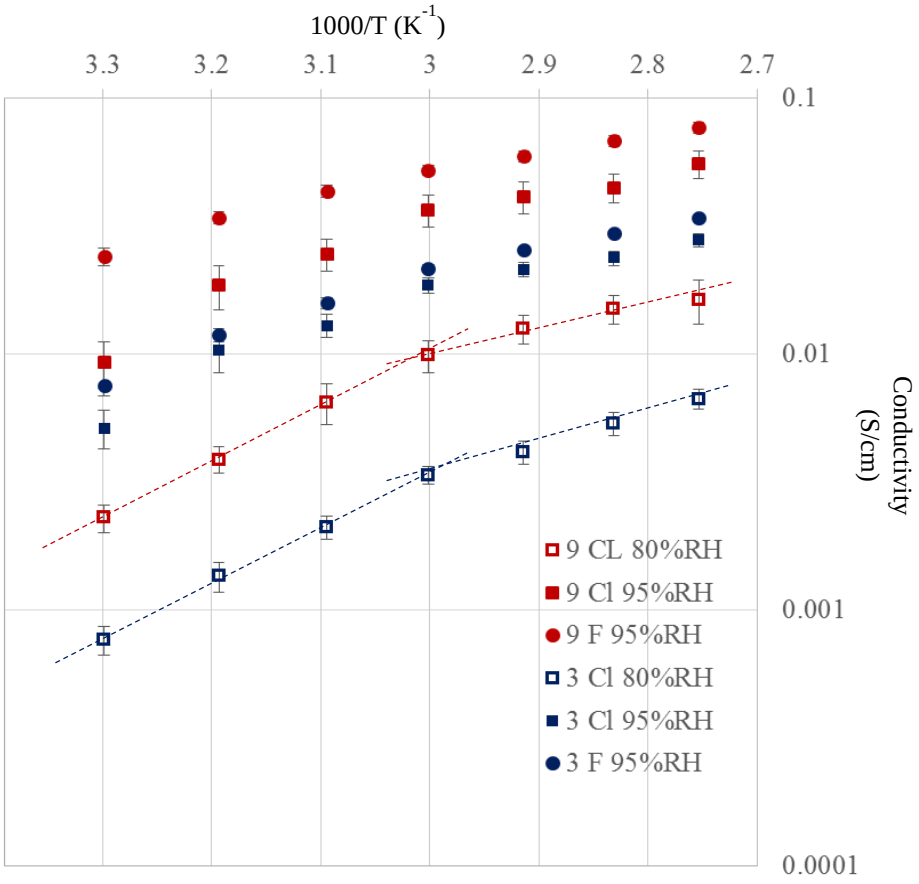


**Figure 53: Temperature Effect on Conductivities.**

To investigate if the melting transition of the PCOE block affected the ion transport properties, TAEM 3 and TAEM 9 were subjected to conductivity testing in both $Cl^-$ and $F^-$ forms, shown in Figure 53. Under all of the testing conditions, a transition was found between 50 and 60

$^{o}$C, which is at the end of PCOE melting transition. At lower temperatures, the conductivities were strongly affected the temperature as proved by the steep slope. When above the transition temperature, the conductivities were still affected by temperature, however, the slope was much shallower. Since the slope in this plot can be interpreted as the activation energy of ion transport, assuming Arrhenius behavior, it was found that after the transition, ion motion was facilitated. It was also noticed that the transition in conductivity was actually a change in the slope instead of a sudden boost of conductivity values. This was because PCOE, similar to many other semicrystalline polymers, has a relatively long melting transition range. Even at temperature as low as 40 $^{o}$C, the smaller crystals began to melt, and the melting did not complete until ~60 $^{o}$C. The decrease in activation energy is attributed to three possible mechanisms. One is the smoothened domain interface upon the melting of PCOE phase, which decreased the tortuosity of the transport pathway at the interface. Another factor might be the nanocrystals limited the relaxation of polycation blocks anchored to the interface and thus decelerated the anion exchange between ammonium side groups.[194–196] The last possible mechanism is that the crystallinity affected the water distribution in the hydrophilic domain, as discussed previously on the swelling phenomena. This study gives a direct evidence of melting/crystallization of the hydrophobic domain impacts ion conduction significantly, although the mechanism is not fully understand yet. It is possible to decrease the activation energy of ion conduction in semicrystalline state by applying annealing to engineer the domain interface, including the density of BCP junction points, and water distribution.

By comparing the $Cl^-$ conductivity under 80% and 95% RH, it was concluded that these materials did not over swell under the testing conditions. Otherwise, the conductivity should be lower with the higher humidity. In addition, it was noticed that $F^-$ transported faster than $Cl^-$, which was explained by the smaller size.

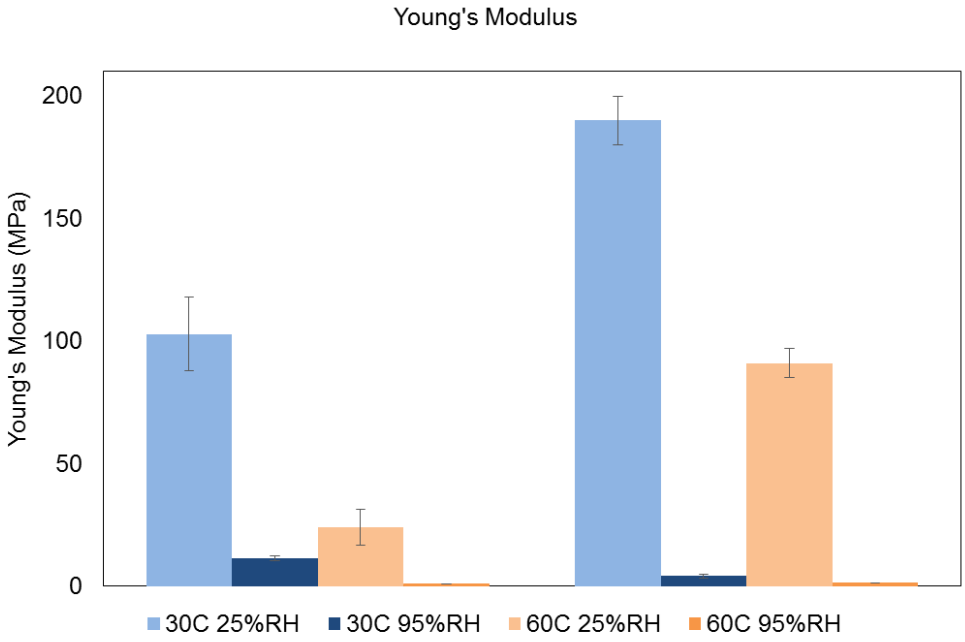


**Figure 54: Modulus of TAEM 3 and 9 under Controlled Environmental Conditions.**

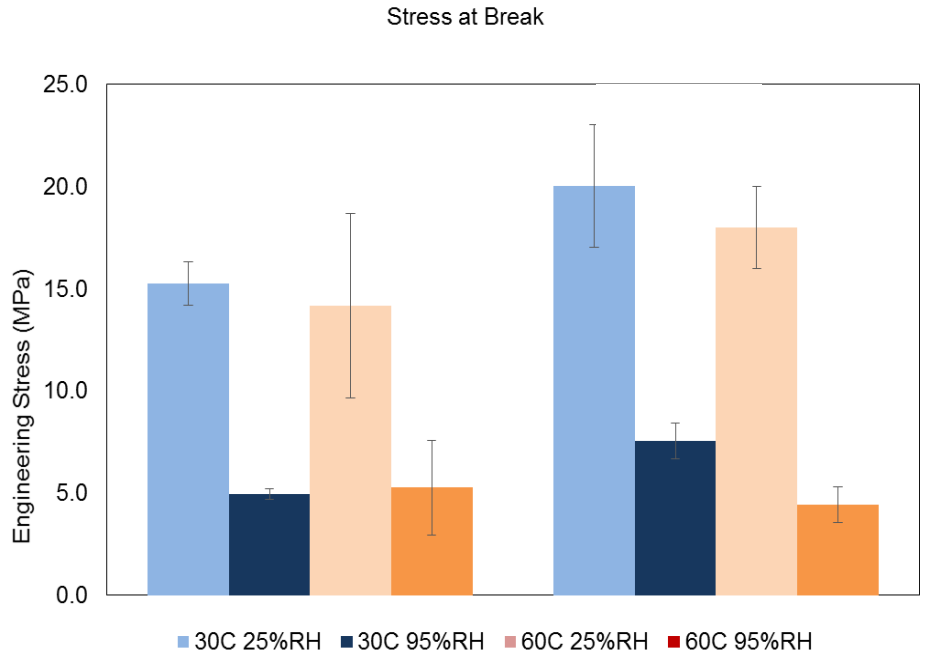


**Figure 55: Stress at Break of TAEM 3 and 9 under Controlled Environmental Conditions.**

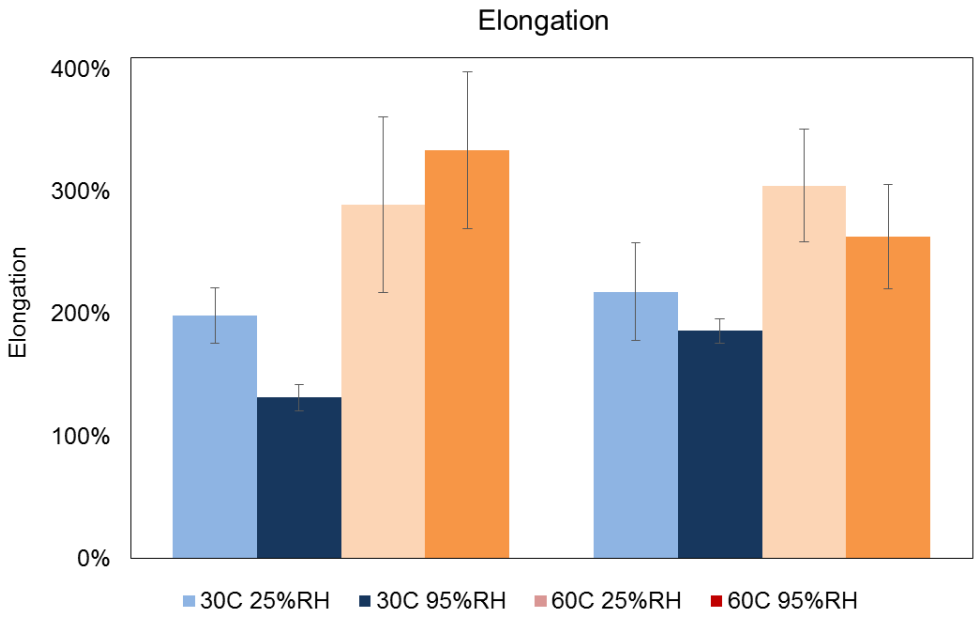


**Figure 56: Elongation of TAEM 3 and 9 under Controlled Environmental Conditions.**

### 4.3.6 Mechanical Properties

Microphase separated block copolymer have been widely used for tunable mechanical properties. Typical examples are polystyrene-*b*-polybutadiene-*b*-polystyrene (SBS), polystyrene-*b*-polyisoprene-*b*-polystyrene (SIS), and polystyrene-*b*-poly(ethylene-co-butylene)-*b*-polystyrene (SEBS) linear triblock copolymers. In these copolymers, the PSt, with a $T_g$ above the operation temperature acts as physical crosslinks, while the soft midblock are used as the rubbery matrix. The mechanical properties are highly affected by the material morphology as widely accepted.[84,197–199]

The modulus, stress at break, and maximum elongation were investigated under controlled environmental conditions (Figure 54, 55, and 56). It was found that both TAEM 3 and TAEM 9 showed higher moduli at low RH than 95% RH. This was attributed to the fact that the pure ionic domain has a high $T_g$, while it was significantly plasticized by water at high humidities. Considering the high moduli values at low RH, the glassy domain should be in a continuous phase, which is in good agreement with the assumption of lamellar morphology. The moduli decreased when the

temperature was increased, which was a consequence of increased water sorption and the removal of physical crosslinks in PCOE domain upon reaching the melting transition. In addition, TAEM 9 possessed higher moduli than TAEM 3 under low RH conditions, due to the high content of the hard polycation block. In contrast, TAEM 9 was a weaker material than TAEM 3 when the RH was raised to 95%. This was because upon hydration, the polycation block turned to be a rubbery block, which probably had no entanglements due to the high chain rigidity. TAEM 9 has a higher content of polycation, so it was more significantly affected than TAEM 3.

Both TAEM 3 and TAEM 9 displayed greater ultimate engineering stress at low humidity. This was again attributed to the water plasticization effect at 95% RH. Temperature seems to provide less effect here. It was also observed that the membranes had larger ultimate elongation values at high temperature, which was likely due to the absence and physical crosslinking in the PCOE domain.

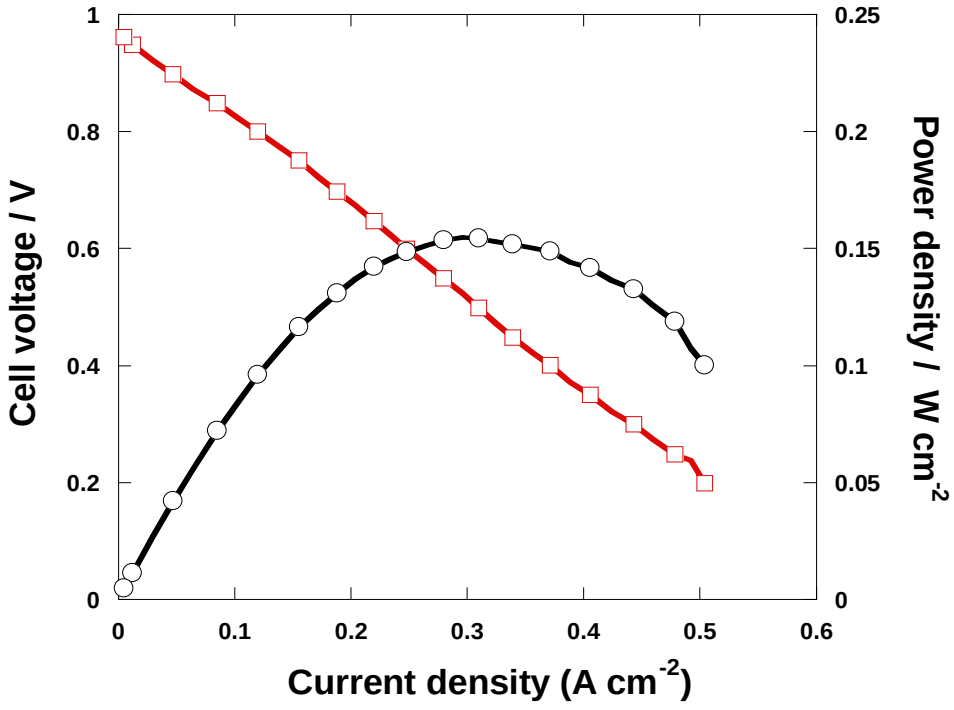


**Figure 57: Fuel Cell Performance of TAEM 6.**

### 4.3.7 Fuel Cell Performance

Membrane TAEM 6, with a thickness of 102 μm, was subjected to fuel cell testing. At 55$^{o}$C, the opening circuit voltage was 0.97 V and the peak power density was as high as 152 mW/cm$^2$ (Figure 57). These results were comparable with the Tokuyama A901 membrane, which had a thickness of 10 μm and displayed a peak power density of 215mW/cm$^2$. This was due to the low cell resistance, 0.14 Ω *cm$^2$, in TAEM 6 (vs. 0.11 Ω*cm$^2$ in Tokuyama A901). The fuel cell testing was conducted at U.S. Army Research Laboratory.

## 4.4 Conclusions

A special CTA was designed and synthesized in high yield using nucleophilic substitution and single unit insertion reaction. Mediated by the CTA, a series of triblock copolymers based on COE and CMS was synthesized using ROMP and RAFT polymerizations. Membranes were prepared by sequential drop-casting, solid state quaternization, and thermal/solvent annealing process.

By SAXS, it was found that the membranes were in a poorly ordered lamellar morphology. The d-spacing was affected by hydration from environmental humidity, where the hydrophobic domain decreased its thickness while the hydrophilic domain became thicker. The crystallinity of the PCOE block ($T_m$ ~ 50 $^{o}$C) was shown to have a strong impact on the domain contraction/expansion. The melting transition was also observed to have an influence on anion conduction, by possibly smoothening the domain interface, facilitating polycation chain relaxation, and changing water distribution. It was also shown that the melting transition affected the mechanical properties. This work provides a direct investigation of the effect from the crystallinity in hydrophobic domain on block copolymer ion exchange material.

# CHAPTER 5

# SYNTHESIS AND SELF-ASSEMBLY OF IONIC STAR BLOCK COPOLYMERS

## 5.1 Introduction

As discussed in Chapter 3 and 4, one very interesting property of block copolymers is that they can self-assemble into well-ordered structures. By tuning the architecture, the morphological behavior can be significantly affected. First of all, the chain organization can be modulated. For example, the midblock in a microphase separated symmetric triblock copolymer, can adopt either a bridged or looped conformation upon microphase ordering, so that the midblock microdomains consist of a bimodally dispersed mixture of conformationally different blocks.[200,201] In addition, the d-spacing can also be tuned, which will be discussed in the next chapter. Most importantly, the phase diagram can be shifted. This means that by applying polymer architecture, it is possible to achieve different ordered microphases, when the volume fraction is held constant.[84,202,203] When the shift is obtained in the vertical direction of the phase diagram, ordered microphase separation can be either facilitated or suppressed. For example, Figure 58 shows a theoretical phase diagram of a nine-armed star diblock copolymer with conformational symmetry, which was plotted using the volume fraction of the inner block.[204] It can be observed the topology of the phase diagram was maintained while there is a preference for the inner block of the arms to be located on the inside of cylindrical and spherical structures. It was also noticed that the critical $\chi N$ value for the formation of an order morphology was 6, instead of 10.5 in the case of conformationally symmetric diblock copolymers. N here is the DP of one arm for a star block copolymer or the DP of the whole chain for a diblock copolymer. This implies that the microphase separation can be facilitated by using a star block copolymer architecture, and thus it is possible to achieve ordered morphologies with lower molecular weight polymers. Since the domain spacing is primarily affected by N,[205] this is

further beneficial for achieving smaller repeating features, which is an urgent need for advances in many applications, such as ultrahigh areal density nanowires, bit-patterned media, and graphene nanotransistors.[206–209]

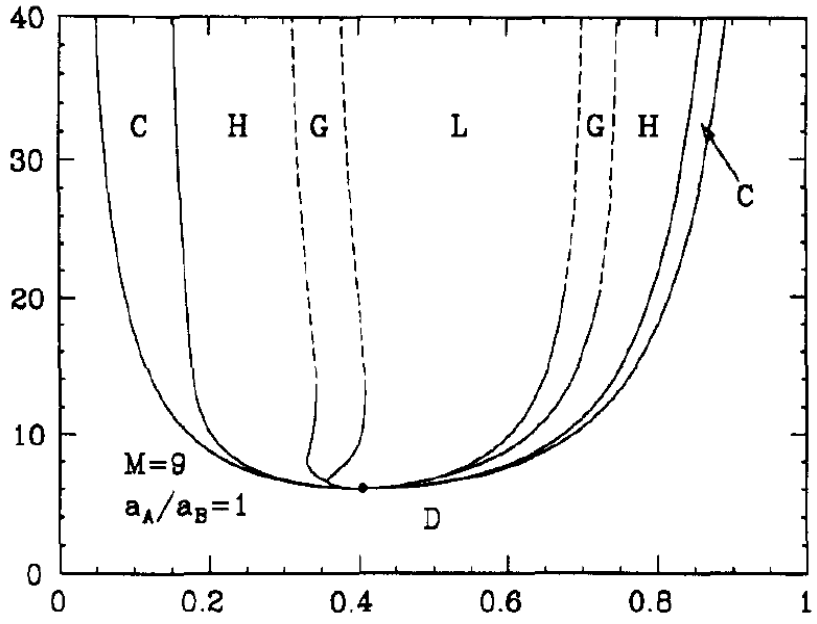


**Figure 58: Phase Diagram of Nine-Armed Star Diblock Copolymer.**

**Figure adopted from Ref 204.**

## 5.2 Experimental Section

### 5.2.1 Materials

Styrene, chloromethylstyrene (a mixture of *para*- and *meta*-isomers, CMS), *n*-butylacrylate (nBA), and 2-vinylpyridine (2VP) were passed through a short column of basic alumina and stored under -30 $^{o}$C before use. Thermal initiator, 2,2'-Azobis(2-methylpropionitrile) (AIBN) was recrystallized from MeOH. The carboxylic functionalized RAFT agent, 4-cyano-4-[(butylsulfanylthiocarbonyl)sulfanyl]pentanoic acid (COOH-CTA, Figure 59A), was synthesized using a modified method from a previously reported synthesis protocol for 4-cyano-4-

[(dodecylsulfanylthiocarbonyl)sulfanyl]pentanoic acid.[210] Pentaerythritol tetrakis[2-(dodecylthiocarbonothioylthio)-2-methylpropionate] ($TTC_4$) was purchased from Sigma-Aldrich. Other chemicals were used as received.

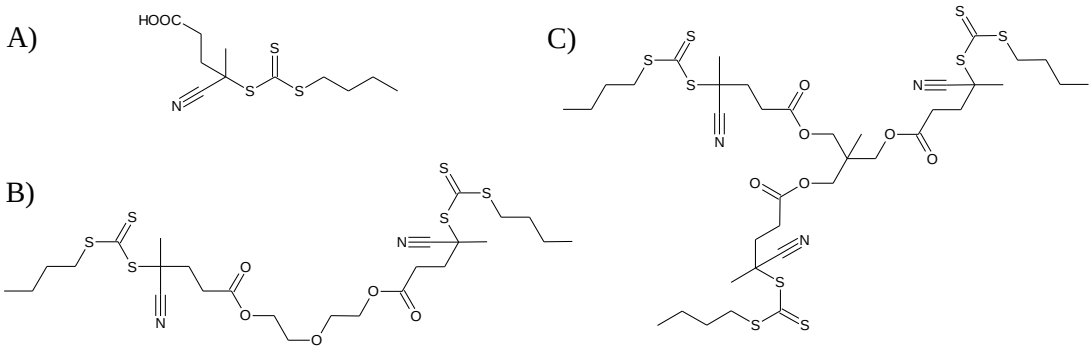


**Figure 59: Chemical Structures of Synthetic RAFT Agents.**

**A) COOH-CTA; B) $TTC_2$; C) $TTC_3$.**

### 5.2.2 Synthesis of RAFT Agents

The RAFT agent with two trithiocarbonate, $TTC_2$ (Figure 59B), was synthesized using the following protocol. Into 30 mL dichloromethane was charged 2.55 g COOH-CTA, 2.04 g DCC, 0.95 g DMAP, and 0.446 g diethylene glycol. The mixture was stirred for 1 hour and then warmed to RT and allowed to react overnight. After column chromatography with hexane/ethyl acetate (v:v=3:1) as eluent, 2.61 g yellowish red oil was achieved (yield = 94%). NMR characterization is shown in Figure 60.

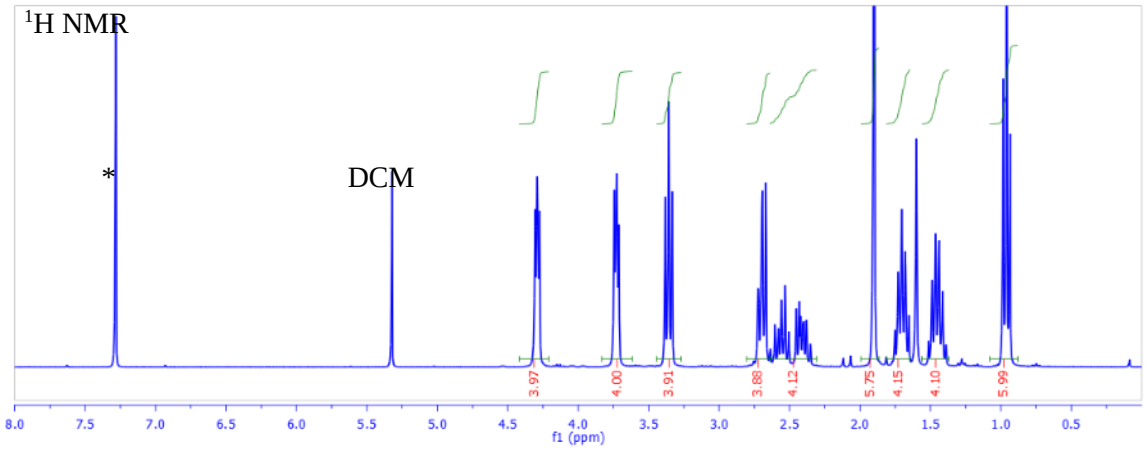
$^{1}$H NMR
*
DCM
3.97
4.00
3.91
3.88
4.12
5.75
4.15
4.10
5.99
8.0 7.5 7.0 6.5 6.0 5.5 5.0 4.5 4.0 3.5 3.0 2.5 2.0 1.5 1.0 0.5
f1 (ppm)

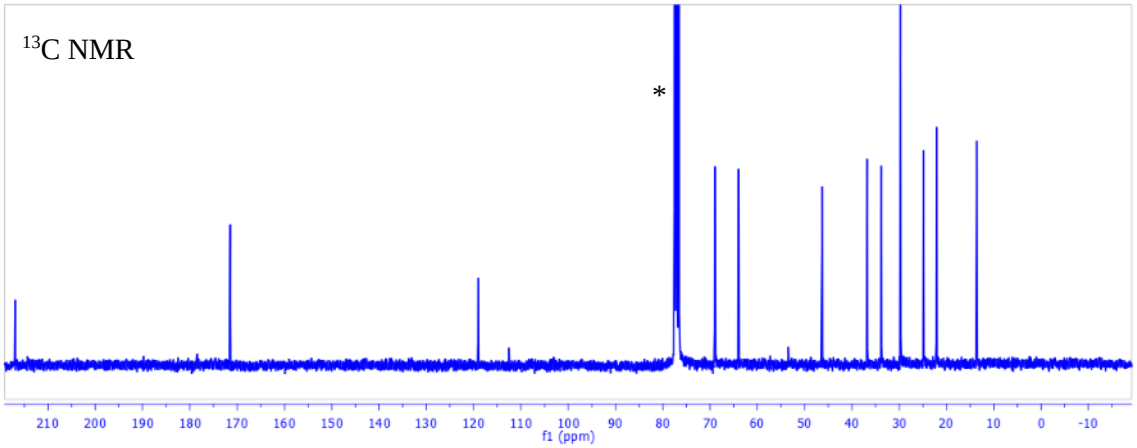
$^{13}$C NMR
*
210 200 190 180 170 160 150 140 130 120 110 100 90 80 70 60 50 40 30 20 10 0 -10
f1 (ppm)

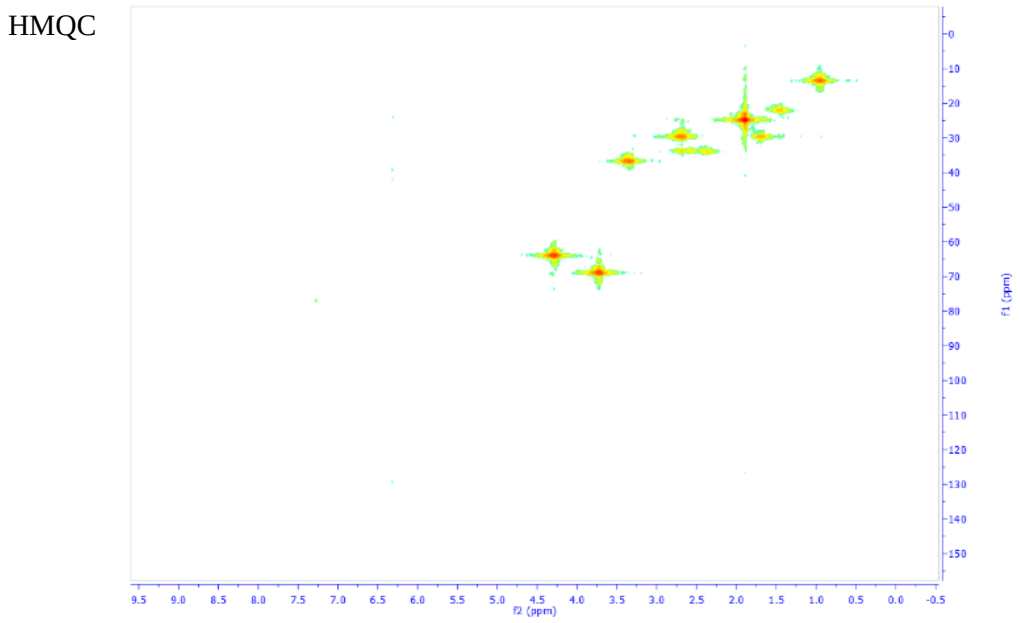


**Figure 60: NMR Characterization of $TTC_2$.**

Using a similar method, $TTC_3$ (Figure 59C) was prepared. In 25 mL preheated 1,4-dioxane, 154 mg 1,1,1-tris(hydroxymethyl)ethane was dissolved. After cooling to RT, 1.19 g COOH-CTA and 50 mg DMAP was added. Then, 1.01 g DCC was slowly added over 30 minutes at 0 ºC. The reaction was allowed to warm to RT and reacted for 24 hours. After column chromatography, 1.01 g yellowish red oil was achieved (yield = 84%). NMR characterization is shown in Figure 61.

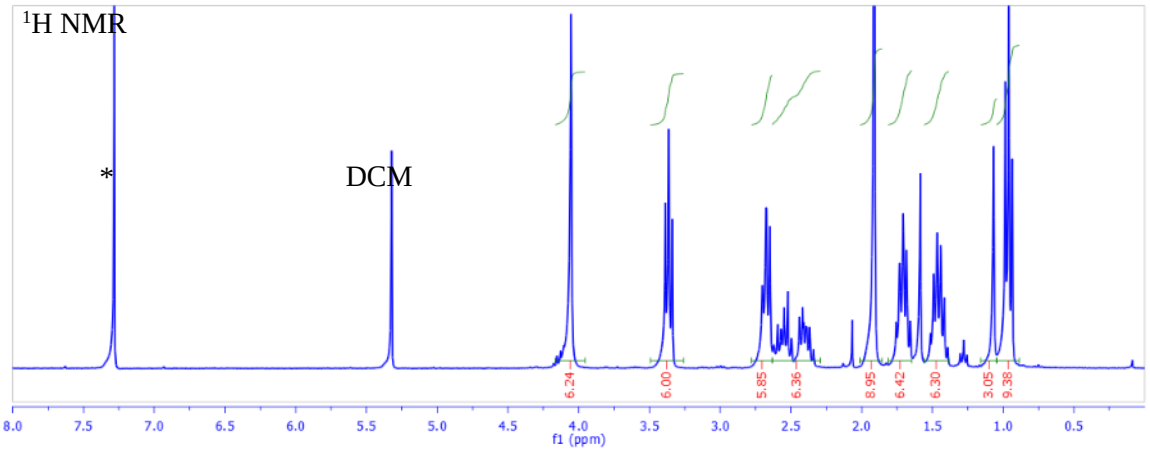

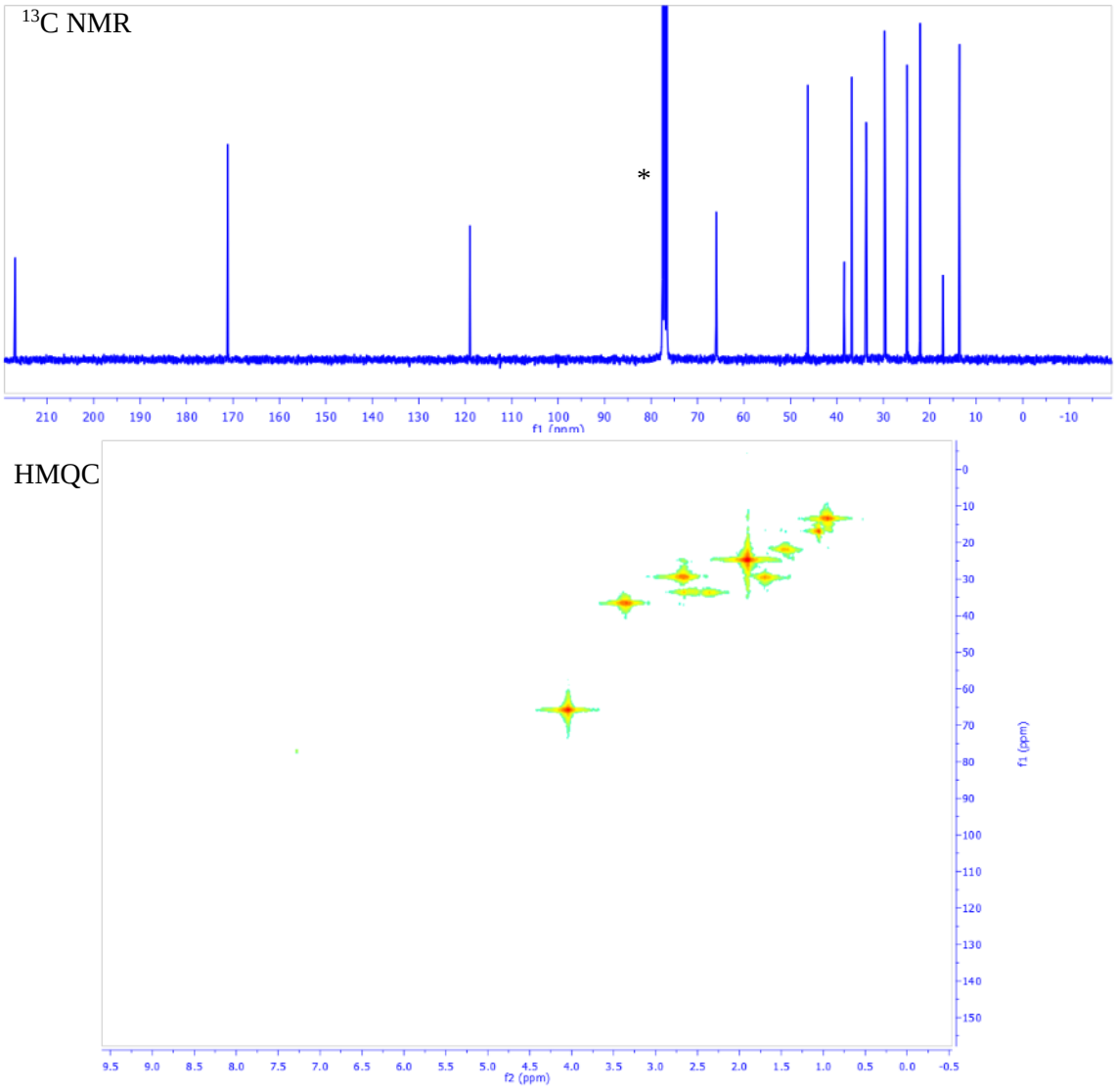


**Figure 61: NMR Characterization of $TTC_3$.**

### 5.2.3 Synthesis of P(CMS-*ran*-St)-*b*-PnBA

In the first step, P(CMS-*ran*-St)$_n$ was polymerized using RAFT technique, where n denotes the number of arms (n = 1 for diblock, 2 for symmetric triblock, and 3 for 3-armed star). In a reaction vessel, CTA (O-CTA for hemitelechelic polymer, $TTC_2$ for telechelic polymer, and $TTC_3$ for 3-armed star polymer), 100 equiv. (relative to trithiocarbonate moieties) of CMS, 150 equiv. of St, and 0.03-0.04 equiv. of AIBN were mixed, and then degassed by purging with nitrogen for 30

minutes. The reaction was initiated by heating the sealed container in an oil bath at 60 °C. After a certain period of time, the reaction was quenched to 0 °C and precipitated into hexanes three times to remove unreacted CMS and St. The MW was calculated by end-group analysis using $^1$H NMR. A representative spectrum of 3-armed star is shown in Figure 62. The peak at δ ≈ 3.3 ppm was assigned to the methylene adjacent to trithiocarbonate, with the two peaks between δ ≈ 4.2 and 4.7 ppm attributed to the chloromethyl protons. The dispersity was measured by GPC using polystyrene calibration.

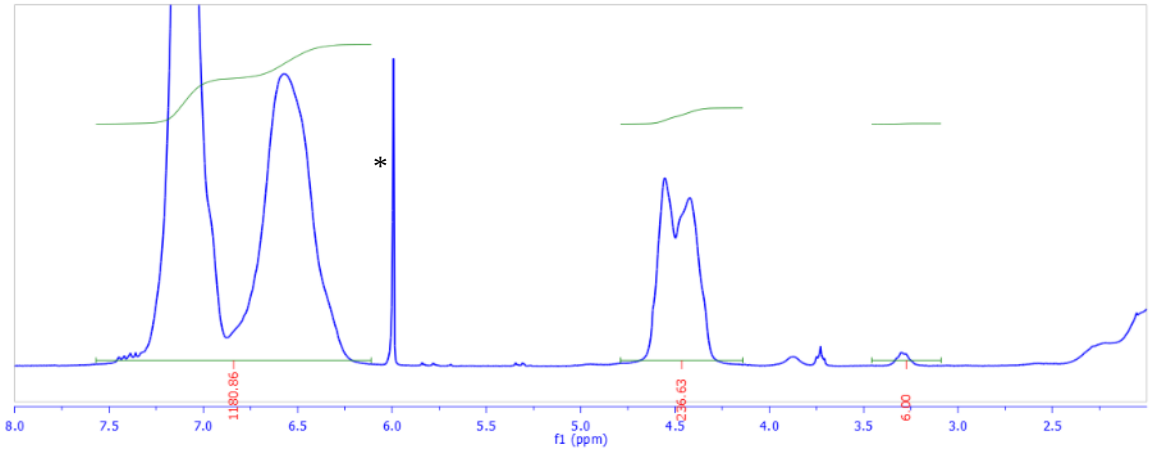


**Figure 62: A Representative $^1$H NMR Spectrum of P(CMS-*ran*-St)$_3$.**

In the second step, the random copolymer was dissolved in 300 equiv. (relative to trithiocarbonate moieties) of dioxane and 300 equiv. of nBA, together with 0.03-0.04 equiv. of AIBN. After degassing, the mixture was heated to 60 °C to start the chain extension. After a certain period of time, the resulting polymer was precipitated three times into MeOH/$H_2O$ mixture (2:1 = v:v) to remove residual monomer. The DPs of nBA was calculated by the ratio between nBA and CMS using $^1$H NMR. An example spectrum of PnBA-*b*-P(CMS-*ran*-St)-*b*-PnBA is given in Figure 63, where the peak between δ ≈ 4.20 and 3.85 ppm was assigned to the -COOC**H**$_2$CH$_2$- protons.

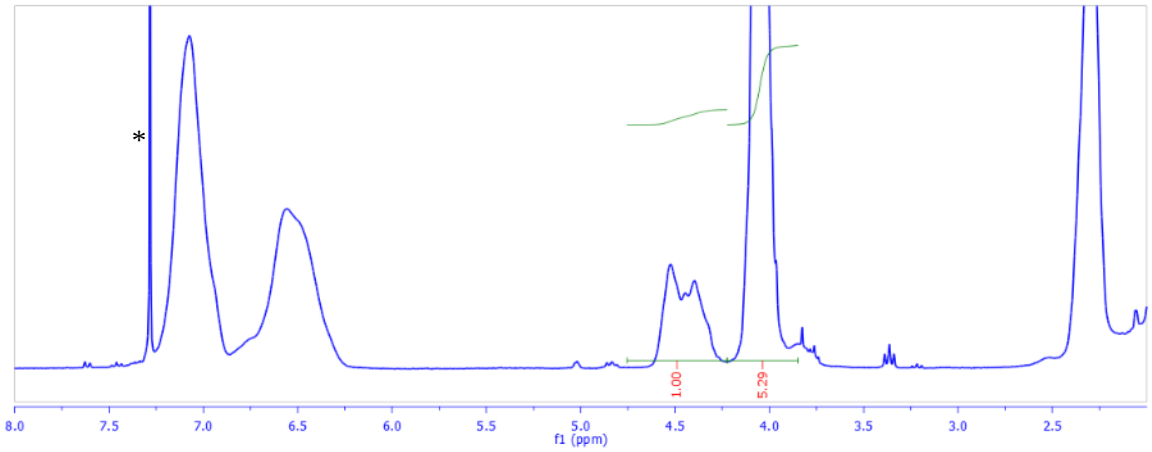


**Figure 63: Representative $^{1}$H NMR Spectrum of a Triblock Copolymer.**

The block copolymers were subject to GPC analysis. A representative GPC trace of [P(CMS-*ran*-St)-*b*-PnBA]$_3$ is displayed in Figure 64. The narrow, symmetric major peak was attributed to the 3-armed star polymer, while the low MW peak, was a mixture of P(CMS-*ran*-St)-*b*-PnBA diblock, P(CMS-*ran*-St) dead chains, and PnBA homopolymer, which are grouped together and referred to as the free arm fraction in this dissertation. These were all inevitable products due to the nature of RAFT polymerization and generated by the extra chains produced from the radical input. It should be noticed that in the polymerization conducted in this chapter, the feed ratio of AIBN was kept very low, which was intended for suppressing the generation of free arm fractions. The weight percentage of the free arm fraction can be estimated by comparing the peak area with the major peak. Among the three components, the diblock is the major fraction, since the radical input is very small with AIBN being 0.03-0.04 equiv. to trithiocarbonate in each step. The block copolymers synthesized here are summarized in Table 7.

**Table 7: Summary of [P(CMS-*ran*-St)-*b*-PnBA]$_n$.**

| n[a] | $DP_{CMS+S}$[b] | $Đ_{ran}$[c] | $DP_{nBA}$[b] | $Đ_{BCP}$[c] | faf[d] |
|---|---|---|---|---|---|
| 1 | 33.7+37.3 | 1.07 | 90 | 1.09 | - |
| 1 | 33.7+37.3 | 1.07 | 258 | 1.11 | - |
| 1 | 33.7+37.3 | 1.07 | 147 | 1.10 | - |
| 2 | 29+32.6 | 1.07 | 69*2 | 1.09 | ND |
| 2 | 32.5+36.2 | 1.09 | 107*2 | 1.12 | ND |
| 2 | 70.1+78 | 1.07 | 146*2 | 1.14 | ND |
| 2 | 70.1+78 | 1.07 | 172*2 | 1.14 | ND |
| 3 | (35.3+41.4)*3 | 1.15 | 104*3 | 1.18 | 0.09 |
| 3 | (35.3+41.4)*3 | 1.15 | 152*3 | 1.20 | 0.10 |
| 3 | (35.3+41.4)*3 | 1.15 | 152*3 | 1.22 | 0.11 |

[a]Number of arms, where 1, 2, and 3 are for diblock copolymer, triblock copolymer, and 3-armed star block copolymer, respectively. [b]The degrees of polymerization of CMS plus St and nBA, respectively. [c]$Đ_{ran}$ is the dispersity index for the P(CMS-*ran*-St) block and $Đ_{BCP}$ is the overall dispersity index for the block copolymer. [d]The free arm fraction, determined by the peak area in GPC traces.

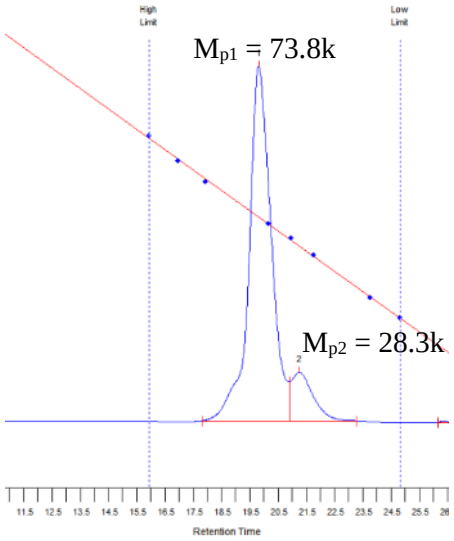


**Figure 64: A Representative GPC Trace of [P(CMS-*ran*-St)-*b*-PnBA]$_3$.**

### 5.2.4 Quaternization of P(CMS-*ran*-St)-*b*-PnBA

In 3:1 (v:v) mixture of ethanol and trimethylamine aqueous solution (50wt%), P(CMS-*ran*-St)-*b*-PnBA was dissolved at a concentration of 0.1 g/mL. The mixture was stirred at room temperature for 3 days to convert benzyl chloride group into benzyl trimethyl ammonium chloride, and then dried under a flow of nitrogen to remove ethanol, $H_2O$, and trimethylamine. The quaternized block copolymers were redissolved in DMF and cast onto clean Teflon sheets to form uniform and transparent membranes. However, under high humidity conditions at 60 $^oC$, these membranes absorbed too much water and quickly turn gel-like and finally a viscous solution. This was a result of the lack of chain entanglements, due to the entanglement MW for PnBA being as high as 28 kg/mol.[211]

### 5.2.5 Synthesis of Star PSt

In a reaction vessel, CTA ($TTC_3$ for 3-armed star polymer and $TTC_4$ for 4-armed star polymer), 100 equiv. (relative to trithiocarbonate moieties) of St, and 0.03-0.04 equiv of AIBN

were mixed, and degassed by purging with nitrogen for 30 minutes. Then the reaction was initiated by heating the container in an oil bath, which was preheated at 60 °C. After a certain period of time, the vessel was removed from the oil bath and quenched to 0 °C and precipitated into methanol three times to remove unreacted St and isolate $(PSt)_n$, where n denotes the number of arms (3 for 3-armed star and 4 for 4-armed star). The MW was calculated by end-group analysis using $^1$H NMR. A representative spectrum of $(PSt)_3$ is shown in Figure 65. The peak at $\delta \approx 3.2$ ppm was assigned to the methylene adjacent to trithiocarbonate, while the broad peak between $\delta \approx 4.5$ and 5.0 ppm was assigned to the proton at benzylic carbon attached to trithiocarbonate, with the region between $\delta \approx$ 6.2 and 7.2 ppm integrated as the aromatic protons. The dispersity was measured by GPC calibrated by polystyrene standards.

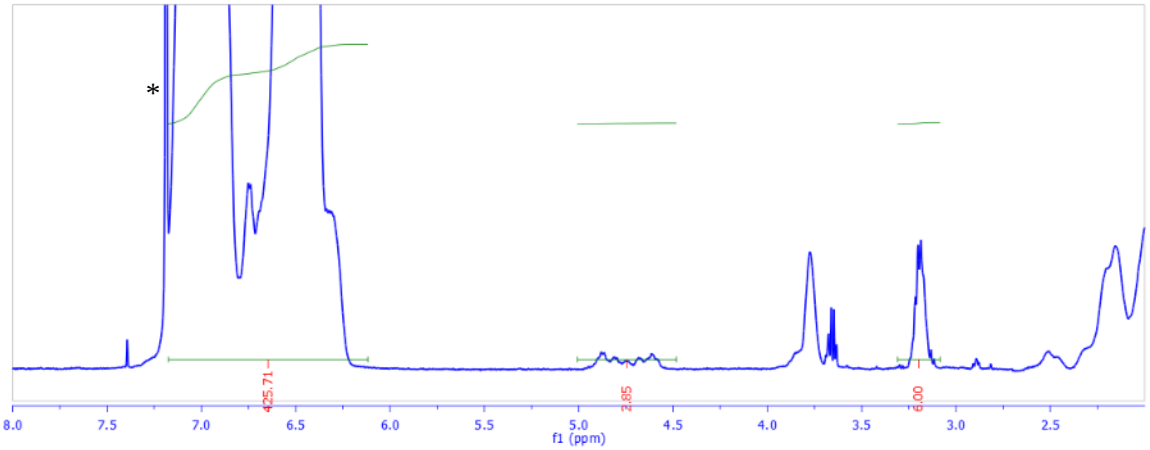


**Figure 65: A Representative $^1$H NMR Spectrum of $(PSt)_3$.**

### 5.2.6 Synthesis of Star PSt-*b*-P2VP

The star PSt was dissolved in 200 equiv. (relative to trithiocarbonate moieties) of dioxane and 100 equiv. of 2VP, together with 0.03-0.04 equiv. of AIBN. After degassing, the mixture was heated to 60 °C to start the chain extension. After a certain period of time, the resulting polymer was precipitated three times into hexanes to remove residual monomer. The DPs of 2VP was

calculated by the ratio between 2VP and St using $^{1}$H NMR. An example spectrum of 4-armed star PSt-*b*-P2VP is given in Figure 66, where the peak between $\delta \approx 8.1$ and 8.7 ppm was assigned to the -aromatic protons at the *ortho*-position to the nitrogen atom, while the peaks between $\delta \approx 6.1$ and 7.7 ppm were attributed to the rest of aromatic protons. It was also noticed that running $^{1}$H NMR on P2VP in deuterated dichloromethane or 1,1,2,2-tetrachloroethane gave better spectra than in chloroform, which was due to the complexation between chloroform and pyridine groups.[212]

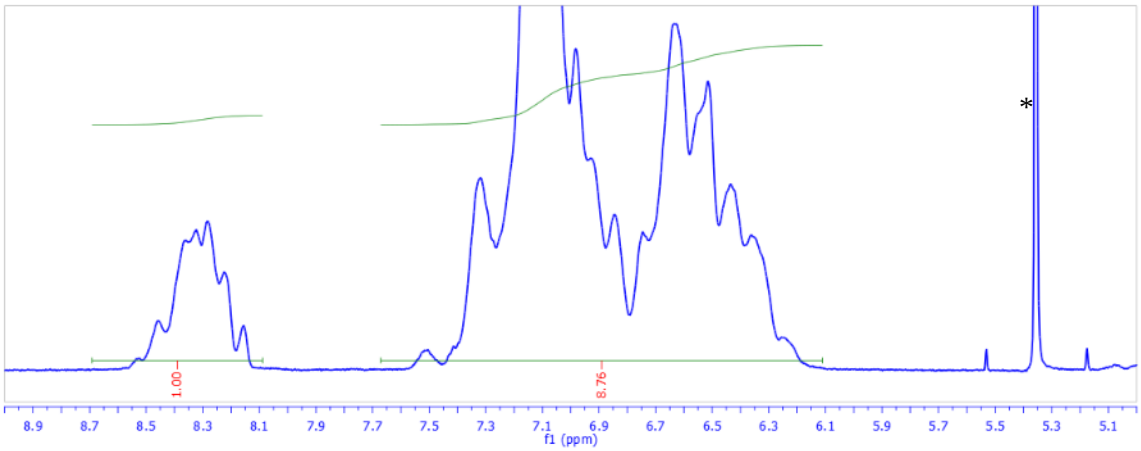


**Figure 66: A Representative $^{1}$H NMR Spectrum of (PSt-*b*-P2VP)$_4$.**

### 5.2.7 Copper(II) Chloride Doping and Small Angle X-ray Scattering

Copper (II) chloride salt and (PSt-*b*-P2VP)$_n$ star block copolymer were premixed in THF solution and freeze-dried at high vacuum, obtaining copper (II) chloride doped block copolymer solid with prescribed doping ratio. Then the block copolymer/copper salt mixtures were annealed at 180 $^{o}$C for 24 h and encapsulated within a Kapton® film for small angle X-ray scattering measurement. The SAXS measurement was performed using a Ganesha SAXSLAB with a copper X-ray source and sample heating stage. For the high temperature SAXS measurement, samples

were pre-annealed at 180 ºC for 24 hours at vacuum oven beforehand, before being encapsulated in Kapton® film and equilibrated for 10 min at designated temperature before measurement.

### 5.2.8 Thin film patterning

Block copolymer thin films with lamellae perpendicular to the substrates were prepared using a method similar to that of a previous report.[213] (PSt-*b*-P2VP)$_n$ block copolymer were premixed with $HAuCl_4$ in THF solution, where the mole ratio of $HAuCl_4$ to P2VP repeat unit was 6%. Then the salt doped block copolymer (5 mg/mL) was spin-coated onto a silicon wafer with neutral P(St-*r*-2VP-*r*-HEMA) brush at 4000 rpm, obtaining thin films with ca. 15 nm thickness. Line patterns with sub-15 nm domain spacing could be observed after annealing in acetone vapor to a swelling ratio of 140%.

## 5.3 Results and Discussion

### 5.3.1 Star Block Copolymer Synthesis

As mentioned above, the feed ratio of AIBN was intentionally kept at a low level to reduce the generation of free arms in the synthesis of (PSt-*b*-P2VP)$_n$. However, a non-negligible amount of free arms were still observed by GPC. This was due to the mechanism of RAFT polymerization, where a small amount of radical input is always necessary to initiate the reaction. At the same time, introducing a free radical results in the production of extra chains, which turn out to be free arms in star polymer synthesis. Considering that in a styrene RAFT polymerization the chain transfer site (such as trithiocarbonate) is constantly shuttling between different polymer chain-ends, most of the as-produced free arm polystyrene will eventually be terminated with a CTA group, a trithiocarbonate in this work, and reactive in the next step of polymerization. However, it should be noted that the chain length of the free arms produced here has a broader MW distribution than the arms attached to the core, due to the fact that the radicals were slowly introduced by AIBN

degradation in our experiments, and thus the free arms were slowly generated and experienced different propagation times. Similar reactions happened in the chain extension with 2VP. Finally, after sequential polymerization of St and 2VP, the major product in the free arm fraction should be PSt-*b*-P2VP and P2VP homopolymer, with a small quantity of PSt carrying non-reactive chain-ends. The star block polymers synthesized are summarized in Table 8.

**Table 8: Summary of (PSt-*b*-P2VP)$_n$s.**

| n[a] | $DP_{St}$[b] | $Đ_{PSt}$[c] | $DP_{2VP}$[b] | $Đ_{Star}$[c] | faf[d] |
|---|---|---|---|---|---|
| 3 | 24*3 | 1.09 | 19*3 | 1.21[e] | 0.03[e] |
| 3 | 24*3 | 1.09 | 21*3 | 1.24[e] | 0.03[e] |
| 3 | 24*3 | 1.09 | 31*3 | 1.25[e] | 0.04[e] |
| 3 | 30*3 | 1.08 | 31*3 | 1.27[e] | 0.04[e] |
| 3 | 37*3 | 1.09 | 28*3 | 1.34[e] | 0.06[e] |
| 3 | 42*3 | 1.12 | 58*3 | 1.17 | 0.09 |
| 3 | 42*3 | 1.12 | 42*3 | 1.17 | 0.05 |
| 3 | 37*3 | 1.09 | 58*3 | 1.15 | 0.03 |
| 3 | 52*3 | 1.14 | 24*3 | 1.16 | 0.05 |
| 3 | 52*3 | 1.14 | 44*3 | 1.18 | 0.07 |
| 3 | 52*3 | 1.14 | 45*3 | 1.19 | 0.07 |
| 3 | 41*3 | 1.08 | 57*3 | 1.30 | 0.04 |

| | | | | | |
|---|---|---|---|---|---|
| 3 | 41*3 | 1.08 | 50*3 | 1.23 | 0.04 |
| 4 | 32*4 | 1.09 | 23*4 | 1.22[e] | 0.03[e] |
| 4 | 32*4 | 1.09 | 24*4 | 1.25[e] | 0.04[e] |
| 4 | 32*4 | 1.09 | 27*4 | 1.24[e] | 0.05[e] |
| 4 | 32*4 | 1.09 | 28*4 | 1.31[e] | 0.05[e] |

[a]Number of arms, where 3 and 4 are for 3- and 4-armed star block copolymers, respectively. [b]The degrees of polymerization of the St and 2VP, respectively. [c]$Đ_{PSt}$ is the dispersity index for PSt core and $Đ_{Star}$ is the overall dispersity index for the polymer including the free arms. [d]The free arm fraction, determined by the low MW peak area ratio in GPC traces. [e]Measured by GPC using DMF as the eluent and calibrated against poly(methyl methacrylate) standards, others measured by GPC in THF calibrated against polystyrene standards.

It is possible to remove those free arm fractions using fractional precipitation and obtain pure star block copolymer. However, considering the significant time requirements and material handling losses, it was deemed efficient for the study conducted here to not pursue the removal of the free arm fraction, since the percentage (≤10%) of free arms should have only a minor effect on the microphase separation.

### 5.3.2 Bulk Morphology Study

Because of the low MWs in each arm of these star block copolymers, these block copolymers showed no sign of ordered microphases. To increase the $\chi_{eff}$ value, there are several successful approaches reported in the literature. For example, disordered Pluronic® triblock copolymer, $PEO_{37}$-*b*-$PPO_{54}$-*b*-$PEO_{37}$, was blended with polyacrylic acid or poly(styrene sulfonic acid), which formed hydrogen-bonds with the PEO blocks, and thus promoted the microphase

separation to achieve feature sizes around 5 nm.[214,215] Complexing BCPs with inorganic salt has also been reported to effectively transform disordered morphologies into ordered phases.[122,140,216] Here, $CuCl_2$ is adopted to complex with P2VP blocks, taking the advantage of its bivalency, which may lead to stronger coordination bonding.[213]

6

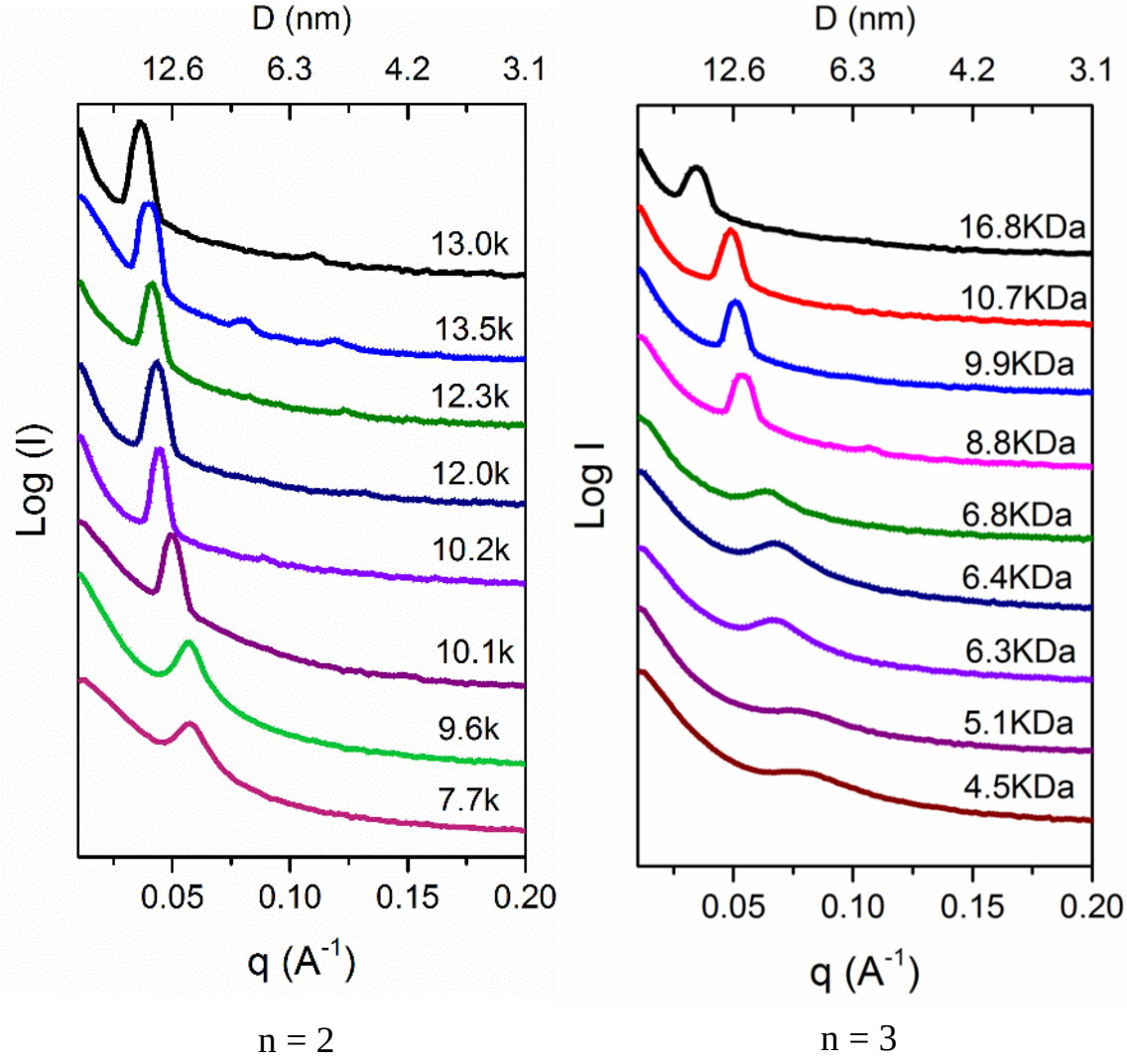


**Figure 67: SAXS Profiles of (PSt-*b*-P2VP)$_n$ Doped with 6% $CuCl_2$ at 150 ºC. The arm MWs were labelled aside the scattering pattern.**

The 3-armed star block copolymer were blended with 6% (relative to 2VP units) $CuCl_2$ and equilibrated at 150 ºC. As shown in Figure 67, the low MW polymers presented a broad peak with low intensity, which indicated a disordered morphology. When the MW was higher, a sharp primary peak and higher order peaks can be observed, indicating the formation of ordered nanophases. It was also found with the arm MW being 9.6 kg/mol, for the n = 2 star, or triblock copolymer displayed a disordered morphology, while the 3-armed star had ordered microphase separation with the arm MW being 8.8 kg/mol. This was in good agreement with theoretical prediction that increased arm number (n) can facilitate microphase separation.[217] Another observation was that the primary peak position shifted to the left, indicating increased d-spacing and feature size, when the arm MW was raised. This was attributed to the fact that the domain spacing was directly related to the polymer chain length, or arm MW, similar to what was found in diblock copolymers.[205]

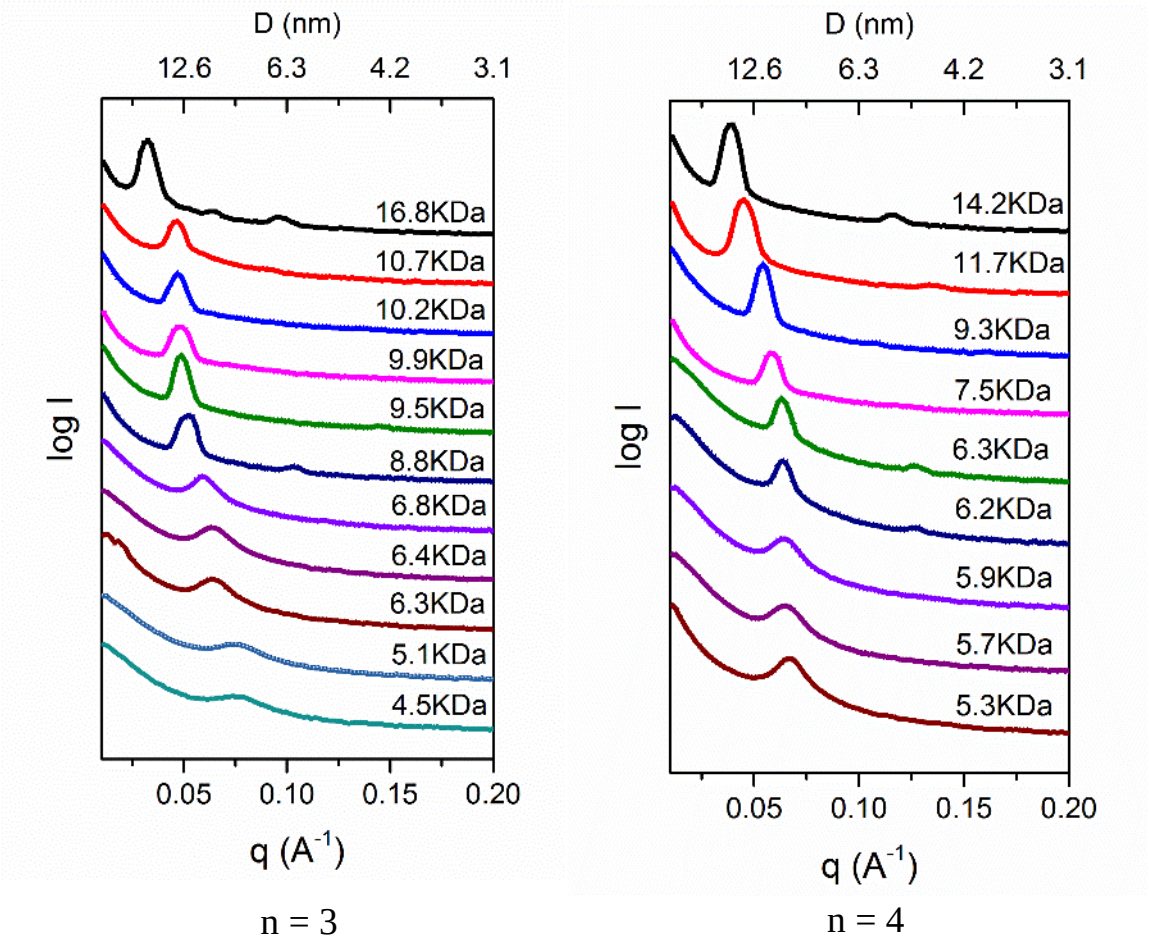


**Figure 68: SAXS Profiles of (PSt-*b*-P2VP)$_n$ Doped with 10% $CuCl_2$ at 150 °C. The arm MWs were labelled aside the scattering pattern.**

Similar trends were observed, when the comparison between 3-armed and 4-armed stars were conducted. Figure 68 shows the SAXS profiles of star block copolymers blended with 10% $CuCl_2$ and equilibrated at 150 °C. This time, it was found that with the arm MW being 6.8 kg/mol, the 3-armed star displayed a disordered morphology, while the 4-armed star had ordered microphase separation with the arm MW being 6.2 kg/mol, which was again a result of star block architecture facilitating microphase separation.

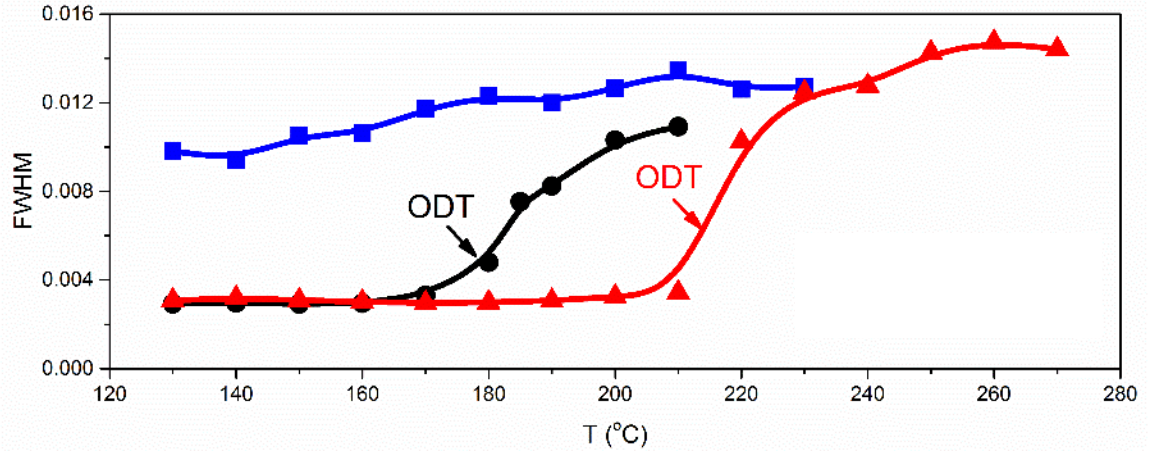


**Figure 69: Measurement of ODT Temperatures.**

**The arm MWs are 9.6, 8.8, and 8.3 kg/mol for n = 2 (■), 3 (●), and 4(▲), respectively.**

Other evidence of ordering was achieved by measure the order-disorder transition (ODT) temperature for star block copolymers with n = 2, 3, and 4. To probe this transition, the full-width at half-maxima of the primary peak in SAXS pattern was plotted against annealing temperature, shown in Figure 69. Star block copolymers (doped with 6% $CuCl_2$) with similar arm MWs were tested in this experiment. The higher FWHM value plateau is the sign of a disordered state, while the lower value region was a result of sharp primary peak and corresponds to an ordered morphology. It was found that the n = 2 star was in a disordered state across the temperature range that was tested, while the n = 3 star showed a clear ODT at ~180 °C. The n = 4 star polymer did not reach its ODT until approximately 215 °C. This demonstrated that in the PSt-*b*-P2VP/$CuCl_2$ system, by increasing the n value by 1, the ODT temperature can be raised for > 30 °C. It also proved that adopting a star block copolymer architecture can significantly promote microphase separation.

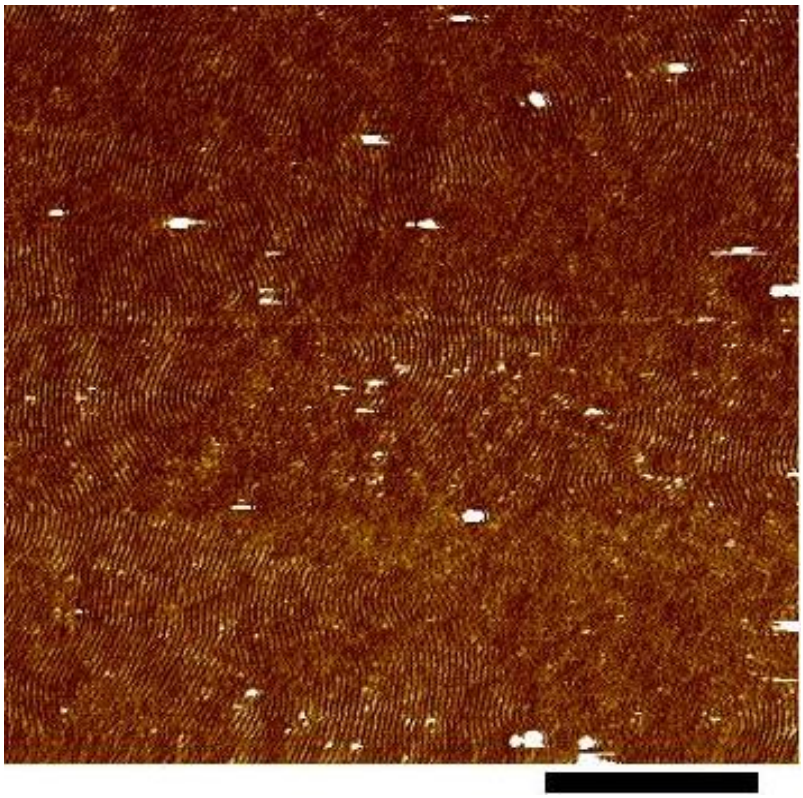

**Figure 70: AFM Height Image of a Salt Doped ($PSt_{32}$-*b*-$P2VP_{58}$)$_3$ Thin Film. The scale bar is 400 μm.**

To prove the concept of using star block copolymers to achieve ultra-small features, especially line patterns, on a thin film, ($PSt_{32}$-*b*-$P2VP_{58}$)$_3$ was subjected to thin film preparation. Since domain orientation of BCP thin films is strongly affected by the pair wise interactions, at both BCP/air and BCP/substrate interfaces,[218–222] two strategies were used in synergy to assist the formation of lamella perpendicular to the surface. The first was to modify the substrate surface with a neutral coating layer, which is often a copolymer with a composition similar to the thin film BCP.[223–226] A random copolymer of St and 2VP (~1:1 = mol : mol) with ~2 mol% poly(hydroxy ethyl methacylate) was prepared by radical polymerization, and anchored onto the silicon wafer surface to balance the interfacial preference. Another strategy was to use solvent vapor annealing (SVA), where the presence of solvent in the swelled BCP thin film can mediate the interfacial interactions.[227–229] It was found when the BCP was doped with HAuCl4 (6 mol% relative to 2VP

units) and annealed in acetone vapor to a swelling ratio of 140%, ordered fingerprint pattern could be achieved, indicating the perpendicular orientation of lamella. In Figure 70, a representative AFM image is shown on $(PSt_{32}$-*b*-$P2VP_{58})_3$, and the domain spacing was measured to be 12.4 nm.

### 5.4 Conclusions

In this chapter, star block copolymers were synthesized using RAFT polymerization mediated by multi-functional CTAs. Due to the mechanism of RAFT polymerization, the formation of free arms was inevitable, however, these were suppressed by reducing the feed ratio of radical initiator. By investigating the bulk morphology of $CuCl_2$ doped PSt-*b*-P2VP copolymers by SAXS, it was confirmed that adopting the star block copolymer architecture can significantly facilitate microphase separation, and the greater number of arms in a star polymer lead to a stronger tendency to form ordered morphologies. Using substrate surface modification and SVA, salt doped star block copolymer can self-assemble into lamella oriented perpendicular to the surface. This work is also potentially useful for understanding the structure-property correlation in the catalyst layer of a fuel cell device.[68,230–232]

# CHAPTER 6

# SELF-ASSEMBLED THINS FILMS OF UV CLEAVABLE BLOCK COPOLYMERS FOR HIERARCHICAL NANOPATTERNS

## 6.1 Introduction

Nanomaterials have been widely demonstrated to be promising in numerous applications due to their unique electronic, interfacial, optical, and magnetic properties, imparted by their sizes. To facilitate the utilization of nanomaterials, it is necessary to develop alternative high-efficiency preparation pathways beyond expensive conventional lithographic technique. Microphase separated block copolymer (BCP) thin films have received extensive research interests as a convenient and cost-efficient methodology for nanopattern fabrication in applications such as data storage,[209,233,234] templates for nanotransistor/nanowire preparation,[207,208] and substrates for cellular behavior study.[235,236] Uniform surface morphologies, including parallel lines, hexagonally and tetragonally packed dots,[237] can be achieved using thermal annealing, or solvent vapor annealing conditions. However, in most reports, the self-assembled patterns possessed only one phase, and it has always been challenging to obtain 2-dimensional spatial arrangements of domains with different surface patterns, which is critical for field effect transistors,[238] hard disk drives,[233] and surface plasmonic waveguides.[239]

One successful approach to fabricate hierarchical morphologies is to utilize post-self-assembly regional pattern generation. For examples, thin films of polyisoprene-*b*-polystyrene-*b*-polyferrocenylsilane were annealed with solvent vapor and then subjected to sequential reactive ion etching and surface reconstruction.[237] This method requires large etching contrast between polymer blocks, which significantly limits the availability and thus applications of the BCPs. Alternatively, zone-based methods were adapted from metallurgy, which is regarded as promising

in continuous processing method for production.[240,241] The zone casting methodology using BCP solution flow was demonstrated to be capable of preparing hierarchical morphologies with different topologies and feature sizes by varying the BCP identities.[242,243] Instead of depositing BCPs, a raster annealing technique was developed to deliver solvent vapor, or heat, to induce the order-disorder transition.[244] Though capable of providing complexed hierarchical patterns, these approaches require sophisticated instrumentation. A more convenient method is to control the substrate surface properties, which has been demonstrated to have important effects on BCP domain orientation.[221,223,245,246] This approach was adopted by etching the substrate surface to either change the chemical composition or tune the physical topology.[228,247–251] Besides, grafting surface with silanes in gradient was reported to lead to the morphology of polystyrene-*b*-polyisoprene-*b*-polystyrene thin film changing from parallel cylinders to hexagonally perforated lamellae.[252] Reactive polymer coating layers were designed to treat the substrate surface, which alters the preference of the surface towards the BCPs and this effect can be easily tuned upon UV exposure.[219,253–255] Utilizing regional UV treatment, well controlled spatial placement of perpendicular and parallel lamellar phases were achieved. Despite the versatility of the coating layer and the relatively convenient processing conditions, these surface treatment methods still requires careful design of the chemical structure to interact with BCPs having various chemical compositions.

Interestingly, methodologies based on chemical reactions of the BCP thin films have been scarcely investigated. The photoacid induced conversion of tert-butyl ester into carboxylic acid group was utilized to transform strongly segregated thin films into the disordered state.[256] Another approach was to use crosslinking chemistry to lock the morphology of the desired area, while allowing the non-crosslinked region to undergo order-order transition following an annealing process.[257,258] However, there are two significant disadvantages of these approaches. First, the selection of monomers is highly constrained in these approaches to accommodate either

reactivity/inertness towards photoacids or UV crosslinking. In addition, they provide little chance to tune the feature size, which is primarily dominated by the BCP molecular weight (MW) for a given BCP system.[198,205]

To overcome the first drawback, it was conjectured that using a high-efficiency reactive junction instead could provide a more universal platform. Despite the difficulties in changing the BCP MWs, it is feasible to change the polymer architecture, which can have remarkable impacts on domain spacing.[200,259] In this work, a series of poly(ethylene oxide)-ONB-polystyrene-*b*-poly(ethylene oxide) (EO-*hv*-SEO) copolymers were designed and synthesized, where ONB is a photo-cleavable *ortho*-nitrobenzyl ester junction.[260–262] These BCPs can undergo polymer architecture transformation upon UV exposure.

## 6.2 Experimental Section

### 6.2.1 Materials

Styrene was passed through a short column of basic alumina and stored under -30 $^{o}$C before use. Thermal initiators, 2,2'-Azobis(2-methylpropionitrile) (AIBN) was recrystallized from MeOH. Other chemicals were used as received. The acid functionalized RAFT agents, 2-(dodecylthiocarbonothioylthio)-2-methylpropionic acid ($C_{12}$COOH-CTA), 5-propargylether-2-nitrobenzyl alcohol (Yne-ONB-OH), and azide terminated poly(ethylene oxide)s (PEOs), were synthesized using previously reported methods, respectively.[261,263,264] Other chemicals were used as received.

### 6.2.2 Synthesis of Acid Functionalized RAFT Agent

The RAFT agent, 4-cyano-4-[(butylsulfanylthiocarbonyl)sulfanyl]pentanoic acid (COOH-CTA), was synthesized using a reported synthetic protocol for 4-cyano-4-

[(dodecylsulfanylthiocarbonyl)sulfanyl]pentanoic acid.[210] The NMR characterization (Figure 71) confirmed the chemical structure.

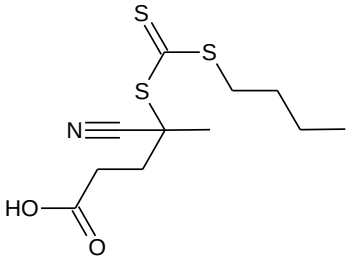


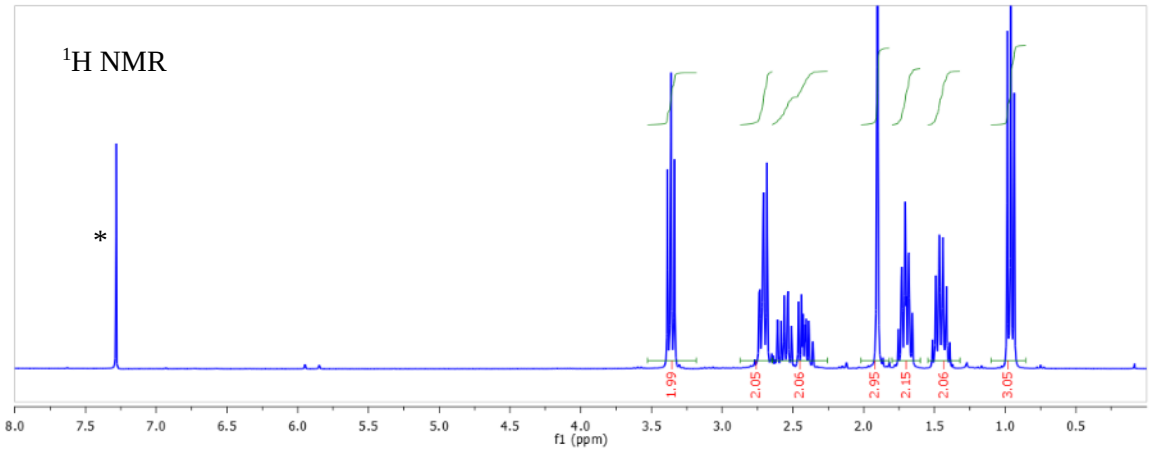


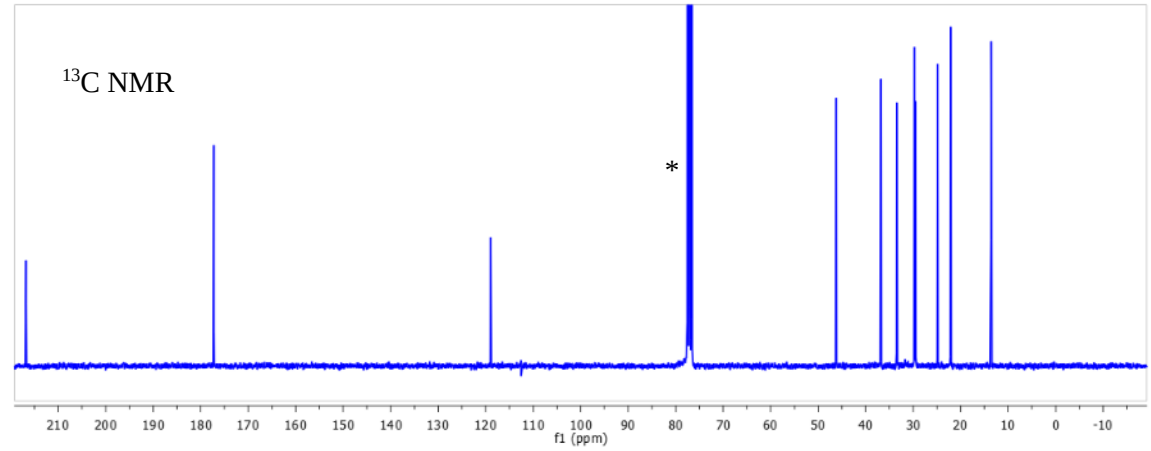

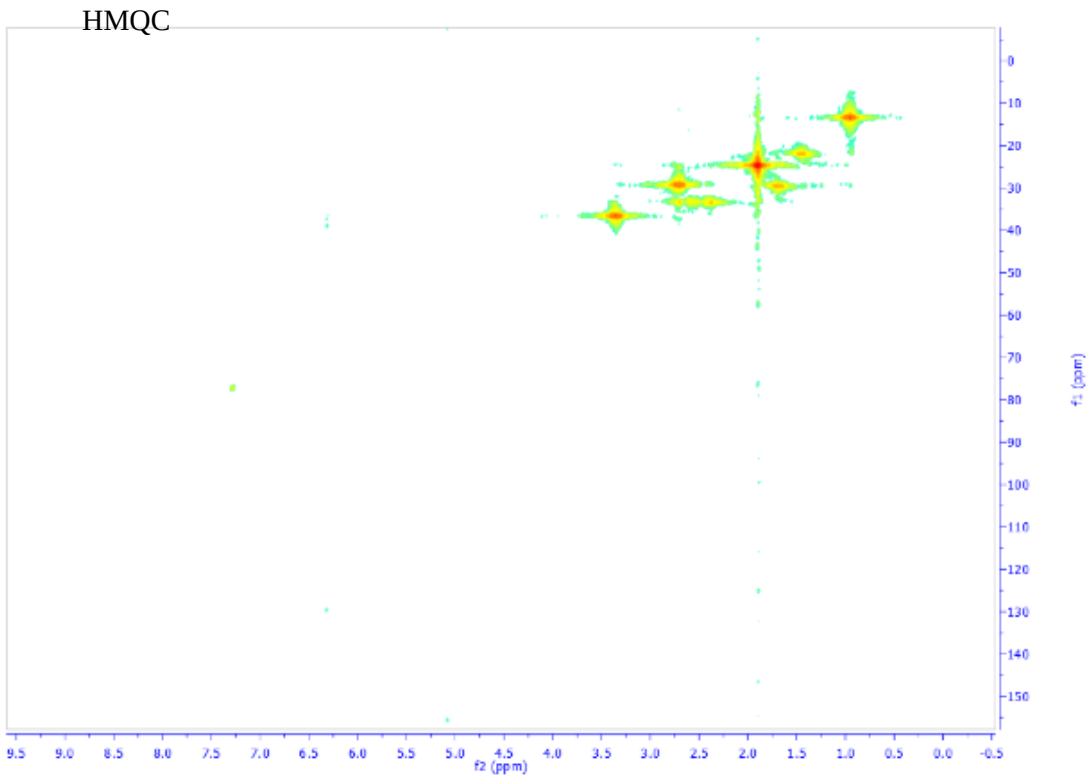


**Figure 71: Chemical Structure and NMR Characterization of COOH-CTA.**

### 6.2.3 Synthesis of ONB Functionalized CTAs

To synthesize the ONB functionalized CTA based on COOH-CTA, 2.09 g Yne-ONB-OH, 2.70 g COOH-CTA, and 121 mg 4-dimethylaminopyridine (DMAP) were dissolved in 40 mL dichloromethane at 0 °C. To the stirring mixture, 2.36 g N,N'-Dicyclohexylcarbodiimide (DCC) was slowly added. The reaction was allowed to run overnight and then filtrated to remove dicyclohexyl urea. The concentrated mixture was purified using column chromatography (hexanes:ethyl acetate = 3:1, v:v) to obtain a yellow solid as the product, Yne-ONB-CTA (3.65 g, yield = 82%). The chemical structure was confirmed by NMR (Figure 72).

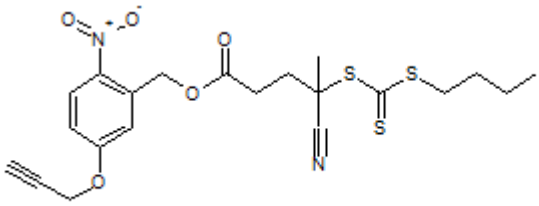

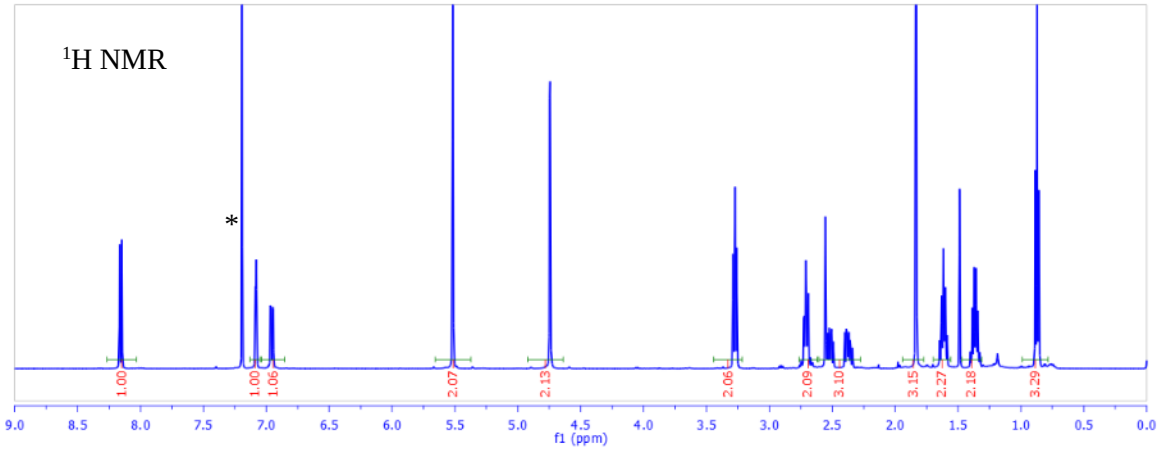
$^{1}$H NMR
*
1.00
1.00
1.06
2.07
2.13
2.06
2.09
3.10
3.15
2.27
2.18
3.29
9.0 8.5 8.0 7.5 7.0 6.5 6.0 5.5 5.0 4.5 4.0 3.5 3.0 2.5 2.0 1.5 1.0 0.5 0.0
f1 (ppm)

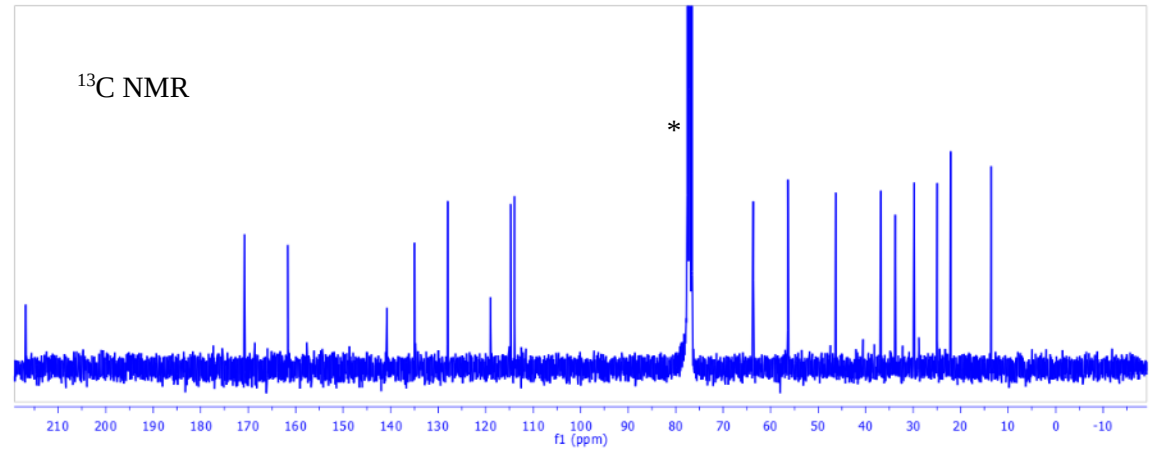
$^{13}$C NMR
*
210 200 190 180 170 160 150 140 130 120 110 100 90 80 70 60 50 40 30 20 10 0 -10
f1 (ppm)

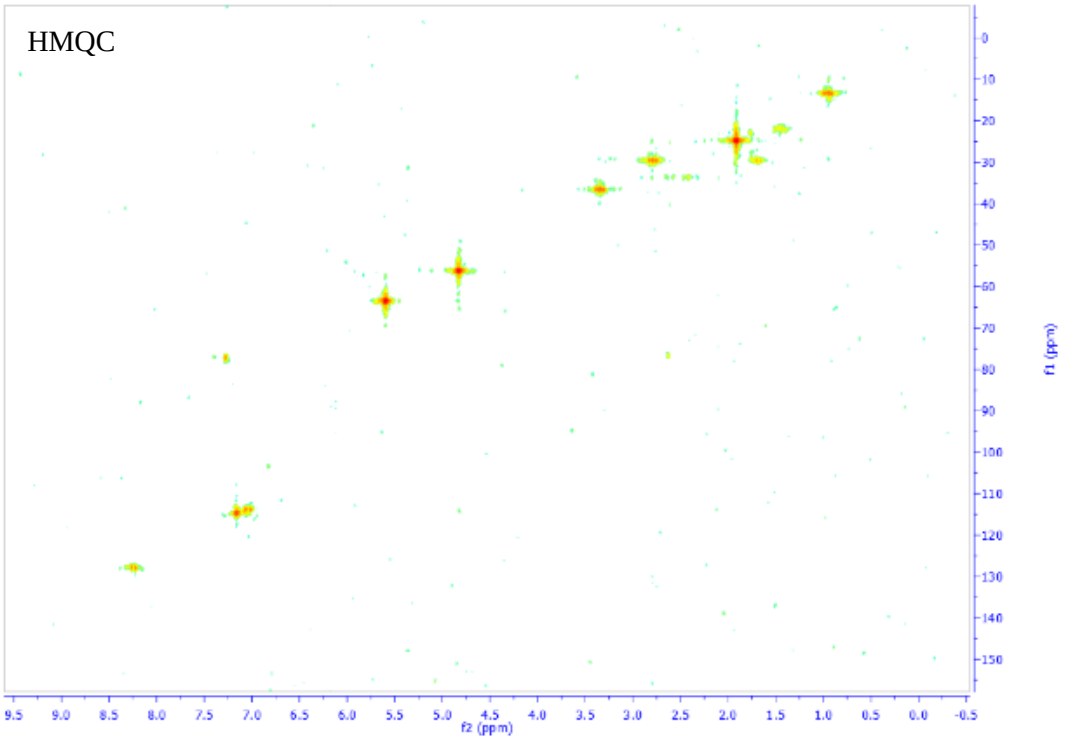


**Figure 72: Chemical Structure and NMR Characterization of Yne-ONB-CTA.**

The ONB functionalized CTA based on $C_{12}$COOH-CTA was synthesized in a similar manner. In 50 mL dichloromethane, 1.82 g Yne-ONB-OH, 3.54 g $C_{12}$COOH-CTA, and 114 mg 4-dimethylaminopyridine (DMAP) were dissolved at 0 $^{o}$C. To the stirring mixture, 1.86 g N,N'-dicyclohexylcarbodiimide (DCC) was slowly added. The reaction was allowed to run overnight and then filtrated to remove dicyclohexyl urea. The concentrated mixture was purified using column chromatography (hexanes:ethyl acetate = 5:1, v:v) to obtain a yellow solid as the product, Yne-ONB-CTA-$C_{12}$ (2.21 g, yield = 45%). The chemical structure was confirmed by NMR (Figure 73).

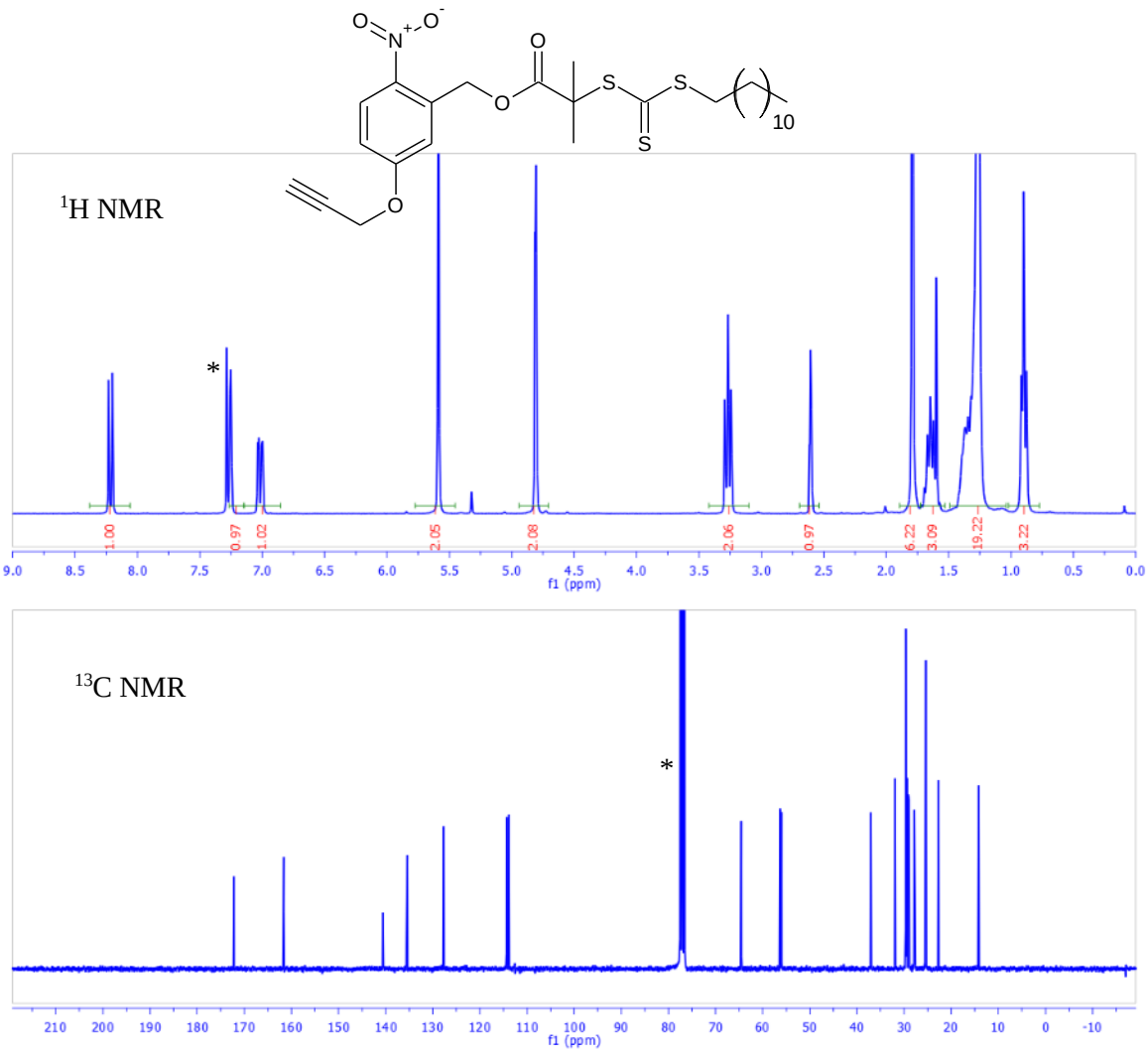
1H NMR
13C NMR
f1 (ppm)
f1 (ppm)

COSY $^{1}$H NMR

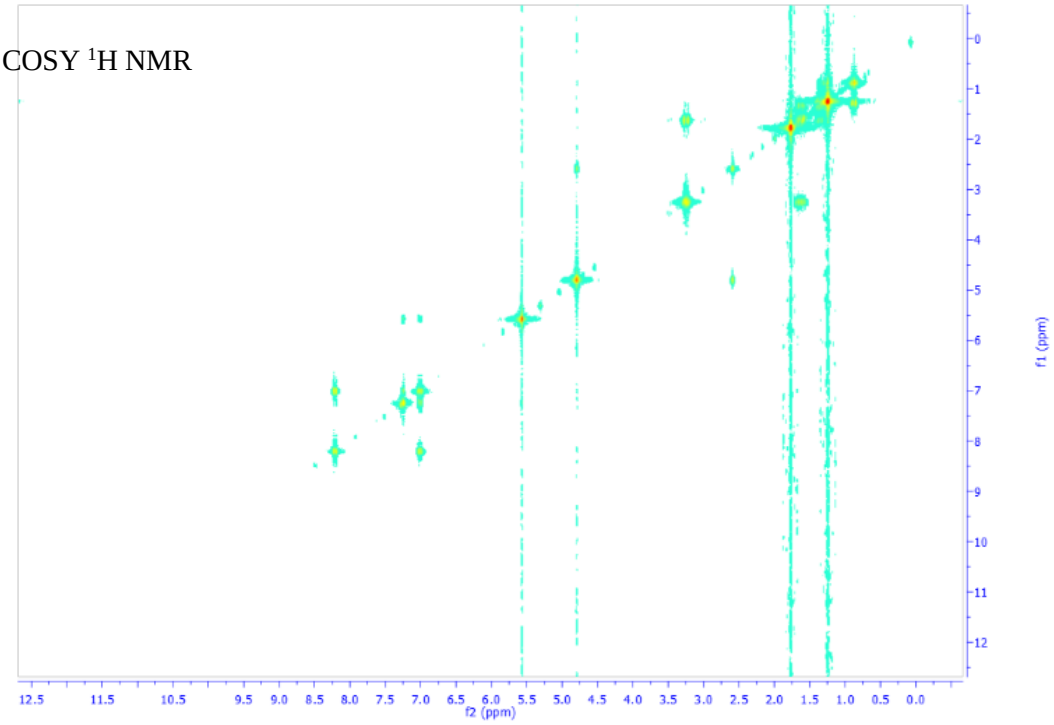


HMBC

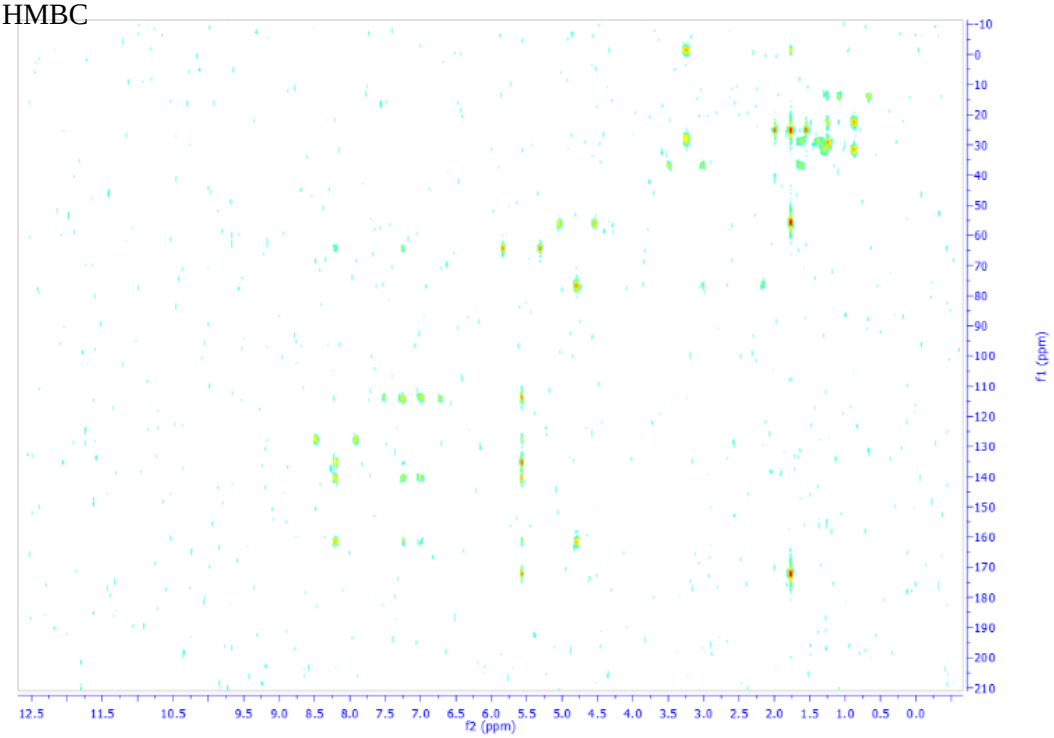

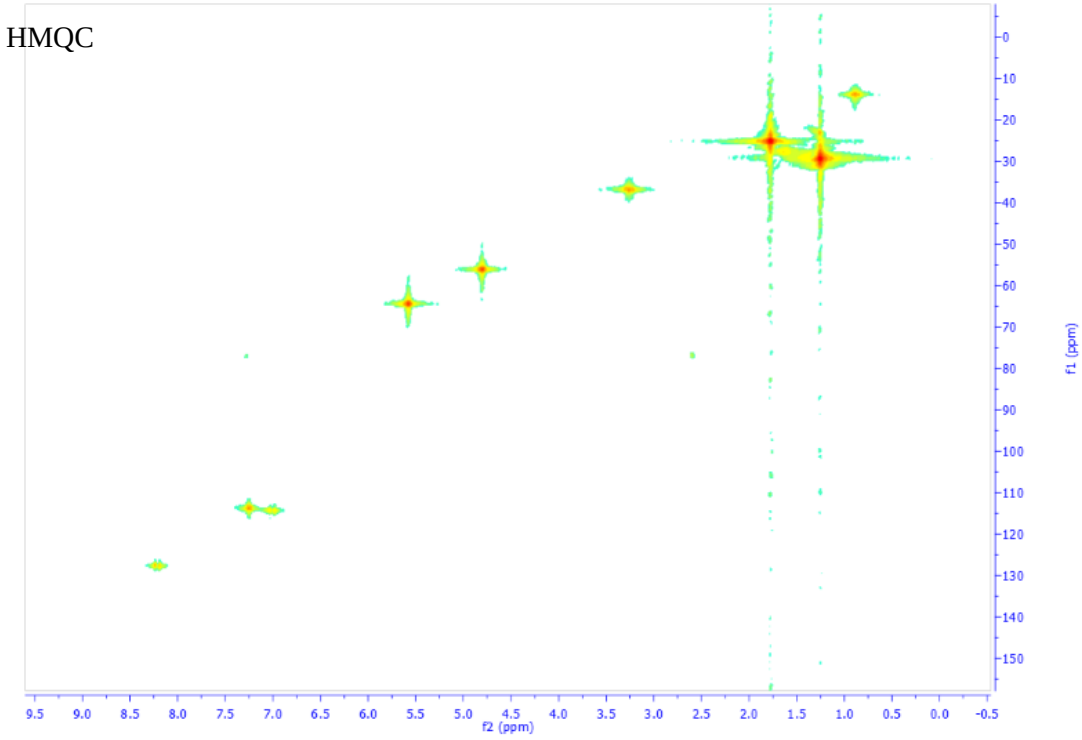


**Figure 73: Chemical Structure and NMR Characterization of Yne-ONB-CTA-$C_{12}$.**

### 6.2.4 Synthesis of Maleimides with an Alkyne Functionality

In the first place, the Steglich esterification mediated by DCC and DMAP was conducted to react 6-maleimidohexanoic acid with propargyl alcohol. However, it did not result in the desired product but only a dark reddish oil with high viscosity. The alternative approach was to use traditional acid catalyzed esterification reaction. In 40 mL toluene, 5.09 g 6-maleimidohexanoic acid was dissolved together with 2.68 g propargyl alcohol. Then 3 drops of sulfuric acid was carefully added before the mixture was heated to reflux. After reacting for 14 hours, the reaction was allowed to cool to room temperature. The mixture was quenched with sodium bicarbonate aqueous solution and then extracted with ethyl acetate (2*100 mL). The organic phase was collected and concentrated. Finally, column chromatography was used to isolate the product (MI-Yne, 4.09 g, 69% yield) as a slightly yellow oil. The structure was confirmed by NMR (Figure 74, trace residual ethyl acetate was observed) and FAB-MS (theo. 249.10, found 250.08 as M+H).

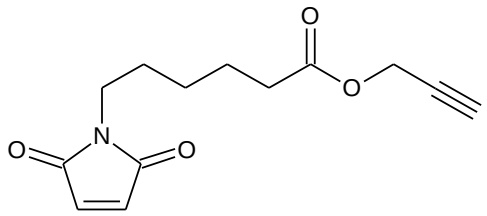
O
O
N
O
O

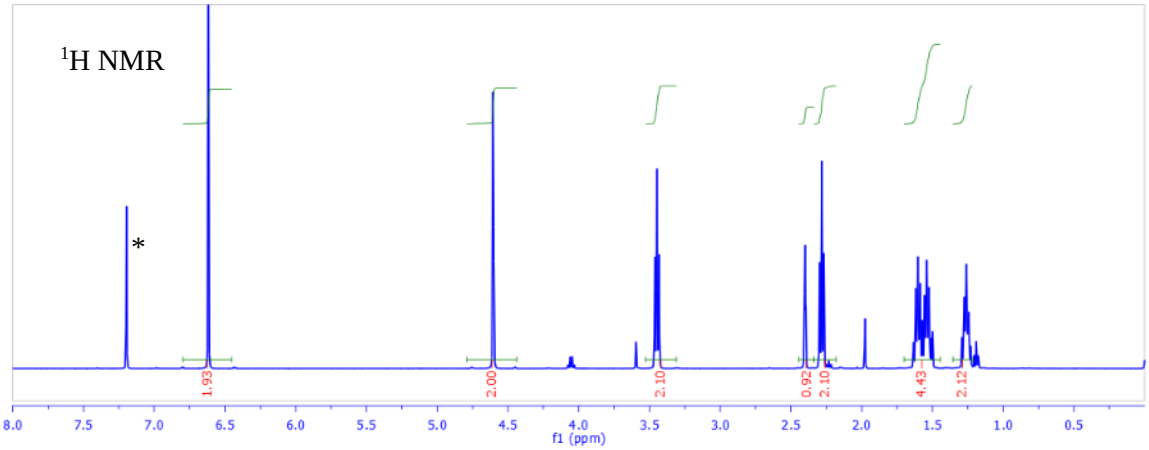
1H NMR
*
1.93
2.00
2.10
0.92
2.10
4.43
2.12
8.0
7.5
7.0
6.5
6.0
5.5
5.0
4.5
4.0
3.5
3.0
2.5
2.0
1.5
1.0
0.5
f1 (ppm)

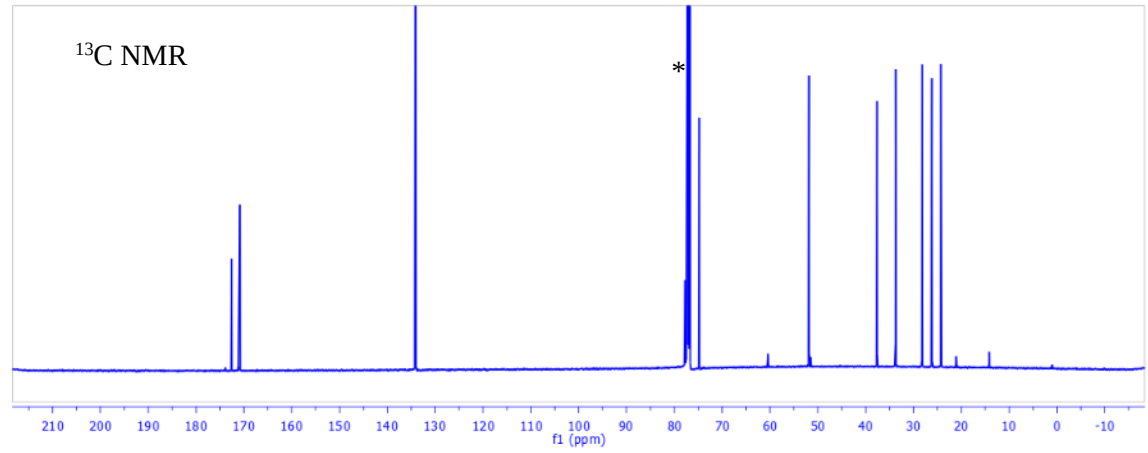
13C NMR
*
210
200
190
180
170
160
150
140
130
120
110
100
90
80
70
60
50
40
30
20
10
0
-10
f1 (ppm)

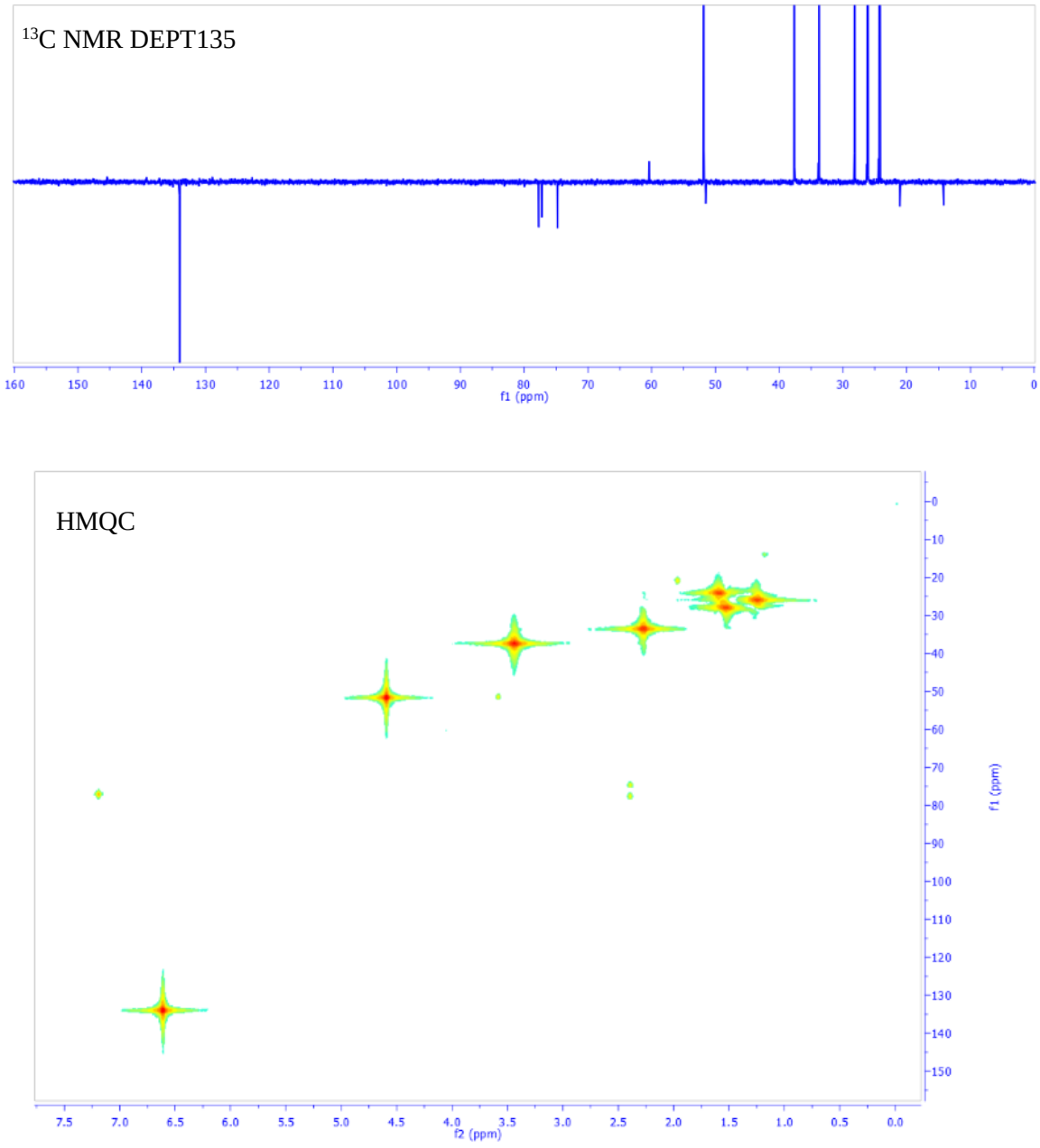


**Figure 74: Chemical Structure and NMR Characterization of MI-Yne.**

A similar esterification reaction was performed to synthesize the maleimide carrying the alkyne functionality with a longer spacer from the ester bond (MI-$C_4$-Yne). In 50 mL toluene, 9.0

g 6-maleimidohexanoic acid was dissolved together with 3.5 g 3-butyn-1-ol. Then 3 drops of sulfuric acid was carefully added before the mixture was heated to reflux. After reacting for 20 hours, the reaction was allowed to cool to room temperature. The mixture was quenched with sodium bicarbonate aqueous solution and then extracted with ethyl acetate (2*100 mL). The organic phase was collected and concentrated. Finally, column chromatography with hexanes/ethyl acetate (3:1 = v:v) as eluent was used to isolate the product (7.82 g, 71% yield) as a slightly yellow oil. The structure was confirmed by NMR (Figure 75) and FAB-MS (theo. 263.1, found 264.2 as M+H).

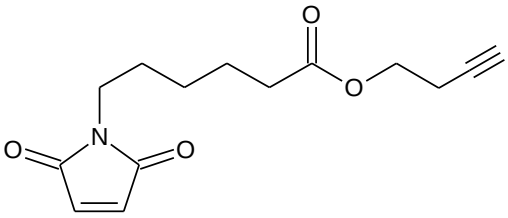
O
O
N
O
O

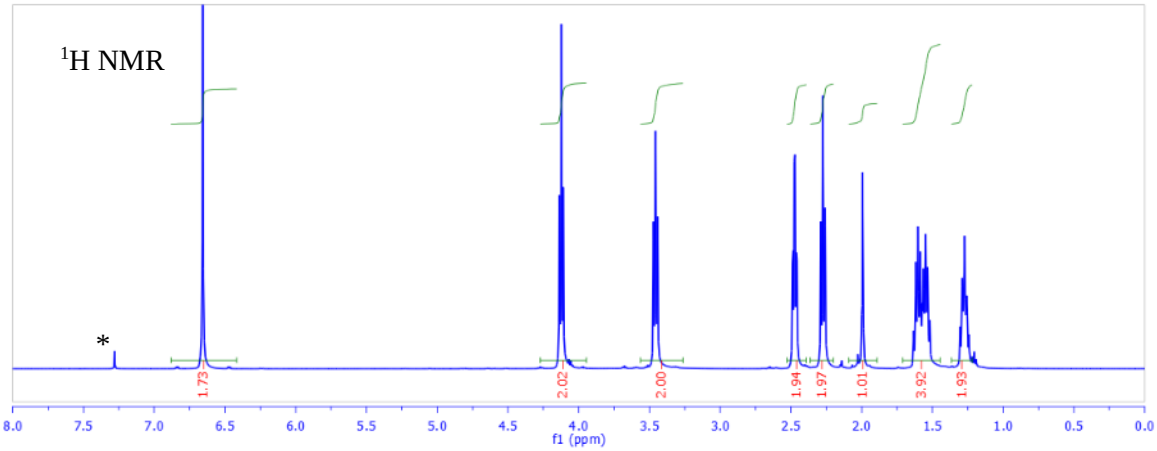
1H NMR
*
1.73
2.02
2.00
1.94
1.97
1.01
3.92
1.93
8.0 7.5 7.0 6.5 6.0 5.5 5.0 4.5 4.0 3.5 3.0 2.5 2.0 1.5 1.0 0.5 0.0
f1 (ppm)

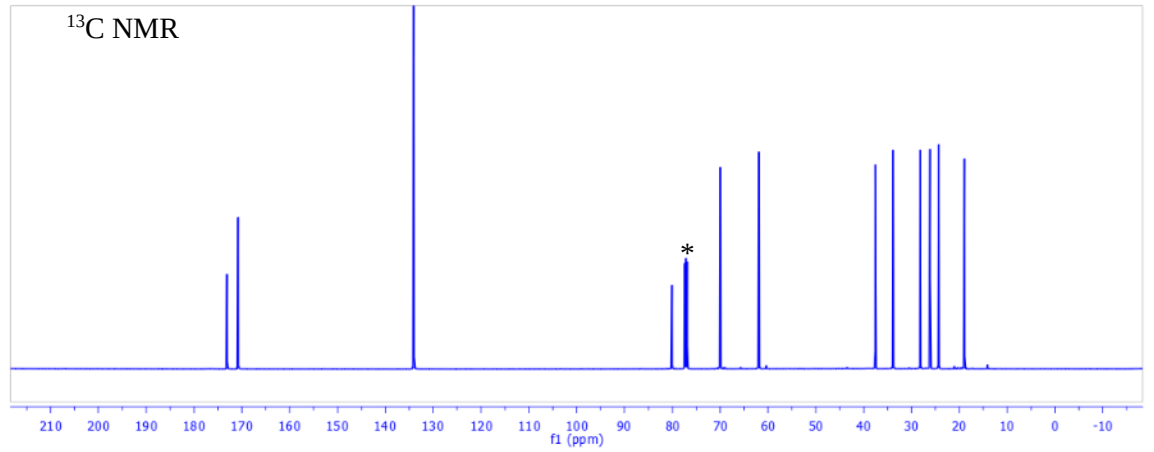
13C NMR
*
210 200 190 180 170 160 150 140 130 120 110 100 90 80 70 60 50 40 30 20 10 0 -10
f1 (ppm)

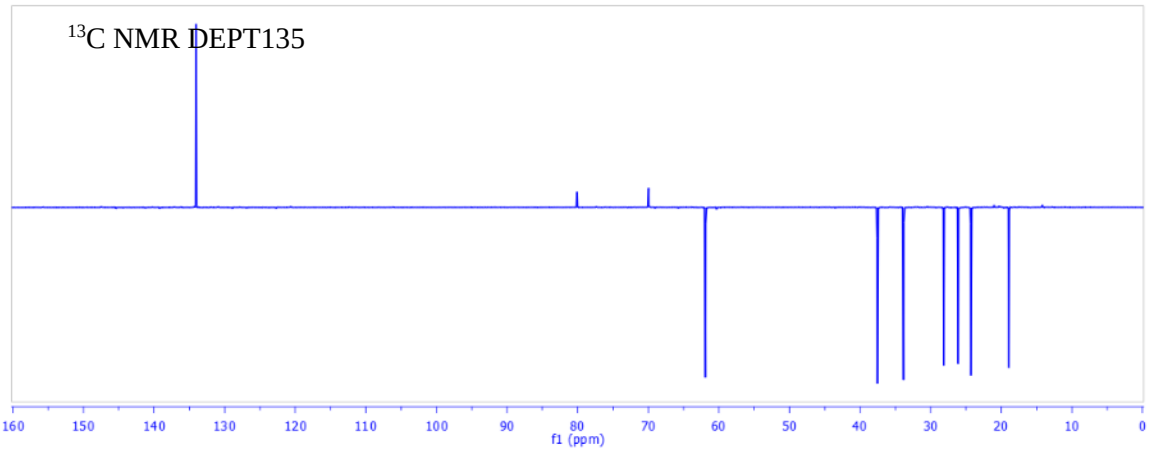
13C NMR DEPT135
160 150 140 130 120 110 100 90 80 70 60 50 40 30 20 10 0
f1 (ppm)

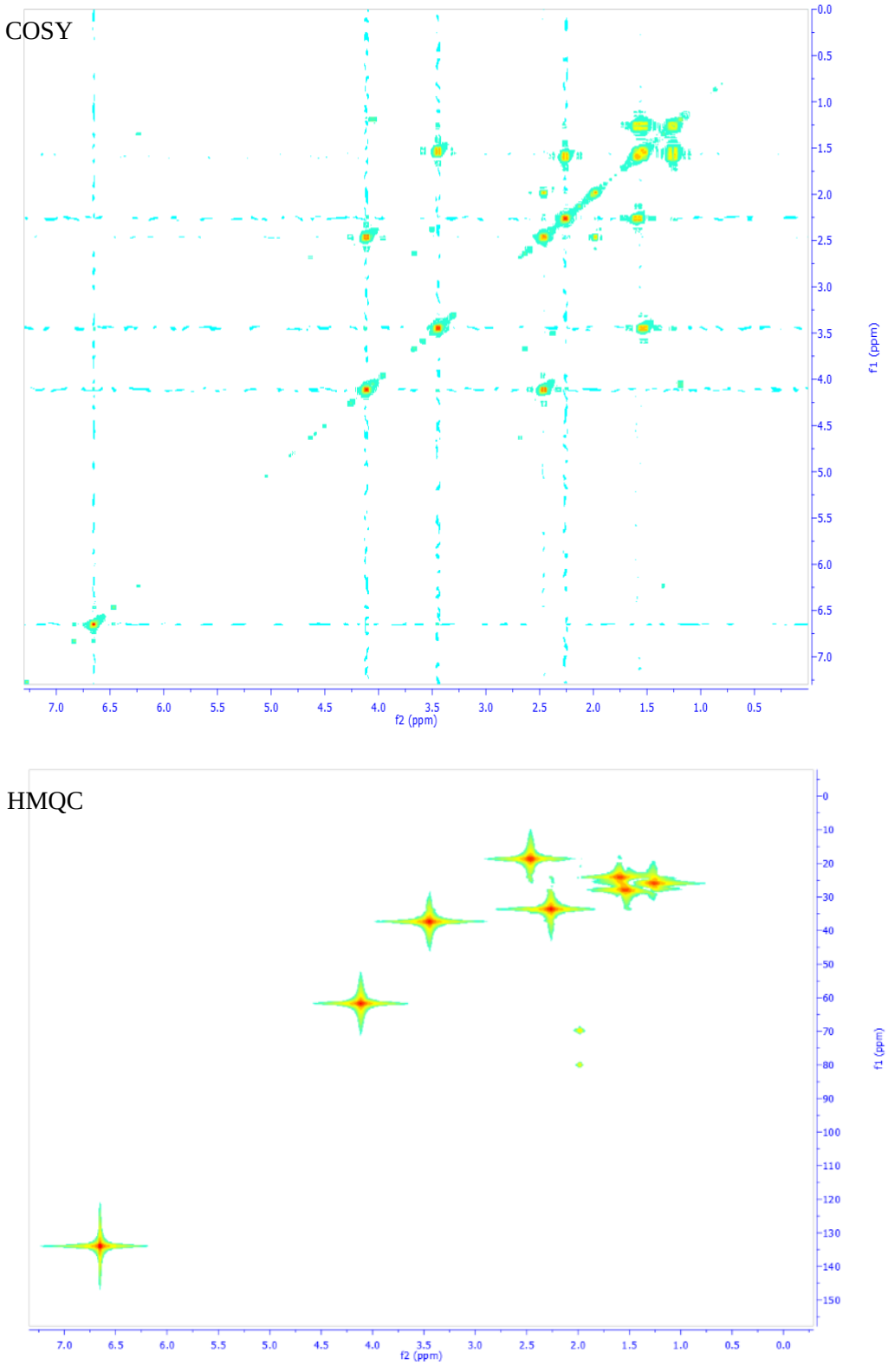


**Figure 75: Chemical Structure and NMR Characterization of MI-$C_4$-Yne.**

### 6.2.5 Styrene Polymerization Mediated by Yne-ONB-CTA

In a Schlenk tube, Yne-ONB-CTA (1 equiv.), styrene (1500 equiv.), AIBN (0.1 equiv.), and a predetermined amount of solvent was mixed. The solution was subjected to three freeze-pump-thaw cycles, before being heated to 70 $^{o}$C to initiate the polymerization. After a period of time, the reaction tube was queched to 0 $^{o}$C and a small aliquot was extracted for conversion determination. Polystyrene with ONB end functionalization was purified by precipitating into a large amount of methanol three times to remove unreacted styrene monomer. Gel permeation chromatography using THF as the eluent was conducted to determine the MW against PSt standards.

### 6.2.6 Single Unit Insertion of MI-Yne

The ONB functionalized polystyrene (1 equiv.) was dissolved in dioxane (10 mL per gram of polymer), together with 3~5 equiv. of MI-Yne and AIBN (0.1 equiv.). After being purged with $N_2$ for 20 minutes, the mixture was heated to 70 $^{o}$C for 2 days. The polymer was purified by precipitation and vacuum drying.

### 6.2.7 "Click" Synthesis of Triblock Copolymers

The MI-Yne modified polystyrene was mixed with 4 equiv. of PEO-$N_3$, 0.5 equiv. of Cu(I)Br, and 1,4-dioxane (10 mL for each gram of polymer). The mixture was purged with nitrogen for 20 minutes, and N,N,N',N'',N''-pentamethyldiethylenetriamine (1 equiv.) was added by a microsyringe. The "click" reaction was allowed to proceed for 2 days, before being precipitated into hexanes. The precipitated materials was passed through a short column of basic $Al_2O_3$ to remove residual Cu salts and precipitated into hexanes to recover the polymer. After that, the polymer was stirred in methanol (20 mL for each gram of polymer) for two days, and filtered, before it was rinsed with methanol (100 mL for each gram of polymer), to remove excess PEO-$N_3$. The product was dried in vacuum to provide pure EO-*hv*-SEO.

### 6.2.8 Preparation of Block Copolymer Thin Films

The EO-*hv*-SEO thin films were prepared by spin-coating a toluene solution (0.7 wt%) onto silicon substrates, where the thickness was controlled to be ~$1L_o$, and followed by solvent annealing in a $H_2O$ atmosphere for 1 hour and in a THF atmosphere for 2 hours, sequentially. To cleave the ONB junction, the thin films were kept in a nitrogen atmosphere under UV exposure at a wavelength of 365 nm (1 cm away from Blak-Ray Model B, UVL-56) for certain periods of time. After that, the treated thin films were annealed again in a $H_2O$ atmosphere for 1 hour and in a THF atmosphere for 2 hours.

### 6.2.9 Grazing Incidence Small Angle X-Ray Scattering (GISAXS)

The testing was conducted in Advanced Light Source (ALS) Beamline 7.3.3 in Lawrence Berkeley National Laboratory. The beam energy was 10 keV with wavelength of 0.124 nm. The incident angle was 0.16°.

## 6.3 Results and Discussion

The preparation of the EO-*hv*-SEOs started with the synthesis of ONB functionalized chain transfer agent (Yne-ONB-CTA) for reversible addition-fragmentation chain transfer radical polymerization (RAFT). A previously published procedure was adopted to prepare 5-propargylether-2-nitrobenzyl alcohol, which was coupled to 4-cyano-4-[(butylsulfanylthiocarbonyl)sulfanyl]pentanoic acid using an esterification reaction mediated by 1,3-dicyclohexylcarbodiimide and 4-(dimethylamino)pyridine to give a yellow solid product (isolated yield 82%). As shown in Figure 76, Yne-ONB-CTA was utilized to mediate the RAFT polymerization of styrene to provide polystyrene (PSt) with an alkyne and a ONB group at the α-terminus. It was found that the selection of solvent can have a significant effect on the polymerization kinetics (Table 9), which was possibly due to the polarity affecting the

fragmentation step in RAFT polymerization. All of the polymerizations resulted in narrow MW distribution (Đ ~ 1.2) measured by gel permeation chromatography (GPC), and thus indicated the preservation of the functionalities.

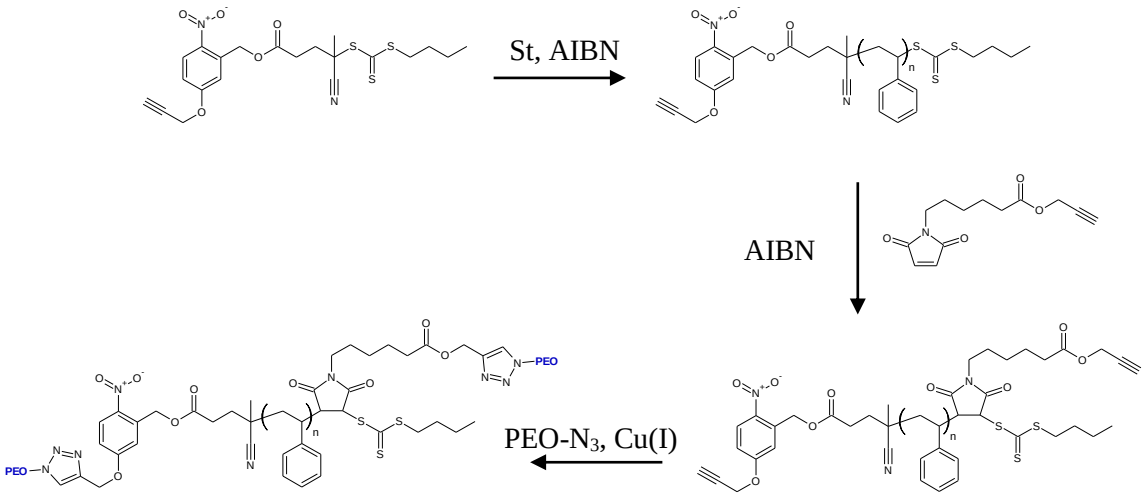


**Figure 76: Synthetic Protocol of EO-*hv*-SEOs.**

**Table 9: Solvent Effect on Yne-ONB-CTA Mediated Styrene Polymerization.**

| Solvent | [St]:[CTA]:[AIBN] (:[Solvent])[a] | Conv. (%) | $M_n$[b] (g/mol) | Đ[b] |
|---|---|---|---|---|
| Bulk | 500:1:0.11 | 28 | 11600 | 1.16 |
| Cyclohexane | 500:1:0.11(:500) | 15 | 7200 | 1.15 |
| DMF | 500:1:0.11(:500) | 21 | 10400 | 1.15 |
| Dioxane | 500:1:0.11(:500) | 41 | 20200 | 1.23 |
| Dioxane | 500:1:0.11(:1000) | 35 | 17600 | 1.20 |

[a]The polymerizations were performed at 70 °C for 18 hours. [b]Measured by GPC against polystyrene standards.

To install another alkyne at the ω-terminus, single unit insertion was performed by reacting the isolated PSt (1 equiv.), 2,2′-azobis(2-methylpropionitrile) (AIBN, 0.1 equiv.), and a maleimide carrying propargyl ester (MI-Yne, 3~5 equiv) in a 1,4-dioxane solution at 70°C. This procedure was essentially a RAFT chain extension process that was limited to propagate for only one unit of maleimide, due to its fast kinetics of reacting with a PSt propagating radical center while sluggishness in homopolymerization. The reaction was clean and quantitative, which was evidenced by the disappearance of the benzylic proton (broad) adjacent to trithiocarboante and the rising of a new alkyne proton in $^1$H NMR (Figure 77), as well as narrow GPC traces (Figure 78).

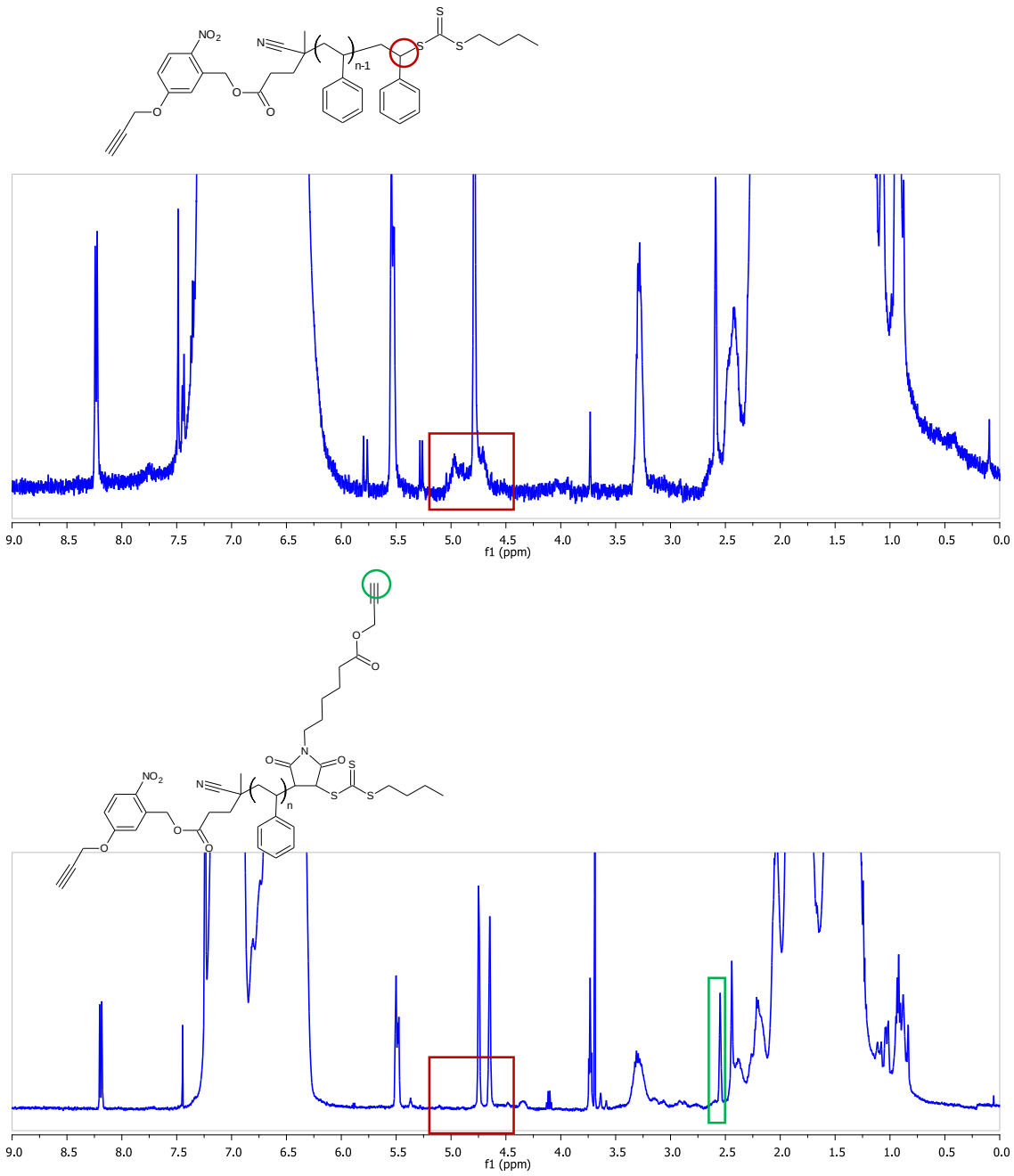


**Figure 77: NMR Characterization of Polystyrene Before and After MI-Yne Insertion.**

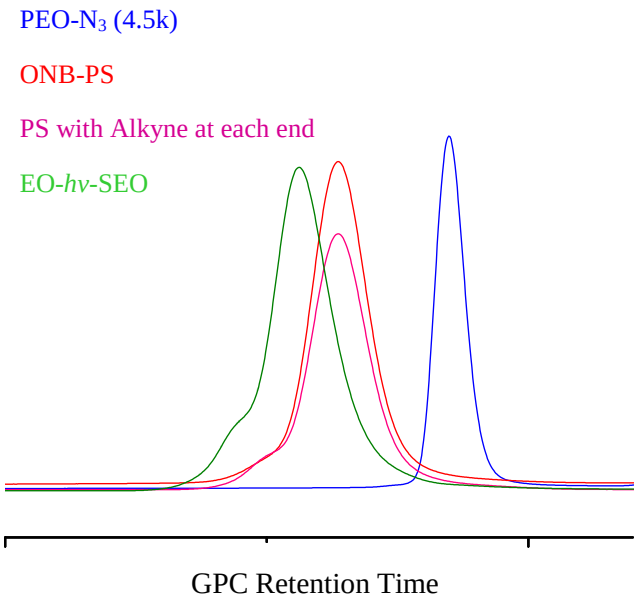


**Figure 78: GPC Traces of PEO, PSt, and EO-*hv*-SEO.**

Finally, Cu(I) catalyzed alkyne-azide cycloaddtion was employed to efficiently link two identical azide terminated poly(ethylene oxide) (PEO) to the alkyne groups at both chain ends of PSt (evidenced by the $^{1}$H NMR in Figure 79), so that a topologically symmetric triblock copolymer was produced. The retained narrow MW distribution measured by GPC (Figure 78) confirmed that side reactions were neglegible. This synthetic protocol provides a general pathway, by which various monomers can be polymerized and the compositions can be easily tuned. It should also be pointed out that different polymer blocks can be attached to each alkyne in the PSt to form asymmetric triblock copolymers, if a "click" reaction is conducted on the α-terminus alkyne before the single unit insertion reaction. This allows the feasibility of achieving more complexed polymer structure and thus brings more versatality to the system.

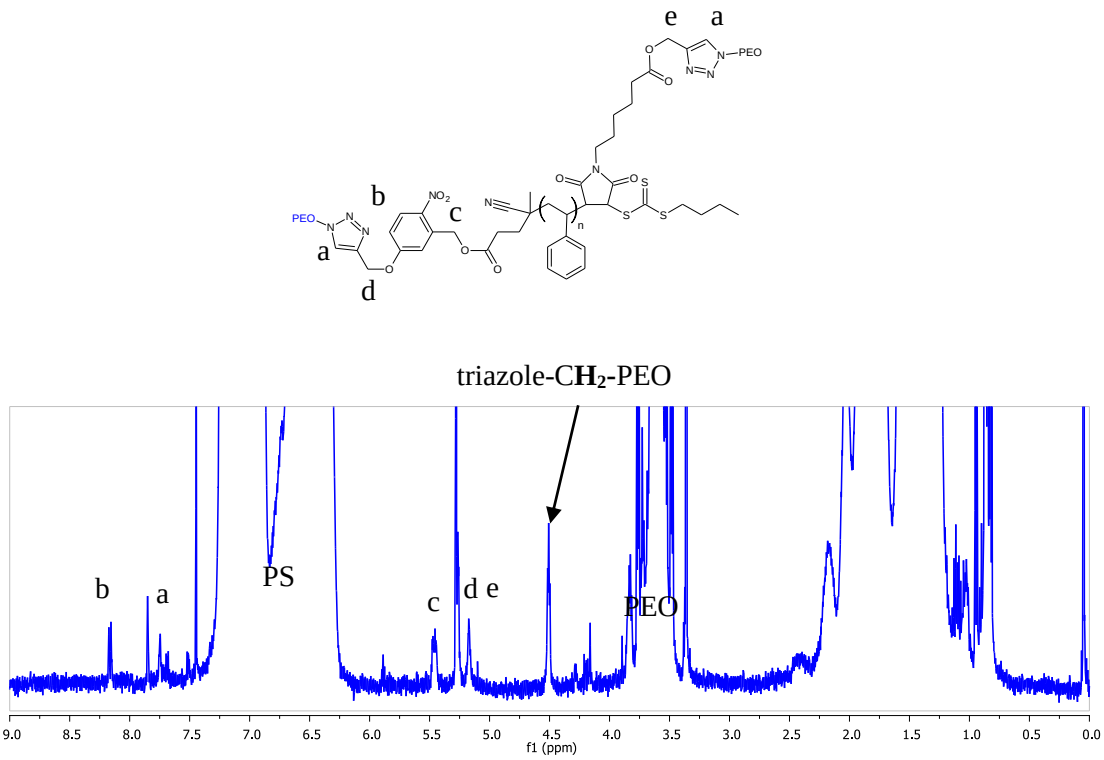


**Figure 79: NMR Characterization of EO-*hv*-SEO.**

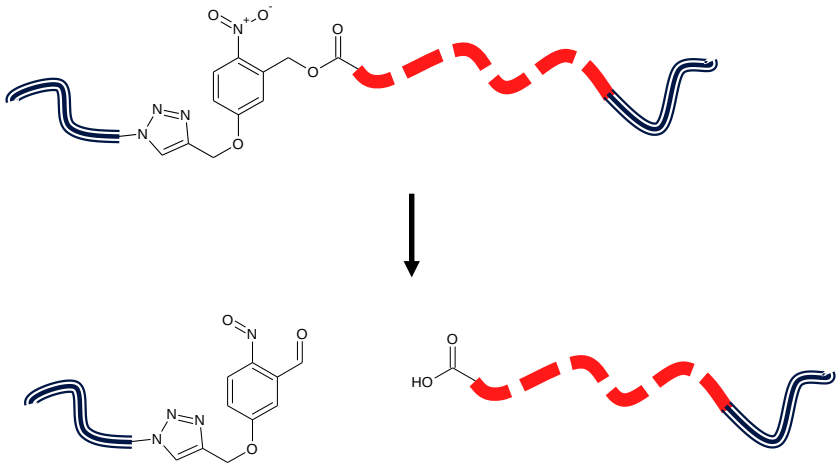


**Figure 80: UV Cleavage Reaction of EO-*hv*-SEO.**

Three BCPs (Table 10) were investigated in this chapter and the BCP thin films were developed using solvent vapor annealing (SVA) and UV exposure. In the first step, EO-*hv*-SEO-1 was spin-coated from toluene solution onto clean silicon wafers. Then, the as-spun films were annealed in a $H_2O$ atmosphere for 1 hour and tetrahydrofuran (THF) for 2 hours, sequentially, to achieve fingerprint patterns shown by Atomic Force Microscopy (AFM, Figure 81). After being exposed to UV light (365 nm) for various time to convert $PEO_{4.5k}$-ONB–$PSt_{27k}$-*b*-$PEO_{4.5k}$ into $PSt_{27k}$-*b*-$PEO_{4.5k}$ and $PEO_{4.5k}$ (Figure 80), these thin films were re-annealed in $H_2O$/THF atmosphere, where the annealing time was previously found to be the key factor for domain orientation.[265] It was found that sequential SVA in $H_2O$ for 1 hour and THF atmosphere for 2 hours is optimal for developing morphology into hexagonal packed cylinders oriented perpendicular to the surface. Grazing-Incident Small Angle X-ray Scattering (GISAXS) was conducted to confirm the domain spacing, which was in excellent agreement with AFM measurements. It was found that the thin film without UV exposure had a domain spacing of 32.1 nm, while the spacing was gradually increased to 35.7 nm with the exposure time extended to 1 hour (Figure 81 and 82). The ~11% increase in spacing was due to two proposed mechanisms. In the first place, the cleavage product $PSt_{27k}$-*b*-$PEO_{4.5k}$ was expected to display a large spacing than the original triblock (which should theoretically possess a spacing more comparable to or slightly larger than that of $PSt_{13.5k}$-*b*-$PEO_{4.5k}$).[200] When the ONB junctions were gradually cleaved, the amount of diblock copolymers in the thin films increased, while the ratio of triblock copolymers decreased. As a consequence the domain spacing was amplified. In addition to the architecture switching from diblock to triblock copolymer, the PEO homopolymer induced swelling could also be an important factor affecting the domain spacing.[266,267] As another product of the UV induced reaction, $PEO_{4.5k}$ was generated in a 1:1 (mol:mol) ratio with $PSt_{27k}$-*b*-$PEO_{4.5k}$, and could swell the PEO domain to enlarge the features to further increased the spacing. After UV treatment, the long range order of the self-assembled thin films was slowly lost, as observed by AFM as well as indicated by the broadened peaks in

GISAXS patterns, which was possible due to UV induced side reactions, such as UV induced crosslinking reactions, as well as broadened MW distribution and inhomogeneous ONB cleavage. It should be noted that the ONB cleaving efficiency was not quantitative, since 1:1 (mol:mol) mixture of PEO and PSt-*b*-PEO usually displays macrophase separated morphologies, which was not observed at such extent of UV treatment. Extended exposure time failed to further increase the spacing, and even a slight reduction was observed (34.4 nm for 2 hours exposure), which is presumably attributed to that only fractional ONB junctions resulted in PEO/PSt-*b*-PEO upon UV cleavage. Although it remain unclear, we suspect that this might be due to UV induced homolysis at the trithiocarbonate sites and radicals were generated at PSt chain ends.[268,269] The formed radicals could couple with *o*-nitrosobenzaldehyde groups to give $(PEO_{4.5k})_2$-$PSt_{27k}$ miktoarm copolymer (Figure 83), which is expected to show a spacing smaller than that of $PEO_{4.5k}$-*b*-$PSt_{27k}$.[259]

**Table 10: List of EO-*hv*-SEOs Investigated.**

| # | PSt MW[a] (kg/mol) | $Đ_{PSt}$[b] | PEO MW[a] (kg/mol) | $Đ_{PEO}$[b] | $Đ_{BCP}$[b] |
|---|---|---|---|---|---|
| 1 | 27 | 1.14 | 4.5 | 1.05 | 1.17 |
| 2 | 49 | 1.15 | 6.7 | 1.10 | 1.33 |
| 3 | 76 | 1.22 | 6.7 | 1.10 | 1.28 |

[a]The MWs of PSt and PEO were determined by GPC and NMR, respectively. [b]The Đs of the PSt block, PEO block, and overall BCP were measured by GPC against polystyrene standards.

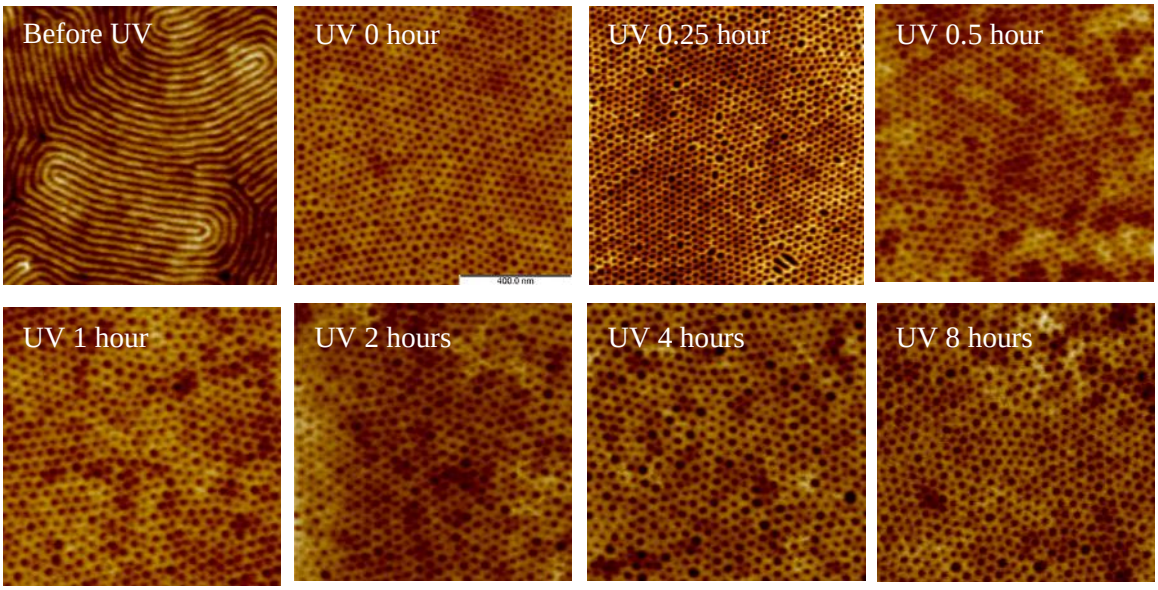


**Figure 81: AFM Height Images of EO-*hv*-SEO-1 Thin Films.**

**The size of the images are 1 µm * 1 µm.**

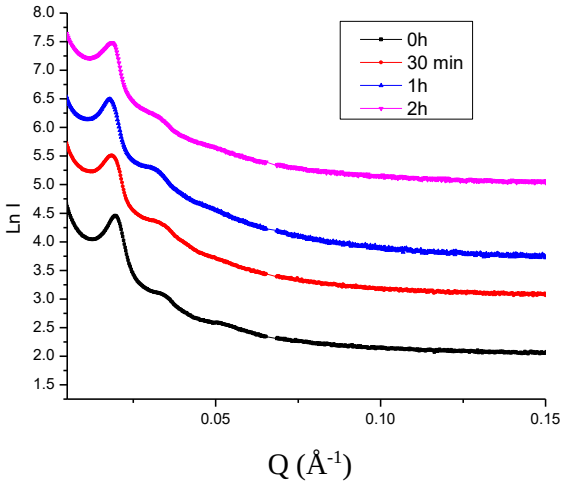


**Figure 82: Azimuthally Integrated GISAXS Profiles of EO-*hv*-SEO-1 Thin Films.**

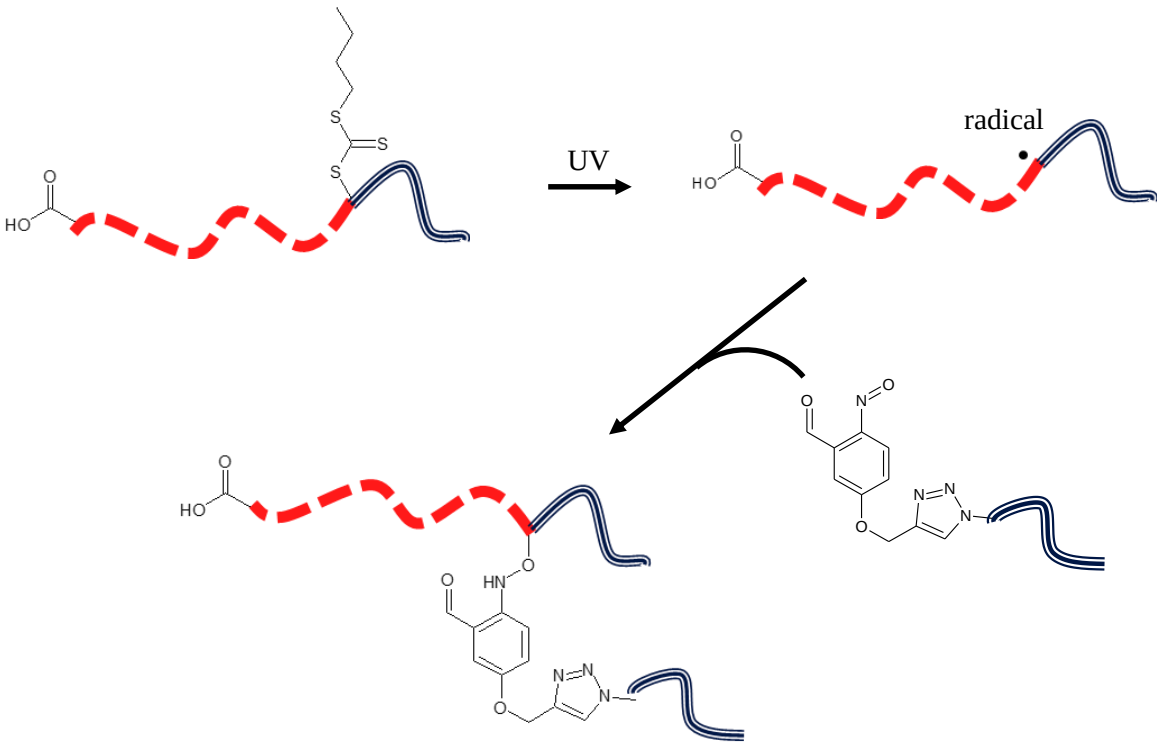


**Figure 83: Proposed Side Reactions during UV Exposure.**

On EO-*hv*-SEO-2 thin films, the spacing was increased by 21% (from 33.9 nm to 40.9 nm), when the UV treatment was applied for 1 hour, while the spacing experienced no further enhancement with extended exposure. The results are presented in Figure 84 and Figure 85.

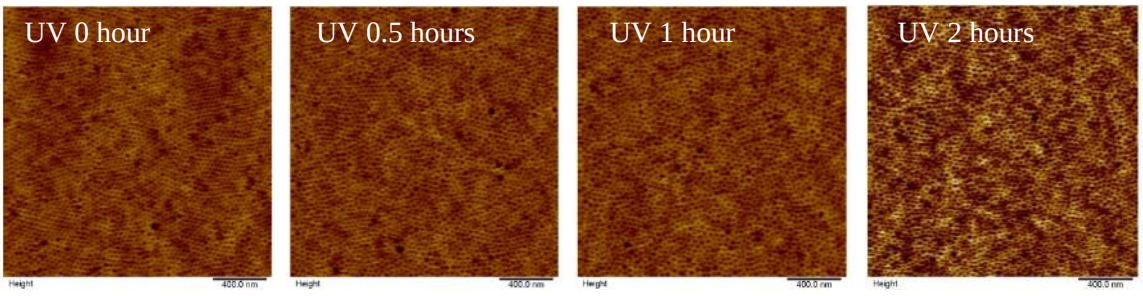


**Figure 84: AFM Height Images of EO-*hv*-SEO-2 Thin Films.**

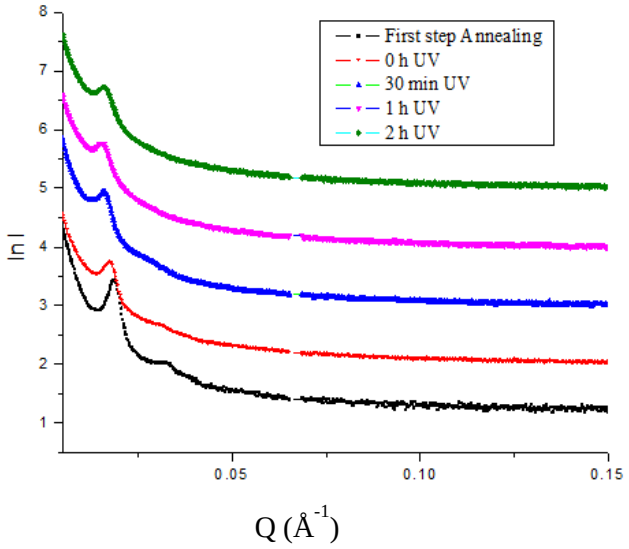


**Figure 85: Azimuthally Integrated GISAXS Profiles of EO-*hv*-SEO-2 Thin Films.**

The thin film of EO-*hv*-SEO-3 showed a nanopattern consisting of dots, after SVA with $H_2O$/THF. However, based on the composition ($f_{PEO}$ = 12% in bulk material), it is more likely that the pattern consisted of spherical arrays instead of perpendicular cylinders. After the standard procedure of UV exposure and SVA, it was found that the spacing was increased from 39.6 nm to 44.9 nm, 47.6 nm, 49.1 nm, and 51.7 nm after UV treatment for 1, 2, 4, and 8 hours, respectively (Figure 86 and Figure 87). By comparing the maximum spacing increase in the three BCPs (11%, 21%, and 31% respectively), it was found that more significant change could be achieved in higher MW samples. The cause of this trend is possibly due to the higher MW leading to dilution of ONB junctions at the PEO/PSt interface, and thus reduced chance of the side reaction involving trithiocarbonate and nitroso groups to suppress spacing increase.

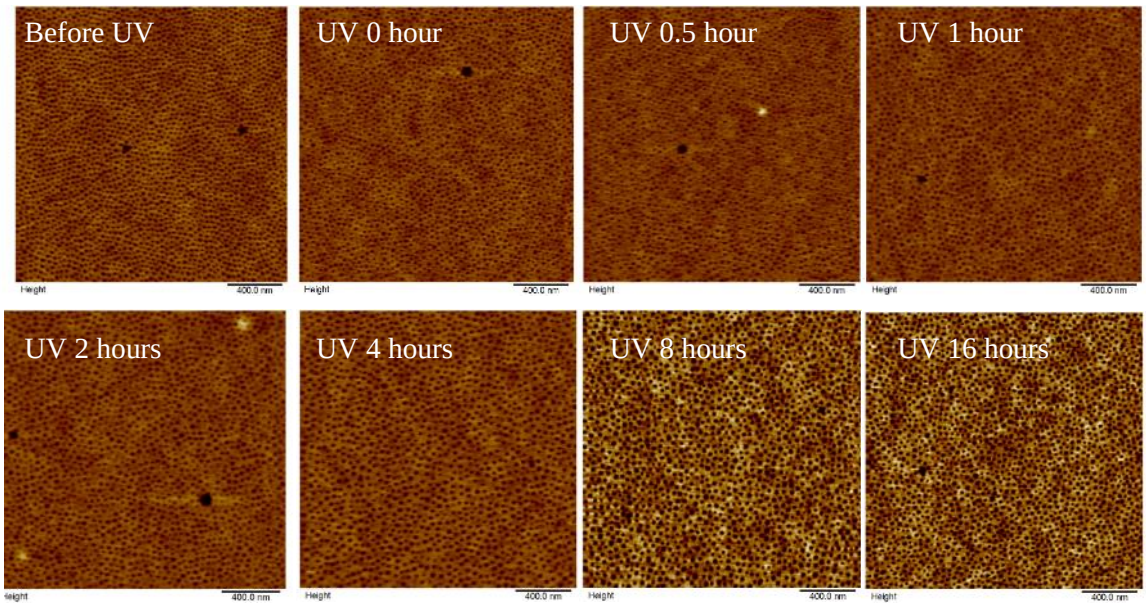


**Figure 86: AFM Height Images of EO-*hv*-SEO-3 Thin Films.**

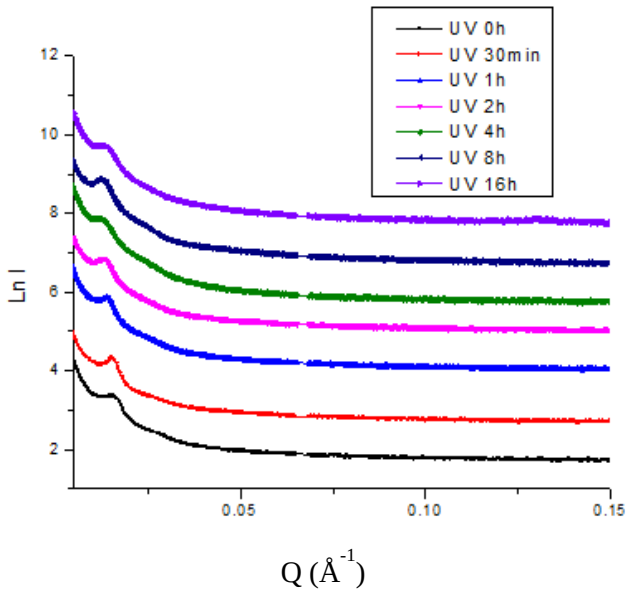


**Figure 87: Azimuthally Integrated GISAXS Profiles of EO-*hv*-SEO-3 Thin Films.**

To demonstrate the spacing change mechanism(s), the effect of UV exposure on $PSt_{19k}$-*b*-$PEO_{6.7k}$ without ONB junction was investigated. It was found that after 0~2 hours UV treatment and sequential SVA process, the domain spacing was almost constant at ~34 nm (Figure 88 and

89). This confirms that the reaction on the ONB junction was the key to achieving tunable d-spacing, and random degradation along the polymer backbone was absent.

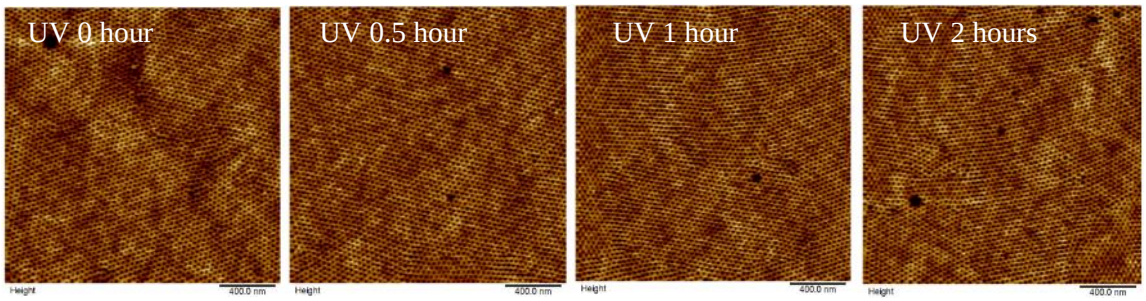


**Figure 88: AFM Height Images of $PSt_{19k}$-*b*-$PEO_{6.7k}$ Thin Films.**

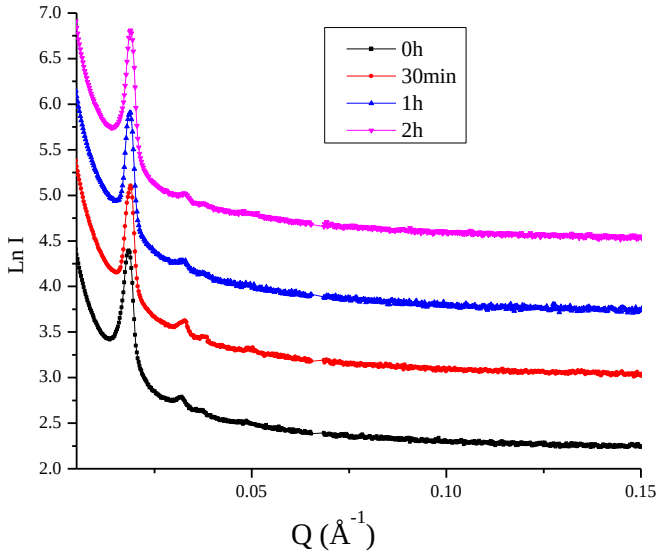


**Figure 89: Azimuthally Integrated GISAXS Profiles of $PSt_{19k}$-*b*-$PEO_{6.7k}$ Thin Films.**

In order to further understand the contribution from both the architectural change and homopolymer swelling mechanisms to the spacing increase, comparison experiments were conducted on EO-*hv*-SEO-3 thin films. The UV exposed EO-*hv*-SEO-3 films were immersed in ethanol to extract the cleaved PEO homopolymer, before being treated by SVA with $H_2O$/THF to develop to nanopattern. This time, it was observed that the spacing was raised from 37.2 nm to 37.4

nm, 40.3 nm, 41.6 nm, and 42.6 nm after 1, 2, 4, and 8 hours UV exposure (Figure 90 and Figure 91). After that, no sign of further increase was observed in the domain spacing. It demonstrates that, indeed, the cleaved diblock displayed a larger spacing than the original triblock as predicted by theory. Since the ethanol extraction process suppressed the spacing increase, it also proves that, beside the change in polymer architecture, the cleaved PEO homopolymer has a critical contribution to spacing increase as well. Based on the spacing enhancement in the two parallel experiments, it was found these two influences were contributing on a comparable level, at least in this case, to the d-spacing increase.

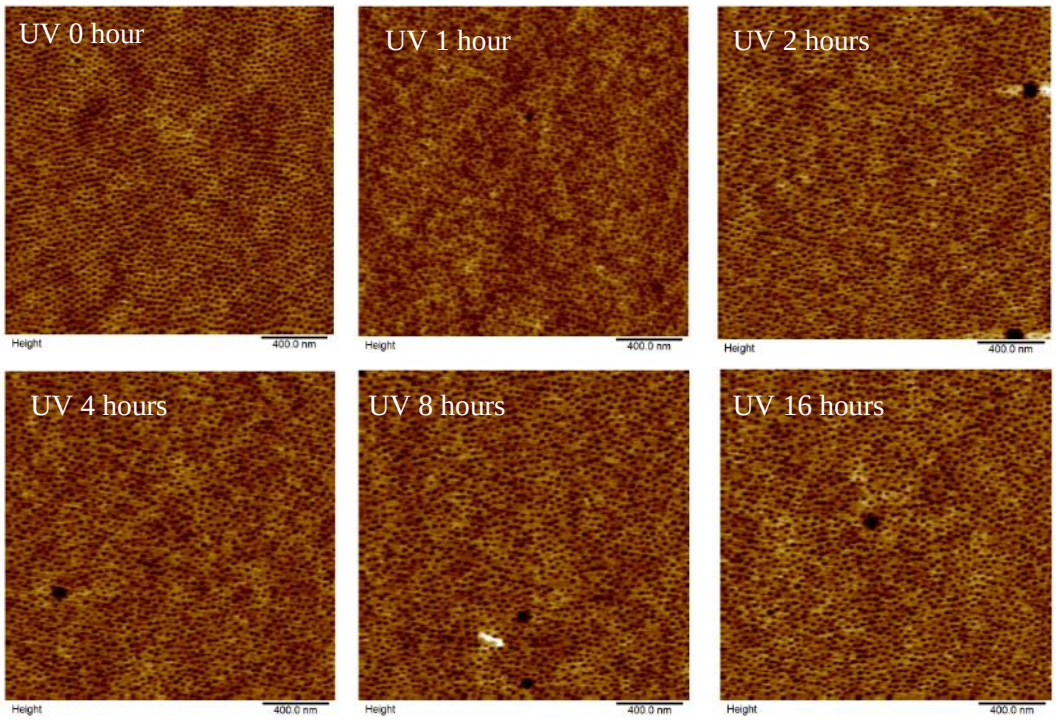


**Figure 90: AFM Height Images of EO-*hv*-SEO-3 Thin Films with PEO Removed.**

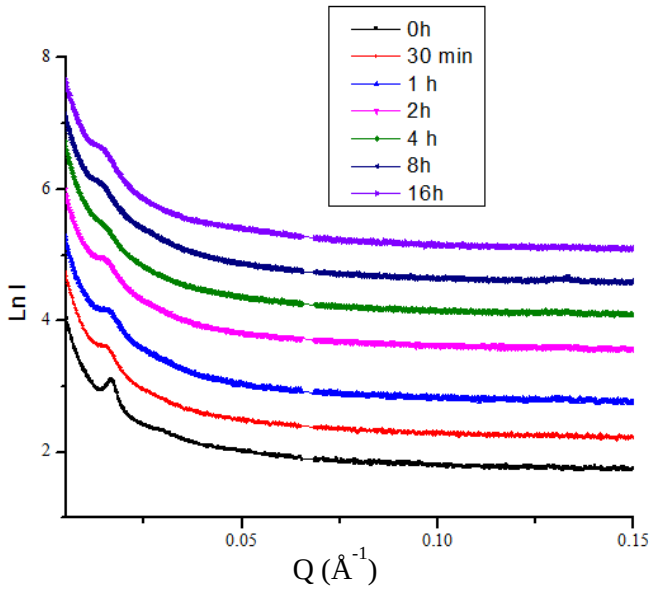


**Figure 91: GISAXS Profiles of EO-*hv*-SEO-3 Thin Films with PEO Removed.**

Given the responsiveness of these materials to UV, we sought to demonstrate the concept of fabricating hierarchical patterns (Figure 92). A thin film of EO-*hv*-SEO-1, prepared by spin-coating and SVA, was exposed to UV for 2 hours, with the left half of the sample being covered by a photo mask. After the second SVA treatment, nanodots were achieved with the spacing being determined to be 32 and 36 nm for the left and right halves, respectively. The spacing values were in good agreement with our previous results achieved on unmasked film, indicating good reproducibility. This experiment demonstrates the opportunity of combining photolithography and ONB containing BCPs to spatially control the placement of two distinctly sized features. It is also possible to achieve multiple domain spacings by simply applying carefully determined UV exposures to selected areas.

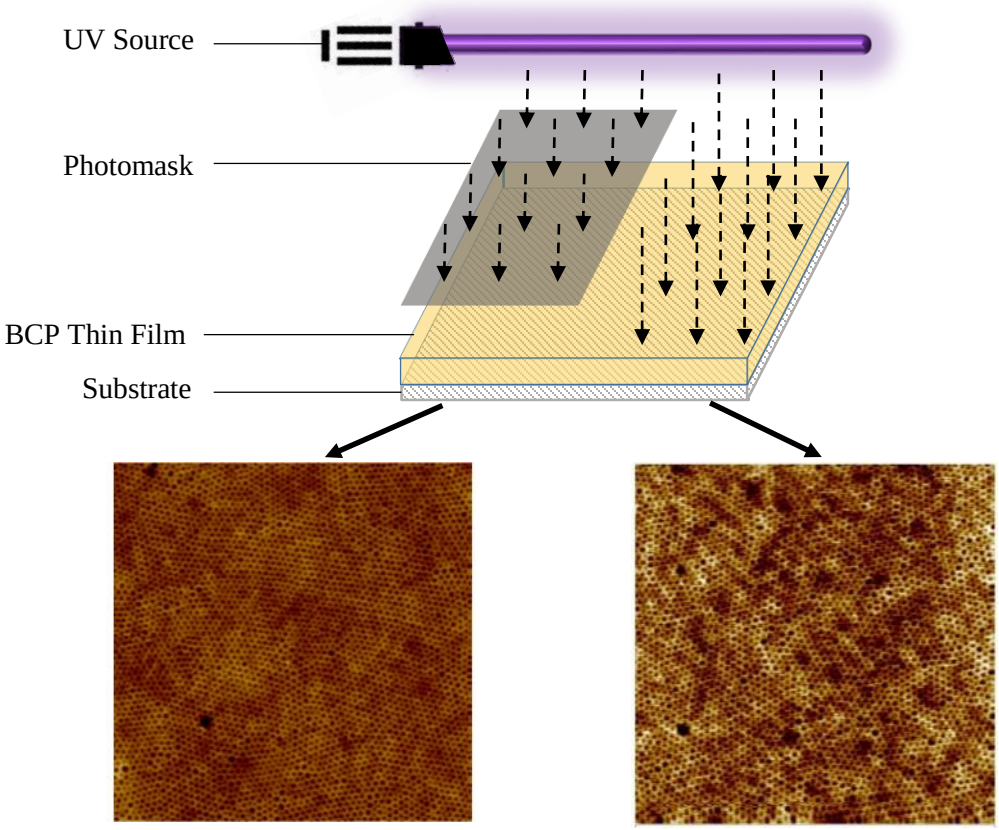


**Figure 92: Hierarchical Pattern Fabrication by Regional UV Exposure.**

**The sizes of the AFM images are 2 μm * 2 μm.**

### 6.4 Conclusions

In conclusion, a series of triblock copolymers with an ONB junction is reported in this work. Well-defined PEO-ONB-PSt-*b*-PEO triBCPs were successfully synthesized by sequential RAFT polymerization, single maleimide unit insertion, and Cu(I) catalyzed "click" chemistry. Polymer thin films, developed by SVA-UV exposure-SVA process, displayed domain spacings that can be conveniently tuned by varying exposure time. The most significant spacing increase achieved in this work was ~30%. The spacing increase was a result of both polymer architectural change and homopolymer induced swelling, caused by the photocleavage at the ONB junction.

This BCP design provides opportunities for the fabrication of thin films with tunable domain spacings in spatially controlled regions. We also suggest that by doing an additional step of "click" reaction during the polymer synthesis, it is possible to introduce more components into the system for fabrication of more complexed hierarchical pattern, for example ABA' and ABC triblock copolymers.

# CHAPTER 7

# FUNCTIONAL RAFT AGENTS: SYNTHESIS BY SINGLE MONOMER INSERTION AND CONTROLLED POLYMERIZATION

## 7.1 Introduction

Reversible Addition-Fragmentation Chain Transfer Radical Polymerization /Macromolecular Design by Interchange of Xanthates (RAFT/MADIX) polymerization has been widely used in polymer synthesis due to its mild reaction conditions and excellent tolerance to functionalities. In the polymerization mechanism, the key molecule is a highly efficient chain transfer agent (CTA), which undergoes rapid reversible switching between polymer chain ends.[134] The fast chain transfer reaction averages the number of monomers added to each chain and thus enables the production of polymer chains with similar lengths. The chain transfer rate is primarily controlled by the structure of the thioester groups, in other word, the identities of trithiocarbonate, dithiobenzoate, xanthate, etc. However, careful selection of the leaving groups in CTAs is also very important for efficient chain transfer reactions, otherwise it may result in partial initiation and thus a broad MW distribution.

Relative easy incorporation of functionalities to polymer chain terminus is another advantage of the RAFT/MADIX technique.[270] It can provide precise control over not only the identities but also the positions of the functionalities in the resulting polymers. This often requires sophisticated design of RAFT CTAs. The functional groups can be introduced into either the leaving group or the Z group, resulting in α- or ω-end functionalized polymers, respectively. However, more often the α-terminus is preferable in functionalization, because the ω-end group can be easily cleaved due to the labile nature of thioesters.[271–274]

One popular method to introduce functionalities is by esterification or amidification reactions.[74,169,275–277] Thanks to the tremendous advancement in mild and high efficient synthesis in ester and amide bonds, numerous CTAs were synthesized by coupling the carboxylic acid group with hydroxyl or amine linked functional groups. However, ester and amide linkages are not always preferable. One reason may be that they are readily hydrolyzable. Another widely adopted method is to use nucleophilic substitution of nucleophilic thio-compound towards functional benzyl halide.[278] For example, the bromomethylphenyl group attached to terpyridine was substituted with thiourea and then converted into dithiobenzoate. This CTA was used to synthesize terpyridine functionalized polymers, and the polymers can be linked together via the coordination between terpyridine and ruthenium cation.[279] Alkoxysilyl functionalized benzyl halides were substituted by trithiocarbonate salt, and were used in surface functionalization.[280,281] Substituting α,α'-dibromo-*p*-xylene (DXB) yielded symmetric CTA, which were applied to synthesize symmetric (co)polymers.[132,282–284] Multifunctional CTAs can be simply prepared by substituting the core molecule carrying multiple benzyl halide groups, which were used in star-like polymer synthesis.[75,285,286] Vinylbenzyl imidazole dithiobenzoate were reported in branched polymer synthesis,[287] while silylbenzyl trithiocarbonate was used for facile end-group analysis.[288] An alkoxyamine-benzyl chloride was reacted with trithiocarbonate to synthesize NMP/RAFT dual functional initiator/CTA.[289] Chloromethylbenzyl alcohol can be reacted to install thioesters in the first step, and a variety of chemistries were conducted on the hydroxyl group for further functionalization.[290–293] In addition, remarkable work in literature was put forth into desymmetrization reactions of α,α'-dibromo-*p*-xylene (DBX) or similar molecules. DBX was mono-substituted to form organic salts, such as ammonium and phosphonium.[294–298] These synthetic efforts were facilitated by the significantly different solubility of monocationic, dicationic, and non-cationic species in organic solvents. As for non-ionic molecules, they can be isolated with more careful procedures. A large amount of DBX was used to ensure the mono-substitution product

being obtained in good yields. In one report, DBX was mono-substituted by alcohols, and then the remaining benzyl bromide was substituted by various thioacid salts.[299,300] The polymerization was carefully investigated and the norbornene (NBE) linked polymers were subjected to thiol-ene and tetrazine-NBE reactions for further functionalization.[301] However, relatively broad MW distribution (Đ~1.3) were achieved and sometimes reduced end-group efficiency was observed.

To broaden the library of RAFT CTA synthesis methodologies, herein we adopt the single monomer insertion technique to take advantage of the enormous availability of various commercial or synthetic styrenic monomers. High efficient single monomer insertion of several functional styrenic molecules is performed on a basic RAFT CTA, to prepare functional CTAs in excellent yields. This highly efficient technique was recently discovered as the selective initiation phenomenon in RAFT polymerization.[302–306] However, it had been scarcely explored in CTA synthesis. Diphenylanthracenyl with two vinyl groups was reacted with 2 equivalents of 2-cyano-2-propyl dithiobenzoate in the presence of catalytic AIBN, the product of which was isolated in high yield and mediated the synthesis of narrowly dispersed poly(acenaphthylene)s with a diphenylanthracenyl group in the middle of the chain.[307] Perylene diimide, poly(3-hexyl thiophene),[58] and coumarin[308] based RAFT CTAs were synthesized in a similar manner. A RAFT CTA based on 4-tert-butoxystyrene was synthesized and applied in mediating styrene (St) polymerization to achieve phenol terminated polymer after hydrolysis.[309] In addition, it was found that after the insertion of a single styrene monomer, an isopropylacrylamide can be sequentially added.[310] Another drawback is that no detailed discussion on the controlled polymerization was present in the literature, as far as we are aware. The efficiency in RAFT polymerization was analyzed on representative monomers by synthesizing end functionalized (co)polymers. Multiblock copolymers and graft copolymer were synthesized by end-group transformation.

## 7.2 Experimental Section

### 7.2.1 Materials

Styrene (St), *n*-butyl acrylate (nBA), *t*-butylstyrene (tBS), 2-vinylpyridine (2VP), 4-chlomethylstyrene (4CMS), divinylbenzene (DVB, mixture of *para*- and *meta*- isomers), vinyl acetate (VAc), and isoprene were passed through a short column of basic alumina and stored under -30 $^{o}$C before use. N-Isopropylacrylamide (NIPAAm) and 2,2'-Azobis(2-methylpropionitrile) (AIBN) were recrystallized from hexanes and MeOH, respectively. Dried ethyl acetate was stirred over $MgSO_4$ for at least 48 hours before being used. The acid functionalized RAFT agents, 4-cyano-4-[(butylsulfanylthiocarbonyl)sulfanyl]pentanoic acid (COOH-CTA), and benzyl *n*-butyl trithiocarbonate were synthesized using reported synthetic protocols.[132,210] Alkyne and azide terminated PEOs were synthesized using previously reported methods.[261,311] Other chemicals were used as received.

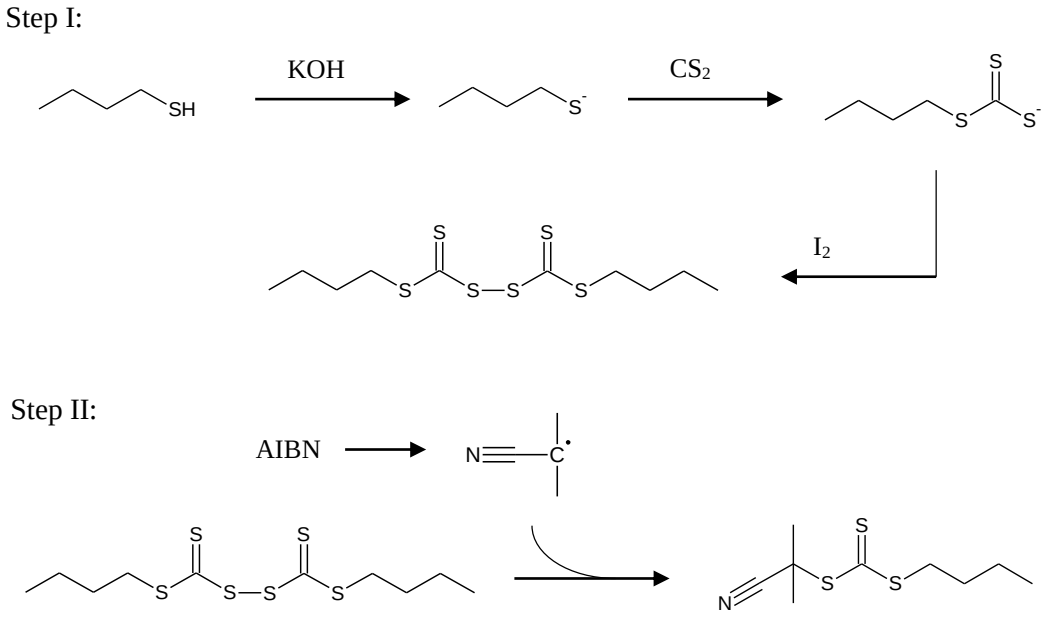


**Figure 93: Synthetic Protocol of O-CTA.**

### 7.2.2 Synthesis of 2-Cyano-2-propyl butyl trithiocarbonate

The base RAFT agent, 2-Cyano-2-propyl butyl trithiocarbonate (O-CTA), was synthesized using a previously reported protocol and scaled up to a larger batch.[210,312,313] The synthetic protocol is shown in Figure 93.

In the first step, 16.5 mL n-butanethiol was added into a conical flask containing 50 mL $H_2O$ and 100 mL diethyl ether. Then, 9.01 g KOH in pellet form was gradually added during a period of 20 minutes, and mixture was stirred for another 10 minutes. When 15 mL carbon disulfide was added dropwise into the stirring phase-separated liquid mixture, the top organic layer slowly turned yellow. One hour later, 21.02 g elementary iodine was added in portions (~1g), and the organic layer became reddish yellow first and then turned dark. The reaction was kept for another hour and quenched by adding ~4 g sodium ascorbate to reduce iodine to non-toxic iodide. The reddish yellow organic layer was diluted with 100 mL diethyl ether and washed with 200 mL deionized water four times. Removing diethyl ether by rotary evaporation resulted in bis(butylsulfanylthiocarbonyl) disulfide.

The product was used directly in the second step without further purification. In a Schlenk flask was added the disulfide compound as well as 16.4 g crude AIBN and 100 mL ethyl acetate. The mixture, was degassed nitrogen purge for 20 minutes and then sealed by a rubber septum, before being heated at 80 $^{o}$C to initiate the reaction. (Be careful: large amount of nitrogen can be produced during this reaction.) A needle was left in the septum to balance the pressure. After 48 hours, the mixture was filtrated and concentrated. Column chromatography was used to isolate O-CTA (31.2 g, yield = 74%). The structure was confirmed by $^{1}$H NMR (Figure 94).

$^1$H NMR

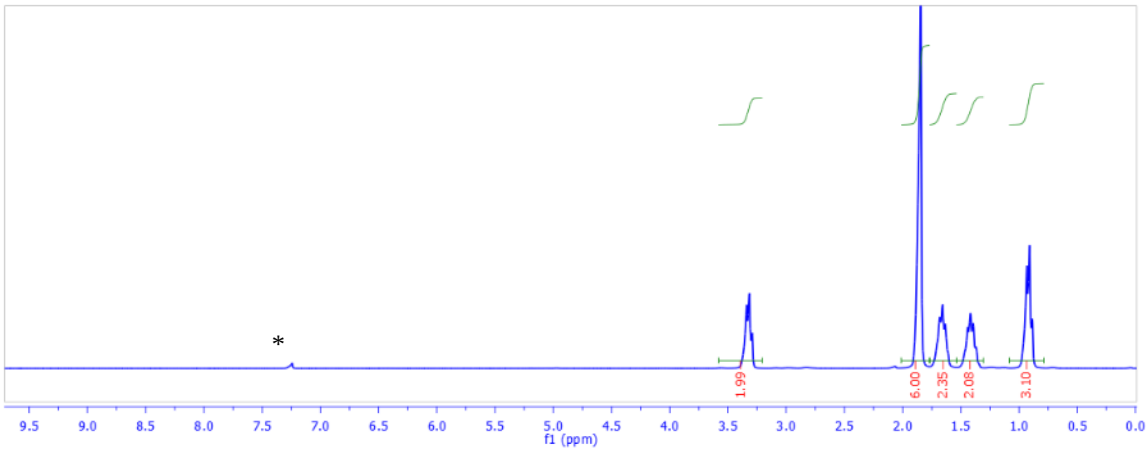


**Figure 94: $^1$H NMR of O-CTA.**

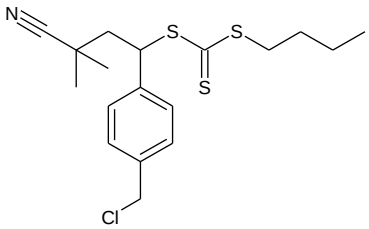


$^1$H NMR

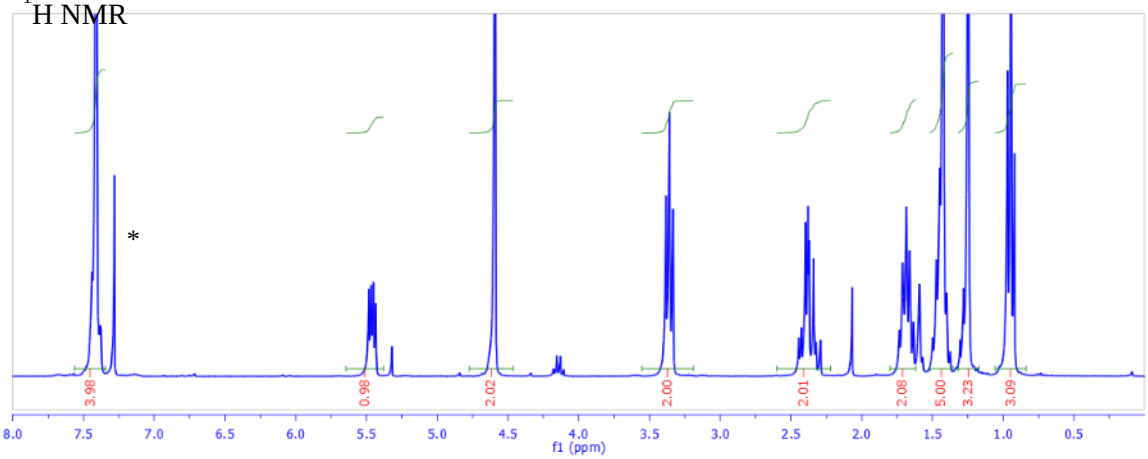

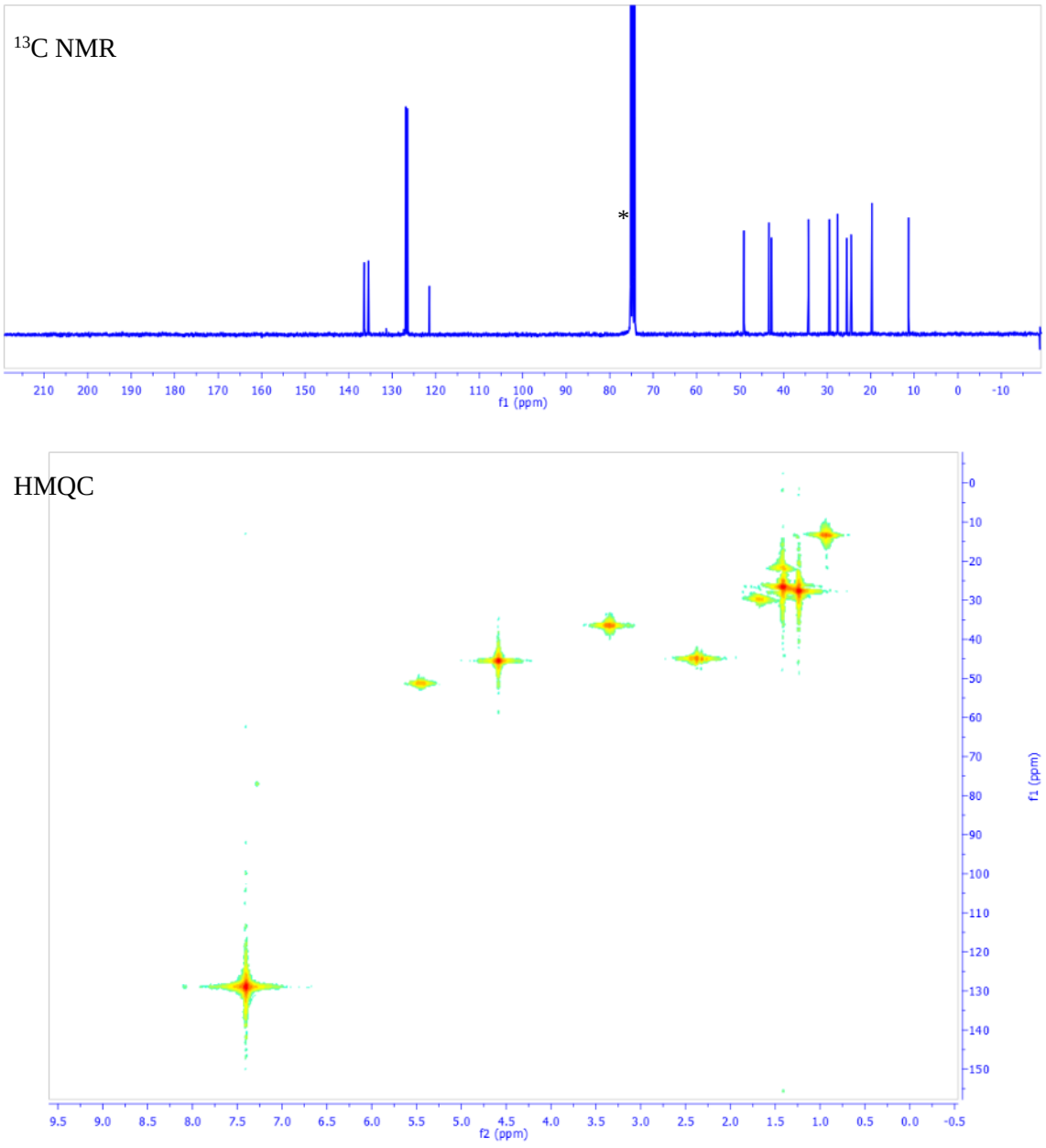


**Figure 95: Chemical Structure and NMR Characterization of Cl-CTA.**

### 7.2.3 Synthesis of Benzyl Chloride Functionalized CTA

In a reaction vessel, 1.581 g 4CMS was mixed with 2.338 g O-CTA, 152 mg AIBN, and 6 mL ethyl acetate. The yellow solution was degassed by purging with nitrogen for 30 minutes and

then sealed with a rubber septum before being heated to 70 °C. (Be careful: a significant amount of nitrogen can be produced and a needle was plugged to balance the pressure.) After 48 hours, the solution was concentrated and subject to column chromatography using hexanes: ethyl acetate = 20:1 (v:v) as the eluent to yield a yellow oil with high viscosity as the product Cl-CTA (3.50 g, yield = 90%). The chemical structure was confirmed by NMR (Figure 95) and MS (Theoretical 385.1, ES-MS 385.1 for M+).

### 7.2.4 Synthesis of Telechelic CTA from Divinylbenzene

In a reaction vessel, 0.28 g divinylbenzene (DVB) was mixed with 1 g O-CTA, 138 mg AIBN, and 3 mL ethyl acetate. The yellow solution was degassed by purging nitrogen for 20 minutes and then sealed with a rubber septum before being heated to 70 °C. (Be careful: a significant amount of nitrogen can be produced.) A needle was left in the septum to balance the pressure. After 48 hours, the solution was concentrated and subject to column chromatography using hexanes: ethyl acetate = 10:1 (v:v) as the eluent to yield a yellow oil with high viscosity as the product DVB-CTA (1.14 g, yield = 88%). The chemical structure was confirmed by NMR (Figure 96) and MS (Theoretical 596.2, FAB-MS 597.3 for M+H, EI-MS 596.4 for M+).

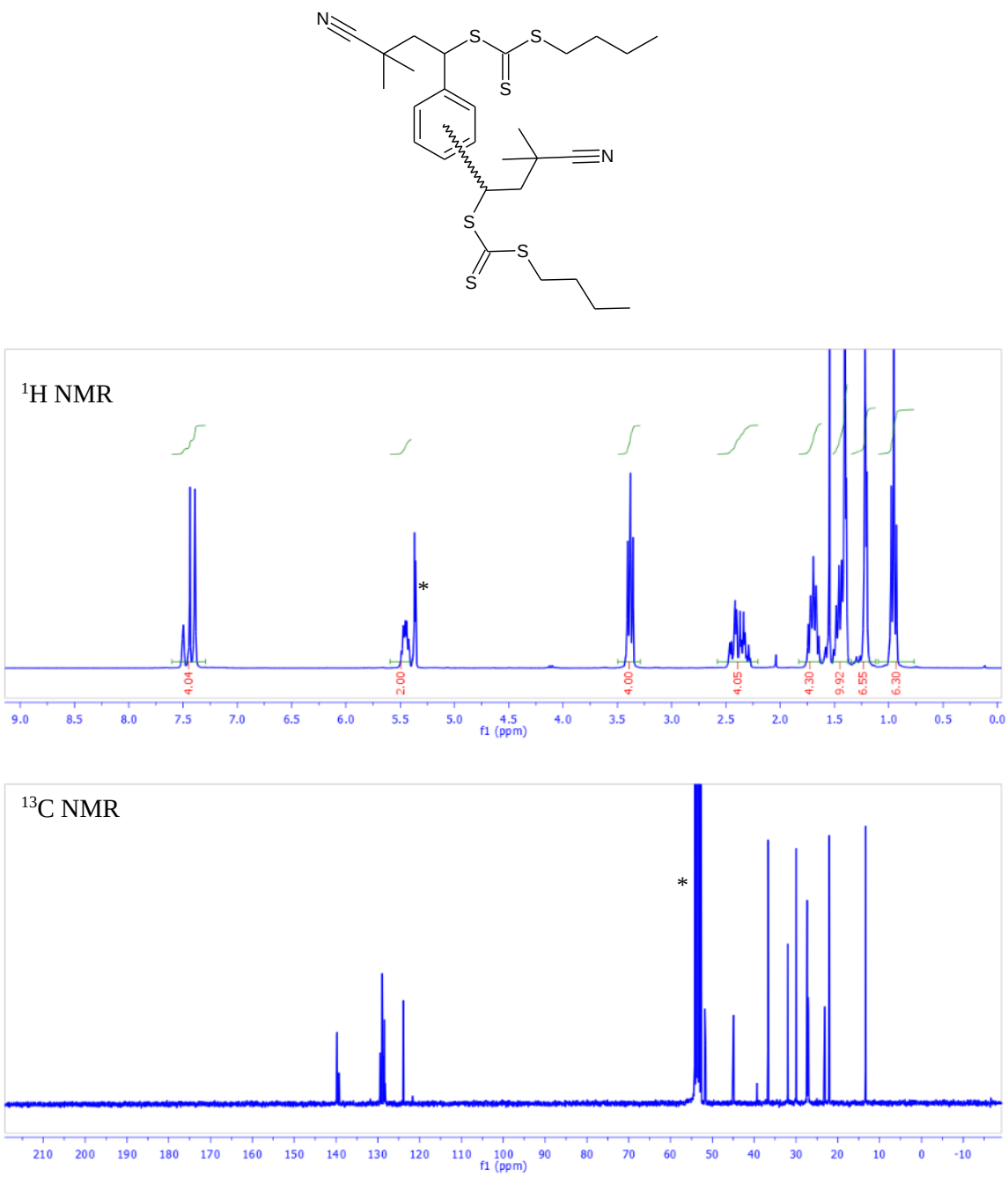


**Figure 96: Chemical Structure and NMR Characterization of DVB-CTA.**

### 7.2.5 Synthesis of Pentafluorophenyl Functionalized CTA

Pentafluorophenyl vinylbenzyl ether (StF5) was synthesized using a reported method, as proved by $^{1}$H NMR (Figure 97).[314]

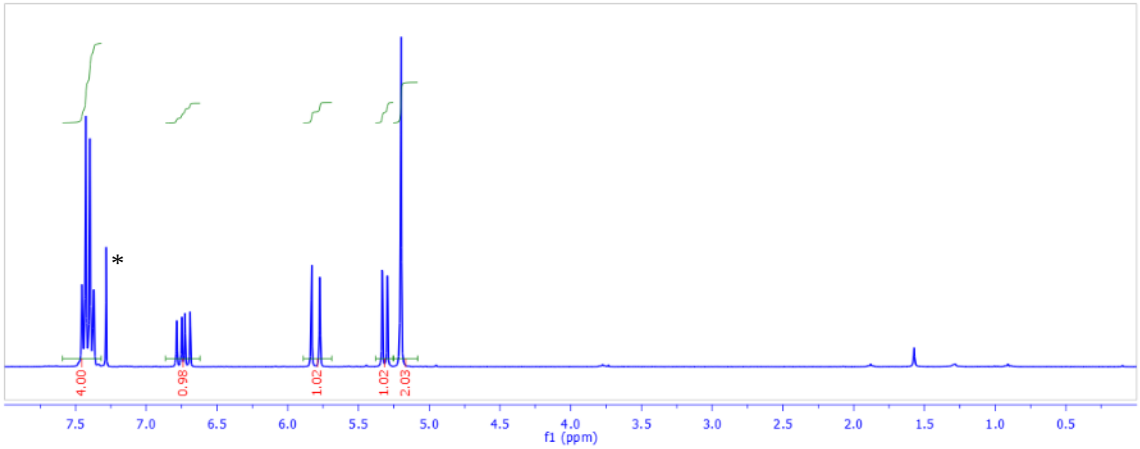


**Figure 97: $^{1}$H NMR Characterization of F5-CTA.**

In a reaction vessel, 2.30 g StF5 was mixed with 1.91 g O-CTA, 150 mg AIBN, and 10 mL dried ethyl acetate. The yellow solution was degassed by purging nitrogen for 20 minutes and then sealed with a rubber septum before being heated to 70 $^{o}$C. (Be careful: a significant amount of nitrogen can be produced.) A needle was left in the septum to balance the pressure. After 48 hours, the solution was concentrated and subject to column chromatography using hexanes: ethyl acetate = 5:1 (v:v) as the eluent to yield a yellow oil with high viscosity as the product F5-CTA (3.67g, yield = 90%). The chemical structure was confirmed by NMR (Figure 98) and MS (Theoretical 533.09, FAB-MS 534.10 for M+H). It was observed that affected spin-spin coupling with fluorine atoms, the signals of carbon atoms on the pentafluorophenyl ring splitted into multiplets.

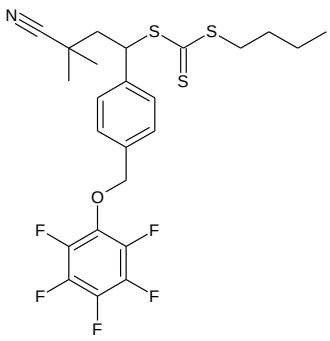
N
S
S
S
O
F
F
F
F
F

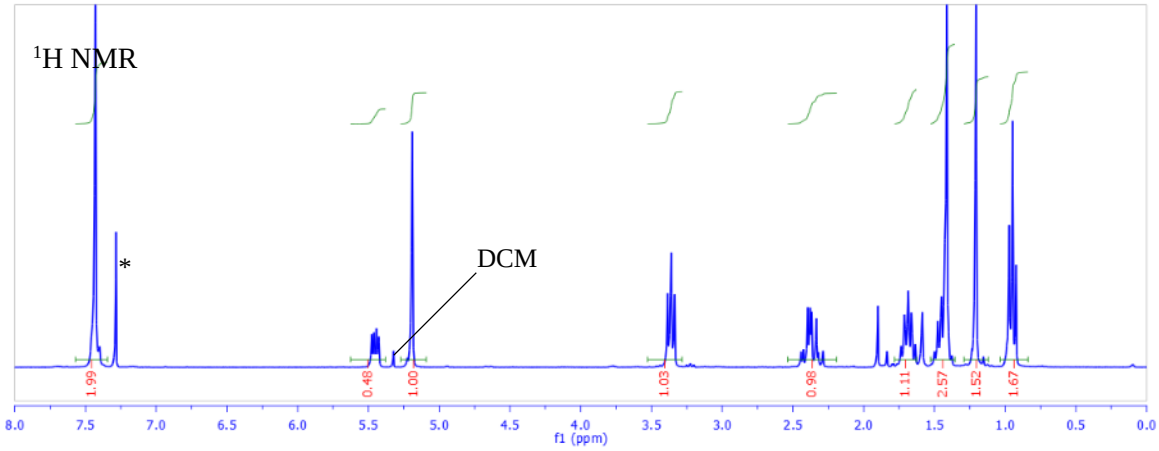
1H NMR
*
DCM
1.99
0.48
1.00
1.03
0.98
1.11
2.57
1.52
1.67
8.0
7.5
7.0
6.5
6.0
5.5
5.0
4.5
4.0
3.5
3.0
2.5
2.0
1.5
1.0
0.5
0.0
f1 (ppm)

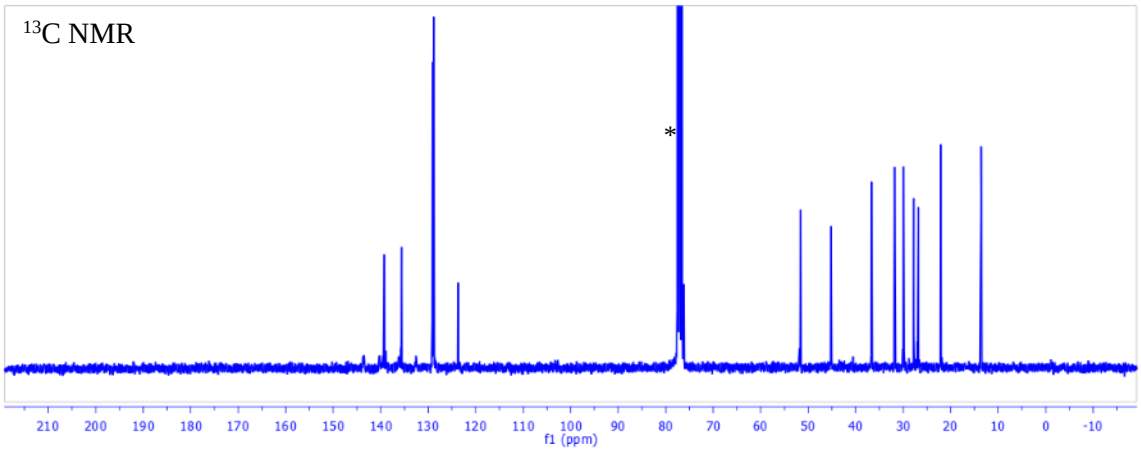
$^{13}$C NMR
*
210 200 190 180 170 160 150 140 130 120 110 100 90 80 70 60 50 40 30 20 10 0 -10
f1 (ppm)

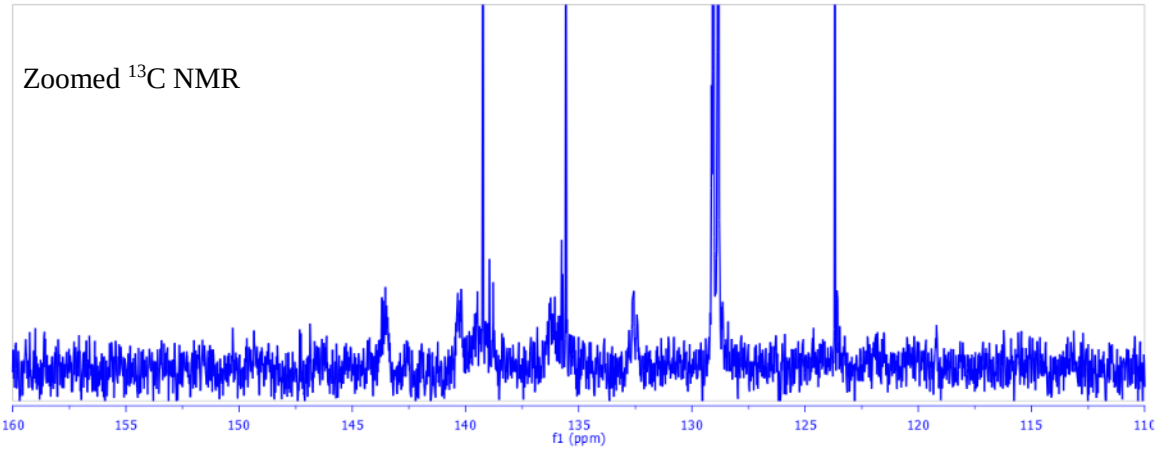
Zoomed $^{13}$C NMR
160 155 150 145 140 135 130 125 120 115
f1 (ppm)

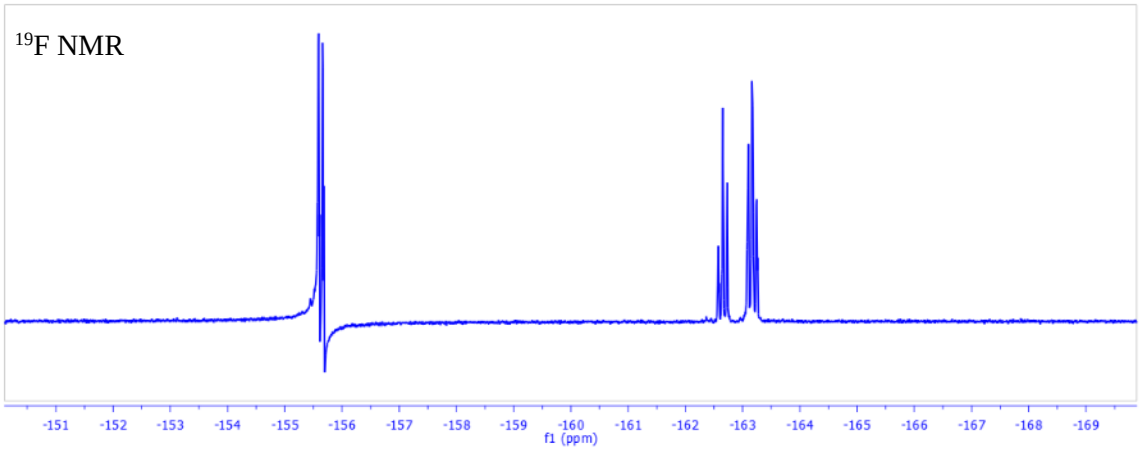
$^{19}$F NMR
-151 -152 -153 -154 -155 -156 -157 -158 -159 -160 -161 -162 -163 -164 -165 -166 -167 -168 -169
f1 (ppm)

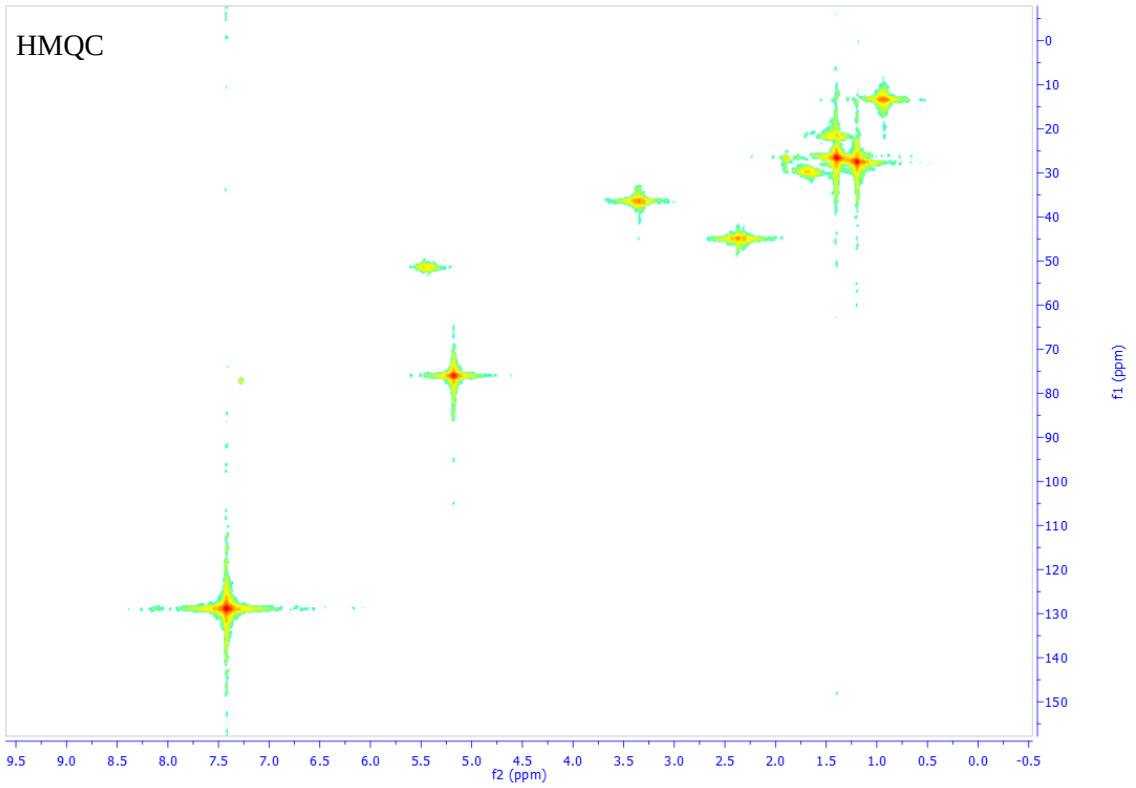


**Figure 98: Chemical Structure and NMR Characterization of F5-CTA.**

### 7.2.6 Synthesis of Alkyne Functionalized CTAs

Two version of alkyne functionalized CTAs were synthesized.

The first one was synthesized via Steglich esterification. At 0 °C, 850 mg propargyl alcohol, 2.03 g COOH-CTA, and 87 mg 4-dimethylaminopyridine (DMAP) were dissolved in 20 mL dichloromethane. To the stirring mixture, 1.71 g N,N'-Dicyclohexylcarbodiimide (DCC) was slowly added. The reaction was allowed to run overnight and then cooled down to -30 °C before being filtrated to remove dicyclohexyl urea. The concentrated mixture was purified using column chromatography (hexanes:ethyl acetate = 5:1, v:v) to obtain a reddish yellow oil as the product, Yne-Ester-CTA (1.99 g, yield = 87%). The chemical structure was confirmed by NMR (Figure 99).

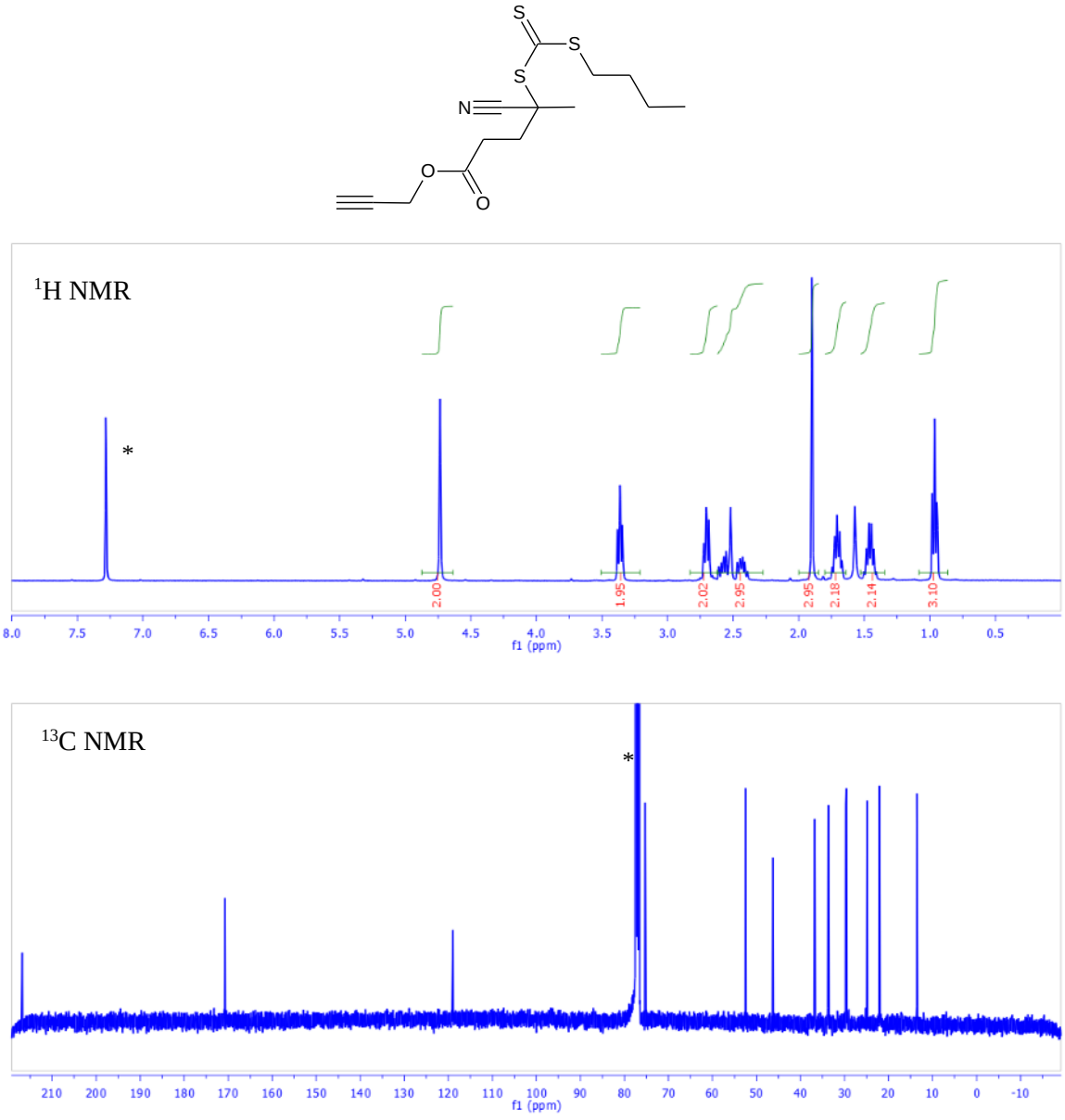


**Figure 99: Chemical Structure and NMR Characterization of Yne-Ester-CTA.**

The second alkyne functionalized CTA was synthesized via a two-step strategy. In the first step, propargyl vinylbenzyl ether (StYne) was synthesized using a reported method.[57] The chemical structure was confirmed by $^{1}$H NMR (Figure 100).

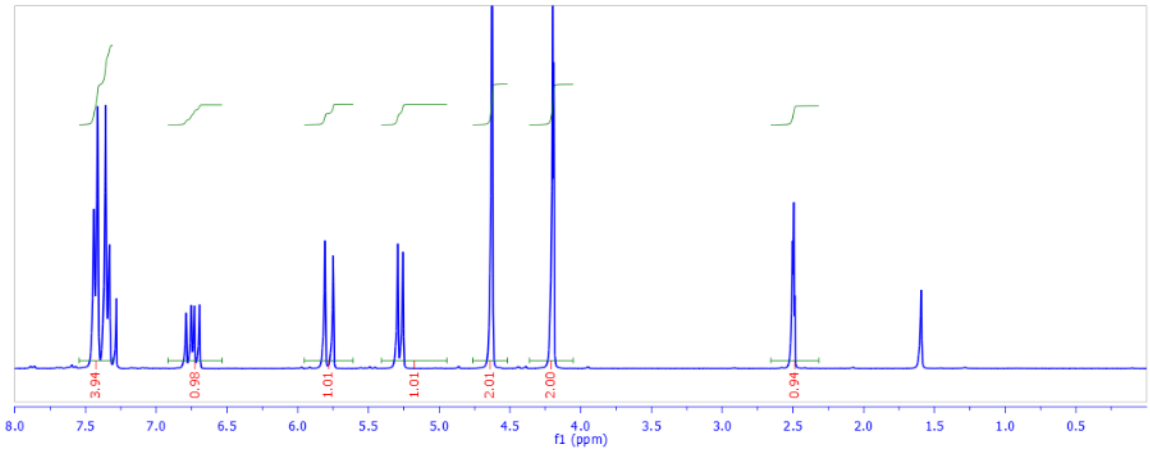


**Figure 100: $^{1}$H NMR Characterization of StYne.**

In a reaction vessel, 2.13 g StYne was mixed with 3.20 g O-CTA, 208 mg AIBN, and 10.1 g dried ethyl acetate. The yellow solution was degassed by purging nitrogen and then sealed with a rubber septum for 20 minutes before being heated to 70 ºC. (Be careful: a significant amount of nitrogen can be produced.) A needle was left in the septum to balance the pressure. After 48 hours, the solution was concentrated and subject to column chromatography using hexanes: ethyl acetate = 10:1 (v:v) as the eluent to yield a yellow oil with high viscosity as the product Yne-CTA (4.03 g, yield = 80%). The chemical structure was confirmed by NMR (Figure 101) and MS (Theoretical 405.1, FAB-MS 406.1 for M+H). One impurity fraction was isolated as A side product in the single monomer insertion reaciton (Figure 102).

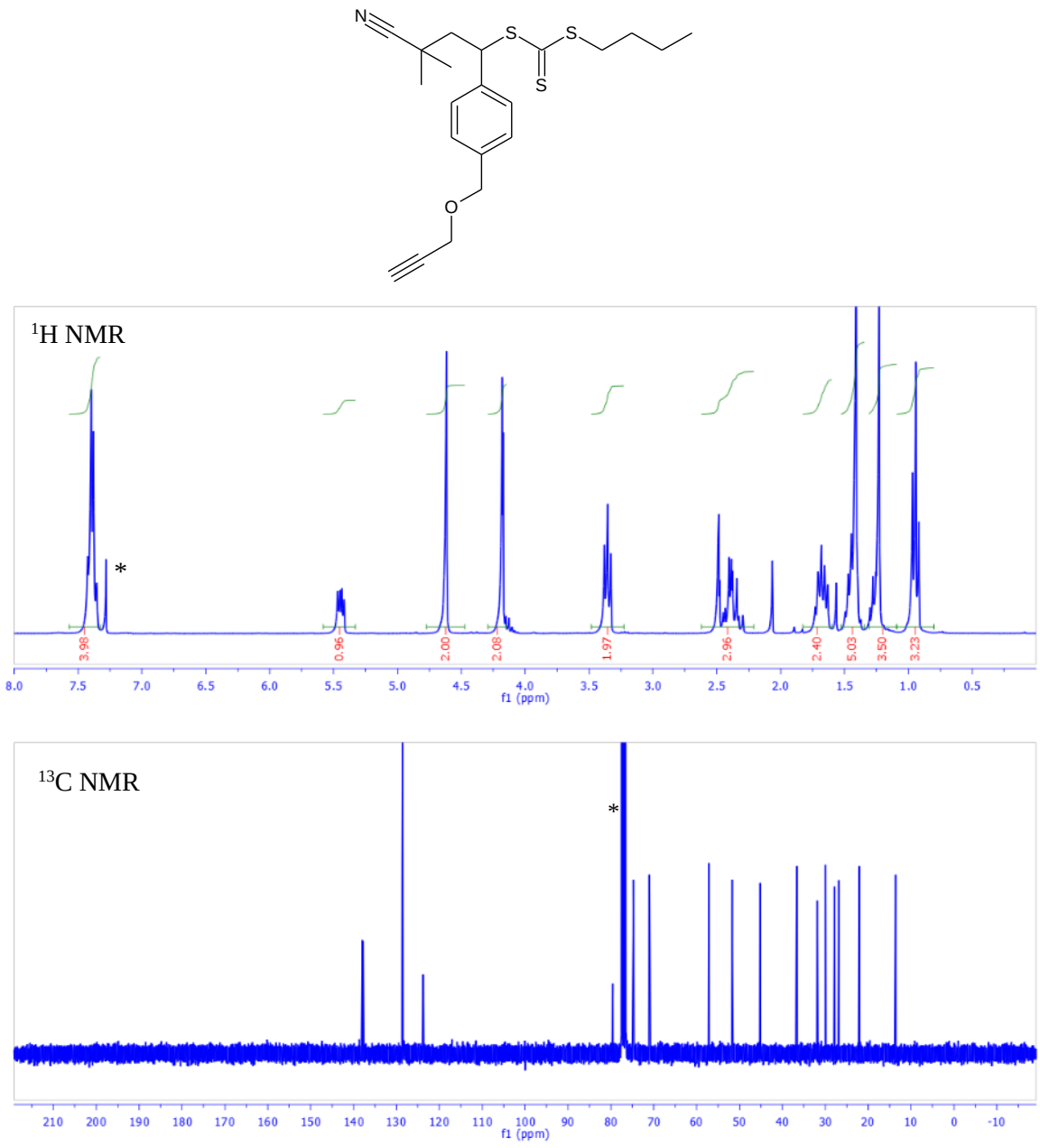


**Figure 101: Chemical Structure and NMR Characterization of Yne -CTA.**

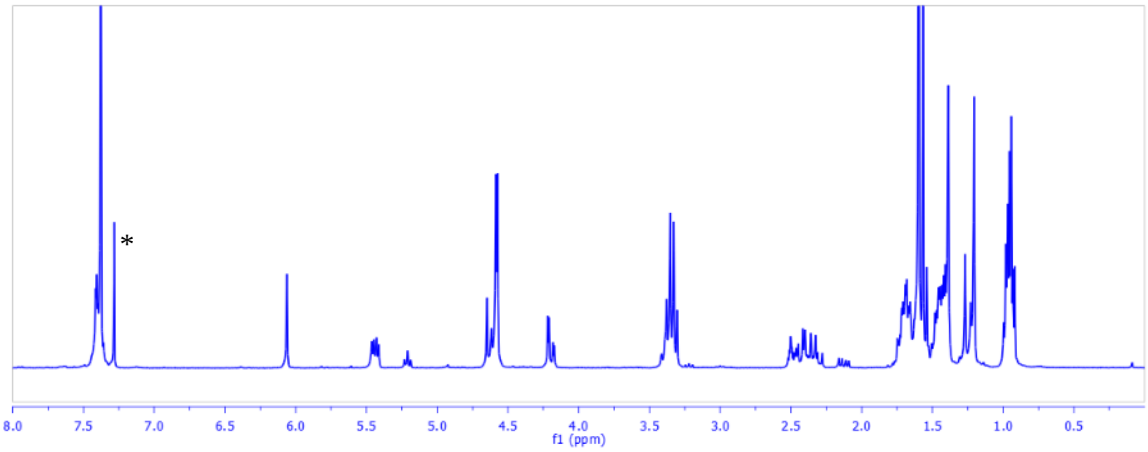


**Figure 102: $^{1}$H NMR Characterization of a Side Product in Yne-CTA Synthesis.**

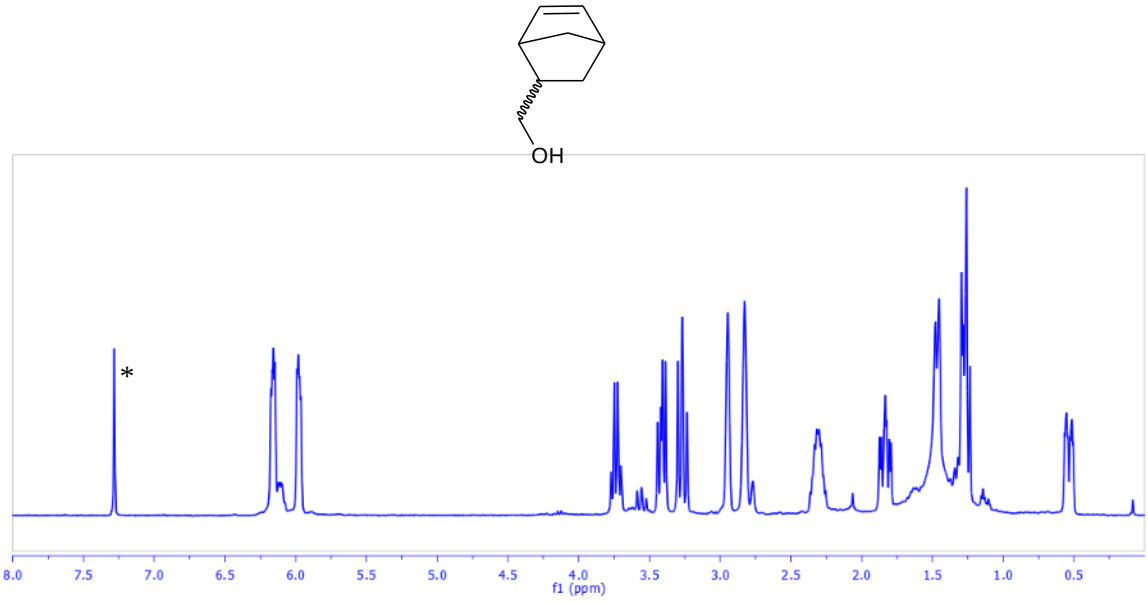


**Figure 103: Chemical Structure and $^{1}$H NMR Spectrum of 5-Norbornene-2-methanol.**

### 7.2.7 Synthesis of Norbornene Functionalized CTA

In the first step, 5-norbornene-2-methanol (mixture of *endo*- and *exo*-isomers) was synthesized by reducing 5-norboenen-2-carboxaldehyde. Into a conical flask was added 25 g 5-norboenen-2-carboxaldehyde and 200 mL MeOH. At 0 ºC, 21.6 g sodium tetrahydroborate was

added in portions (~1 g) to the stirring mixture. After 12 hours, the reaction was quenched with 100 mL HCl solution (~1 M) and 100 mL deionized water. The product was extracted with ethyl acetate from water layer, and purified by passing a short column. The structure was confirmed by $^1$H NMR (Figure 103).

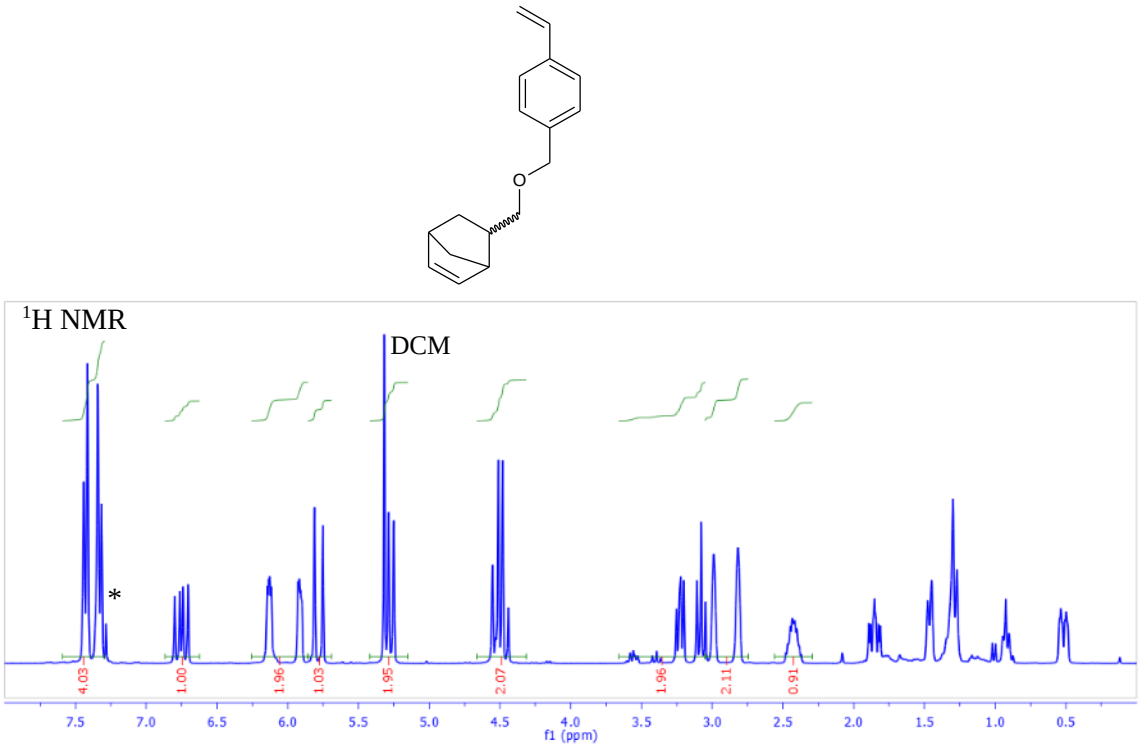


**Figure 104: Chemical Structure and $^1$H NMR Characterization of StNBE.**

In the second step, sodium hydride (60% suspension in oil, 4.43 g) was stirred with hexanes and then quickly filtered before use. Into a conical flask, 7.74 g potassium iodide, 14.47 g 4CMS, 9.05 g 5-norbornene-2-methanol, and 150 mL DMF was charged at 0 $^o$C. While stirring the mixture, NaH was slowly added during a period of 10 minutes. One hour later, the reaction was allowed to warm to room temperature and run overnight. Finally, the reaction was quenched by slowly adding water. The mixture was partitioned between $H_2O$ and diethyl ether. The organic layer was collected and washed with $H_2O$ for 3 times. Finally, the organic layer was concentrated and purified using

column chromatography with hexanes/ethyl acetate (20:1 = v:v) being the eluent to yield a slightly yellow transparent oil as the product, StNBE. The chemical structure was confirmed by NMR (Figure 104).

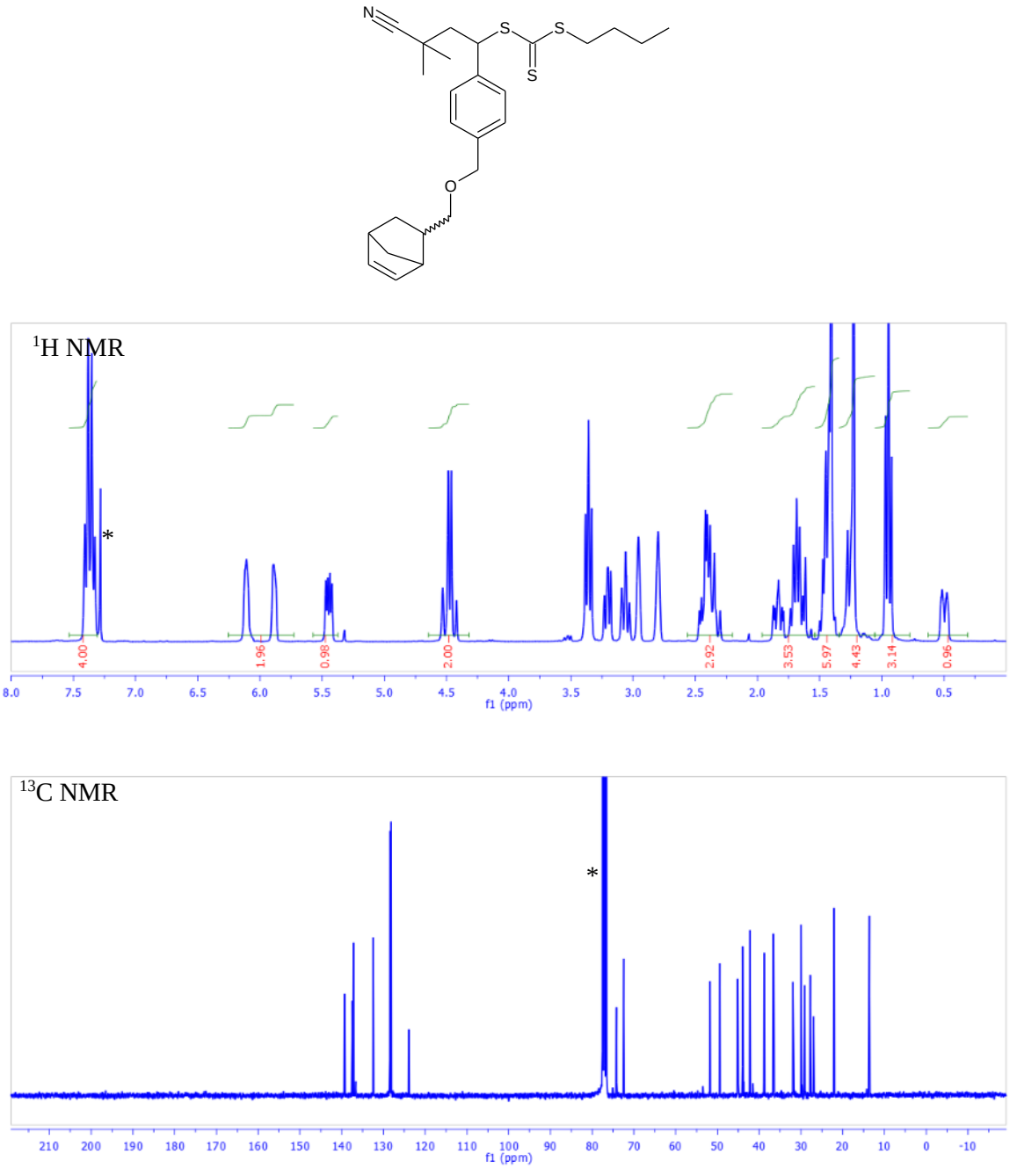


**Figure 105: Chemical Structure and NMR Characterization of NBE-CTA.**

In the third step, 6.49 g StNBE was mixed with 6.40 g O-CTA, 520 mg AIBN, and 14.16 g dried ethyl acetate in a Schlenk flask. The yellow solution was degassed by purging nitrogen for 20 minutes and then sealed with a rubber septum before being heated to 70 $^{o}$C. (Be careful: a significant amount of nitrogen can be produced.) A needle was left in the septum to balance the pressure. After 48 hours, the solution was concentrated and subject to column chromatography using hexanes: ethyl acetate = 8:1 (v:v) as the eluent to yield a yellow oil with high viscosity as the product NBE-CTA (9.563 g, yield = 74%). The structure was confirmed by NMR (Figure 105) and MS (Theoretical 473.19, FAB-MS 474.18 for M+H).

### 7.2.8 Synthesis of a CTA with 2 Alkyne and 2 Trithiocarbonate Groups

In a Schlenk flask, 639 mg StYne was mixed with 980 mg $TTC_2$, 56 mg AIBN, and 6.00 g dried ethyl acetate. The yellow solution was degassed by purging nitrogen for 20 minutes and then sealed with a rubber septum before being heated to 70 $^{o}$C. (Be careful: a significant amount of nitrogen can be produced.) A needle was left in the septum to balance the pressure. After 48 hours, the solution was concentrated and subject to column chromatography using hexanes: ethyl acetate = 5:1 (v:v) as the eluent to yield a yellow oil with high viscosity as the product, $Yne_2TTC_2$ (967 mg, yield = 54%). The structure was confirmed by NMR (Figure 106) and MS (Theoretical 996.3, FAB-MS 995.3 for M-H).

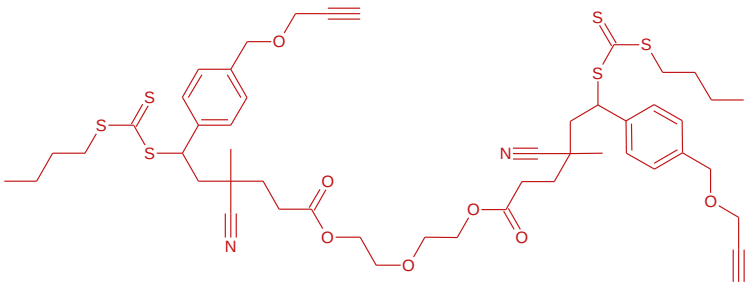

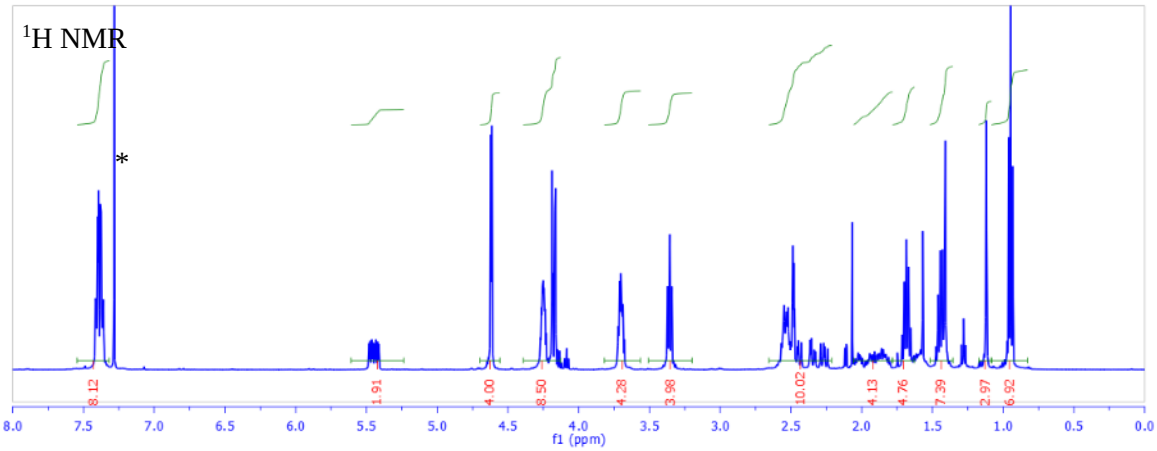
$^{1}$H NMR
*
8.12
1.91
4.00
8.50
4.28
3.98
10.02
4.13
4.76
7.39
2.97
6.92
8.0
7.5
7.0
6.5
6.0
5.5
5.0
4.5
4.0
3.5
3.0
2.5
2.0
1.5
1.0
0.5
0.0
f1 (ppm)

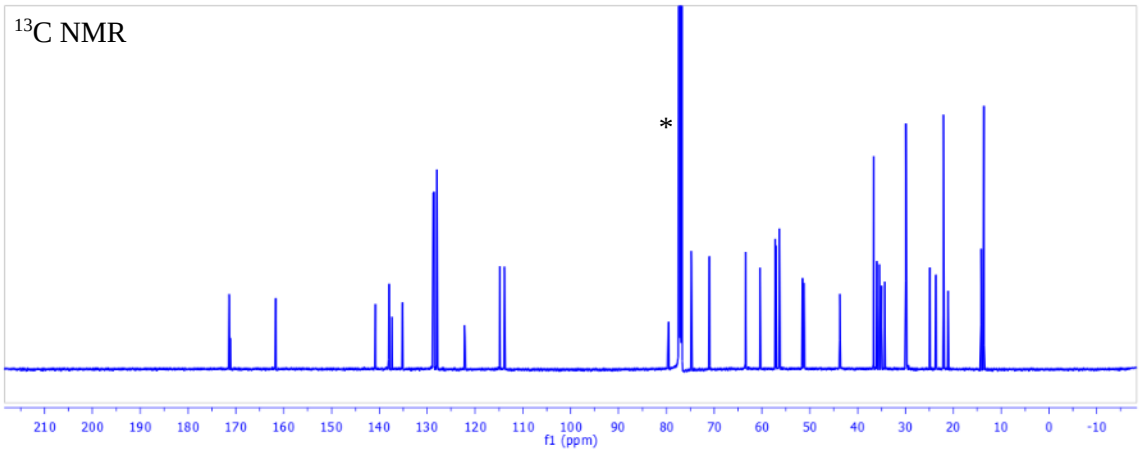
$^{13}$C NMR
*
210
200
190
180
170
160
150
140
130
120
110
100
90
80
70
60
50
40
30
20
10
0
-10
f1 (ppm)

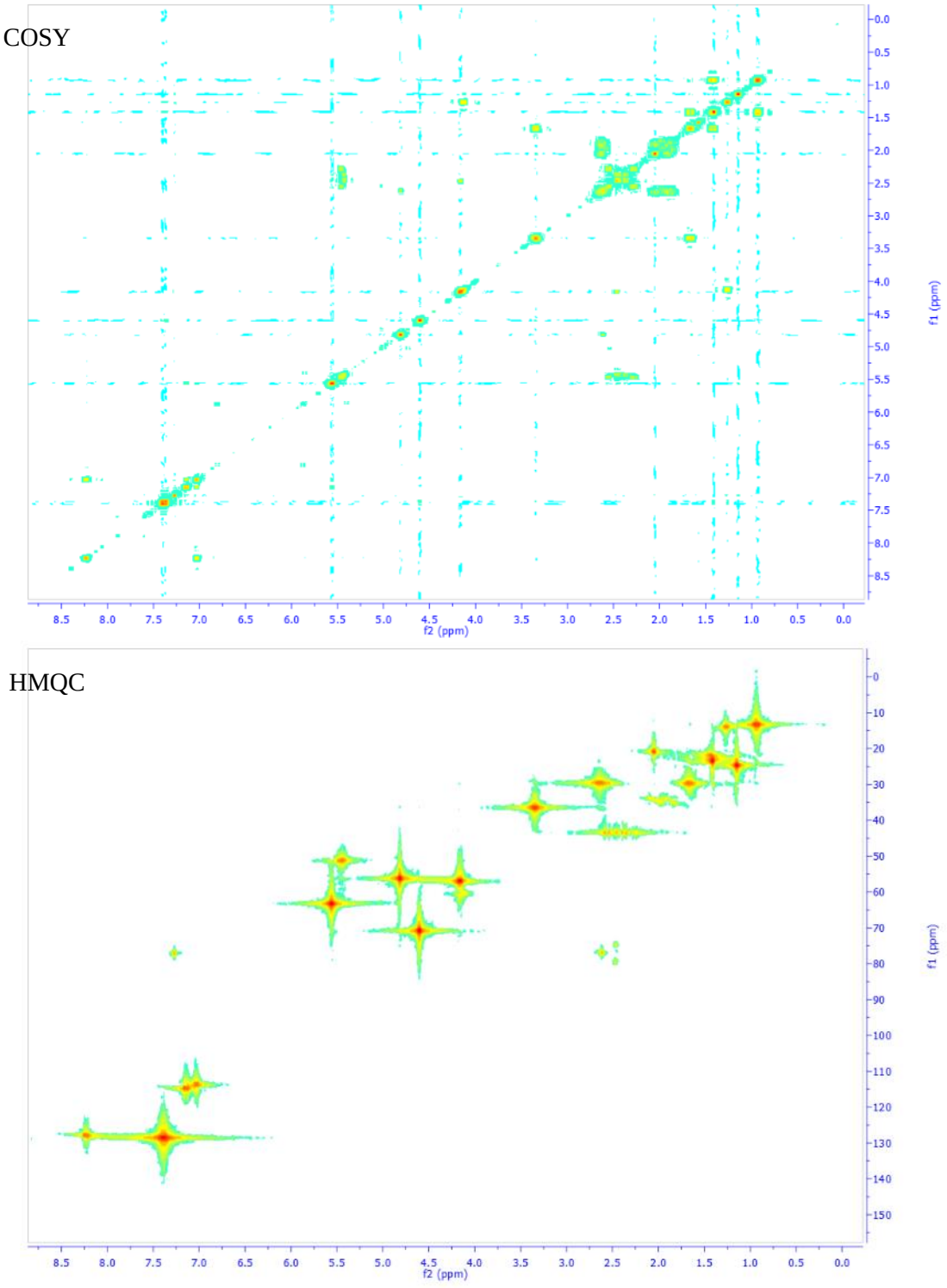


**Figure 106: Chemical Structure and NMR Characterization of $Yne_2TTC_2$.**

### 7.2.9 Synthesis of a CTA with 3 Benzyl Chloride and 3 Trithiocarbonate Groups

In a Schlenk flask, 0.37 g 4CMS was mixed with 0.75 g $TTC_3$, 15 mg AIBN, and 7.41 g 1,4-dioxane. The yellow solution was degassed by purging nitrogen for 20 minutes and then sealed with a rubber septum before being heated to 70 °C. (Be careful: a significant amount of nitrogen can be produced.) A needle was left in the septum to balance the pressure. After 48 hours, the solution was concentrated and subject to column chromatography using hexanes: ethyl acetate = 4:1 (v:v) as the eluent to yield a yellow oil with high viscosity as the product, $Cl_3$-$TTC_3$ (782 mg, yield = 73%). The structure was confirmed by NMR (Figure 107, trace residual ethyl acetate was observed) and MS (Theoretical 1395.3, FAB-MS 1396.4 for M+H).

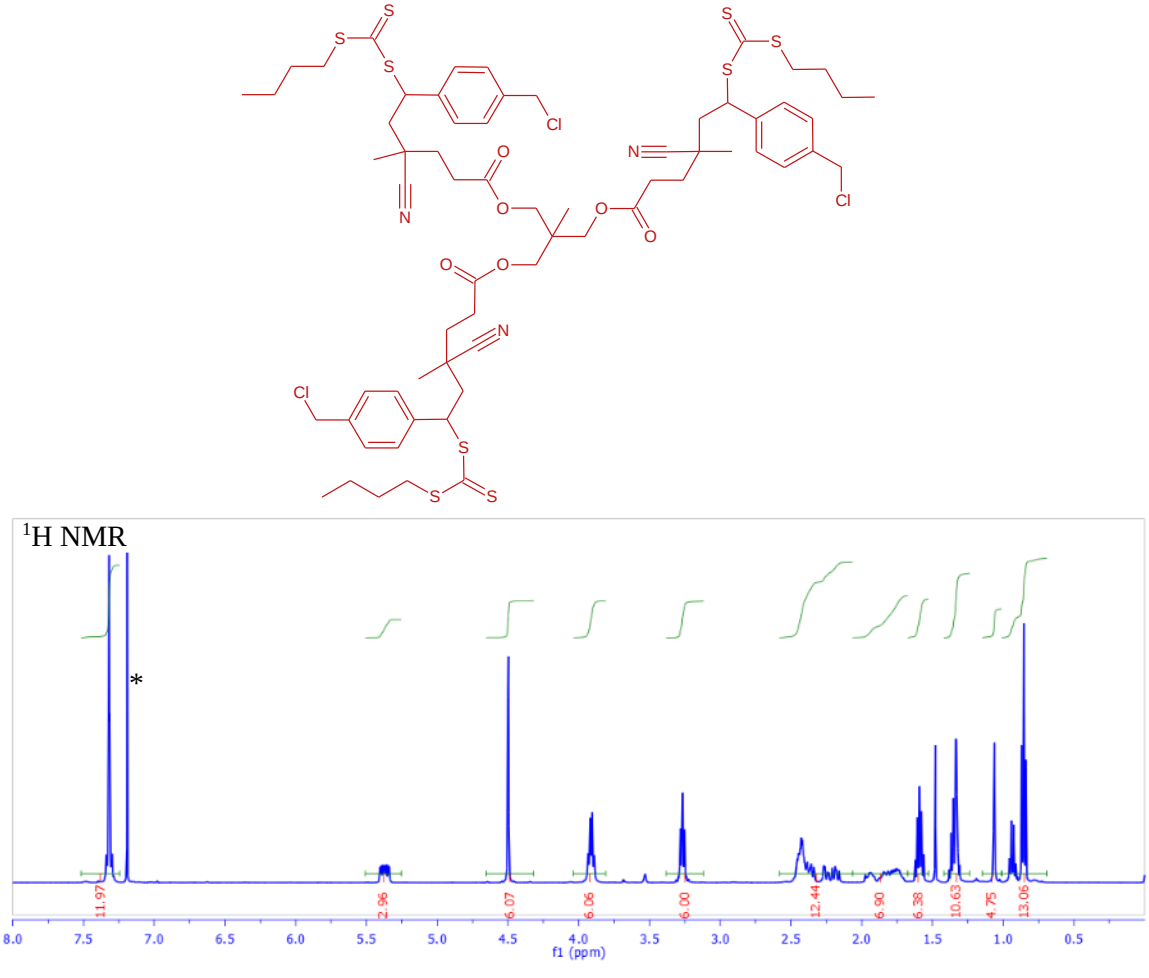

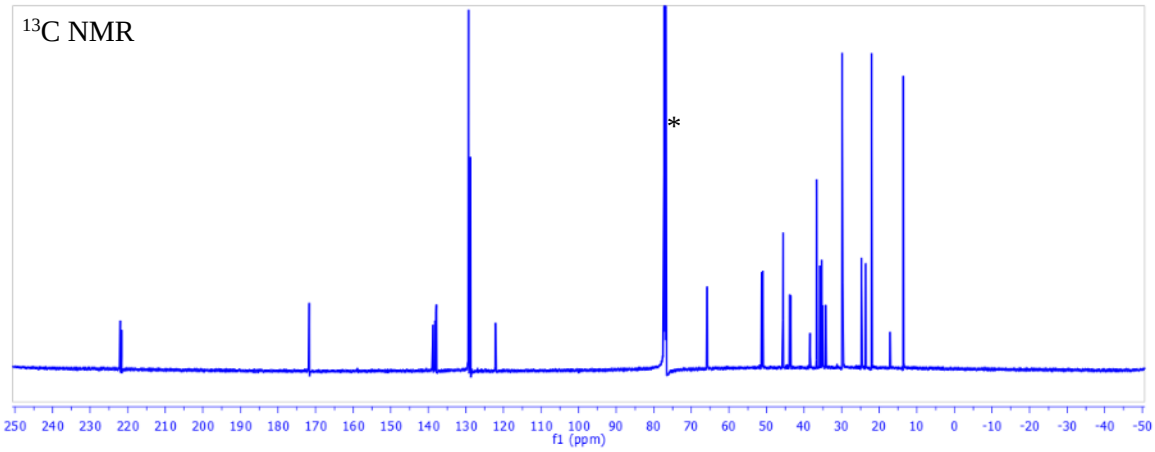
$^{13}$C NMR
*
250 240 230 220 210 200 190 180 170 160 150 140 130 120 110 100 90 80 70 60 50 40 30 20 10 0 -10 -20 -30 -40 -50
f1 (ppm)

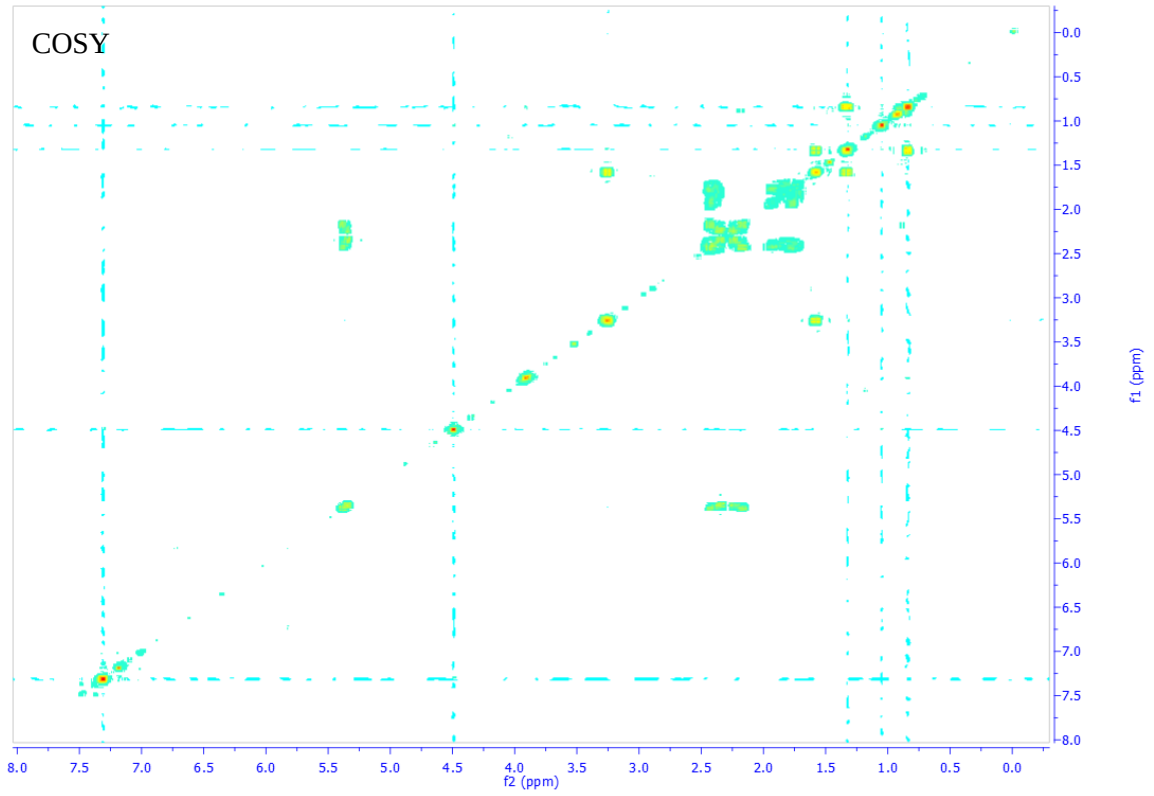
COSY
0.0 0.5 1.0 1.5 2.0 2.5 3.0 3.5 4.0 4.5 5.0 5.5 6.0 6.5 7.0 7.5 8.0
f1 (ppm)
8.0 7.5 7.0 6.5 6.0 5.5 5.0 4.5 4.0 3.5 3.0 2.5 2.0 1.5 1.0 0.5 0.0
f2 (ppm)

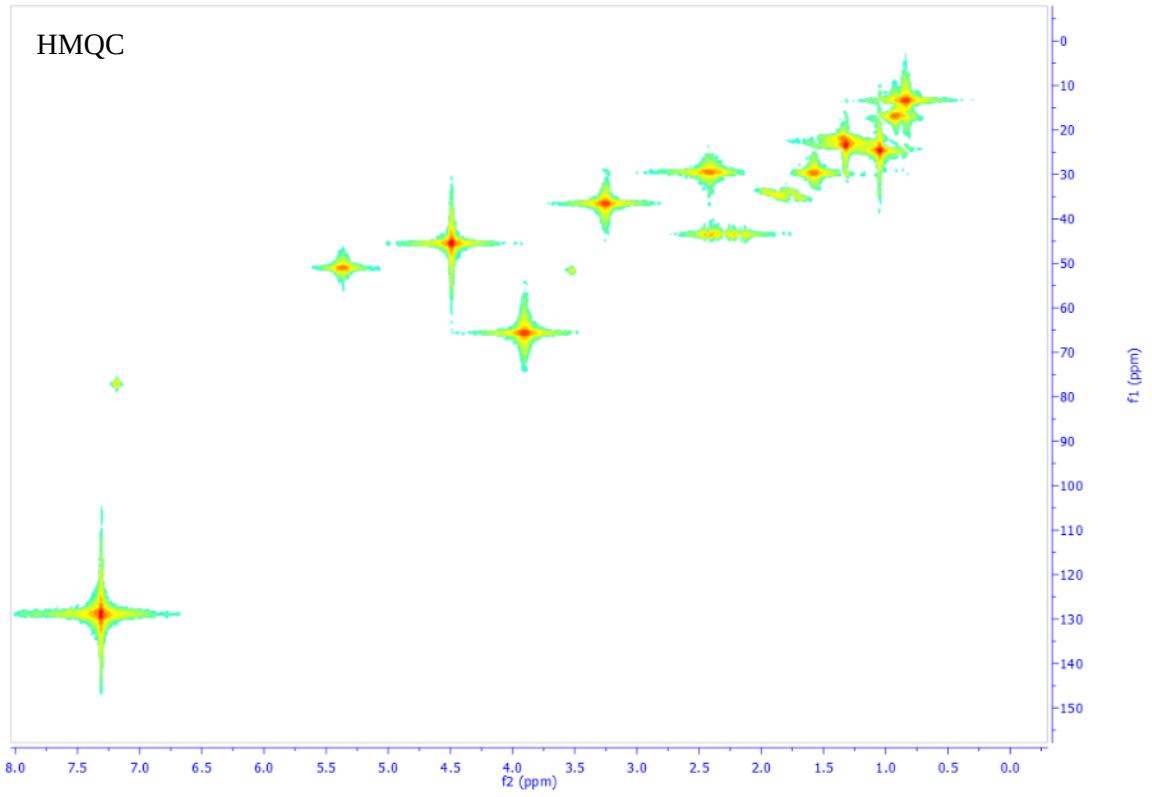


**Figure 107: Chemical Structure and NMR Characterization of $Cl_3$-$TTC_3$.**

### 7.2.10 Synthesis of Benzyl Chloride and Alkyne Functionalized CTA

In a Schlenk flask, 598 mg 4CMS was mixed with 1.13 g Yne-Ester-CTA, 73 mg AIBN, and 4.6 g dried ethyl acetate. The yellow solution was degassed by purging nitrogen for 20 minutes and then sealed with a rubber septum before being heated to 70 ºC. (Be careful: a significant amount of nitrogen can be produced.) A needle was left in the septum to balance the pressure. After 48 hours, the solution was concentrated and subject to column chromatography using hexanes: ethyl acetate = 8:1 (v:v) as the eluent to yield a yellow oil with high viscosity as the product, Yne-Cl-CTA (yield = 66%). The structure was confirmed by NMR (Figure 108) .

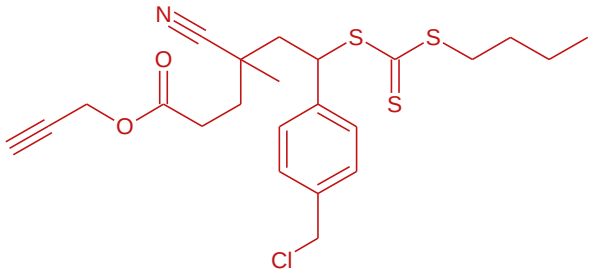
N
O
O
S
S
S
Cl

$^1$H NMR

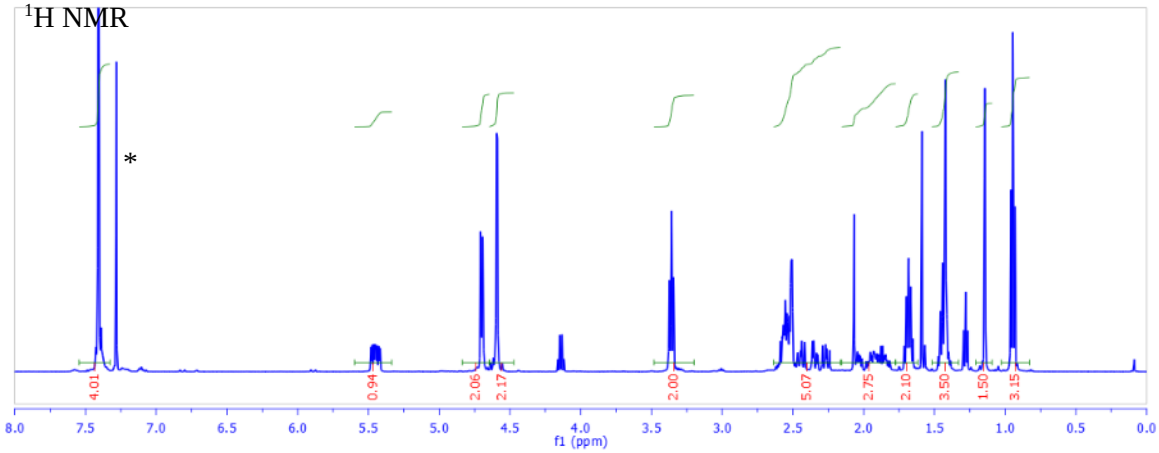
*
4.01
0.94
2.06
2.17
2.00
5.07
2.75
2.10
3.50
1.50
3.15
8.0 7.5 7.0 6.5 6.0 5.5 5.0 4.5 4.0 3.5 3.0 2.5 2.0 1.5 1.0 0.5 0.0
f1 (ppm)

COSY

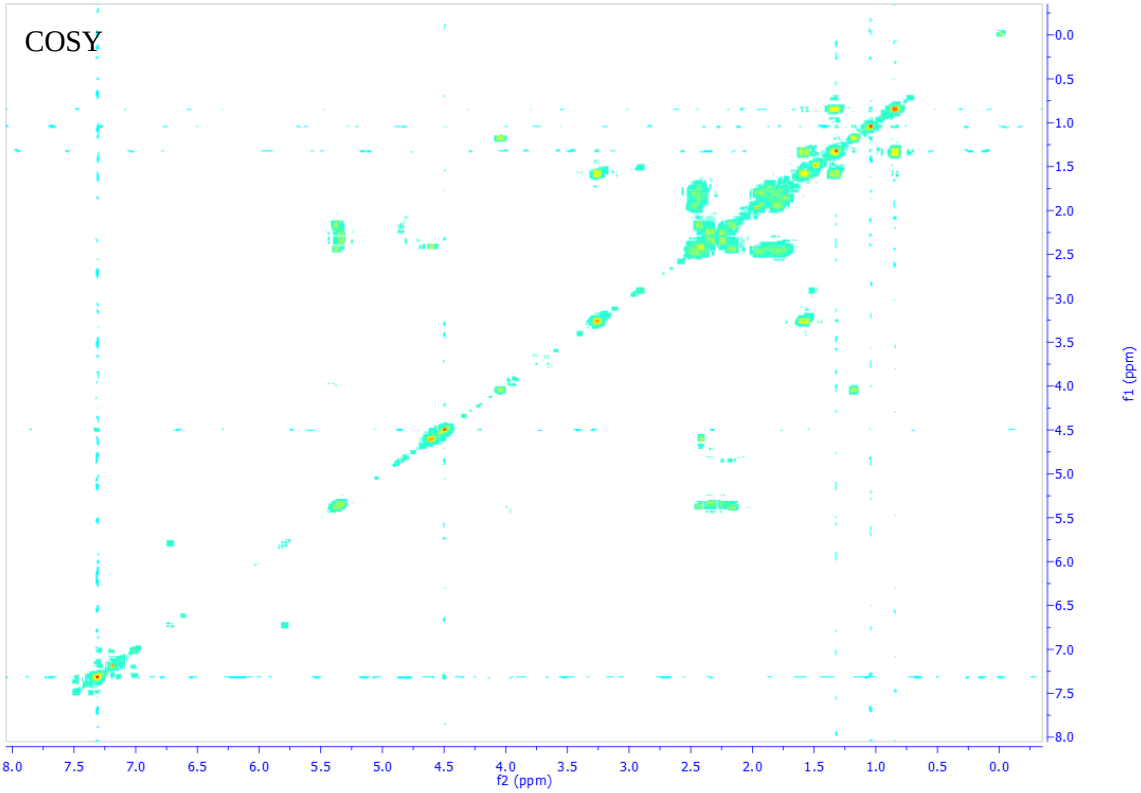
0.0 0.5 1.0 1.5 2.0 2.5 3.0 3.5 4.0 4.5 5.0 5.5 6.0 6.5 7.0 7.5 8.0
f1 (ppm)
8.0 7.5 7.0 6.5 6.0 5.5 5.0 4.5 4.0 3.5 3.0 2.5 2.0 1.5 1.0 0.5 0.0
f2 (ppm)

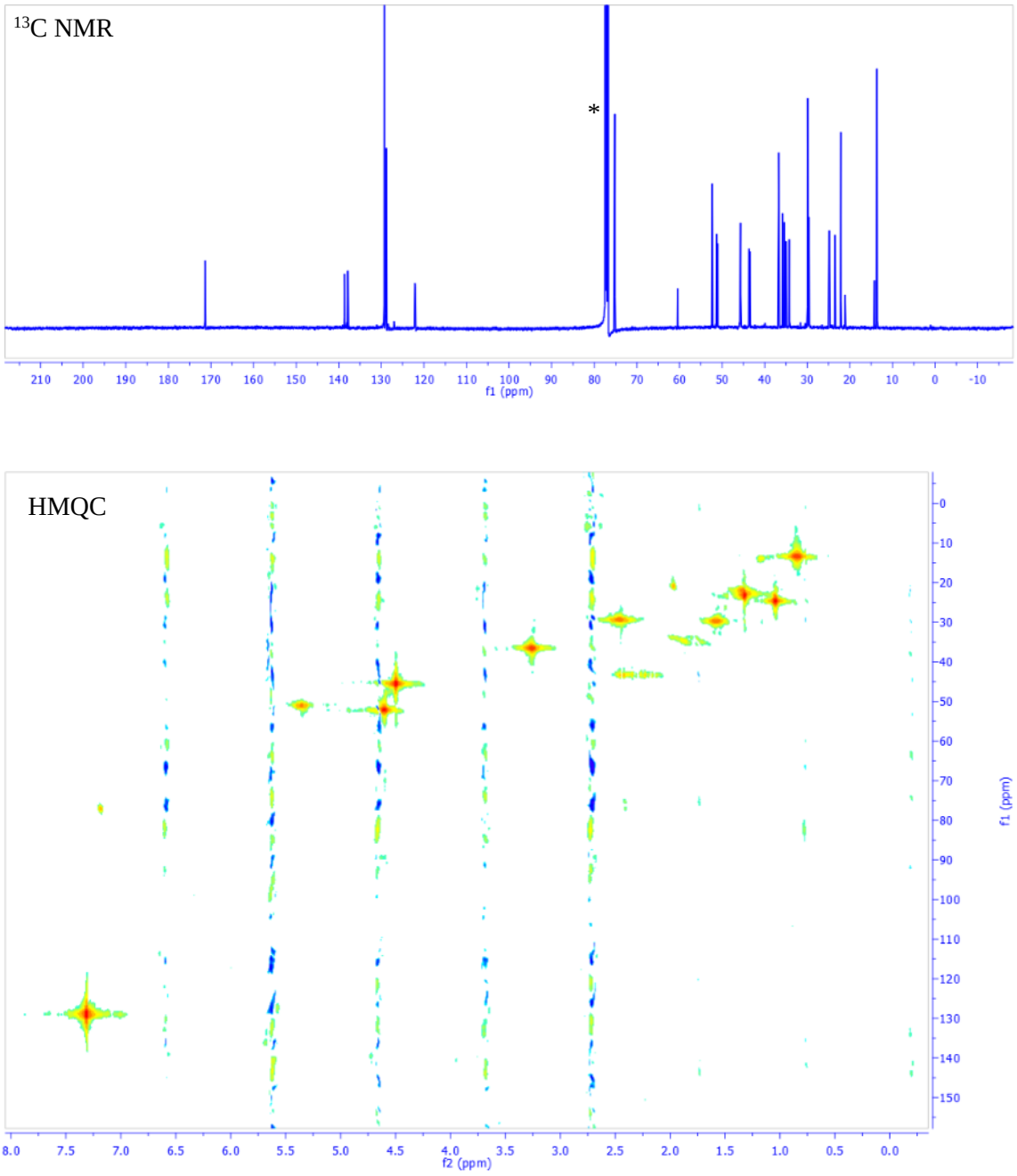


**Figure 108: Chemical Structure and NMR Characterization of Yne-Cl-CTA.**

### 7.2.11 Synthesis of Hydroxyl Functionalized CTA

At 0 °C, 50 mL diethylene glycol, 6.40 g COOH-CTA, and 156 mg 4-dimethylaminopyridine (DMAP) were mixed with 20 mL dichloromethane. The large excess of diethylene glycol was used intentionally to ensure asymmetric esterification. To the stirring mixture, 1.71 g N,N'-Dicyclohexylcarbodiimide (DCC) was slowly added. The reaction was allowed to run overnight and then cooled down to -30 °C before being filtrated to remove dicyclohexyl urea. The concentrated mixture was purified using column chromatography (hexanes:ethyl acetate = 1:1, v:v) to obtain a reddish yellow oil as the product, OH-CTA (6.83 g, yield = 82%). The chemical structure was confirmed by NMR (Figure 109, trace residual ethyl acetate was observed) and MS (Theoretical 379.09, FAB-MS 380.07 for M+H).

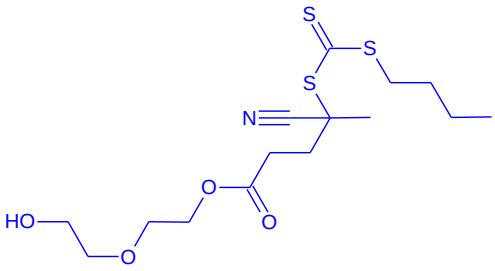


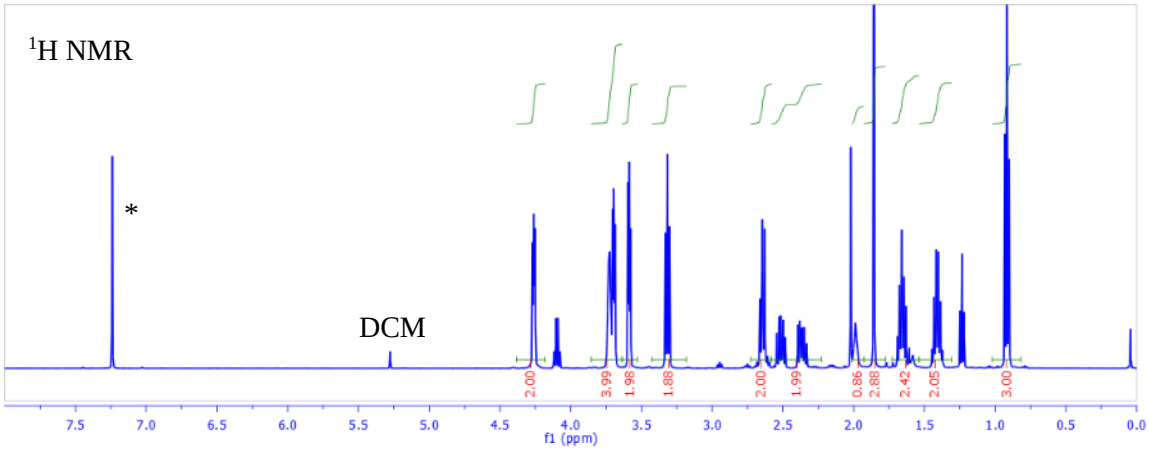

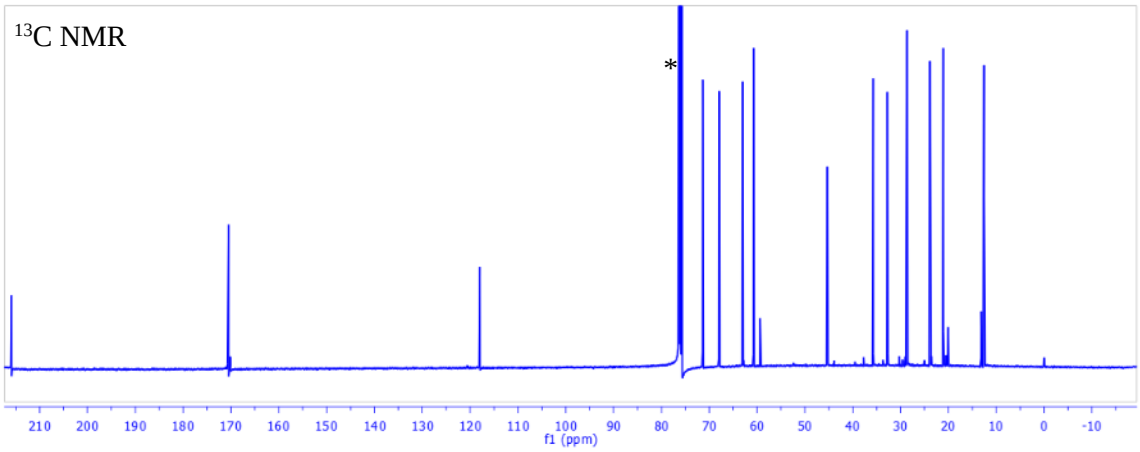
$^{13}$C NMR
*
210 200 190 180 170 160 150 140 130 120 110 100 90 80 70 60 50 40 30 20 10 0 -10
f1 (ppm)

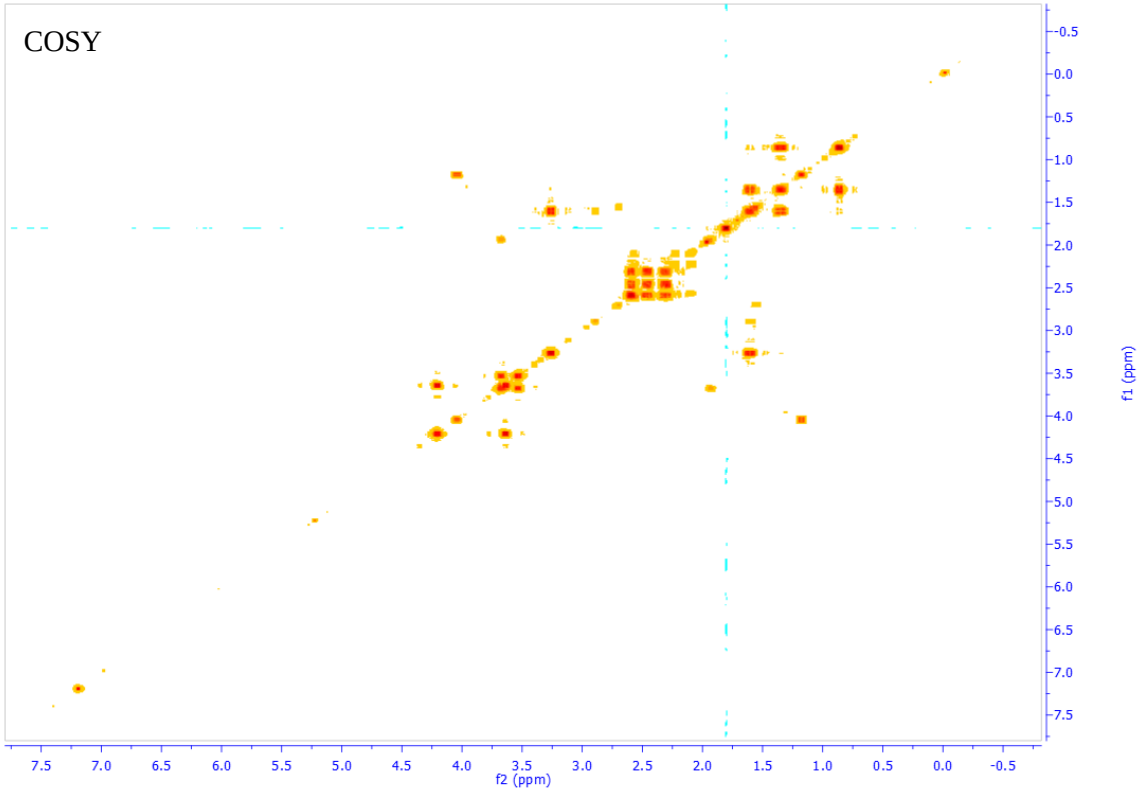
COSY
-0.5 0.0 0.5 1.0 1.5 2.0 2.5 3.0 3.5 4.0 4.5 5.0 5.5 6.0 6.5 7.0 7.5
f1 (ppm)
7.5 7.0 6.5 6.0 5.5 5.0 4.5 4.0 3.5 3.0 2.5 2.0 1.5 1.0 0.5 0.0 -0.5
f2 (ppm)

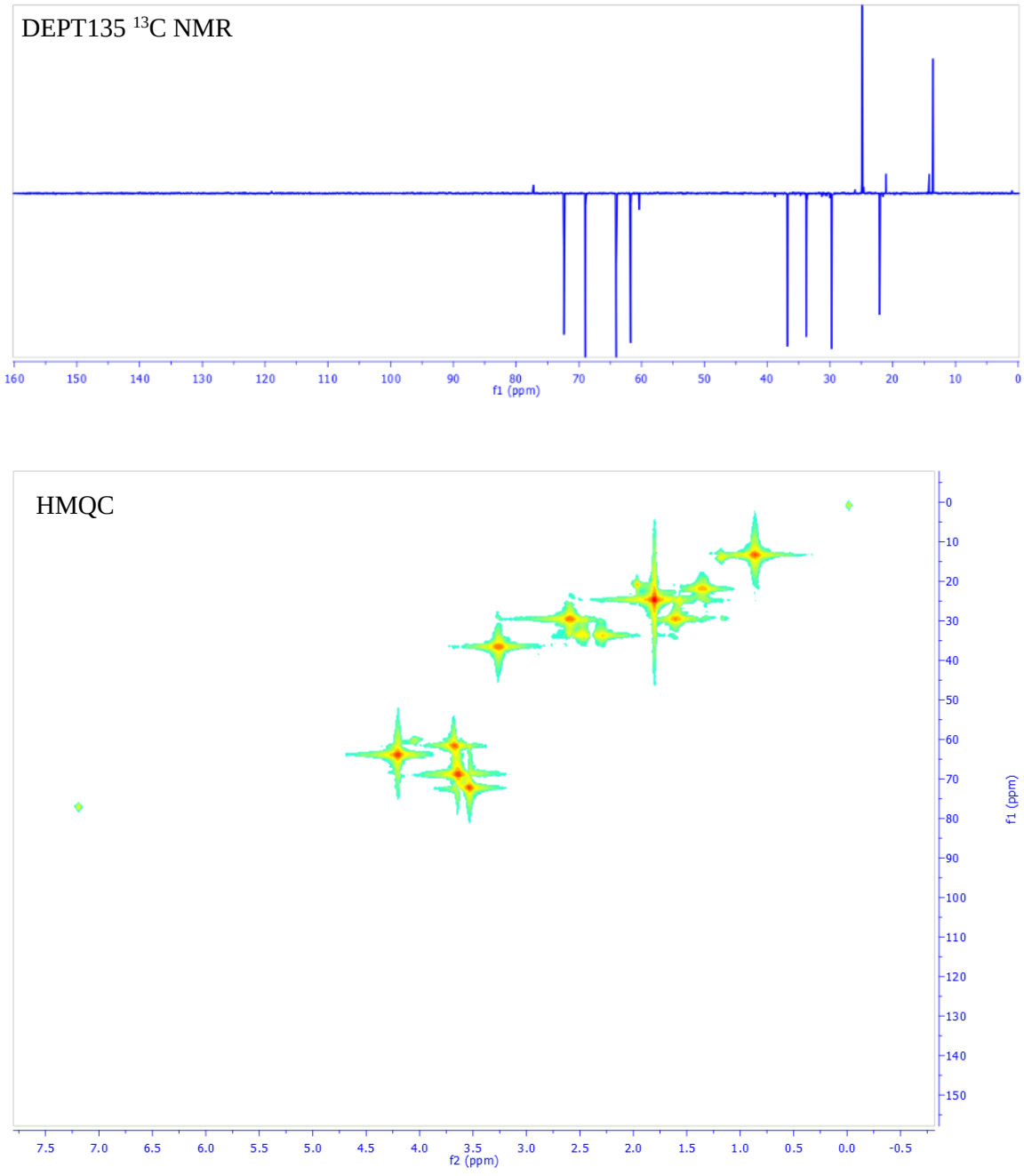


**Figure 109: Chemical Structure and NMR Characterization of OH-CTA.**

### 7.2.12 Synthesis of CTA Based on CMS and Maleimide

In a Schlenk flask, 1.78 g Cl-CTA was mixed with 0.82 g 1,1'-(methylenedi-4,1-phenylene)bismaleimide, 38 mg AIBN, and 25 mL dioxane. The yellow solution was degassed by purging nitrogen for 20 minutes and then sealed with a rubber septum before being heated to 70 °C. (Be careful: a significant amount of nitrogen can be produced.) A needle was left in the septum to balance the pressure. After 48 hours, the solution was concentrated and subject to column chromatography using hexanes: ethyl acetate = 2:1 (v:v) as the eluent to yield a yellow glassy solid as the product, $Cl_2$-$MI_2$-$TTC_2$ (1.622 g, yield = 63%). Preliminary characterization was by $^1$H NMR (Figure 110).

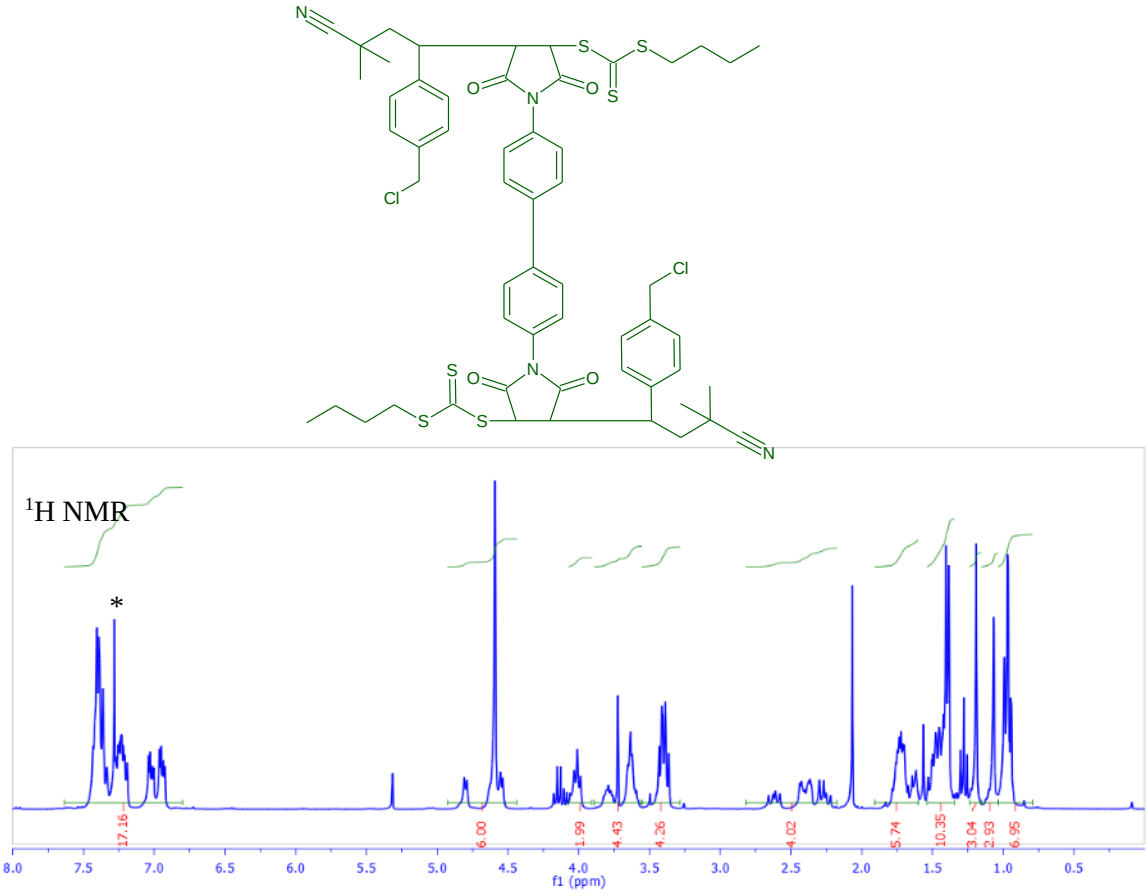


**Figure 110: Chemical Structure and $^1$H NMR Characterization of $Cl_2$-$MI_2$-$TTC_2$.**

### 7.2.13 Synthesis of ONB and Alkyne Functionalized CTA

In a Schlenk flask, 1.60 g Yne-ONB-CTA was mixed with 593 mg StYne, 62 mg AIBN, and 12 g dry ethyl acetate. The yellow solution was degassed by purging nitrogen for 20 minutes and then sealed with a rubber septum before being heated to 70 °C. (Be careful: a significant amount of nitrogen can be produced.) A needle was left in the septum to balance the pressure. After 48 hours, the solution was concentrated and subject to column chromatography using hexanes: ethyl acetate = 2:1 (v:v) as the eluent to yield a yellow oil with high viscosity as the product, Yne-ONB-Yne-CTA (1.88 g, yield = 83%). The chemical structure was confirmed by NMR (Figure 101, residual ethyl acetate was observed).

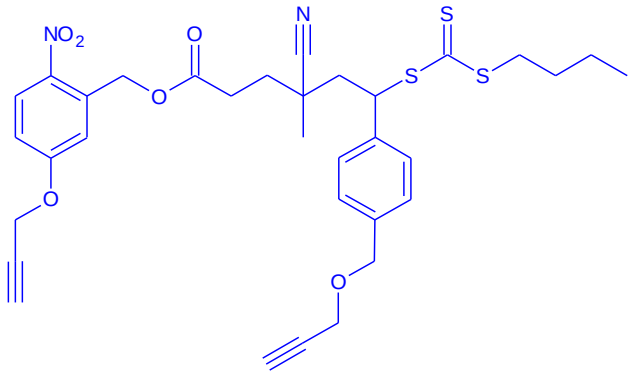


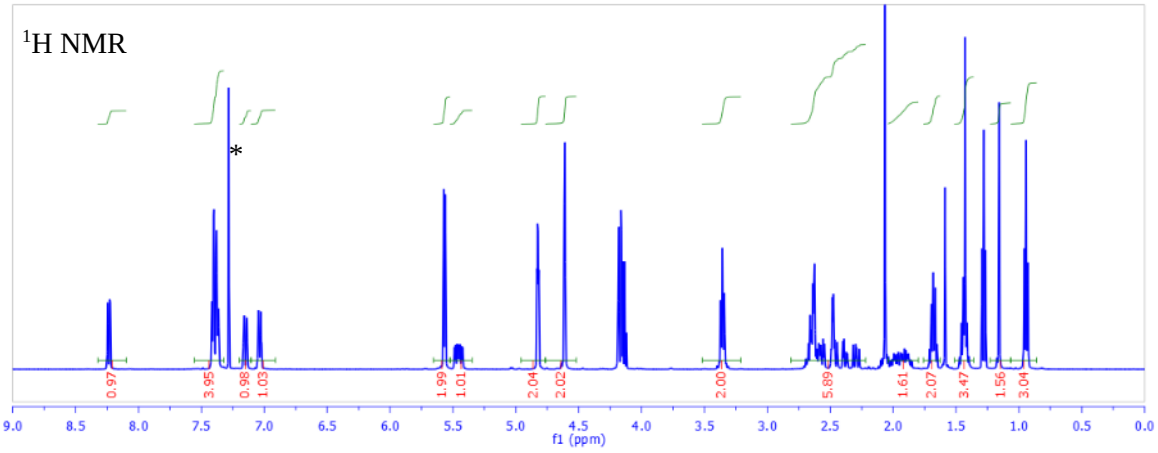

$^{13}$C NMR

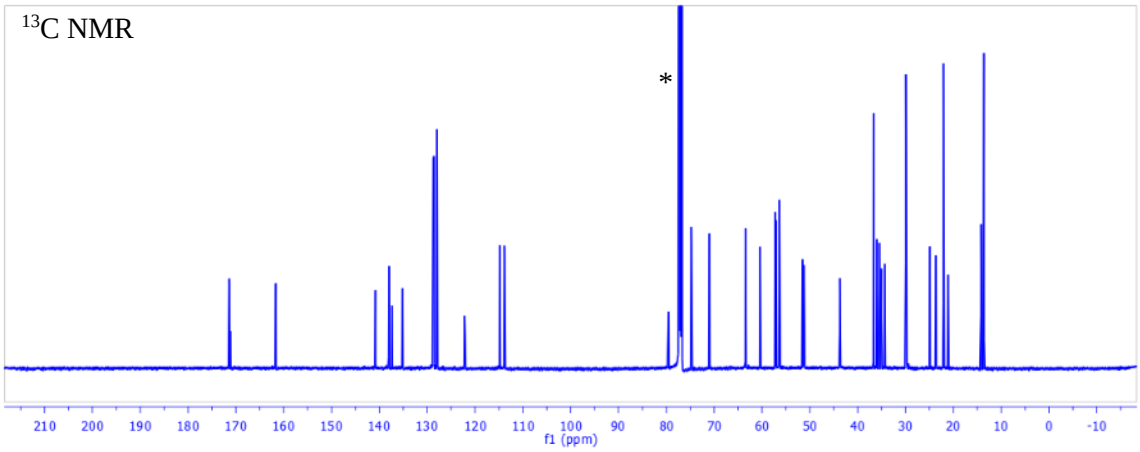
*
210 200 190 180 170 160 150 140 130 120 110 100 90 80 70 60 50 40 30 20 10 0 -10
f1 (ppm)

COSY

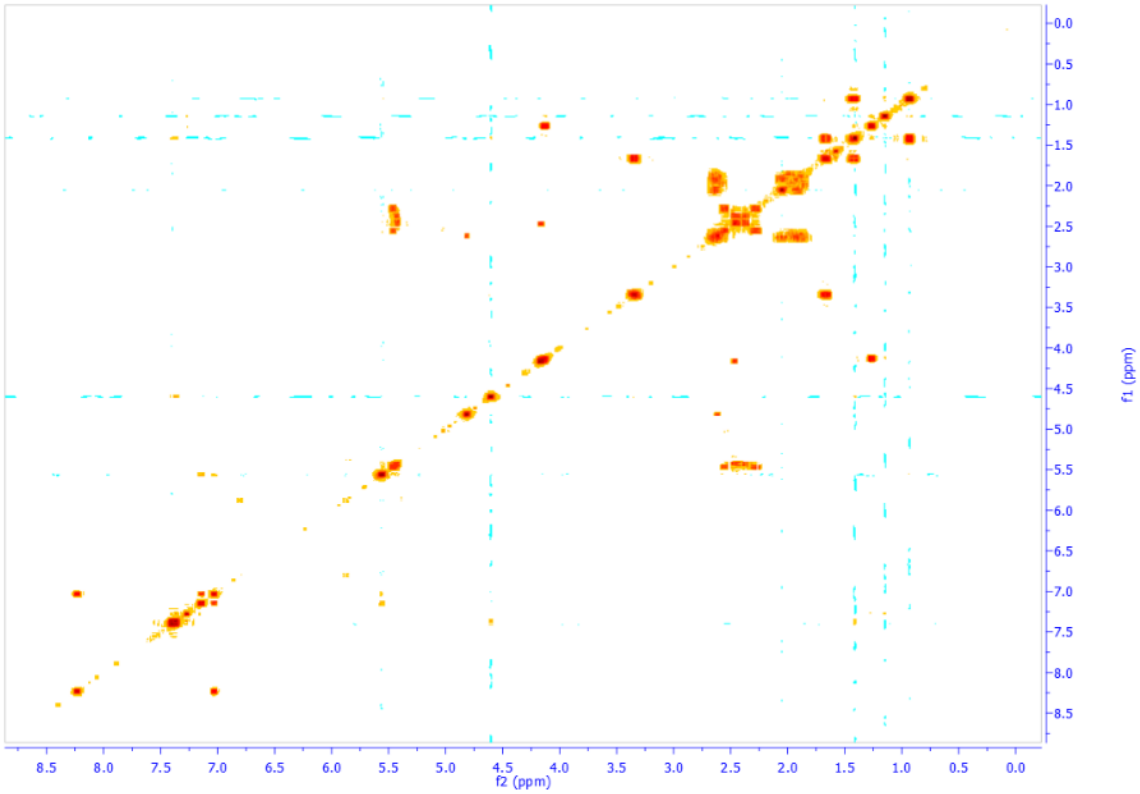
8.5 8.0 7.5 7.0 6.5 6.0 5.5 5.0 4.5 4.0 3.5 3.0 2.5 2.0 1.5 1.0 0.5 0.0
f2 (ppm)
0.0 0.5 1.0 1.5 2.0 2.5 3.0 3.5 4.0 4.5 5.0 5.5 6.0 6.5 7.0 7.5 8.0 8.5
f1 (ppm)

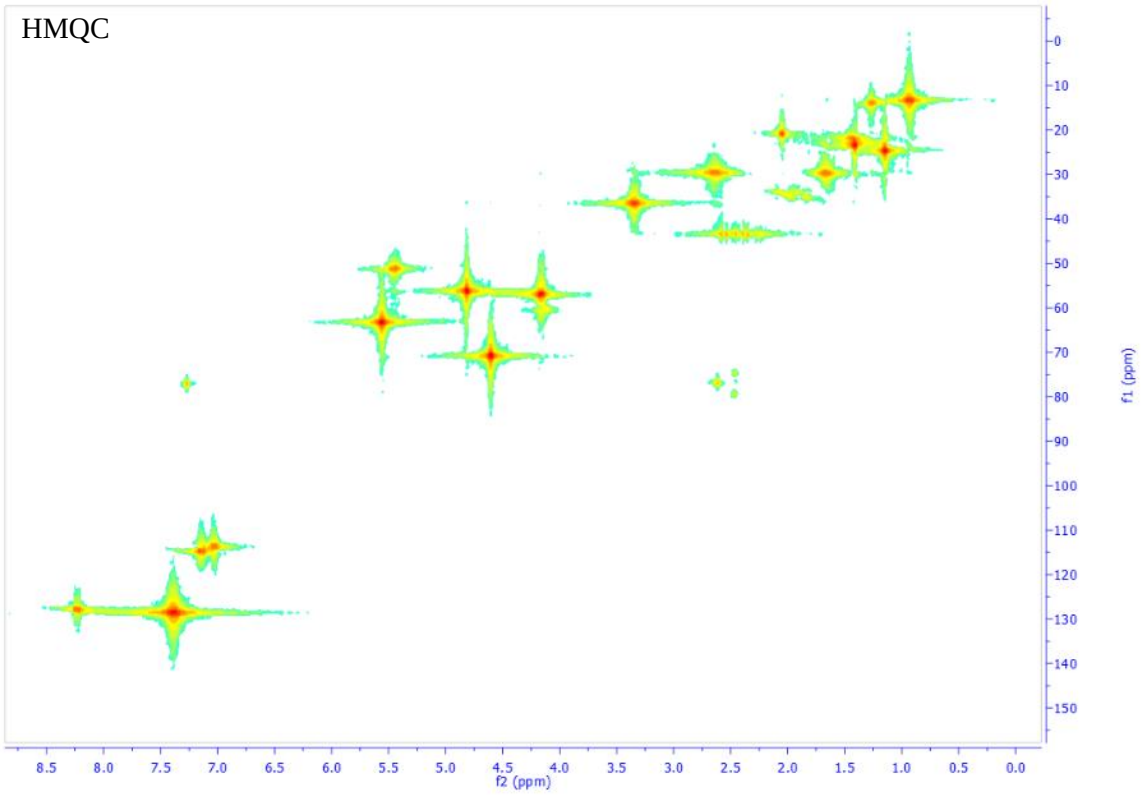


**Figure 111: Chemical Structure and NMR Characterization of Yne-ONB-Yne-CTA.**

### 7.2.14 Synthesis of Cyclooctene Functionalized Xanthate

5-Azido-1-cyclooctene (AzCOE) was synthesized in the first place. In a flask, 20 g cyclooctadiene was charged, and 33 mL HBr (33 wt% in acetic acid) was added gradually over a period of 30 minutes. The reaction was kept overnight, and then diluted with diethyl ether. Sodium bicarbonate solution was added to the stirring organic solution, until no further gas was produced. The organic was collected and washed twice with deionized water, before ethyl acetate was removed. The resulted mixture was purified by column chromatography with 3 v% ethyl acetate in hexanes, to give 5-bromo-1-cyclooctene (BrCOE, 14g, yield = 40%). The chemical structure was confirmed by $^{1}$H NMR (Figure 112).

In a round-bottom flask was added 6 g purified BrCOE, 5 g $NaN_3$, and 25 mL DMF. The mixture was heated to 60 ºC for 72 hours, before it was partitioned between 100 mL ethyl acetate and 100 mL deionized water. The organic layer was collected and washed twice with water, before being dried with magnesium sulfate. After passing through a short column, AzCOE was isolated (2.8 g, yield = 58%). The chemical structure was confirmed by MS (Theoretical 151.1, EI+ MS 151.0 for M+) and $^1$H NMR (Figure 112), as the peak ($\delta$ = ~4.3 ppm) corresponding to $CH_2C\mathbf{H}BrCH_2$ disappeared, while a new peak (($\delta$ = ~3.5 ppm) arised, which was assigned to $CH_2C\mathbf{H}N_3CH_2$.

O-ethyl S-prop-2-ynyl carbonodithioate (C≡C-Xan) was synthesized using a previously reported method.[315] Potassium ethyl xanthogenate (4.7 g), propargyl bromide 80% solution in toluene (3.8 g), and THF (15 mL) were placed in a 50 mL round-bottomed flask in dark. The reaction mixture was stirred overnight at room temperature. The product was isolated by column chromatography, as a pale yellowish oil (Figure 112).

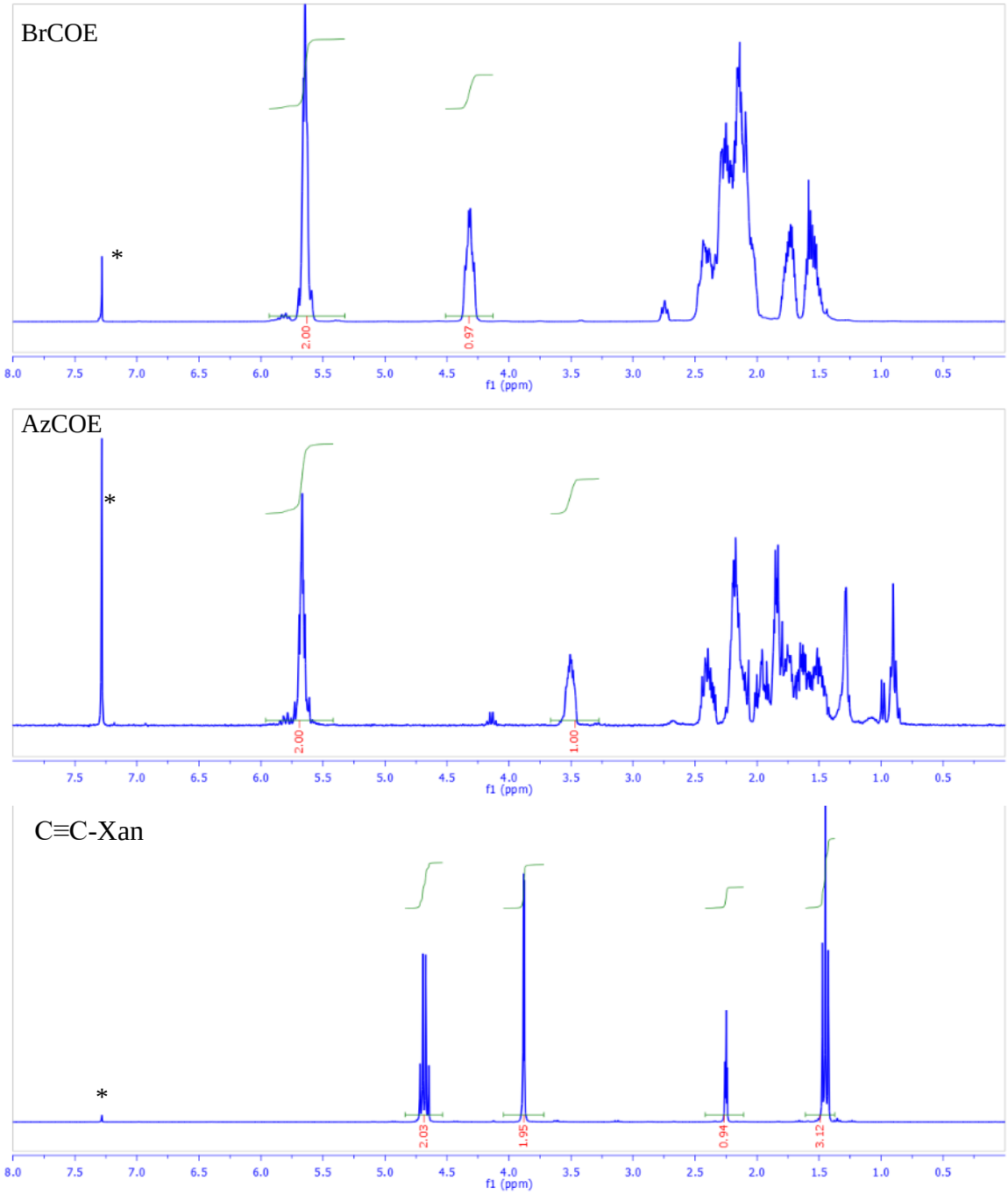


**Figure 112: $^{1}$H NMR Characterization of BrCOE, AzCOE, and C≡C-Xan.**

In the final step, 2.6 g C≡Can, 2.2 g AzCOE, and 15 mL THF were placed in a reaction vessel. At 0 ºC, the mixture was degassed by nitrogen purge for 10 minutes, before 200 mg Cu(I)Br

was added under nitrogen flow. After another 10 minutes of degassing, 200 μL was added by a microsyringe. The reaction mixture was stirred at 0 °C for 1 hour and then warmed up to room temperature. After 16 hours, the solution was concentrated and subjected to column chromatography to yield the cyclooctene functionalized xanthate (COE-Xan, 3.3 g, yield = 73%) as a pale yellowish oil, which slowly solidified when stored in the fridge. The chemical structure was confirmed by NMR (Figure 113) and MS (Theoretical 311.1, FAB-MS 312.1 for M+H).

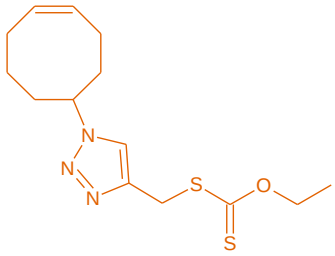


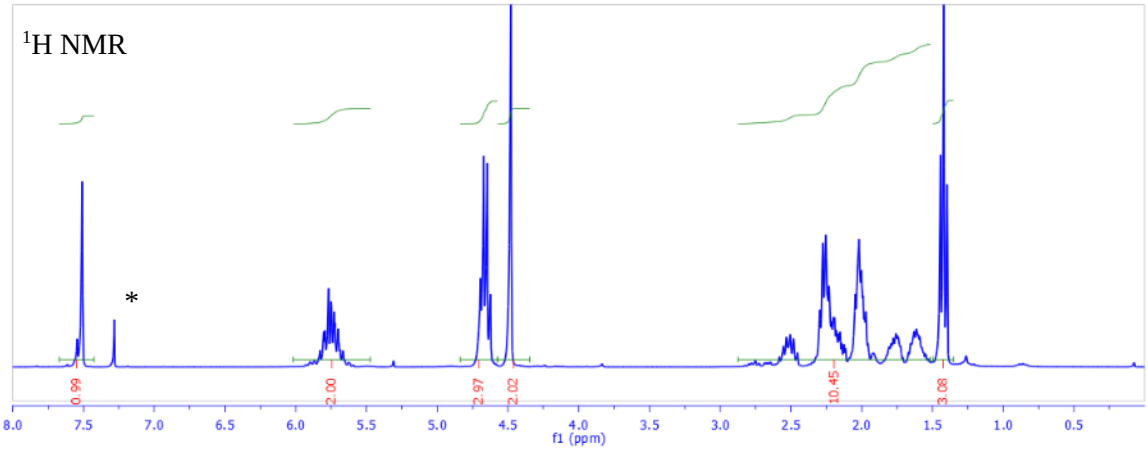


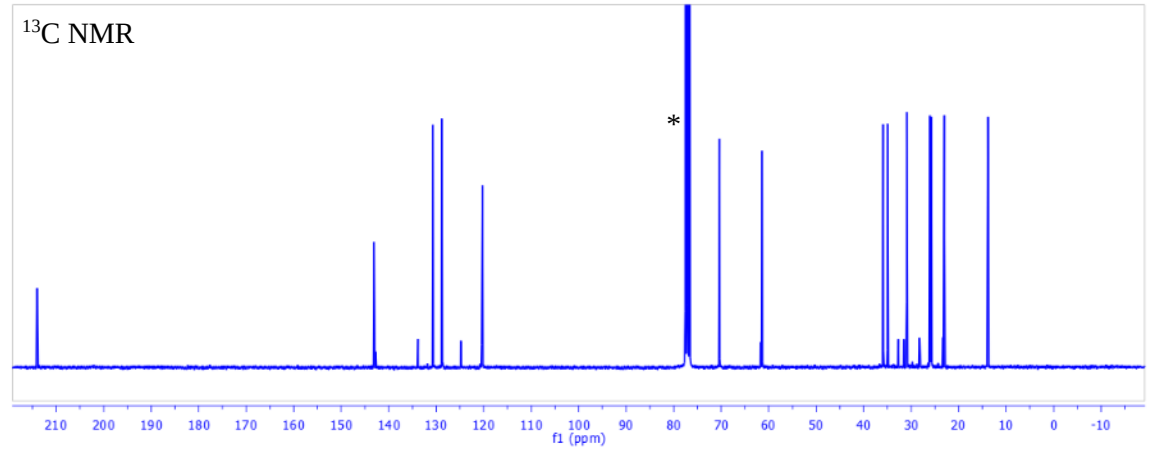

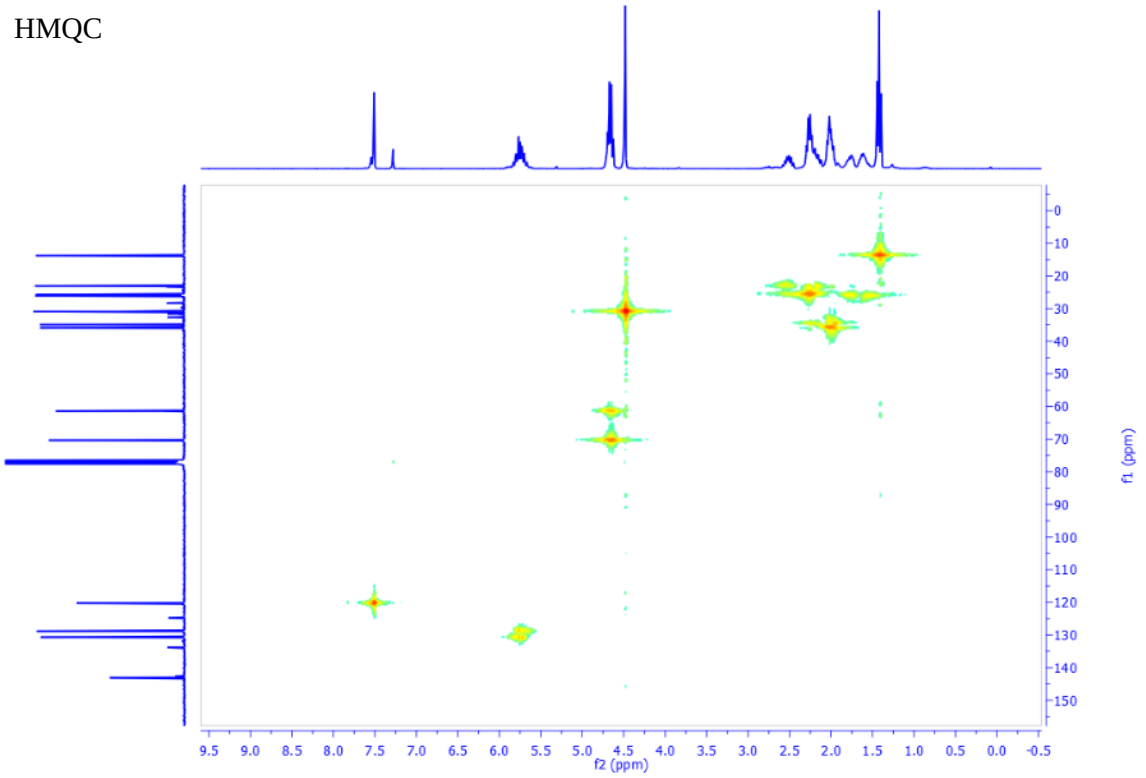


**Figure 113: Chemical Structure and NMR Characterization of COE-Xan.**

### 7.2.15 Controlled Radical Polymerization

A representative procedure is described here. In a reaction tube, 48 mg Cl-CTA, 1.942 g St, and 2.3 mg AIBN were added. The mixture was degassed by nitrogen purge and then sealed before being heated to 60 °C to initiate the polymerization. After 25 hours, the reaction was quenched to 0 °C and a small aliquot was taken for conversion analysis by $^1$H NMR. The polymer was purified by precipitating three times into MeOH. For PnBA, MeOH/$H_2O$ (3:1 = v:v) was used for precipitation; for P2VP, diethyl ether/hexanes (2:3 = v:v) was used; diethyl ether was used for PNIPAAm; hexanes were used for PMMA, P4CMS, and P(St-*ran*-4CMS); MeOH was used for PSt, PIp, and PtBS. The DPs were determined by end-group analysis using $^1$H NMR spectra and the Đs were measured using GPC calibrated against PSt standards.

Chain extension polymerizations were conducted in similar manners. A representative procedure is described here. In a reaction tube, 1.50 g Cl-PSt, 3.91 g nBA, 5.36 g 1,4-dioxane, and 3.3 mg AIBN were added. The mixture was degassed by nitrogen purge and then sealed before being heated to 60 °C to initiate the polymerization. After 6.5 hours, the reaction was quenched to 0 °C. The polymer was purified by precipitating three times into MeOH. The DP of the extended block was determined by the ratio against the first block with previously determined DP using $^1$H NMR and the Đ was measured using GPC calibrated with PSt standards.

### 7.2.16 Kinetics Study of VAc Polymerization Mediated by COE-Xan

In a Schlenk flask, 10.302 g VAc, 13.0 mg AIBN, and 247.8 mg COE-Xan ([VAc] : [AIBN] : [COE-Xan] = 150:0.1:1) were mixed. The mixture was degassed by nitrogen purge for 30 minutes, before being heated to 70 °C to initiate the polymerization. Aliquots were taken carefully with the system protected with gentle nitrogen flow, after predetermined time intervals. The aliquots were subjected to $^1$H NMR and GPC (calibrated with PMMA standards) for conversion and MW analysis. The kinetics data is shown below. Figure 114A shows the relationship between ln(1-conv.) and reaction time. The linear regression of the data points between 4 and 10 hours gives the equation

$$\ln(1\text{-conv.}) = 0.1638*t - 0.5133$$

with an $R^2$ value being 0.9984, where t is in the unit of hour. This means during this reaction time interval, the monomer consumption rate was proportional to the concentration of residual monomer, which is a strong indication of relatively consistent concentration of active radical species. It demonstrates the pseudo-living characteristics of this polymerization. It was also found that this polymerization has an induction period of ~3 hours, which is typical as observed in other reports.[316–318]

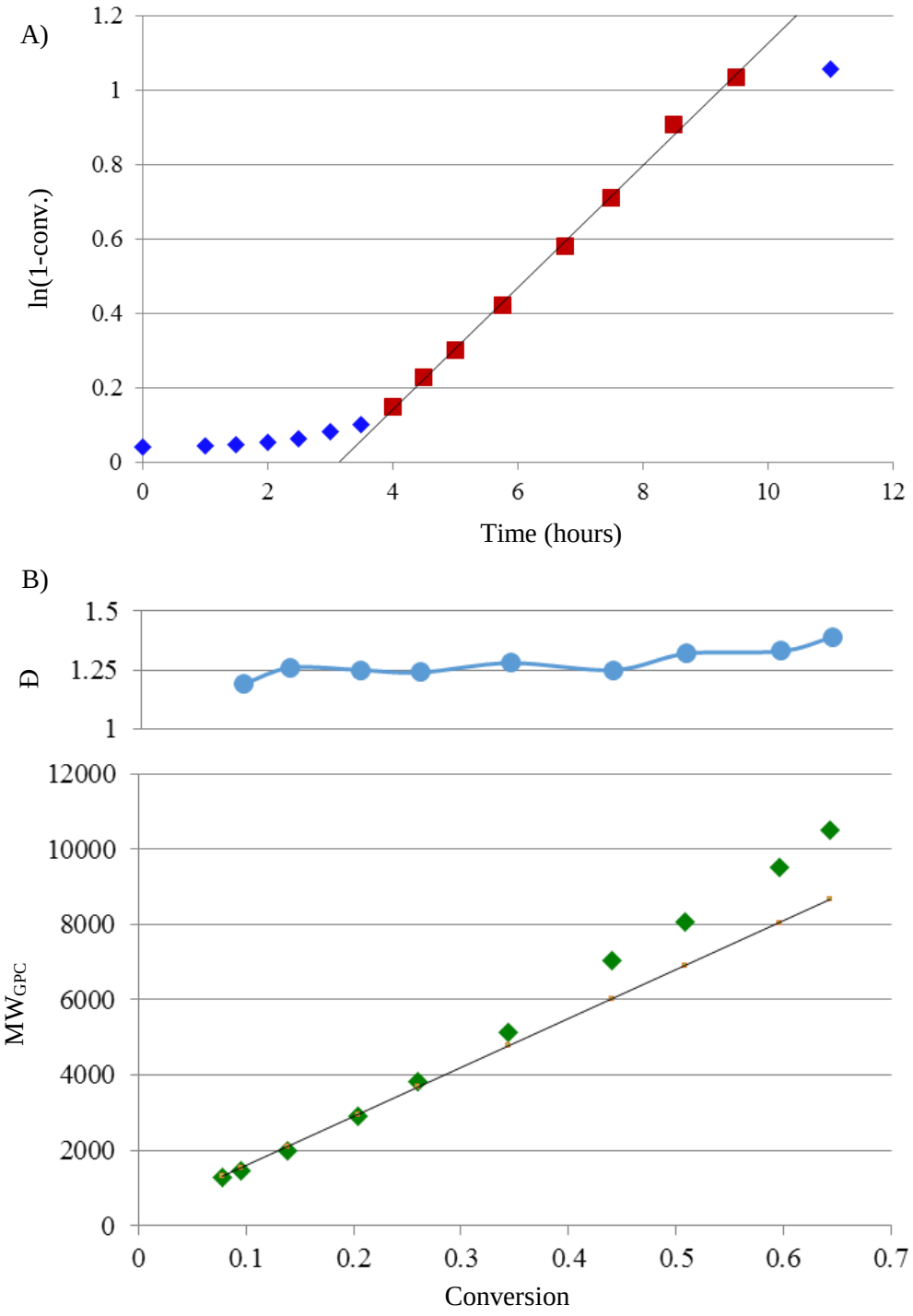


**Figure 114: Kinetics Study of VAc Polymerization Mediated by COE-Xan.**

**A) Conversion vs polymerization time. B) MW vs conversion.**

In Figure 114B, the MW evolution was plotted against the monomer conversion, where the black solid line is the theoretical MW calculated from monomer conversion. It was observed that in the early stage of the polymerization, good agreements between $MW_{GPC}$ and $MW_{theo}$ were achieved, with Đ values around 1.25, indicating well-controlled polymerization kinetics and linear polymer architecture. However, in the later stage, when the conversion went beyond 40%, the measurement $MW_{GPC}$ began to deviate from the theoretical values. These could be attributed to two factors. One is the calibration method using PMMA standards might have led to errors in MW measurement. More important is possibly the presence of side reactions, which is indicated by the raised MW distribution measured by the Đs. Irreversible chain transfer to the allyl position or copolymerization of the C=C in the cyclooctene end-group is highly susceptible.

### 7.2.17 Trithiocarbonate End-group Removal

A typical procedure is described here for polymers with a styrenic end-block. In a reaction vessel, 470 mg Cl-PSt-*b*-PnBA-*b*-PSt (MW ≈ 16.3 kg/mol) was mixed with 27 mg lauroyl peroxide, 120 mg AIBN, 3 mL tolunene, and 2 mL 1,4-dioxane. After being purged with nitrogen for 20 minutes, the vessel was sealed and then heated to 80 ºC. After 10 hours, the reaction mixture was precipitated into EtOH to isolate the modified block copolymer, Cl-PSt-*b*-PnBA-*b*-PSt_ER. The efficiency of the reaction and absence of side reaction were confirmed by $^1$H NMR (Figure 115) and GPC. As shown by the red box in the $^1$H NMR, the SC$\mathbf{H_2}$C$H_2$ peak ($\delta \approx 3.3$ ppm) was seen in the original spectrum, while disappeared in the spectrum after trithiocarbonate cleavage.

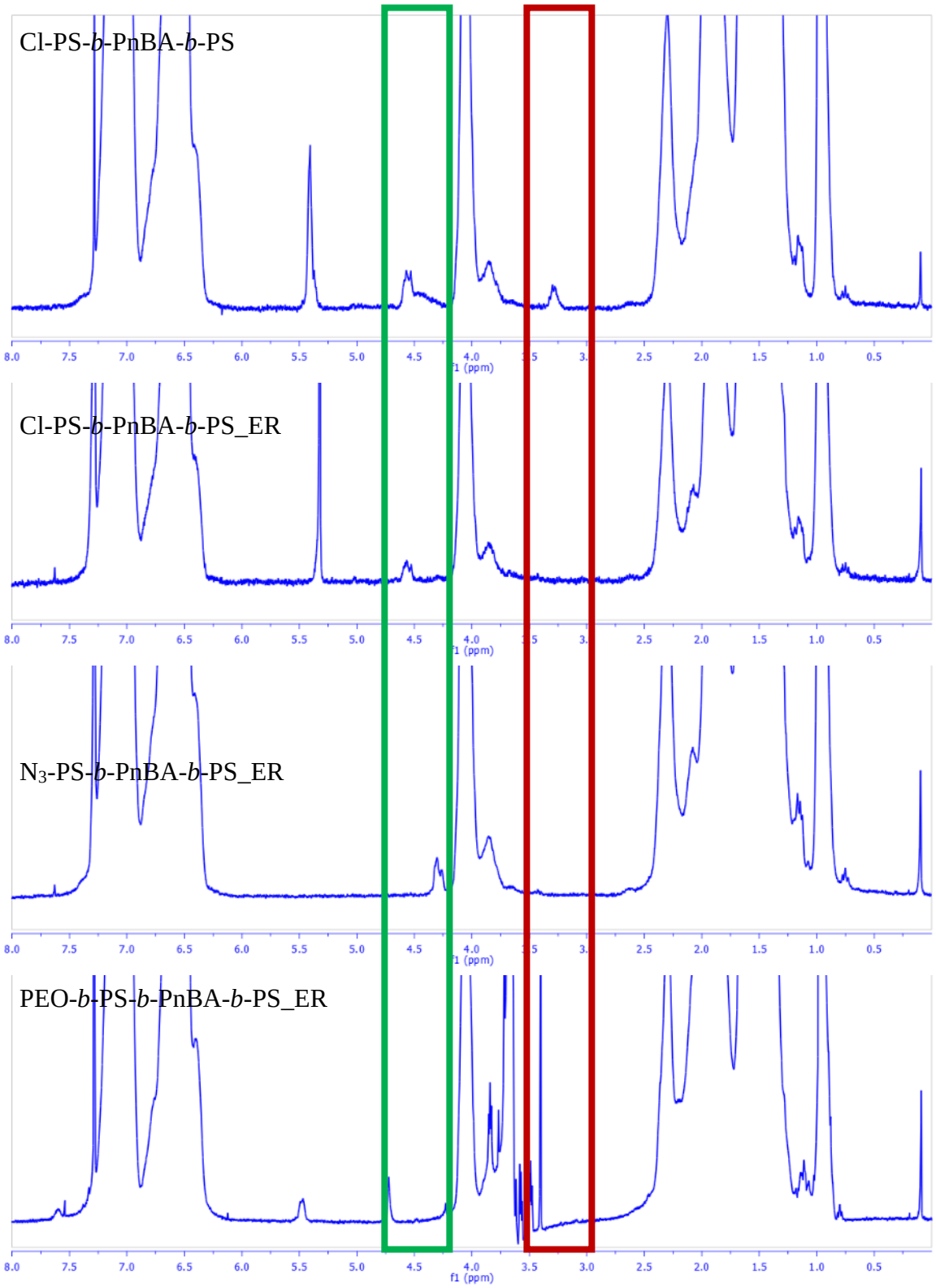


**Figure 115: $^{1}$H NMR Characterization of Cl-PSt-*b*-PnBA-*b*-PSt.**

A typical procedure is described here for polymers with a non-styrenic end-block. In a reaction vessel, 1.86 mg Yne-PMMA (MW ≈ 6.3 kg/mol) was mixed with 238 mg styrene, 3.8 mg AIBN, and 12 mL 1,4-dioxane. After being purged with nitrogen for 20 minutes, the vessel was sealed and then heated to 60 °C. After 48 hours, the reaction mixture was precipitated into hexanes to isolate polymer with a short polystyrene end-block. Then the polymer was subjected to the standard process mentioned above to remove the trithiocarbonate end-group.

### 7.2.18 Azide Installation of Benzyl Chloride Functionalized Polymers

A typical procedure is described here. The polymer, Cl-PSt-*b*-PnBA-*b*-PSt_ER, (310 mg) is dissolved in 3 mL DMF together with 70 mg $NaN_3$. After being heated to 60 °C for 72 hours, the polymer, $N_3$-PSt-*b*-PnBA-*b*-PSt_ER, was isolated by precipitation into methanol twice. Shown by $^1$H NMR in Figure 115 (highlighted with a green box), the peak at δ ≈ 4.6 ppm, assigned to Ar**C$H_2$**Cl disappeared and a new peak at δ ≈ 4.3 ppm was raised, which was assigned to Ar**C$H_2$**$N_3$.

### 7.2.19 "Click" Synthesis of Polymers

A typical procedure is described here. In a reaction vessel, 230 mg alkyne end-functionalized PEO (MW ≈ 4.5 kg/mol) was mixed with 260 mg $N_3$-PSt-*b*-PnBA-*b*-PSt_ER, 5 mg Cu(I)Br, and 5 mL tolunene. The mixture was purged with nitrogen for 20 minutes and then sealed. Using a micro-syringe, 15 μL N,N,N',N",N"-pentamethyldiethylenetriamine (PMDETA) was added to start the reaction. The polymer was precipitated into hexanes and then re-dissolved in dichloromethane to pass through a short column of basic $Al_2O_3$ for removal of Cu species. The polymer was precipitated into hexanes again. Finally, the polymer was stirred for two days in $H_2O$/MeOH (3:1 = v:v) to remove excess PEO. The polymer was filtered and washed with $H_2O$/MeOH (3:1 = v:v) to isolate the product as PEO-*b*-PSt-*b*-PnBA-*b*-PSt_ER. Shown in Figure 115, the peak at δ ≈ 4.3 ppm disappeared indicating the quantitative consumption of the benzyl

azide groups, and the peaks at $\delta \approx 4.7$, 5.5, and 6.6 ppm arose as signals of benzyl triazole. In other cases, hexanes, acetonitrile/MeOH (1:2 = v:v), and diethyl ether/hexanes (1:1 = v:v) were used for the removal of access PtBS, PMMA, and PSt, respectively,

### 7.3 Results and Discussion

First, the syntheses of functional RAFT CTAs are discussed and it will be demonstrated that the single monomer insertion technique is a high-yield preparation platform to incorporate a wide range of functional groups. In the second part, the polymerization of representative monomers, i.e. St, 4-chloromethylstyrene (4CMS), 2-vinylpyridine (2VP), n-butylacrylate (nBA), and N-isopropylacrylamide (NIPAAm), mediated by the synthetic CTAs will be investigated to show the universal efficiency of the CTAs. Comparison with benzyl butyl trithiocarbonate is presented to verify the importance of the chemical structure in controlled polymerization. Finally, examples of end-group transformation on the functionalized polymers will be presented to prove their fidelity during controlled polymerizations.

#### 7.3.1 Synthesis of functional CTAs

Our synthetic protocol, as shown in Figure 116, was based on styrenic monomers and started from O-CTA, since O-CTA had been widely demonstrated highly efficient in mediating the polymerizations of styrenic monomers.

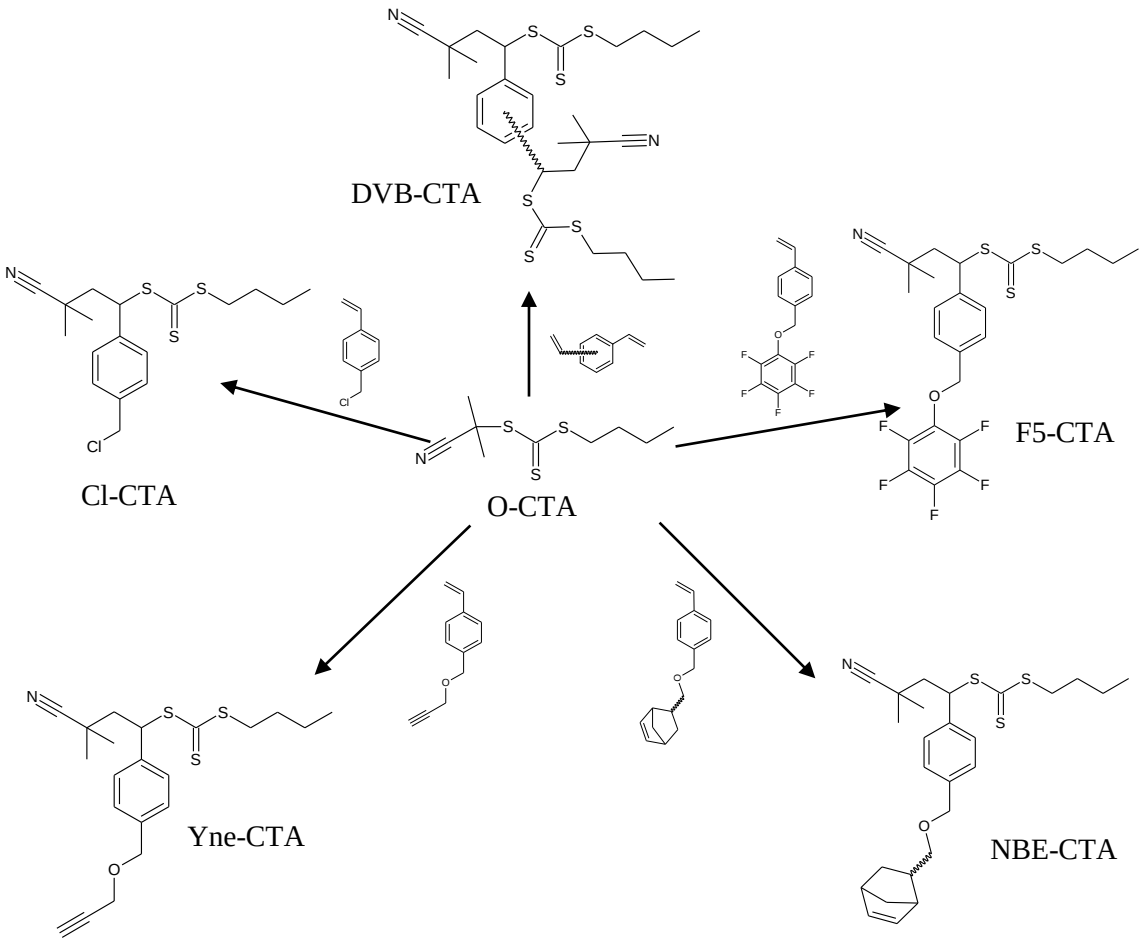


**Figure 116: Synthetic Protocol of Functional RAFT CTAs by Single Monomer Insertion.**

A benzyl chloride group was installed into the first CTA, Cl-CTA, which can be easily transformed into a wide variety of functionalities such as quaternary ammonium, phosphonium, azide, RAFT CTA, etc. To synthesize this molecule, one equivalent of commercial 4CMS was allowed to react with O-CTA, in the presence of 0.1-0.2 equivalent of AIBN as the initiator. This reaction was very similar to a typical RAFT polymerization, except for the amount of the monomer feed ratio was largely reduced. When the reaction was initiated by cyanoisopropyl radical produced by thermal degradation of AIBN, the chain transfer reaction took place. One 4CMS unit was added to an active radical, either from the initiator or the CTA. The chloromethylstyrene unimer radical was quickly capped with a trithiocarbonate before it propagated with a second monomer, due to the

extremely high chain transfer rate of trithiocarbonate. Due to the significantly lower preference in bonding with trithiocarbonate, cyanoisopropyl radical was the dominating active radical species in the chain transfer equilibrium, while most of the unimers were capped with trithiocarbonates, until all of the cyanoisopropyl radicals were consumed (Figure 117). By controlling the feed ratio of monomer, the extent of propagation was limited to only one monomer (DP = 1). Typically, the monomers were fully consumed after 24 hours, leaving the unimer being the major product in the reaction mixture. After column chromatography, Cl-CTA was obtained in 88% yield as a highly viscous yellow oil, indicating that the benzyl chloride group was inert in this radical process. A very interesting phenomenon was observed in the $^{1}$H NMR spectra (Figure 95, 96, 98, 101, and 104). Two singlets were assigned to the two methyl groups of the 2-cyano-2propyl group. This was attributed to the fact that the carbon connecting the phenyl ring and the trithiocarbonate was a chiral center, which differentiated the chemical environments of the methyl groups.

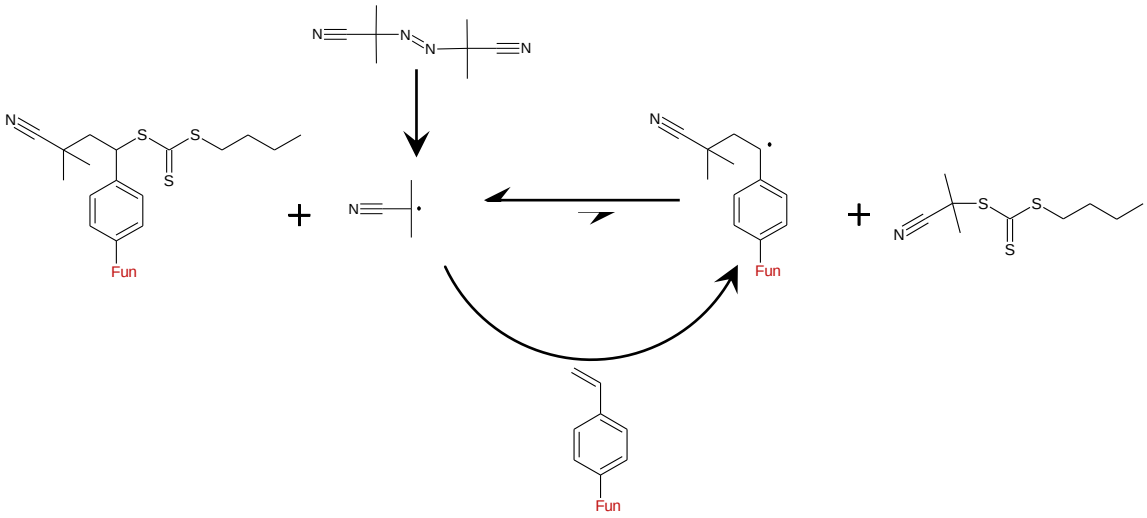


**Figure 117: Reaction Mechanism of Single Monomer Insertion.**

**Table 11: List of Polymerizations Mediated by Cl-CTA, DVB-CTA, and F5-CTA.**

| CTA | # | M | Reaction Time (Hours) | $[M]_0$:[CTA]:$[I]_0$ (:[Solvent]) | conv. | $DP_{theo}$ | $DP_{exp}$ | $MW_{GPC}$ (g/mol) | Đ |
|---|---|---|---|---|---|---|---|---|---|
| Cl | 1 | St | 25 | 150:1:0.11 | 68% | 102 | 99 | 9.8k | 1.06 |
| | 2 | St | 50.5 | 201:1:0.08 | 53% | 106 | 106 | 9.9k | 1.06 |
| | 3 | nBA | 26 | 150:1:0.08(:100) | 97% | 146 | 153 | 21k | 1.06 |
| | 4 | nBA | 11.5 | 150:1:0.1(:100) | 90% | 135 | 139 | 19.3k | 1.07 |
| | 5 | NIPAAm | 18 | 1:50:0.08(:312)[a] | 97% | 48 | 47 | 12.1k | 1.11 |
| | 6 | Ip | 20 | 658:1:0.1 | 19% | 125 | 129 | 12.4k | 1.31 |
| DVB | 1 | St | 24 | 200:1:0.13 | 31% | 62 | 64 | 6.6k | 1.07 |
| | 2 | St | 72 | 200:1:0.07 | 60% | 120 | 123 | 12.3k | 1.06 |
| | 3 | 4CMS | 24 | 122:1:0.11 | 36% | 44 | 45 | 6.3k | 1.09 |
| | 4 | St+4CMS | 46 | (101+143):1:0.09 | N.D. | - | 59+69 | 12.6k | 1.07 |
| | 5 | St+4CMS | 94.5 | (105+144):1:0.09 | N.D. | - | 71+78 | 15.2k | 1.07 |
| | 6 | 2VP | 12 | 200:1:0.11 | 57% | 114 | 121 | 10k | 1.08 |

| | | | | | | | | | |
|---|---|---|---|---|---|---|---|---|---|
| | 7 | nBA | 8.5 | 150:1:0.15(:100) | 84% | 126 | 127 | 18.8k | 1.06 |
| | 8 | NIPAAm | 29 | 150:1:0.12(:766) | 77% | 116 | N.D. | 23.5k | 1.10 |
| F5 | 1 | St | 29 | 100:1:0.07 | 38% | 38 | 36 | 3.9k | 1.06 |
| | 2 | St | 74.5 | 200:1:0.09 | 63% | 126 | 124 | 11.8k | 1.05 |
| | 3 | 4CMS | 24 | 100:1:0.08 | 42% | 42 | 43 | 5.8k | 1.08 |
| | 4 | 2VP | 12 | 100:1:0.1 | 49% | 49 | 50 | 4.2k | 1.06 |
| | 5 | nBA | 11 | 150:1:0.1(:100) | 81% | 122 | 124 | 16.5k | 1.06 |
| | 6 | NIPAAm | 29 | 109:1:0.12(:522) | 87% | 95 | 98 | 17.2k | 1.09 |

[a]Here 1,4-dioxane is used as the solvent, while in other cases chlorobenzene and DMF were used for nBA and NIPAAm, respectively.

The second RAFT agent, DVB-CTA, is a molecule bearing two trithiocarbonate groups, since we realized the tremendous research interests received by symmetric BAB or CBABC multiblock copolymers. This CTA reagent was synthesized by reacting two equivalents of O-CTA with divinylbenzene. Herein, we used the commercial *para*- and *meta*- isomer mixture, and thus the product was actually a mixture of *para*- and *meta*- couterparts. After workup, the isolated yield was as high as 83%. This indicated that the complication in molecular architecture did not affect the efficiency of the synthetic protocol. It should be noted that DVB-CTA is different from DBX-CTA reported in literature,[132,319–321] since it has one methylene groups on each of the benzyl carbon atoms.

To introduce pentafluorophenyl ether, alkyne, and NBE groups, F5-CTA, Yne-CTA, and NBE-CTA were synthesized by similar manners, where synthetic styrenic monomers were used. In the first step, 4-vinylbenzyl chloride was substituted by pentafluorophenolate, 2-propynoxide, or 5-norbornene-2-methoxide (mixture of *endo*- and *exo*-), respectively to conveniently provide the desired molecules. After that, the styrenic monomers were utilized in single monomer insertion. The synthesis of F5-CTA resulted in relatively simple product with high yield (90%) after isolation, because of the high stability of pentafluorophenolate group. However, the other two CTAs were acquired in lower yield (75% and 73% respectively). This was attributed to the non-negligible side reactions on the alkyne and NBE. Likely, radical addition to the C≡C and C=C bonds had a significant contribution. However, it was still reasonable to conclude that our synthetic protocols displayed universal high efficiency and might provide a useful platform for functional CTA synthesis.

### 7.3.2 Controlled Radical Polymerization

The monomers, St, 4CMS, 2VP, isoprene (Ip), nBA, and NIPAAm were subjected to polymerization mediated by the functional CTAs in this section, as they are not only good

representatives of styrenics, dienes, acrylates, and acrylamides, but also widely adopted in various applications.

Cl-CTA was verified in the synthesis of semitelechelic polymers bearing a benzyl chloride group at the α-end. The polymerization results were summarized in the first section of Table 11. The theoretical degree of polymerization ($DP_{theo}$) was calculated from monomer conversions. The experimental degree of polymerization ($DP_{exp}$) was determined by end-group analysis using $^{1}H$ NMR. Our results showed that $DP_{theo}$ matched well with $DP_{exp}$ values. It proved that every CTA molecule propagated into one polymer chain. Both $DP_{theo}$ and $DP_{exp}$ conformed closely to the molecular weight measured by GPC ($MW_{GPC}$), which indicated that the number of chains was determined by the amount of CTA. However, larger deviation on PNIPAAm was detected. We attributed deviation from the failure of the calibration method. The molecular weight (MW) distributions were very narrow as indicated by the Đ values measured by GPC. In most of the polymerizations, the Đs were as low as 1.1 even at very high conversions (>90%), which were close to those achieved in anionic polymerization. Indeed, the Đ value of the telechelic PIp was slightly higher, but it was similar with other reports.[77135] This data provides strong evidence of the absence of side reactions, such as irreversible chain transfer to the benzyl chloride position. Based on all these observations, it was concluded that Cl-CTA could be a universal CTA for controlled polymerizations.

**Table 12: List of Polymerizations Mediated by Bz-CTA.**

| # | M | Reaction Time (Hours) | $[M]_0$:[CTA]:$[I]_0$ (:[Solvent])[a] | conv. | $DP_{theo}$ | $DP_{exp}$ | $MW_{GPC}$ (g/mol) | Đ | CTA conv. |
|---|---|---|---|---|---|---|---|---|---|
| 1 | St | 30 | 100:1:0.07 | 34% | 34 | 45 | 4.5k | 1.19 | 84% |
| 2 | 4CMS | 29 | 100:1:0.08 | 46% | 46 | 85 | 9.5k | 1.34 | 72% |
| 3 | 4CMS | 50 | 100:1:0.09 | 65% | 65 | 98 | 10.9k | 1.32 | 83% |
| 4 | 2VP | 7 | 100:1:0.08 | 45% | 45 | 83 | 6.1k | 1.26 | 79% |
| 5 | nBA | 14 | 150:1:0.08(:100) | 89% | 134 | 138 | 18k | 1.08 | >98% |
| 6 | NIPAAm | 25.5 | 113:1:0.12(:552) | 95% | 107 | N.D. | 19.6k | 1.12 | >98% |
| 7 | Ip | 20 | 182:1:0.1 | N.D. | - | 31 | 3.1k | 1.28 | - |

[a]Chlorobenzene and DMF were used as the solvents for nBA and NIPAAm, respectively.

Similar investigation was conducted on DVB-CTA as shown in the middle section of Table 11. Low Đ values and were observed in all of the polymers, indicating the full conversion of CTAs and the absence of side reactions. Again in most cases, good conformance between $DP_{exp}$ and $MW_{GPC}$ values was obtained. It was rationally concluded that complication in architecture did not sacrifice the efficiency of the CTA.

F5-CTA was applied in mediating polymerizations as well. The resulting polymers all revealed similar low Đ values and excellent agreement between $DP_{theo}$, $DP_{NMR}$, and $MW_{GPC}$. To certify the inertness of the fluorinated terminus, a representative polymerization mixture was tested by $^{19}F$ NMR. Only three broadened peaks were displayed at similar chemical shifts with those of F5-CTA (Figure 118). It was concluded that the pentafluorophenol ether group was preserved during the polymerization.

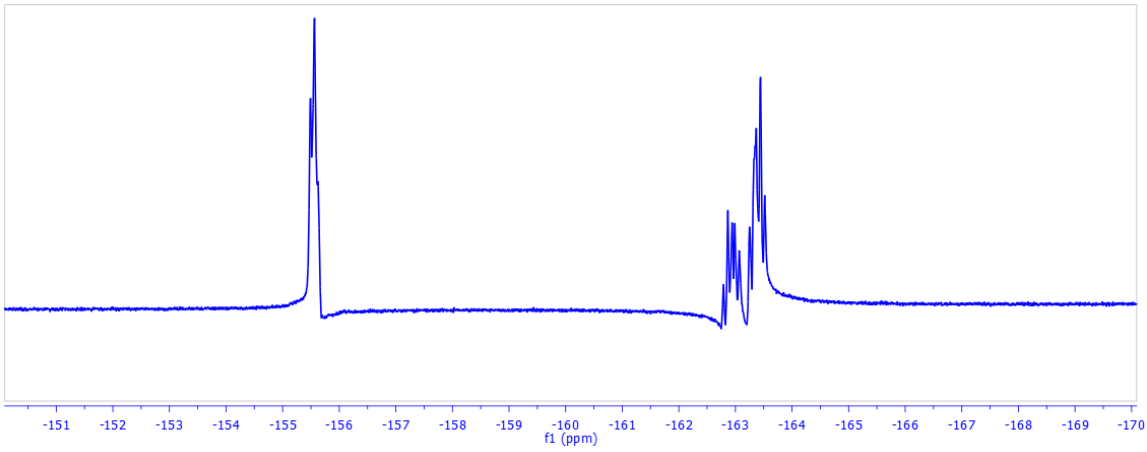


**Figure 118: $^{19}F$ NMR Spectrum of F5-P2VP Polymerization Mixture.**

For comparison, Bz-CTA was applied in similar polymerizations (Table 12). However, significant mismatching between MWs by $^{1}H$ NMR, GPC, and conversion, were observed in St, 4CMS, and 2VP polymerizations. The deviation indicated partial consumption of the CTAs. It was visualized by the yellow solutions after precipitating polymerization mixtures (Figure 119). More

evidence was achieved by performing $^{1}H$ NMR on the polymerization mixtures (Figure 120). It was found that the DP measured by NMR was higher than that calculated from conversions of monomer and CTA. This was caused by the fractionation effect in precipitation. It suggested that the real MW should be slightly lower than $MW_{GPC}$ and the Đ was underestimated. On the contrary, the polymerizations mediated by Cl-CTA, DVB-CTA, and F5-CTA resulted in quantitative CTA conversions within experimental errors and precipitating these polymerization mixtures only provided colorless solutions. In addition, broader MW distributions were obtained with St, 4CMS, and 2VP mediated by Bz-CTA, which was directly related to the incomplete CTA conversions. Since the CTAs were only slowly converted, new polymer chains were gradually generated during the whole polymerization period, instead of fast generation of all the polymer chains in a typical controlled polymerization. That led to a broad distribution of chain lengths. These experiments demonstrated the importance of the extra methylene group at the benzylic carbon on controlled polymerization of styrenic monomers, despite that the functional group on the phenyl ring might provide minor effect on the polymerization control. This was because it provided a hyperconjugation effect to further stabilize the transient benzylic radical. The stability of the leaving radical is critical for successful RAFT chain transfer. Reflecting on the reports regarding the loss of end-group functionalities, we speculate a partial contribution might be from the non-quantitative CTA consumption.[294,295,299,322]

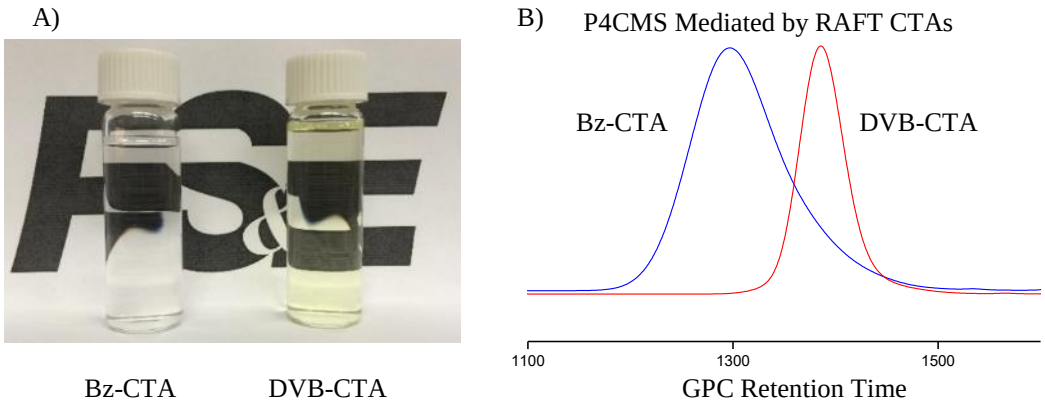


**Figure 119: Comparison between DVB-CTA and Bz-CTA.**

**A) The filtrate produced when precipitating polymers from the polymerization mixture. B) The GPC traces of produced polymers.**

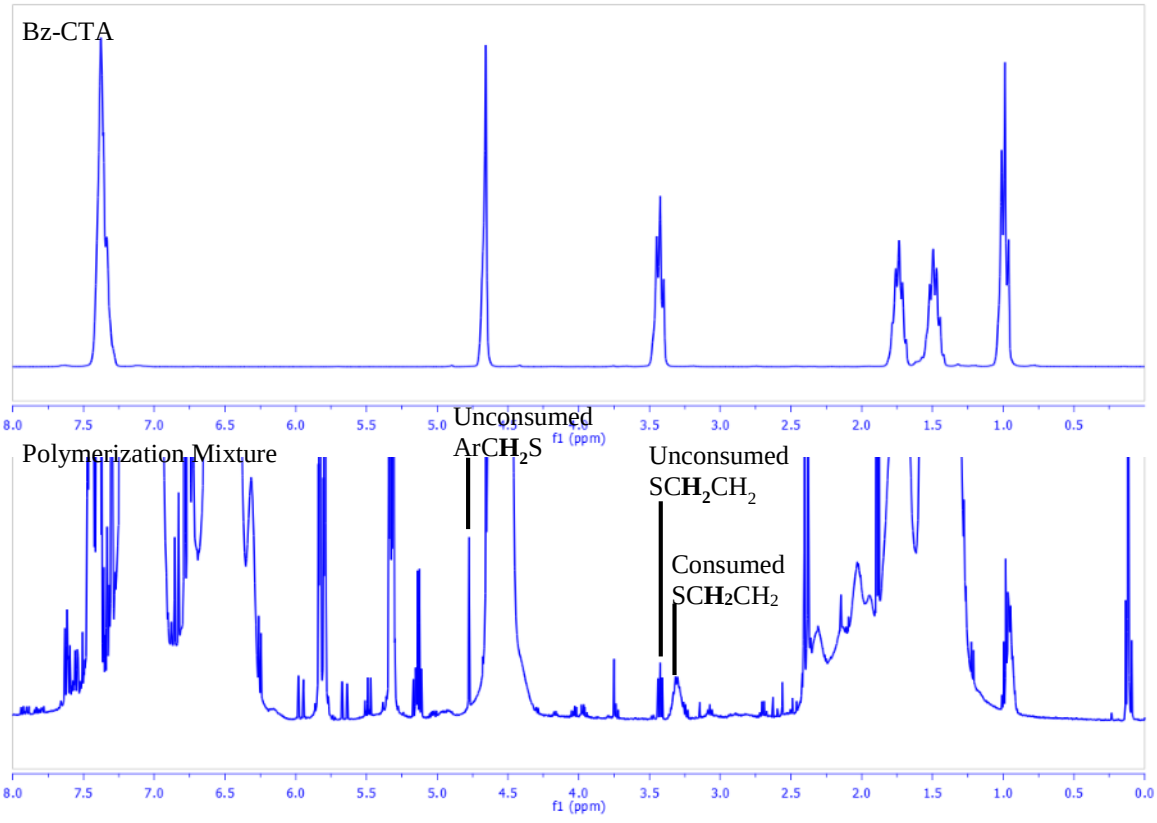


**Figure 120: $^{1}$H NMR of Bz-CTA and a Representative Polymerization Mixture.**

Next, the CTAs bearing more labile groups, i.e. alkyne and norbornene, will be discussed (Table 13). These functional groups had been known to undergo radical additions. Hemitelechelic polymers of St, 4CMS, and 2VP, were achieved with narrow dispersities at relatively high conversions and excellent coincidence in MW analysis. However, the polymerizations of nBA and NIPAAm seemed more complicated. In the case of Yne-CTA mediated nBA polymerizations, the MW distribution slightly broadened at elevated conversions. However, this was not due to partial CTA consumption, since $DP_{exp}$ still matched $DP_{theo}$. Investigating the GPC traces more carefully, a high molecular weight shoulder was clearly observed. The MW at the peak of the shoulder was measured to be precisely twice as high as that of the main peak (Figure 121). It should also be noted that the shoulder observed in GPC continued to even higher MW. It indicated that the alkyne groups underwent radical copolymerization, though its radical homopolymerization was extremely difficult. This assumption was supported by previous research on the copolymerization of acetylene with styrene and acrylate. It was found that 1-hexyne had significantly higher copolymerization tendency with methyl acrylate than with styrene.[323] This was explained by the monomer polarity effect. Alkyne group was usually considered electron rich, and thus preferred to react with an acrylate as a strong electron acceptor, instead of electron donating styrenics, weakly electron accepting NIPAAm, or another alkyne. To suppress this phenomenon, the nBA conversions was reduced to below 50% and unimodal MW distribution was restored.

**Table 13: List of Polymerizations Mediated by Yne-CTA and NBE-CTA.**

| | # | M | Reaction Time (Hours) | $[M]_0$:[CTA]:$[I]_0$ (:[Solvent]) | conv. | $DP_{theo}$ | $DP_{exp}$ | $MW_{GPC}$ (g/mol) | Đ |
|---|---|---|---|---|---|---|---|---|
| Yne-CTA | 1 | St | 45 | 200:1:0.08 | 50% | 100 | 103 | 10.4k | 1.06 |
| | 2 | 4CMS | 27 | 100:1:0.09 | 51% | 51 | 49 | 6.8k | 1.08 |
| | 3 | 4CMS | 70 | 150:1:0.09 | 58% | 87 | 87 | 10.5k | 1.07 |
| | 4 | 2VP | 7.5 | 100:1:0.12 | 59% | 59 | 62 | 5.1k | 1.08 |
| | 5 | nBA | 11 | 150:1:0.1(:100) | 91% | 136 | 133 | 21.3k | 1.18[b] |
| | 6 | nBA | 5.5 | 150:1:0.11(:100)[a] | 71% | 107 | 108 | 15.3k | 1.09[b] |
| | 7 | nBA | 11.5 | 200:1:0.07 | 55% | 110 | 115 | 15.3k | 1.08 |
| | 8 | nBA | 6.5 | 302:1:0.07 | 47% | 142 | 143 | 19.8k | 1.08 |
| | 9 | NIPAAm | 24 | 100:1:0.09(:524 )[a] | 94% | 94 | 91 | 19.4k | 1.13 |

| | # | M | Reaction Time (Hours) | $[M]_0$:[CTA]:$[I]_0$ (:[Solvent])[a] | conv. | $DP_{theo}$ | $DP_{exp}$ | $MW_{GPC}$ (g/mol) | Đ |
|---|---|---|---|---|---|---|---|---|---|
| NBE-CTA | 1 | St | 78 | 200:1:0.08 | 63% | 126 | 126 | 11.5k | 1.05 |
| | 2 | St | 42.5 | 200:1:0.09 | 44% | 88 | 86 | 8.7k | 1.07 |
| | 3 | 4CMS | 48 | 128:1:0.1 | 71% | 91 | N.D. | 13.1K | 1.08 |
| | 4 | 2VP | 15 | 100:1:0.08 | 66% | 66 | 65 | 4.9k | 1.09 |
| | 5 | nBA | 19 | 256:1:0.08(:250) | 83% | 212 | 206 | 37.4k | 1.21[b] |
| | 6 | nBA | 13.5 | 300:1:0.08(:150) | 77% | 231 | 220 | 37.7k | 1.23[b] |
| | 7 | nBA | 19.5 | 100:1:0.03 | 23% | 23 | 21 | 3.3k | 1.12 |
| | 8 | NIPAAm | 24 | 101:1:0.1(:503) | 91% | 91 | 94 | 21.8k | 1.18[b] |
| | 9 | NIPAAm | 18 | 101:1:0.1(:503) | 16% | 16 | 15 | 4.0k | 1.17 |

[a]Here 1,4-dioxane is used as the solvent, while in other cases chlorobenzene and DMF were used for nBA and NIPAAm, respectively. [b]High MW shoulder was observed

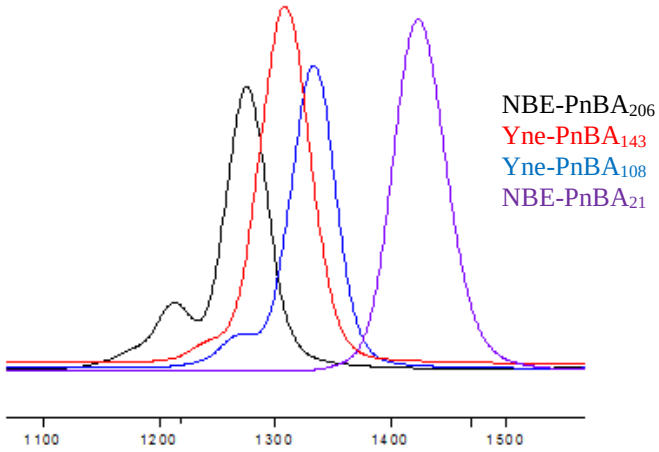


**Figure 121: GPC Traces of PnBA.**

The radical addition to NBE group was even more severe. Despite that styrenic polymerization mediated by NBE-CTA persisted to be unimodal in MW distribution, at high conversions NBE-nBA polymers resulted in very large high MW shoulder in GPC profiles (Figure 121). An observable high MW fraction was also found in NBE-PNIPAAm. This was because the highly strained C=C bond endowed norbornene with remarkably larger polymerization tendency than alkyne in a radical mechanism. [324,325]

Another interesting side reaction should not be neglected in NBE-P4CMS. Suggested by $^{1}$H NMR spectra, the intensity of the C=C bonds in NBE slowly diminished, although very low Đ values were still achieved. However, this side reaction was observed with neither St nor 2VP. It is possible that the benzyl chloride group was slowly hydrolyzed with moisture to generate HCl, which quickly saturated the strain C=C bond in norbornene.

Controlled polymerizations mediated by multifunctional CTAs were also conducted. The results are listed in Table 14

**Table 14: List of Polymerizations Mediated by Multifunctional CTAs.**

| | # | M | Reaction Time (Hours) | $[M]_0$:[CTA]:$[I]_0$ (:[Solvent])[a] | conv. | $DP_{theo}$ | $DP_{exp}$ | $MW_{GPC}$ (g/mol) | Đ |
|---|---|---|---|---|---|---|---|---|---|
| Yne-Cl-CTA | 1 | St | 48 | 200:1:0.08 | 54% | 108 | 104 | 11.1k | 1.08 |
| | 2 | tBS | 22.5 | 200:1:0.08 | 46% | 92 | 91 | 13.4k | 1.10 |
| | 3 | nBA | 14 | 200:1:0.06(:300)[a] | 67% | 134 | 128 | 18.5k | 1.09 |
| $Yne_2$-$TTC_2$ | 1 | tBS | 48 | 240:1:0.12(:240)[a] | 39% | 94 | 101 | 13.8k | 1.13 |
| | 2 | St | 37 | 300:1:0.09 | 47% | 141 | 139 | 13.2k | 1.11 |
| | 3 | 2VP | 18 | 302:1:0.13 | 62% | 187 | 180 | 12.1k | 1.10 |
| $Cl_3$-$TTC_3$ | 1 | nBA | 14 | 602:1:0.25:(:600)[a] | 85% | 513 | 528 | 68.4k | 1.17 |
| | 2 | St | 120 | 1200:1:0.11 | 42% | 504 | 474 | 46.1k | 1.13 |
| | 3 | St | 72 | 601:1:0.08 | 61% | 367 | 348 | 30.0k | 1.16 |

[a]Chlorobenzene is used as the solvent for nBA, while 1,4-dioxane is used for tBS.

### 7.3.3 Reactions of End Functionalities

Copolymers with complex architecture captured a lot of research interests, thanks to their unparalleled potentials in designing nanostructures. Herein, a few examples of the synthesis of complex copolymers using the CTAs prepared in this chapter are given.

The first attempt was to synthesize symmetric BAB and CBABC multiblock copolymers using DVB-CTA. The BCPs were synthesized using sequential the polymerization-purification process, with the A monomer polymerized first as the center block followed by B and C. The symmetric PSt-*b*-PnBA-*b*-P(St-*ran*-4CMS)-*b*-PnBA-*b*-PSt pentablock copolymer was synthesized as an example. Very narrow MW distributions (Đs ≤1.12) were detected after each step of polymerization (Figure 122). This indicated the trithiocarbonate end-group was highly persistent. The higher MW shoulder was caused by minor bimolecular termination, however, the overall MW distribution remained very narrow. It should be noted that the AIBN feed ratio were kept low to minimize the generation of free polymer chains that were not attached to phenylene center group.

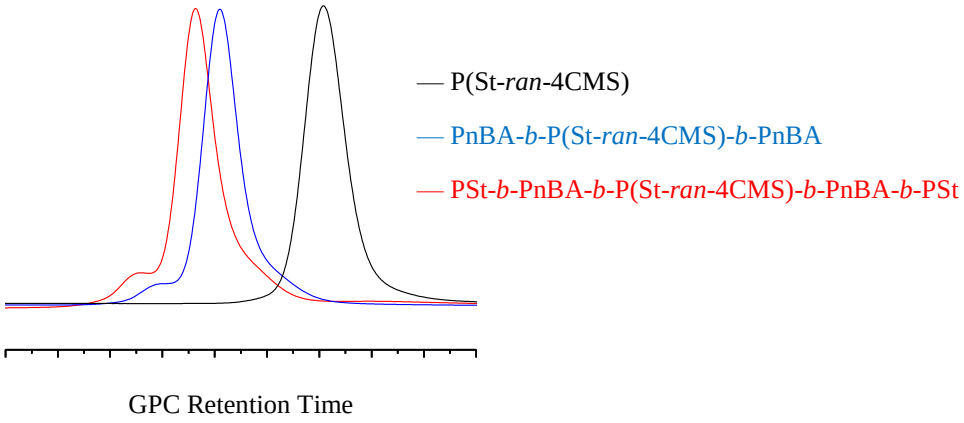


**Figure 122: GPC Traces of PnBA-*b*-P(St-*ran*-4CMS)-*b*-PnBA-*b*-PSt.**

The benzyl chloride functionalities may also be versatile in applications. The chloride was transformed into azido functionality for subsequent "click" incorporation of another block. A Cl-PSt sample was first subjected in trithiocarbonate removal, as it was discovered to be highly reactive with azide anion.[272] The trithiocarbonate terminated polymer was allowed to react with a large excess of AIBN and two equivalents of lauroyl peroxide. This reaction replaced the trithiocarbonate with an inert group, i.e. 2-cyanoisopropyl. During this process, a small high MW shoulder was indeed observed. It was attributed to minor bimolecular termination. Negligible shifts in MW and Đ were detected by GPC, indicating the absence of chain cleavage and other side reactions. Then nucleophilic substitution was conducted with $NaN_3$ at 60°C to incorporate an azido group while eliminate the chloride. The conversion of the substitution reaction was determined to be quantitative by $^1$H NMR. After these procedures, an alkyne terminated polyethylene oxide (Yne-PEO) was installed onto the α terminus, by the Cu(I) catalyzed "click" reaction at room temperature. Following the removal of catalyst, excess PEO was easily eliminated by selective dissolution. Analysis by GPC was utilized to find a uniform shift in MW and a preserved narrow MW distribution (Figure 123). The low MW tail was attributed to the PSt chains that were initiated by AIBN and without Cl functionality.[326] This can be suppressed by reducing the initiator input in the controlled polymerization. Analysis by NMR measurements confirmed the complete conversion of the benzyl azide group and a good match between the PSt and PEO MWs. It was proved that the azido terminus had very high reactivity and well defined PEO-*b*-PSt was prepared.

To prepare more complex polymer, the Cl-PSt was chain extended with nBA and St successively to yield Cl-PSt-*b*-PnBA-*b*-PSt. Similar end-group modification reactions were conducted. As displayed in the GPC plot (Figure 124), installing each block shifted the peaks uniformly without broadening the dispersities. Excellent agreement between the MWs of each blocks was revealed by NMR spectra. These all confirmed that the benzyl chloride group could be

efficiently retained during multiple steps of radical processes and easily modified. So far Cl-CTA was demonstrated to be a universally efficient tool to synthesize complexed polymer structures.

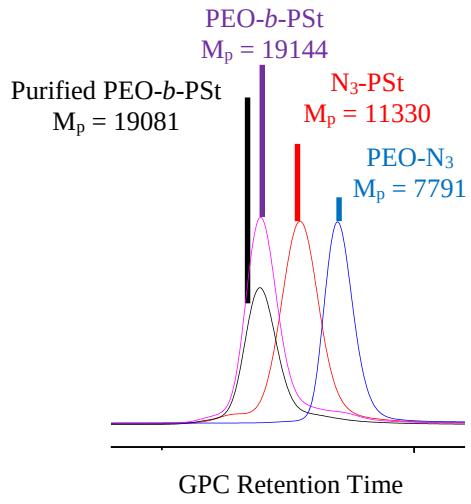


**Figure 123: GPC Traces in PEO-*b*-PSt Synthesis.**

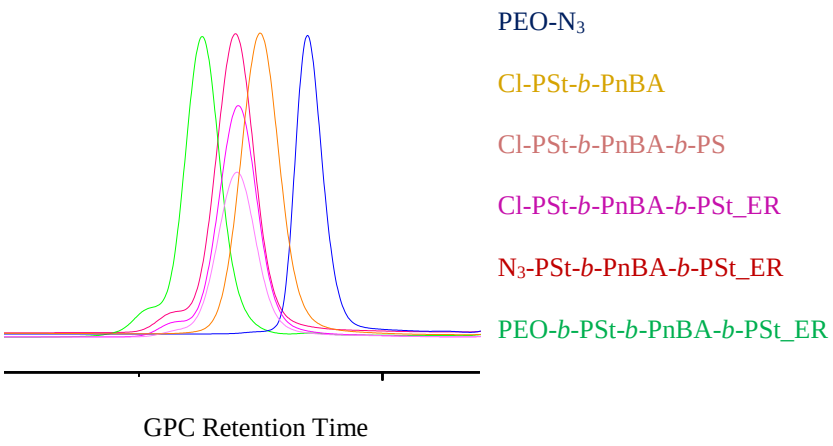


**Figure 124: GPC Traces in PEO-*b*-PSt-*b*-PnBA-*b*-PSt Synthesis.**

An alkyne is another useful functional group. Now to demonstrate this, the alkyne terminated polymers were also used in multiblock copolymer synthesis. These alkyne hemitelechelics seemed more convenient for “click” reactions, if the azido species were readily

available. The removal of trithiocarbonate terminus could be unnecessary, when the reactants and procedures were carefully selected. Transformation of the α end-group was naturally avoided. First, the Yne-PSt was chain extended with nBA to form Yne-PSt-*b*-PnBA. Here, the polymerization of nBA was carefully controlled at very low conversion so that radical addition to alkyne units was prevented. Then the polymer was utilized in "click" reaction with azido-PEO at room temperature. Complete conversion of the alkyne group was easily achieved as proved by $^{1}$H NMR spectra. After passing the DCM solution through $Al_2O_3$ column and precipitation, the precipitated powder was stirred in $H_2O$:MeOH = 3:1 (v:v) mixture to isolated the product. It showed narrow MW distribution (Figure 125).and precise compositional coincidence.

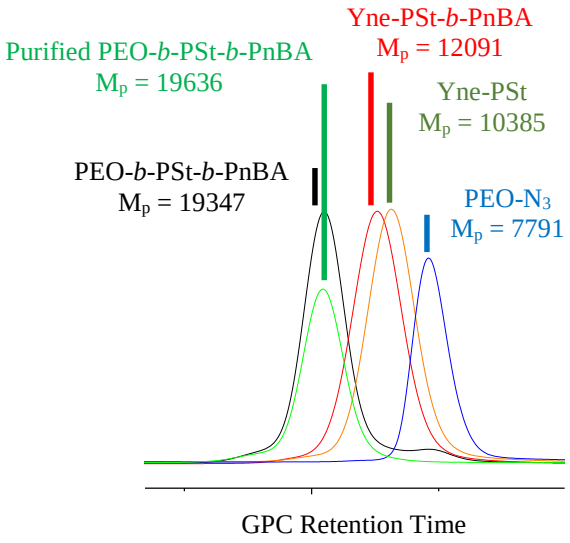


**Figure 125: GPC Traces in PEO-*b*-PSt-*b*-PnBA Synthesis.**

Another example was based on a diblock copolymer, Yne-PSt-*b*-P2VP, which was synthesized by two steps of RAFT polymerization. Although P2VP was known to coordinate strongly with Cu(I) cation, the "click" reaction still proceeded successfully to full conversion of the alkyne moieties. However, the purification workup should be cautiously undertaken. Simply stirring the polymer powder in $H_2O$:MeOH = 3:1 (v:v) mixture was able to isolate well-defined

triblock copolymers by dissolving the residual PEO (Figure 126). But extended interaction time between the solid and liquid resulted in broad MW distribution revealed by GPC tests, where higher MW appeared. It was explained by the fact that the pyridine group in P2VP could react with water to produce a trace amount of pyridinium and hydroxide. Hydroxide anion was so nucleophilic that it cleaved trithiocarbonates, and the resulted free thiol was capable of forming disulfide bonds to alter the overall MW. This is where replacing the trithiocarbonate with an inert group might be necessary.

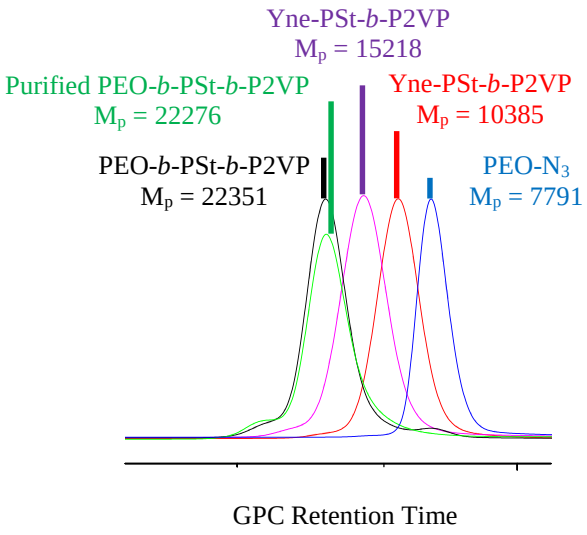


**Figure 126: GPC Traces in PEO-*b*-PSt-*b*-P2VP Synthesis.**

The NBE hemitelechelics were also examined. Among the wide range of chemical reactions involving NBE, Ring-Opening Metathesis Polymerization (ROMP) was performed, where the NBE polymers acted as macromonomers (MM). Grubbs 3$^{rd}$ generation catalyst (G3) was used for its fast initiation kinetics. In this test, NBE-PSt was used in the ratio of [MM]:[G3] = 10:1. After 10 minutes, MM conversion was found to be around 96% based on the integration of GPC profiles. Extended reaction time failed to increase the conversion. The unconverted MMs were not attributed to side reactions on the NBE group. Instead, they were assigned to the non-functional

polymer chains initiated by the radicals from AIBN decomposition. Surprisingly, the resulting graft polymer displayed very narrow MW distribution (Đ = 1.19 for the Poly(NBE-PSt) peak), without any high MW shoulder being observed in GPC traces (Figure 127). This was to the contrary with a previous report,[327] and likely because of the low feed concentration of AIBN used in this chapter, which suppressed the formation of di-norbornene telechelic polymers.

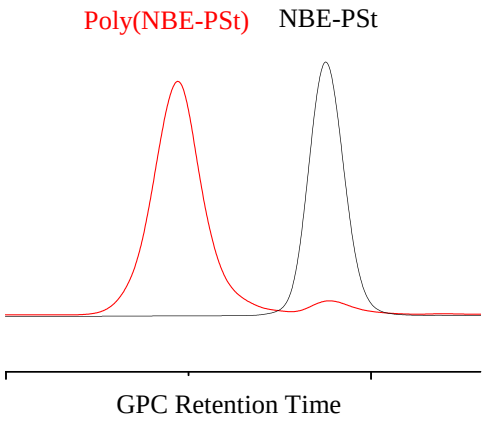


**Figure 127: GPC Traces in Poly(NBE-PSt) Synthesis.**

The synthesis of miktoarm star copolymer is briefly discussed here. Using $Cl_3TTC_3$ as the CTA, $Cl_3(PSt)_3$ was synthesized. Beside a narrow, symmetric major peak in the GPC profile, another low MW shoulder was observed. This was attributed to the free arm fraction as described in Chapter 5. It should be noticed that the free arm polystyrene had no benzyl chloride functionality, due to the fact that the benzyl chloride group was a part of the leaving group that does not shuttle between chains in RAFT mechanism. When calculating the DP of $Cl_3(PSt)_3$, NMR was combined with GPC measurement to give a more accurate value. Since end-group analysis in NMR assumed every polystyrene arm had one trithiocarbonate group, which resulted in $DP_{NMR}$ = 235*3 and was not accurate, the number of styrene units in the free arm fraction was integrated into the star fraction. The free arm peak area fraction was measured by GPC to be 8.6%, and then used as the percentage

of overestimation in NMR results. Subtracting the free arm fraction gave a more realistic value of the DP in the pure star polystyrene being 215*3. The trithiocarbonate cleavage reaction produced narrow dispersed, indicating the suppression of side reactions, such as bimolecular radical coupling. After azide incorporation, the $(N_3)_3(PSt\_ER)_3$ was applied to "click" reaction with Yne-PMMA_ER (DP = 120), which was synthesized by RAFT polymerization mediated by Yne-Ester-CTA and sequential trithiocarbonate cleavage. The resultant polymer was a mixture of $(PMMA)_3(PSt)_3$, Yne-PMMA_ER, and PSt_ER, which was easily purified by washing with diethyl ether/hexanes (1:1 = v:v) and acetonitrile/MeOH (1:2 = v:v). The purified $PMMA_3PSt_3$ showed a narrow peak in GPC, where the high MW shoulder was due to minor intermolecular bimolecular radical coupling, while the low MW shoulder was attributed to an intramolecular termination product (Figure 128). The ratio of polystyrene and PMMA units were well matched with theoretical values, as shown in Figure 129, the peak between δ = 3.4 and 3.7 ppm was assigned to COOC**H**$_3$, while the peak between δ = 6.3 and 7.3 ppm was attributed to aromatic protons in polystyrene.

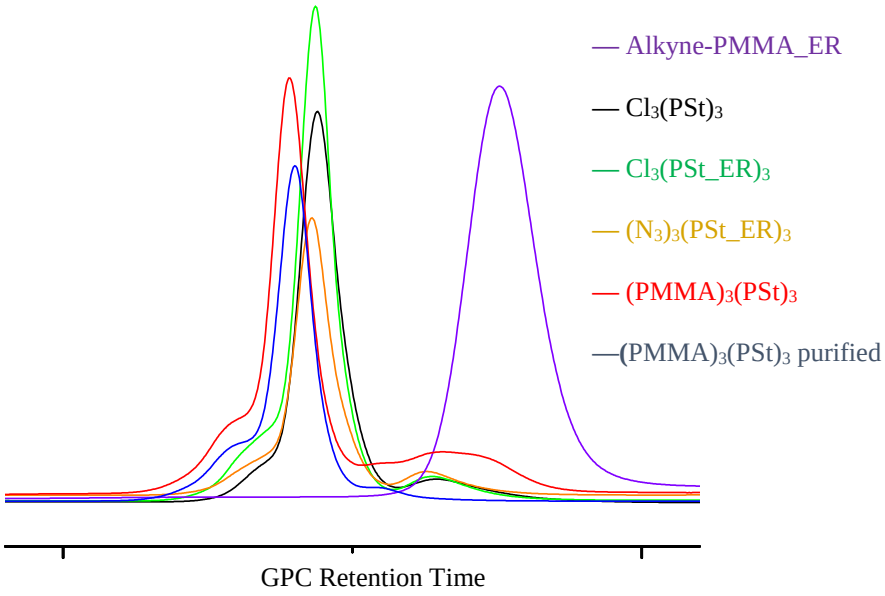


**Figure 128: GPC Traces in $(PMMA)_3(PSt)_3$ Synthesis.**

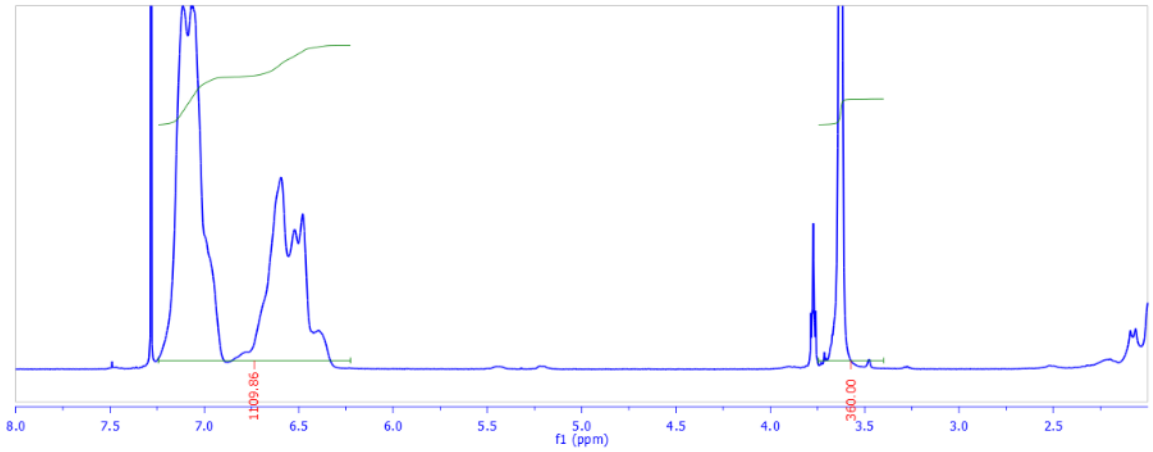


**Figure 129: $^{1}$H NMR Characterization of $(PMMA)_3(PSt)_3$.**

### 7.4 Conclusions

A family of RAFT CTAs are reported in this chapter. They were synthesized via single monomer insertion methodology to introduce functional groups in high yields. Representative monomers were polymerized in the presence of the functional CTAs. By comparison with Bz-CTA, it verified the necessity of the designed chemical structure on controlling the polymerization of styrenic monomers. The controlled polymerization mediated by Yne-CTA and NBE-CTA were carefully investigated. It was found that controlling the conversion of nBA and NIPAAm was critical for obtaining well-defined products. End-group transformation was utilized to demonstrate the preservation of reactivity of the incorporated functionalities. Highly efficient reactions were utilized to prepare multiblock copolymers and graft copolymers. In summary, single monomer insertion can be used as a universal platform for high-efficiency synthesis of functional RAFT CTAs and sequentially applied to produce complex polymer architectures.

# CHAPTER 8

# DISSERTATION SUMMARY AND FUTURE DIRECTIONS

## 8.1 Dissertation Summary

At the beginning of this dissertation, the need for developing fuel cells was addressed because their high power density and reduced emission provide a promising pathway to provide an alternative energy source which may be able to help fill in the gap between energy demand and fossil fuel reserves, as well as limiting global warming. Proton exchange membrane fuel cells were discussed, and the advantages of alkaline anion exchange membrane fuel cells over proton exchange membrane fuel cells were the motivation for this dissertation. In literature, polymeric anion exchange membranes with various architectures were reported, such as random copolymer, block copolymers, and crosslinked polymers. However, the correlation between conductivity and material structure, for example, nanoscale morphology, ion organization, crystallinity in the hydrophobic block, is not well understood. This limits the development of high performance membranes for alkaline anion exchange membrane fuel cells.

In Chapter 2, a series of crosslinked membranes were prepared using a one-step cast/crosslink method, from a neutral precursor, which was synthesized by sequential RAFT polymerization and “click” chemistry. In the quaternized membrane, cationic monomers were covalently linked together. It was demonstrated, by comparing membranes with different compositions, that the organization of ions in the crosslinked membranes can significantly enhance anion conductivity rather than the nanoscale morphology. Excellent hydroxide conductivities were achieved, which were among the highest values ever observed. High performance were obtained on these membranes in fuel cell and water diffusion tests. This work provided a general method to

introduce organization of the functional sites in a crosslinked membrane, and could be widely useful for other transport/separation materials.

Next, block copolymers with phosphonium ions were synthesized by RAFT synthesis of CMS and isoprene based block copolymers and quaternization reaction in Chapter 3. Well-ordered morphologies were achieved. It was found that the ionic blocks preferred to self-assemble into the continuous phases upon solvent cast, evidenced by SAXS and TEM, which was presumably due to the bulky size of phosphonium side group and the charge density. The matrix of hexagonal phases was proved to transport anions significantly faster than lamellae, which expanded the understanding of block copolymer morphology impact on ion conduction.

A special CTA was designed in Chapter 4 to mediate RAFT and ROMP polymerization, which enabled the synthesis of triblock copolymers with a PCOE midblock and PCMS outer blocks. The broad MW dispersity in PCOE block led to poorly ordered morphologies, which, however, provided excellent ion conductivities. It was found that the melting transition (~50 $^{o}$C) of PCOE had important influence on membrane properties. The swelling mechanisms were different: compared with the swelling at 30 $^{o}$C, upon hydration the membrane had significant increase in the inter-domain interface area and thus showed d-spacing decrease until a certain degree of water sorption. The conductivities showed a decrease in the activation energy, when the temperature was increased to above the $T_m$ of PCOE, as well as the loss of mechanical toughness. Although the mechanism of these transitions were not yet fully understood, these materials demonstrated the thermal transition of hydrophobic block can significantly affect both molecular and segmental motion in the hydrophilic domain.

In Chapter 5, star block copolymers were synthesized via RAFT polymerization technique and doped with inorganic salts. The doped polymer were subjected to bulk morphology investigation to demonstrate the concept of adopting polymer architecture to achieve facilitated

microphase separation and smaller feature sizes. In thin films of these salt doped BCPs, SVA was utilized to align the lamellae perpendicular to the substrate to achieve finger print patterns with a d-spacing as small as 12.4 nm.

To achieve hierarchical patterns on a single BCP thin film, an ONB junction containing triblock copolymer, EO-*hv*-SEO, was designed in Chapter 6. Upon UV exposure and sequential SVA, the spacing can be changed for as much as 30%, which was a result of both architecture change and homopolymer swelling. The advantage of this method is that it needs no incorporation of additional monomers, and it is compatible with many monomers that have been used in thin film study.

In Chapter 7, a methodology of RAFT CTA synthesis taking the advantage of the selective initiation phenomenon was investigated. Multiple CTAs were synthesized and applied to controlled radical polymerization. It was demonstrated that this method provides a simple procedure and high yields, and most importantly, can incorporate multiple functional group in an orthogonal manner. It was noted that the chemical structure is important for controlled polymerization of styrenic monomers, by comparison with benzyl butyl trithiocarbonate. Using end-group transformation reaction, these RAFT CTAs were proved to be useful in obtaining complex polymer architectures.

## 8.2 Future Directions

### 8.2.1 Perspective on Chapter 2

The membrane presented in Chapter 2 displayed excellent performance, such as conductivity, water flux, and fuel cell power density. Considering the integrity imparted by the crosslinked network, this material can be a promising candidate for many applications.

One aspect that may need more work on is the chemical stability, although it was found that the membrane showed no obvious degradation after 24 hours in KOH aqueous solution at 80

°C. Various cations have been demonstrated to provide improved base stabilities than benzyl trimethyl ammonium used in this dissertation, such as benzimidazolium and phosphonium.[16,32,128] However, considering neutral precursor polymer is necessary in the membrane formation process, it is recommended to incorporate ammonium with an alkyl bridge[14] or modified imidazolium[69,328,329] by post-casting/crosslinking quaternization. One proposal neutral precursor polymer and the corresponding membrane is shown in Figure 130.

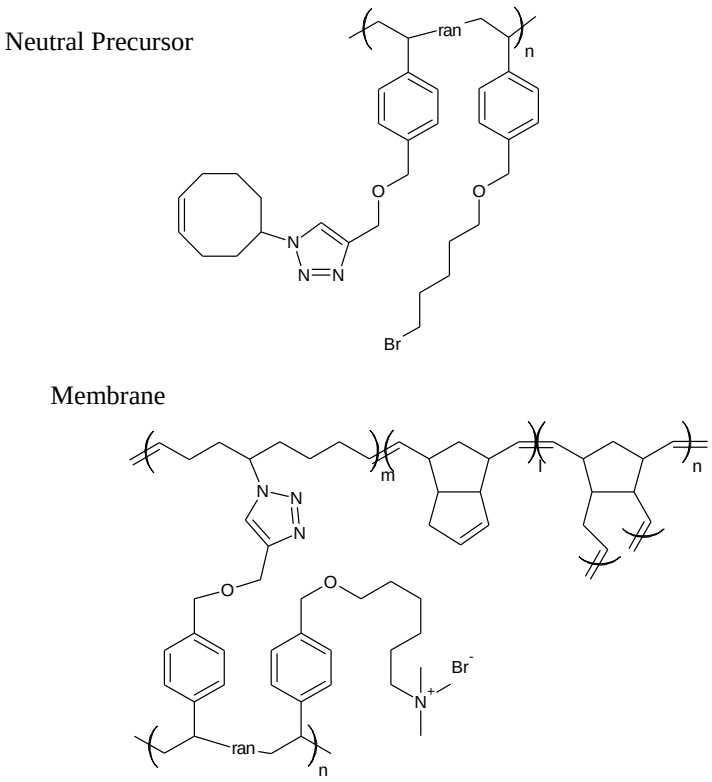


**Figure 130: Proposed Structures for Improved Chemical Stability.**

It is also possible to further improve the conductivity in this material. It was proposed in Chapter 2 that there was an ion conducting channel along the hydrated polycation chain, and thus increasing the ion density along the polycation chain should create a better-defined ionic transport pathway. For example, poly(phenyl oxide) could be brominated on all the methyl groups or installed with chloromethyl or 6-chloro-1-hexyl side groups on all the available phenyl

sites,[17,19,25,29] and thus there will be two alkyl halide groups for quaternization on each monomer unit (Figure 131).

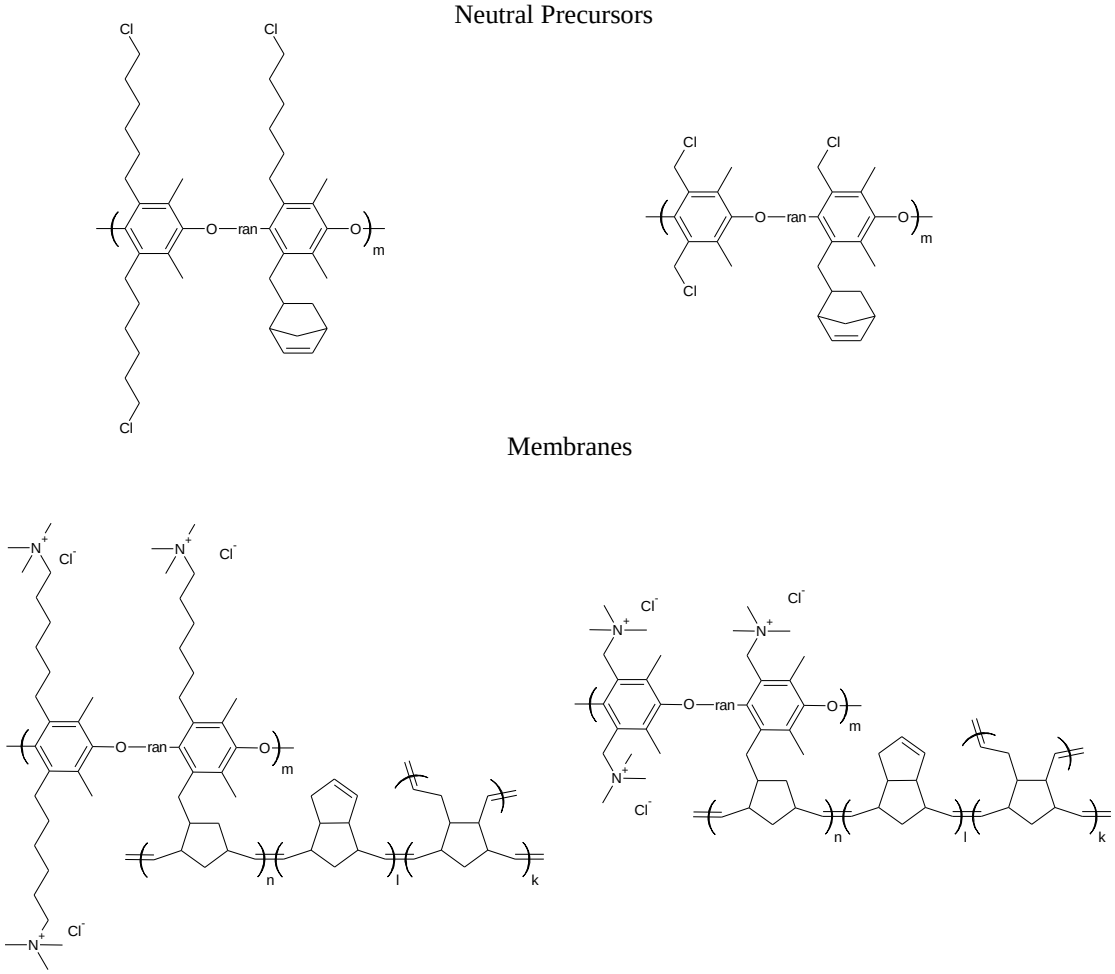


**Figure 131: Proposed Structures for Improved Ion Conduction Channel.**

### 8.2.2 Perspective on Chapter 3

It was found that the phosphonium block copolymers had usually high values of activation energy, which was attributed to the inadequate amount of water molecules absorbed to the ionic domain. Thus, increasing the hydrophilicity may intensely ameliorate the ion conduction. In the synthesis, random copolymer structure was used to increase the solubility and reduce the brittleness

of the ionic block. A directly change would be to use a different comonomer instead of chloromethylstyrene or styrene. Here, it is proposed that a random copolymer of butadiene and chloromethylstyrene can be synthesized via nitroxide mediated polymerization (NMP) in the first step.[330,331] Then the C=C bonds in polybutadiene segments can be readily oxidized into epoxides using 3-chloroperoxybenzoic acid,[332–334] as shown in Figure 132. It should be noted here that NMP has to be used instead of RAFT, considering the reactivity of thioesters based CTAs with peroxy acids.[335] After epoxidation, chain extension with butadiene is expected to yield well-defined block copolymers. Finally, quaternization of CMS and hydrolysis of epoxide are to be undertaken to convert the first block into phosphonium block bearing multiple hydroxyl groups. However, the sequence of quaternization and hydrolysis should be investigated. In addition, it might be better to use acid (HCl is recommended) catalyzed hydrolysis to avoid interrupting the benzyl chloride or phosphonium groups. By adjusting the mole ratio of CMS and butadiene in the first block, and the extent of epoxidation, the hydrophilicity of the ionic block can be systematically tuned and optimized chemical composition can be found.

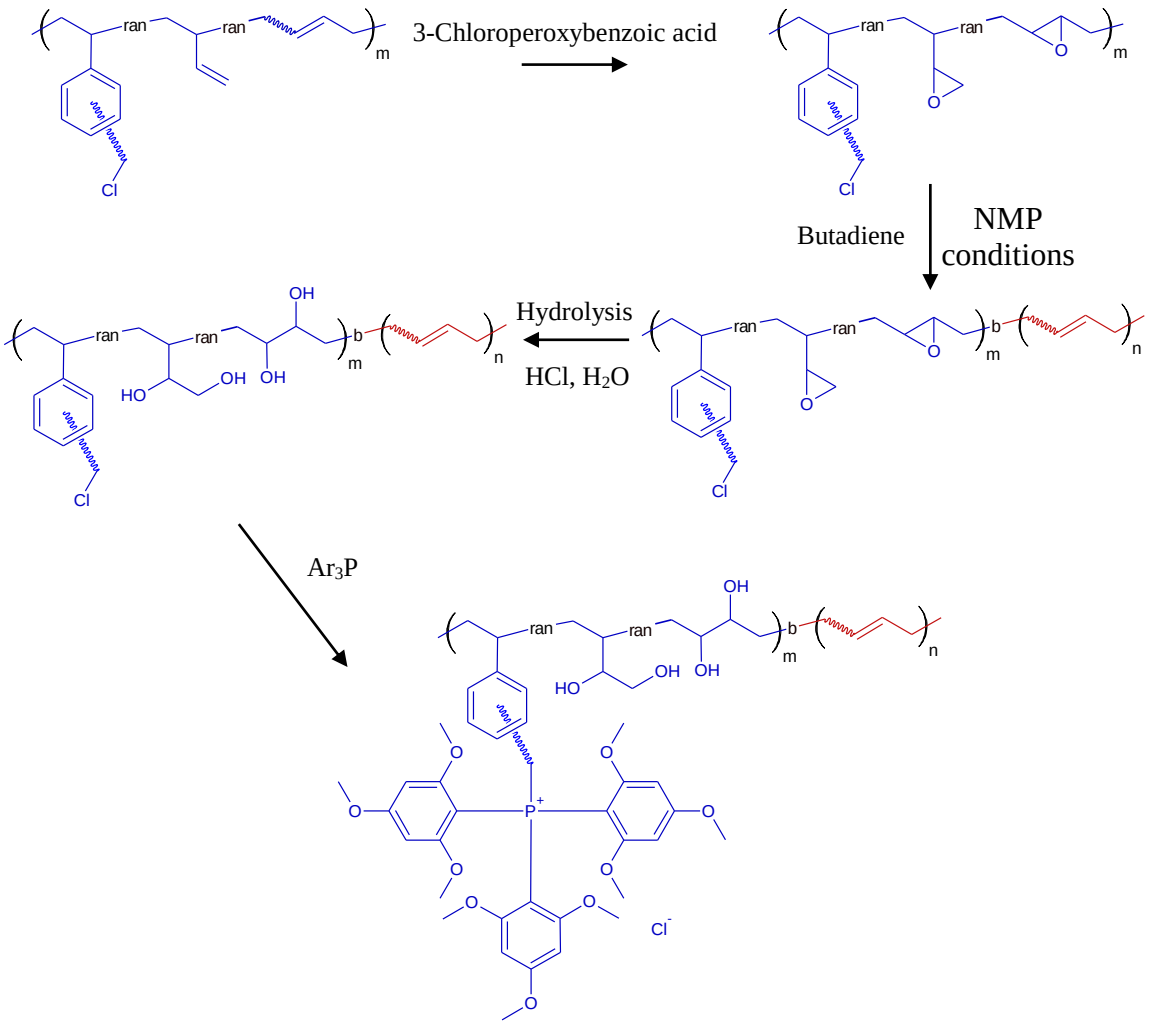


**Figure 132: Proposed Phosphonium BCPs for Improved Water Sorption.**

### 8.2.3 Perspective on Chapter 4

A series of membranes based on triblock copolymers were presented in Chapter 4. The melting transition of PCOE block was shown to affect the membrane properties significantly. However, the mechanism of conductivity transition was not fully understood. Broadband electrical spectroscopy (BES), as a powerful tool being operational in the temperature and frequency range of -105~100 $^{o}$C and 0.01~$10^{7}$ Hz, has been used to understand the electric response and dielectric

relaxations of materials in various hydration states.[336–339] It is expected that BES measurement can reveal more details on the segmental motion and ion mobility.

A direct comparison between low $T_g$ and high $T_g$ polymer as the hydrophobic can be designed in similar manner. Isobutyl methacrylate, ethyl methacrylate, and benzyl methacrylate are optional monomers for the hydrophobic block in a synthetic diblock copolymers because of a few reasons, despite that they are not base stable. First, they are all relatively non-polar monomers and thus should microphase separate strongly from the ionic block, which should facilitate the correlation between morphology and properties. Also, they are readily polymerizable by controlled radical polymerization techniques, which should facilitate the synthesis of well-defined diblock copolymers. Most importantly, the homopolymers of them are show accessible glass transition temperatures (53 $^{o}$C, 65 $^{o}$C, and 54 $^{o}$C,) in the typical operation temperature range (30~90 $^{o}$C) of alkaline anion exchange membrane fuel cells. So it is expected that a transition in membrane performance related to glass transition or fictive temperature can be directly detected within the typical temperatures used in this dissertation.

It also suggested that a reduced $T_g$ in the ionic block should facilitate the investigation under low humidity conditions, since in a high $T_g$ material, the morphology and chain conformation is highly dependent on the processing conditions and thus difficult to isolate the effect of the thermal transition in hydrophobic block. This can be accomplished by polymerizing a carefully selected ionic liquid monomer or synthesizing a random copolymer of ionic/ionizable monomer and lower $T_g$ monomer, such as 2-methoxyethyl acrylate, 2-ethoxyethyl acrylate, and *n*-butyl acrylate. These monomers can be readily polymerized, and also possess relatively low molecular weight, thus copolymerizing which would not change the hydrophobilicity dramatically in the ionic block. The $T_g$ of the homopolymers are -50 $^{o}$C, -50 $^{o}$C, and -54 $^{o}$C, respectively.

In addition, these PCOE based block copolymer may also find applications in shape memory materials. It is known that at the molecular level, the maximum number of temporary shapes a shape memory polymer can memorize correlates directly to the number of discrete reversible phase transitions in the polymer.[340,341] Since the polycyclooctene domain has a readily accessible $T_m$, using the melting/crystallization transition a permanent shape can be stored. At the same time. poly(vinylbenzyl trimethyl ammonium) block has a high $T_g$ but responsive to environmental humidity, which plasticizes the polycation domain to reduce the $T_g$ to below room temperature, and thus another permanent shape can be stored in the ionic domain. This should impart the material at least triple shape memory, since the thermal and humidity responses can be effectively treated as orthogonal signals.[342–344] One advantage of the PCOE triblock copolymer materials is that the segregation is strong, which reduces phase mixing and ensures distinct behaviors of these two domains. Another advantage is that these materials are in poorly ordered lamellar morphologies, which guarantees the material isotropy.

### 8.2.4 Perspective on Chapter 5

This work was originally targeted for investigating the bridge forming polycation chains affecting membrane performance. It has been proposed that in a high hydrated (i.e. soaked in liquid water) ionic block copolymer membrane, part of the absorbed water will phase separate from the ionic block segment with a free chain end to form a water-rich (ion-poor) domain sandwiched between polyion/water layers.[187] This water-rich domain was claim to be beneficial for ion conductivity, although it was not conclusive. It is possible that the observed conductivity enhancement was merely a result of increased water sorption.[345,346] We propose that when the polycation segments forms bridges with both ends anchored to different interfaces of a hydrophilic domain interface, they always have segments placed in the middle of the domain and thus can suppress the formation of water-rich (ion-poor) layer.

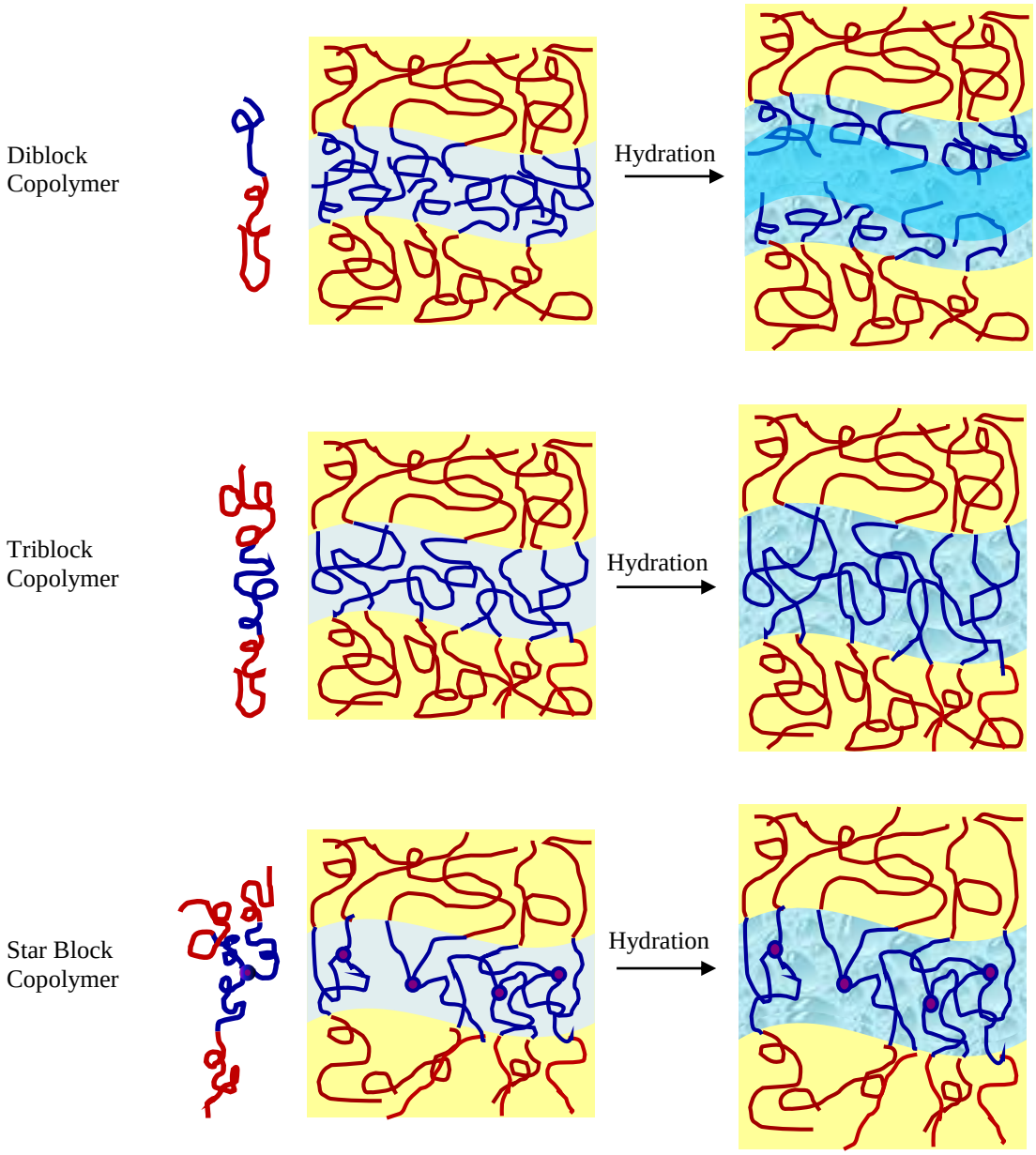


**Figure 133: Polymer Architecture Affecting Water Distribution.**

This can be realized by comparing ionic diblock copolymers with other architectures. It was predicted that in an ordered lamellar phase, symmetric triblock copolymers should have 40~50% of the midblocks forming bridges across the domain with the rest in loop conformation,[200] while adopting star block copolymer architecture can further increase the ratio of bridge forming core-blocks (>90% for a 6-armed star block copolymer), as shown by Dissipative Particle Dynamics

simulation technique.[347] This means by changing polymer architecture, the ratio of bridges can be varied in a broad range. Thus, membranes based on triblock and star ionic block copolymers with the ions in the mid/core-block should have different structure in the hydrophilic domain, compared to diblock membranes (Figure 133). Comparing the conductivities or diffusivities in these membranes is expected to give a clear understanding of the water-rich domain effect on ion conduction, especially when the hydration level is held constant. Using these polymers, it is also possible to investigate how the bridges affect the swelling behavior.

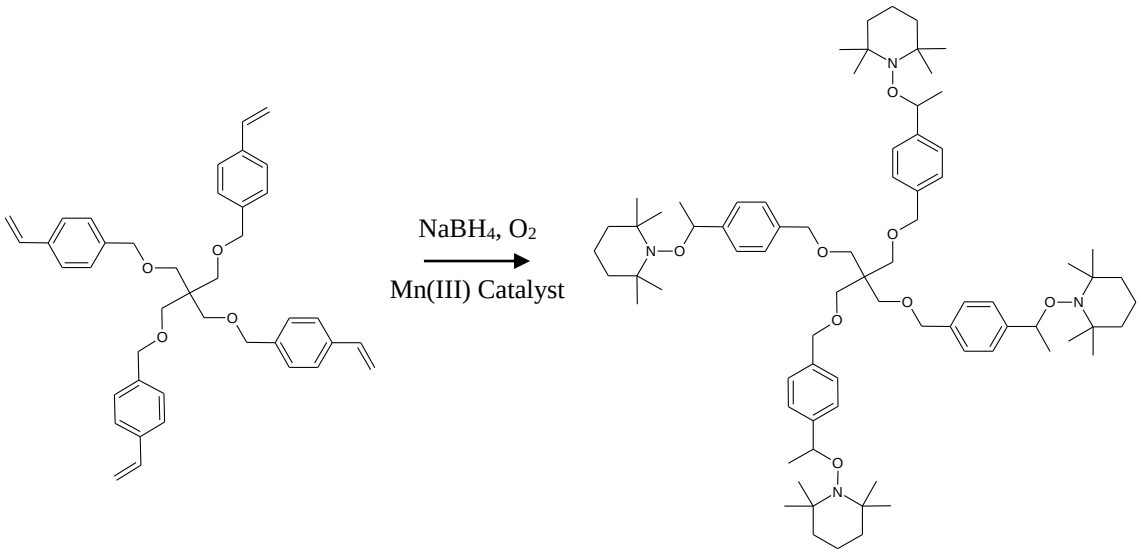


**Figure 134: Synthesis of an Example Alkoxyamine.**

This proposed investigation was not successfully conducted because of the failure in material mechanical integrity, while the necessity of understanding water-rich domain effect is still urgent for the general structure-property correlation in transport/separation materials assisted by hydration.[10,348] It is expected that using hydrogenated polyisoprene or polybutadiene (effectively poly(methyl butylene) or polyethylene) to replace PnBA can largely increase polymer entanglements and thus the mechanical toughness. Before selective hydrogenation on the non-aromatic C=C bonds, NMP can be used to polymerize isoprene or butadiene to achieve relatively

high MW and narrow distribution, where special alkoxyamines are required and can be synthesized using a previously reported method (Figure 134).[331,349–351]

### 8.2.5 Perspective on Chapter 6

Polyhedral oligomeric silsesquioxane (POSS) containing BCPs can be very useful in block copolymer lithography. Similar to polydimethylsiloxane, when coupled with a normal organic block, they can provide a distinct selectivity in react ion etching (RIE).[352,353] On the other hand, the POSS block in BCP thin films has a much lower preference to form a skin layer.[354] This provides an opportunity of using this polymer for direct patterning.

It is proposed here, using methacrylate or styrenic monomer bearing a POSS side group, polystyrene-ONB-poly(POSS)-*b*-polystyrene can be synthesized using the method described in Chapter 6. When the polymer is exposed to UV, it is expected that a polystyrene block can be effectively cleaved, thus the volume fraction in the block copolymer can be tuned. By carefully designing the chemical compositions, it is possible to switch the block copolymer morphology from lamellar to cylindrical. When this material is subjected to thin film self-assembly, upon regional UV treatment and sequential washing with selective solvent, it is possible to achieve different POSS block volume fractions in desired areas. Finally, a solvent vapor annealing step could result in line pattern (perpendicular lamellae) in the unexposed area and dot patterns (perpendicular cylinders) in the UV treated regions. Using RIE, these hierarchical patterns can be directly converted into nano silica lines/dots.

### 8.2.6 Perspective on Modified Domain Interface for BCP AEMs

Block copolymers are known to microphase separate, when the incompatibility is strong enough between each block. However, there is always a certain degree of phase mixing at the interface, the thickness of which was estimated to be at least a few nanometers.[192,355] This means

the interface can have effects on ion transport phenomena, which should be reckoned. In anhydrous ion transport membranes based on polystyrene, it was found that the microphase separated block copolymers exhibited relatively low conductivities, when the ionic domains had smaller thickness, compared with samples with larger domain size.[193,356–358] The scientists attributed this effect to that in these samples, the interface was the dominating part in the ionic domain and the ion mobility was largely limited by the mixed polystyrene chains. It was also point out that the interface affects ion distribution and chain conformation, which are also important factors in ion conduction.[359–361] Similarly in water-assisted ion transport materials, it was observed that block copolymers with thinner ionic domain provided lower conductivity values,[115,362] which is in good agreement with our observation in Chapter 4. This was also believed to be related to the domain interfaces, although it was not fully understood yet. Possibly some ions are embedded in hydrophobic chains and thus can barely contribute in conductivity. Moreover, it was recently reported that the water molecules, as the vital factor in these materials, prefers to distribute in the center of the ionic domain rather than at the surface hydrophobic domain.[187] This means, the BCP membranes has a heterogenous hydration level across the hydrophilic domain, and thus, the ions close to and far away from domain interfaces should have different mobilities.

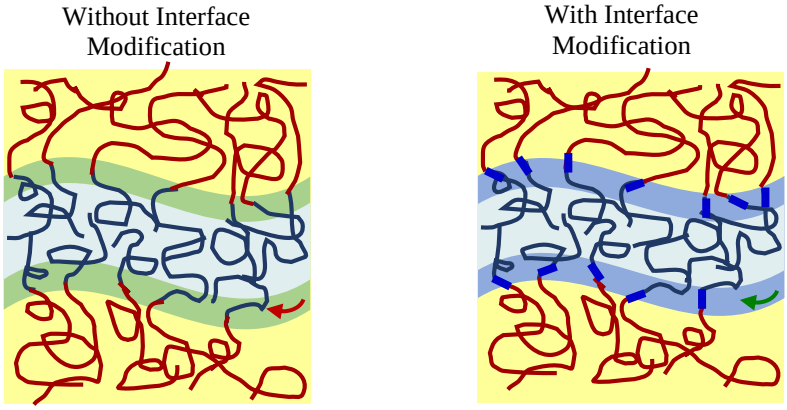


**Figure 135: Scheme of Domain Interface Modification.**

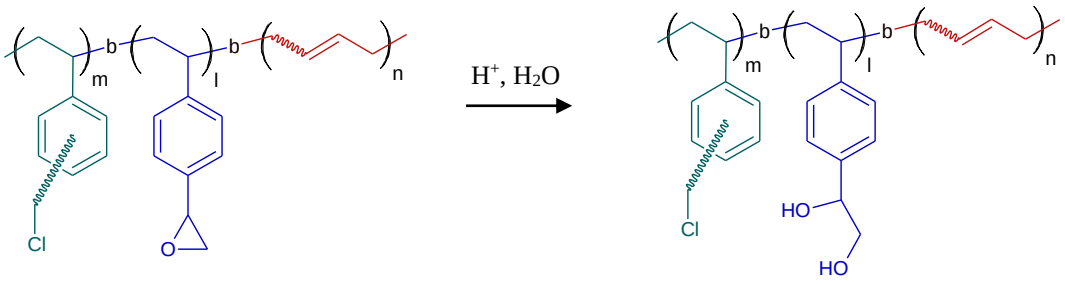


**Figure 136: Synthesis of Block Copolymer for Interface Modification.**

Herein, it is proposed that the domain interface can be engineered to enhance the mobility of the ions nearby. For example, a short block that is highly hygroscopic can be added between polychloromethylstyrene and polystyrene, polyethylene, polybutadiene, or polymethylbutylene, which should reside at the original diblock domain interface and may bring two possible advantages (Figure 135). First, excess water could be absorbed by this hygroscopic block to enhance the local hydration level. In addition, the ions near the interface are now more separated from the hydrophobic domain and more likely to be surrounded by the hygroscopic segment. These two features are expected to facilitate ion motion near the interface. Poly(ethylene oxide) and poly(vinyl alcohol) can be good candidates, however, it requires difficult chemistry work to incorporate them. A newly reported monomer, 4-vinylphenyloxirane (4VPO), can be easily synthesized and polymerized using controlled radical polymerization techniques.[363–365] After the synthesis of polyCMS-*b*-poly4VPO-*b*-polybutadiene, the 4VPO units can be hydrolyzed (with an acid catalyst) into diols, the structure of which is shown in Figure 136. Finally, the block copolymer can be quaternized with either trimethylamine or $Ar_3P$.

# APPENDIX A

## ADDITIONAL CHARACTERIZATION IN CHAPTER TWO

1. Schematic of Experimental Setup in Water Vapor Flux Test

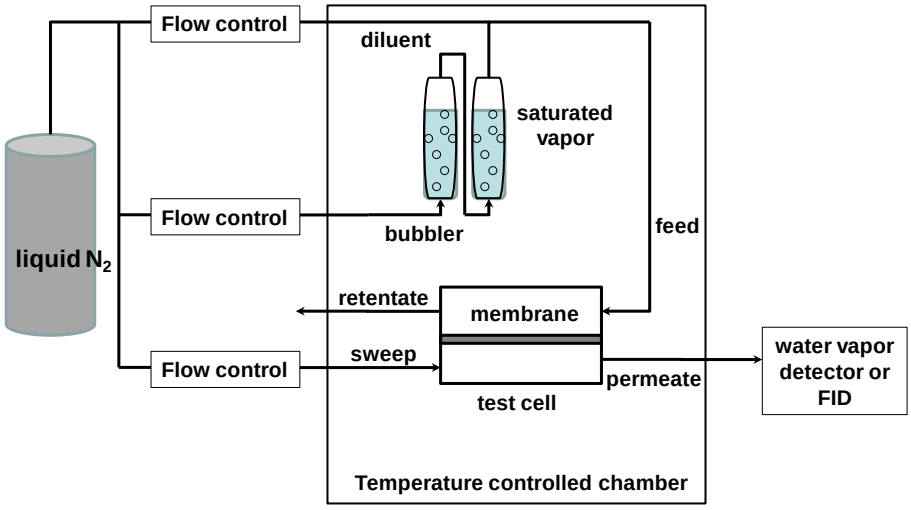


**Figure 137: Experimental Setup of Water Flux Test.**

2. Water Vapor Flux Testing Results at 35 °C

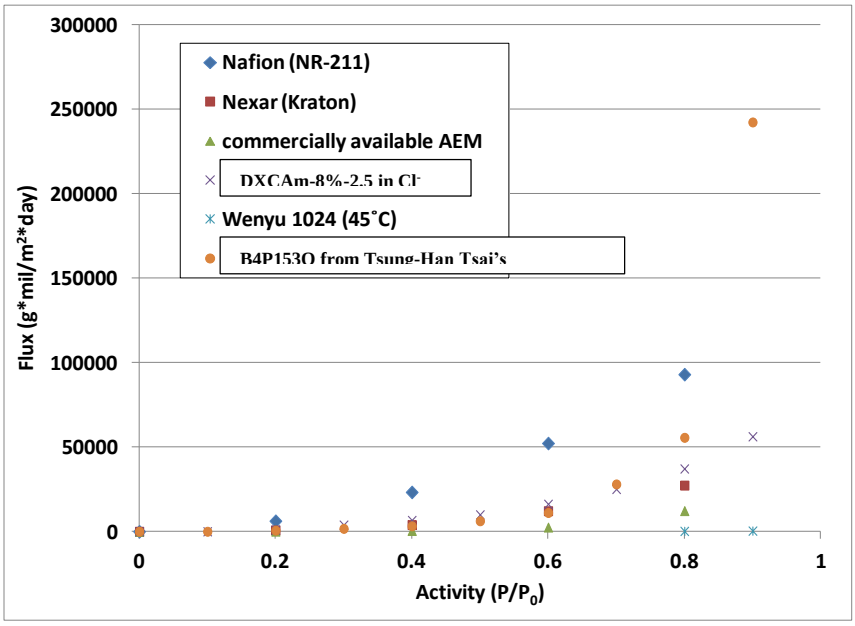


**Figure 138: Water Flux Data.**

3. Water Diffusion Coefficient in Different Anion Forms at Room Temperature

**Table 15: Water Diffusivities in DXCAm-7%-2.0.**

| Anion | Diffusivity (* $10^7$ $cm^2/s$) |
|---|---|
| $BF_4^-$ | 0.98 ± 0.44 |
| $NO_3^-$ | 3.79 ± 0.54 |
| $CO_3^{2-}$ | 5.68 ± 0.96 |
| $HCO_3^-$ | 5.45 ± 1.17 |
| $Cl^-$ | 7.93 ± 0.71 |

## APPENDIX B

## ADDITIONAL CHARACTERIZATION IN CHAPTER THREE

1. Thermogravimetric analysis on a homopolymer of styrenic $BzAr_3P^+Cl^-$

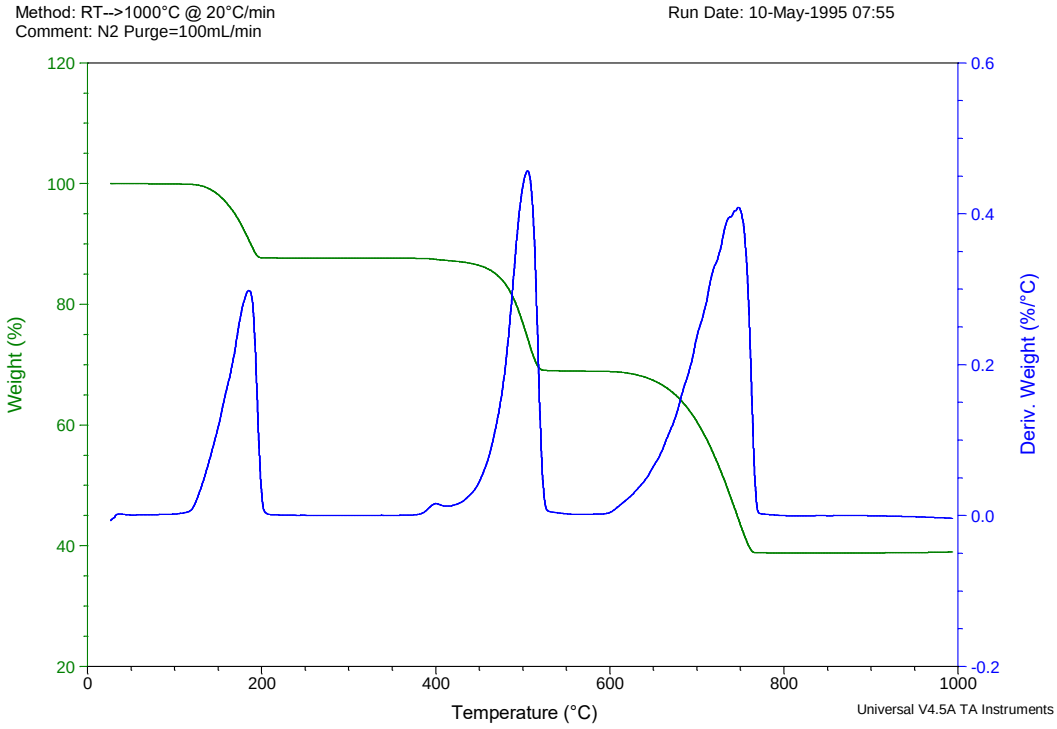


**Figure 139: Thermogravimetric Test of Phosphonium Homopolymer.**

2. Additional SAXS Profiles

AEM 3 at dry state

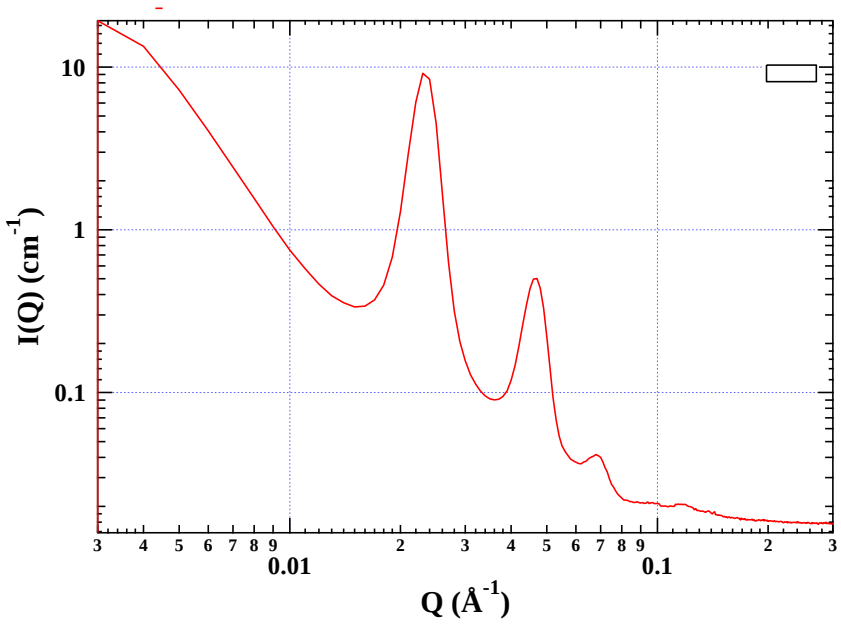


**Figure 140: SAXS Profile of AEM 3.**

AEM 4 with Simulated Form Factor

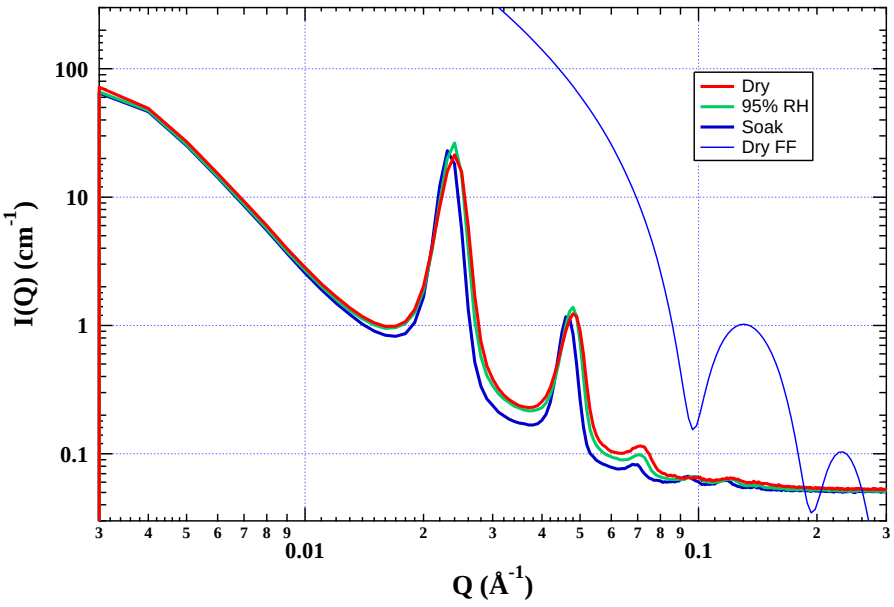


**Figure 141: SAXS Profile of AEM 4.**

AEM 5 at dry state

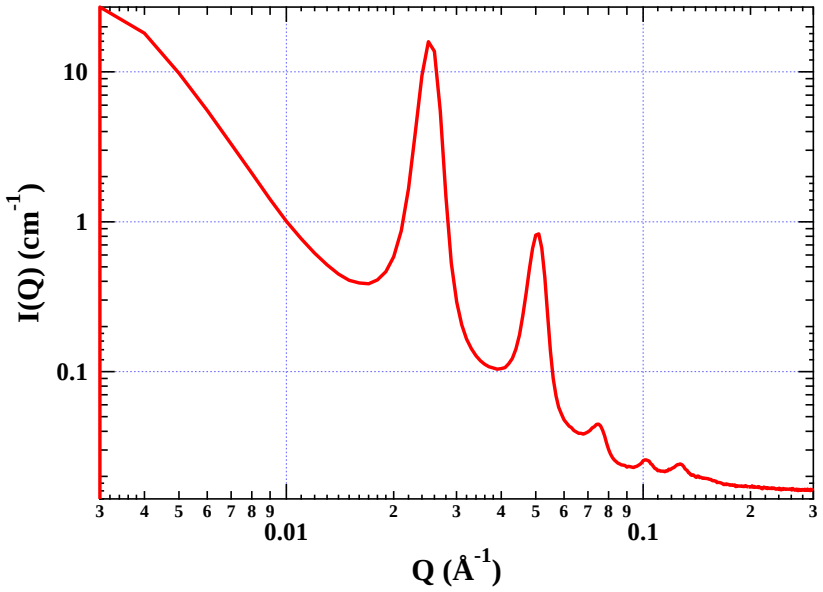


**Figure 142: SAXS Profile of AEM 5.**

AEM 6 at dry state

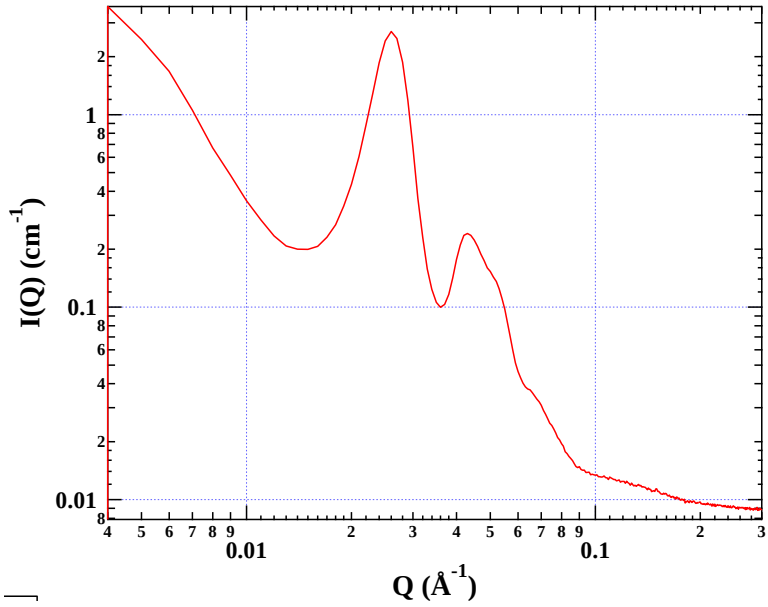


**Figure 143: SAXS Profile of AEM 6.**

AEM 9, 10, and 11 at dry state

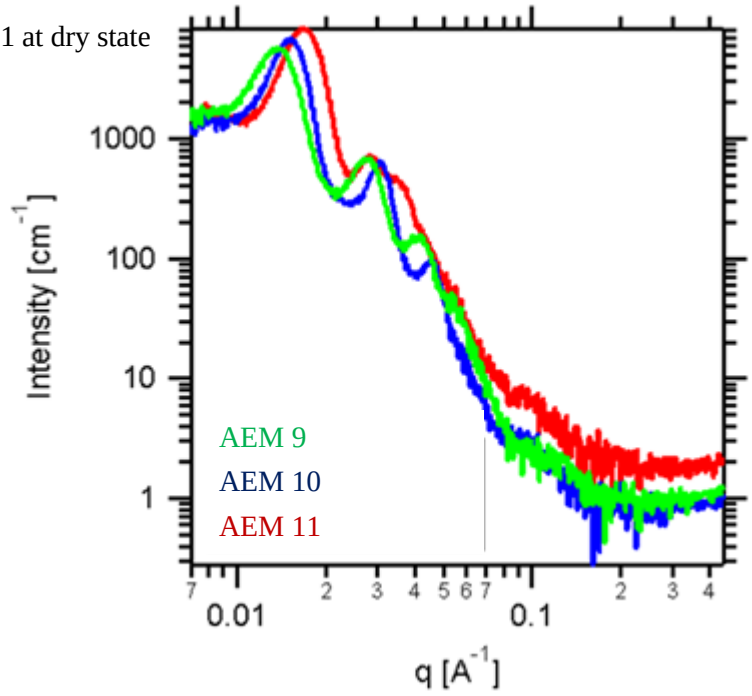


**Figure 144: SAXS Profiles of AEM 9, 10, and 11.**

AEM 12 at dry state

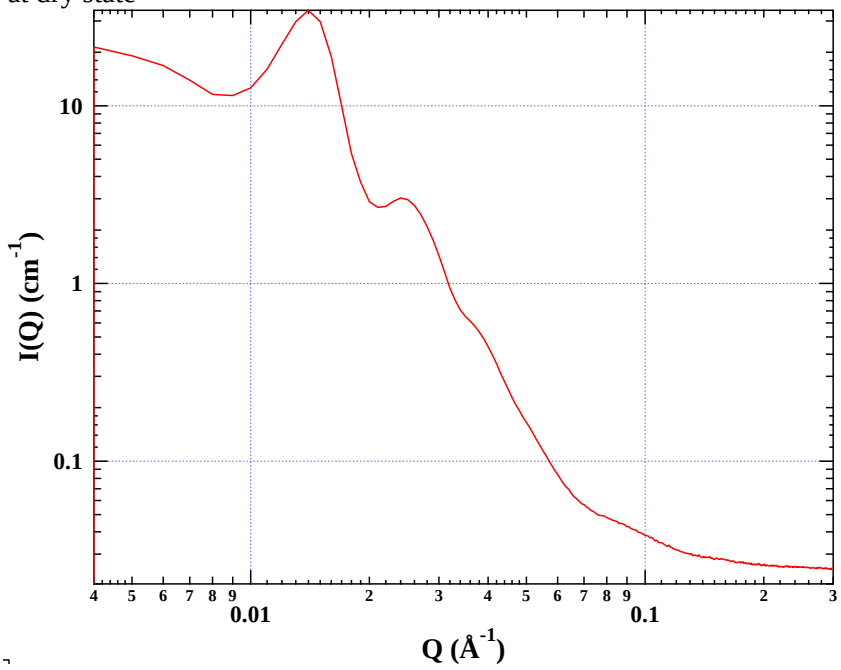


**Figure 145: SAXS Profile of AEM 12.**

AEM 13 at dry state

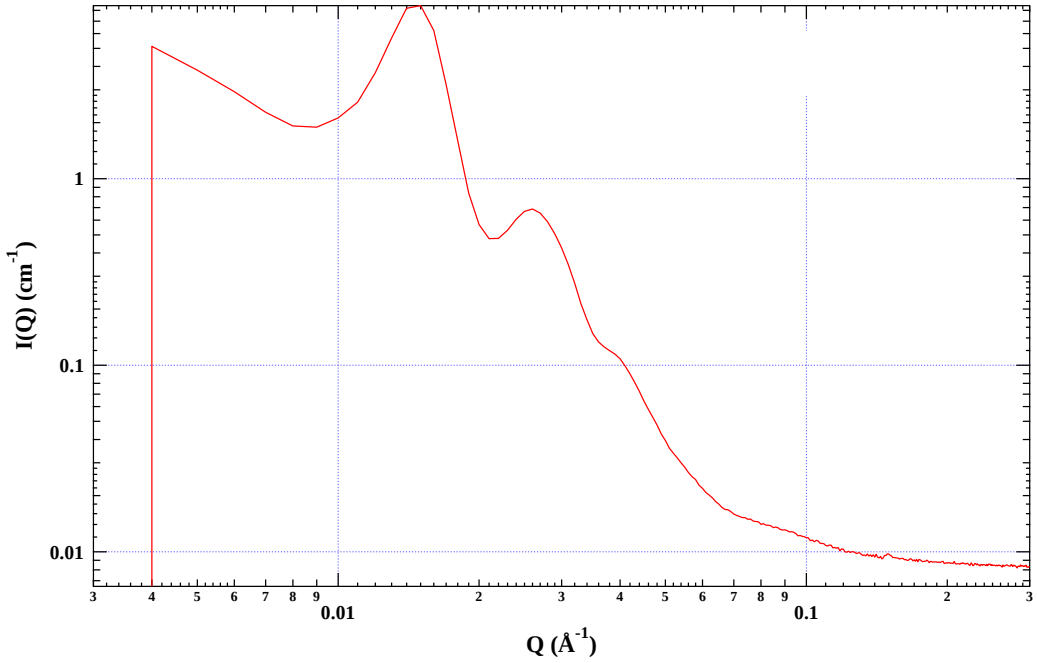


**Figure 146: SAXS Profile of AEM 13.**

AEM 14 at dry state

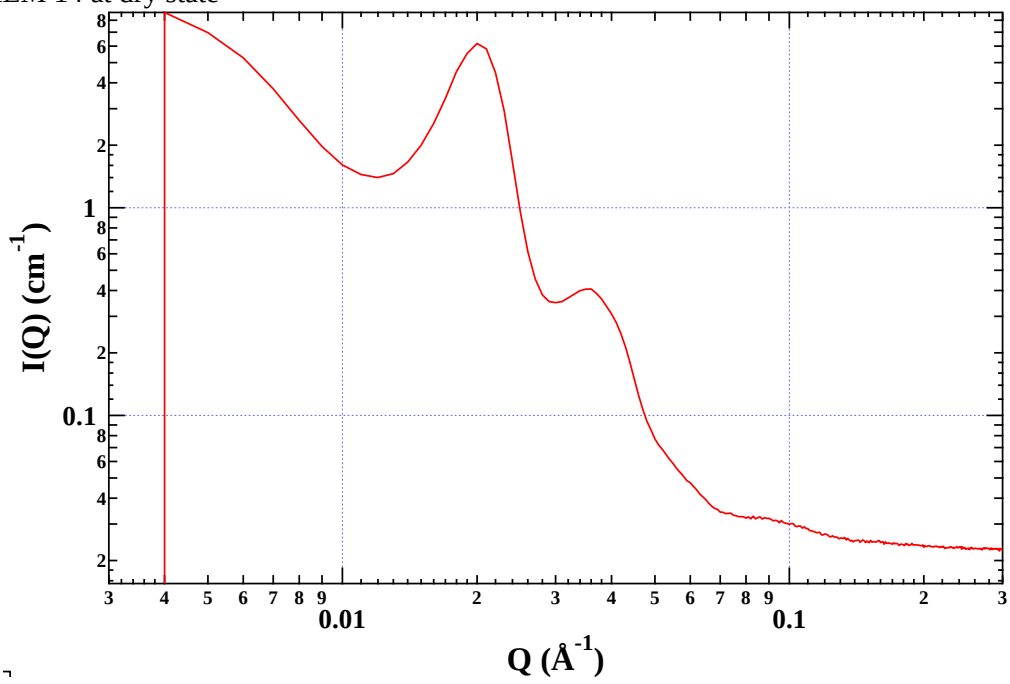


**Figure 147: SAXS Profile of AEM 14.**

AEM 15 at dry state

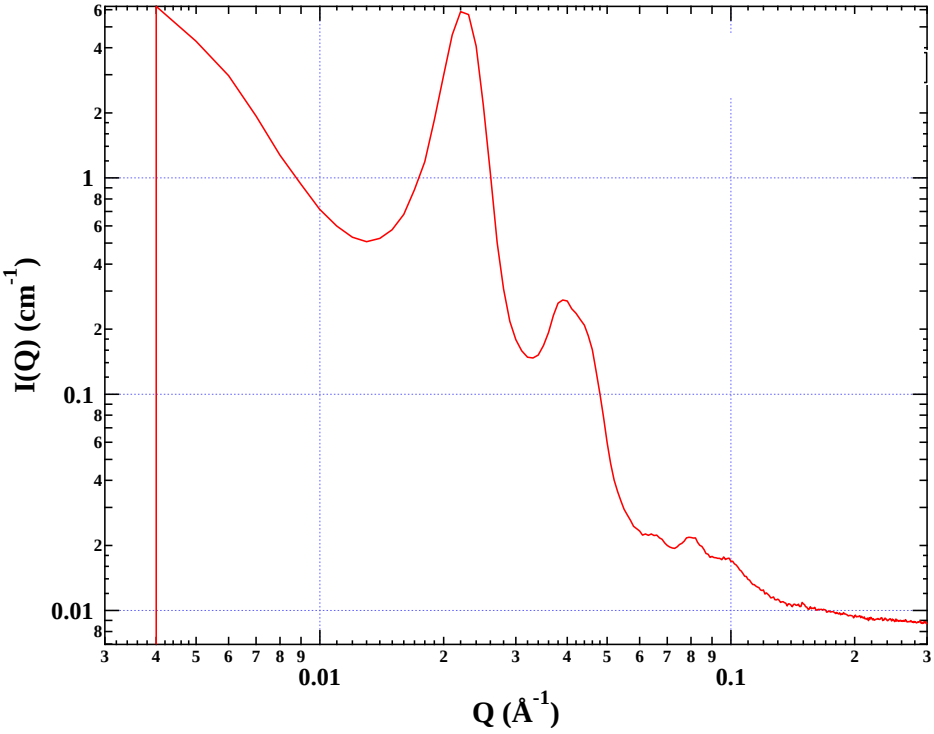


**Figure 148: SAXS Profile of AEM 15.**

## APPENDIX C

## ADDITIONAL CHARACTERIZATION IN CHAPTER FOUR

1. Fourier Transformed Infrared Spectrum of a Representative TAEM

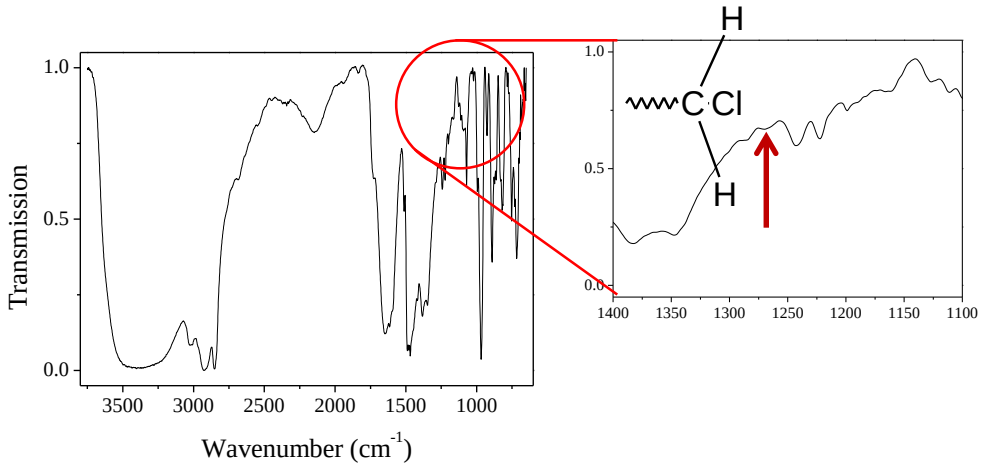


**Figure 149: FT-IR of a Quaternized TAEM.**

2. Additional SAXS Profiles on TAEMs

TAEM 1 at 60 °C

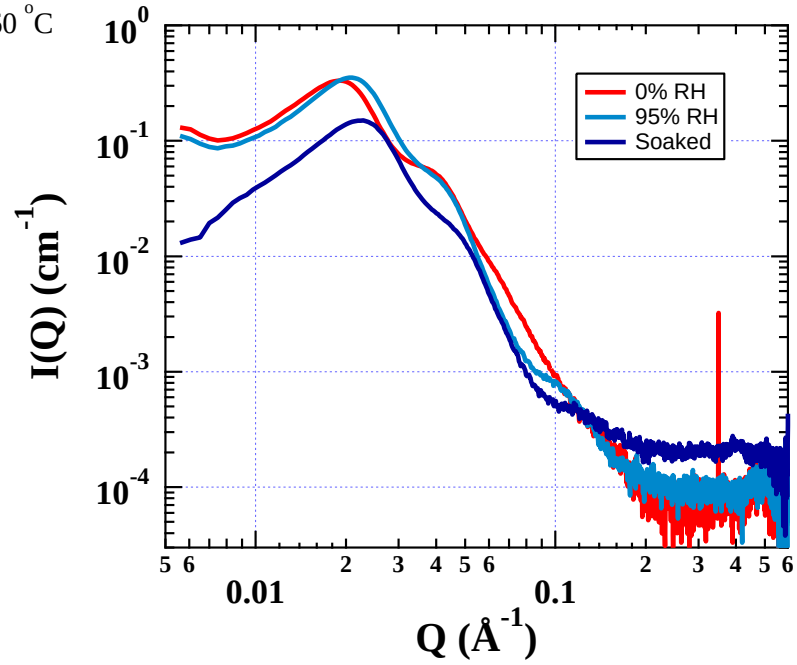


**Figure 150: SAXS Profiles of TAEM 1.**

TAEM 4 at 60 °C

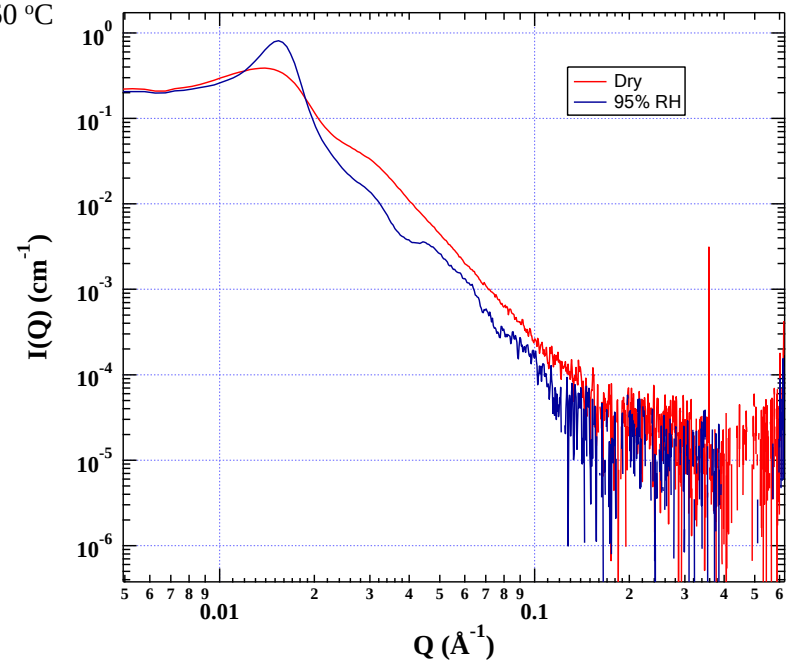


**Figure 151: SAXS Profiles of TAEM 4.**

TAEM 5 at 60 ºC

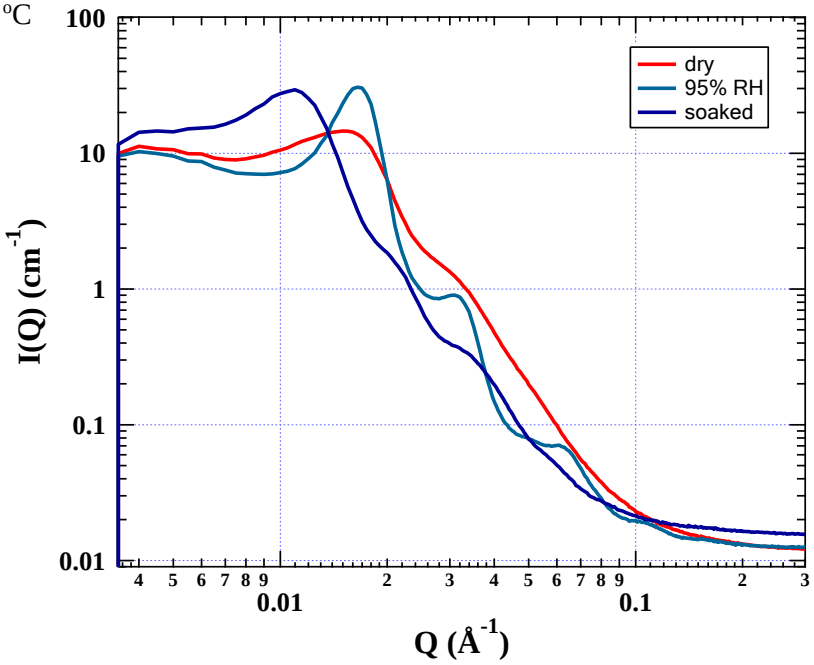


**Figure 152: SAXS Profiles of TAEM 5.**

TAEM 6 at 60 ºC

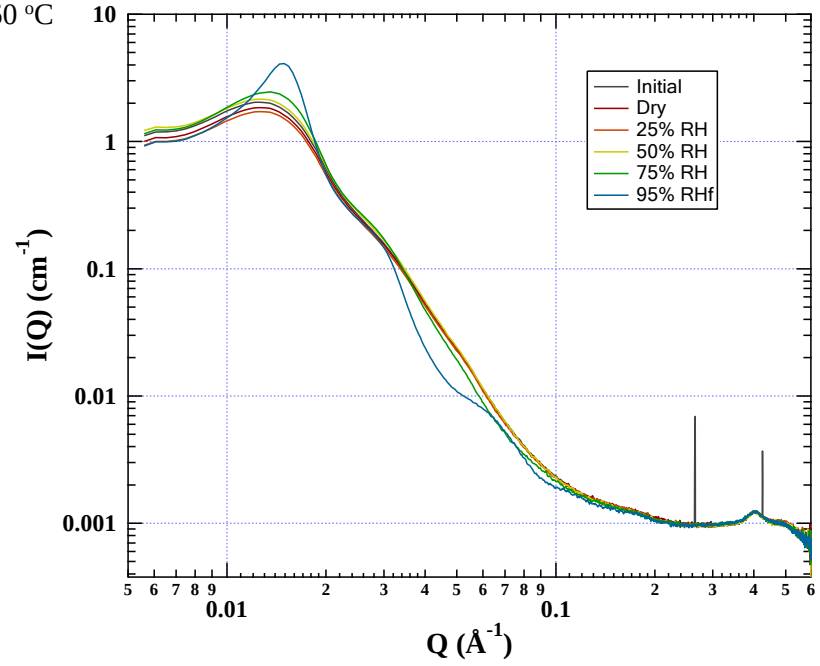


**Figure 153: SAXS Profiles of TAEM 6.**

TAEM 8 at 60 ºC

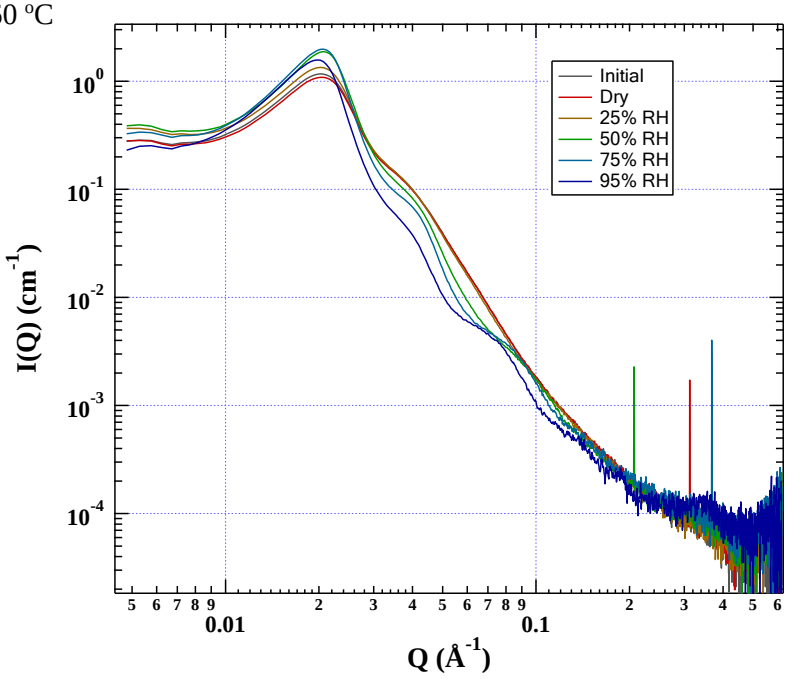


**Figure 154: SAXS Profiles of TAEM 8.**

TAEM 10 at 60 ºC

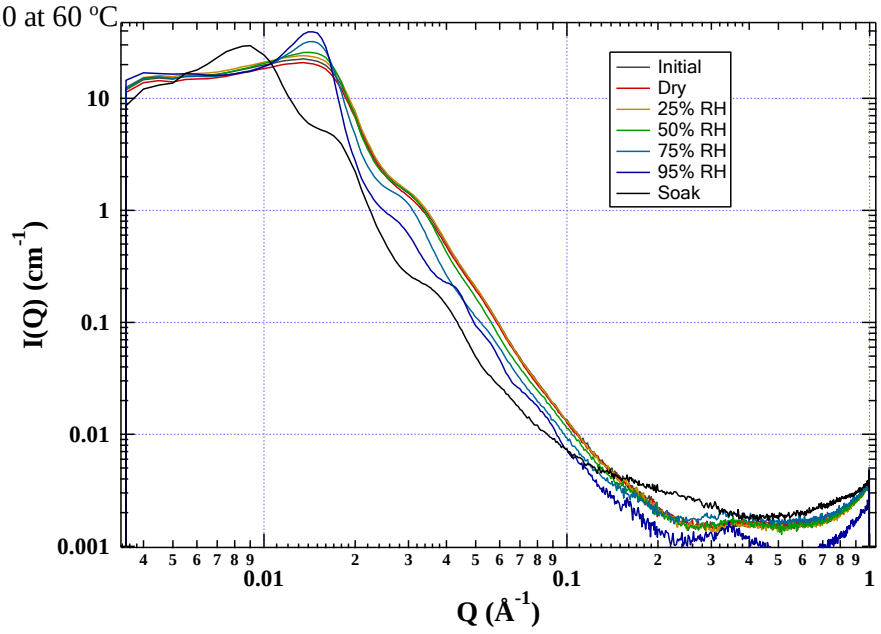


**Figure 155: SAXS Profiles of TAEM 10.**

TAEM 11 at 60 °C

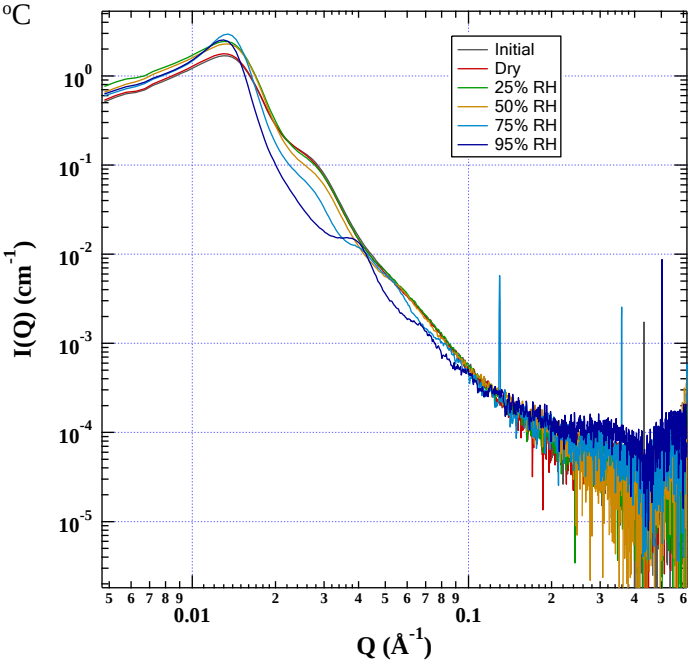


**Figure 156: SAXS Profiles of TAEM 11.**

TAEM 12 at 60 °C

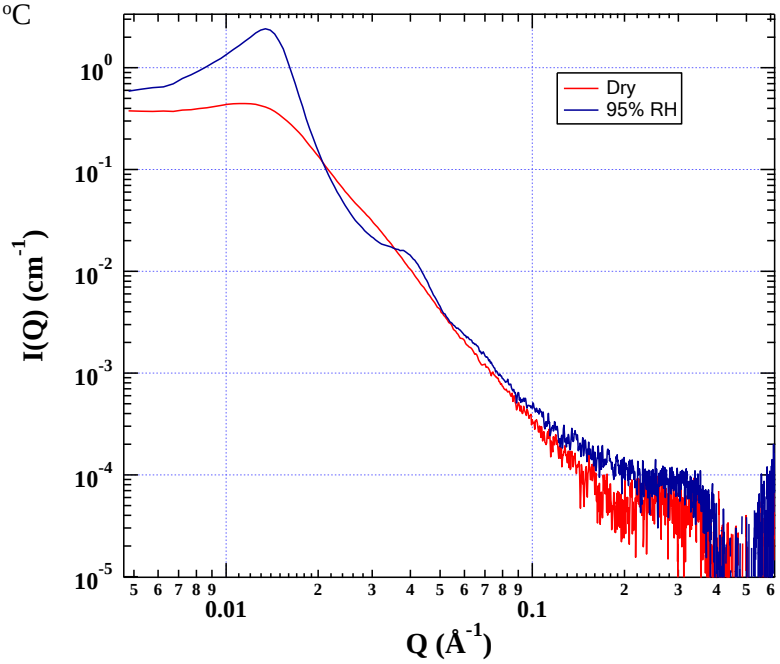


**Figure 157: SAXS Profiles of TAEM 12.**

3. Representative Conductivity on a Sample of AEM 9 showing the reproducibility.

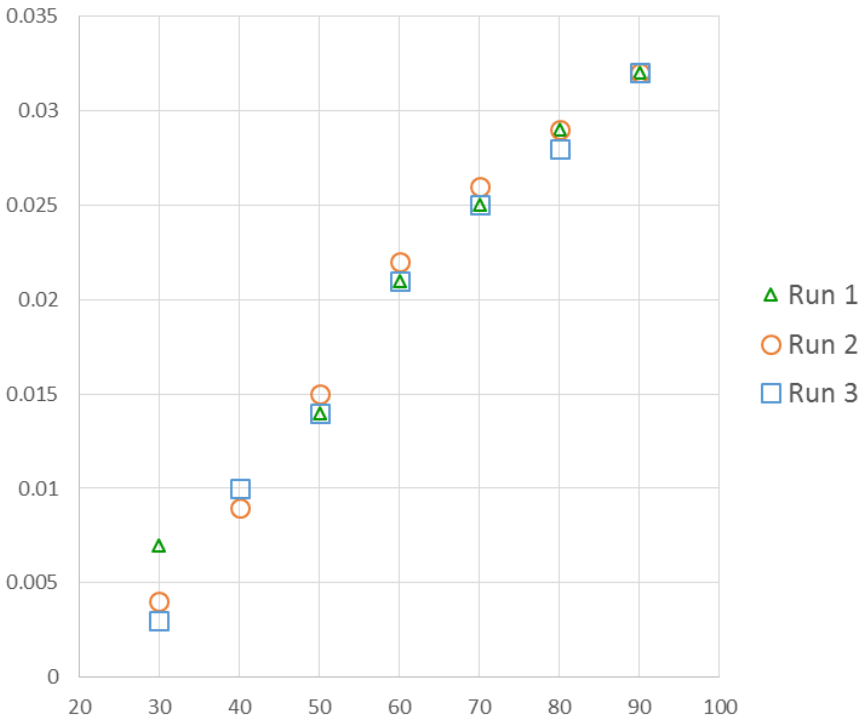


**Figure 158: A Representative Conductivity Test on a Sample of TAEM 9.**

## BIBLIOGRAPHY


(1) Shafiee, S.; Topal, E. When Will Fossil Fuel Reserves Be Diminished? *Energy Policy* **2009**, *37* (1), 181–189.

(2) McGlade, C.; Ekins, P. The Geographical Distribution of Fossil Fuels Unused When Limiting Global Warming to 2 °C. *Nature* **2015**, *517* (7533), 187–190.

(3) Merle, G.; Wessling, M.; Nijmeijer, K. Anion Exchange Membranes for Alkaline Fuel Cells: A Review. *Journal of Membrane Science*. 2011, pp 1–35.

(4) Varcoe, J. R.; Slade, R. C. T. Prospects for Alkaline Anion-Exchange Membranes in Low Temperature Fuel Cells. *Fuel Cells* **2005**, *5* (2), 187–200.

(5) Mehta, V.; Cooper, J. S. Review and Analysis of PEM Fuel Cell Design and Manufacturing. *Journal of Power Sources*. 2003, pp 32–53.

(6) Warshay, M.; Prokopius, P. R. The Fuel Cell in Space: Yesterday, Today and Tomorrow. *J. Power Sources* **1990**, *29* (1-2), 193–200.

(7) Heitner-Wirguin, C. Recent Advances in Perfluorinated Ionomer Membranes: Structure, Properties and Applications. *Journal of Membrane Science*. 1996, pp 1–33.

(8) Mauritz, K. a.; Moore, R. B. State of Understanding of Nafion. *Chem. Rev.* **2004**, *104* (10), 4535–4585.

(9) Gierke, T. D.; Munn, G. E.; Wilson, F. C. The Morphology in Nafion Perfluorinated Membrane Products, as Determined by Wide- and Small- Angle X-Ray Studies. *J. Polym. Sci. Polym. Phys. Ed.* **1981**, *19* (11), 1687–1704.

(10) Schmidt-Rohr, K.; Chen, Q. Parallel Cylindrical Water Nanochannels in Nafion Fuel-Cell Membranes. *Nat. Mater.* **2008**, *7* (1), 75–83.

(11) McLean, G. F.; Niet, T.; Prince-Richard, S.; Djilali, N. An Assessment of Alkaline Fuel Cell Technology. *Int. J. Hydrogen Energy* **2002**, *27* (5), 507–526.

(12) Zhang, H.; Shen, P. K. Recent Development of Polymer Electrolyte Membranes for Fuel Cells. *Chem. Rev.* **2012**, *112* (5), 2780–2832.

(13) Hickner, M. a.; Herring, A. M.; Coughlin, E. B. Anion Exchange Membranes: Current Status and Moving Forward. *J. Polym. Sci. Part B Polym. Phys.* **2013**, *51* (24), 1727–1735.

(14) Tomoi, M.; Yamaguchi, K.; Ando, R.; Kantake, Y.; Aosaki, Y.; Kubota, H. Synthesis and Thermal Stability of Novel Anion Exchange Resins with Spacer Chains. *J. Appl. Polym. Sci.* **1997**, *64* (6), 1161–1167.

(15) Hibbs, M. R. Alkaline Stability of Poly(phenylene)-Based Anion Exchange Membranes with Various Cations. *J. Polym. Sci. Part B Polym. Phys.* **2013**, *51* (24), 1736–1742.

(16) Noonan, K. J. T.; Hugar, K. M.; Kostalik, H. A.; Lobkovsky, E. B.; Abruña, H. D.; Coates, G. W. Phosphonium Functionalized Polyethylene : A New Class of Base Stable Alkaline Anion Exchange Membranes. *J. Am. Chem. Soc.* **2012**, *134* (44), 18161–18164.

(17) Gu, S.; Cai, R.; Luo, T.; Chen, Z.; Sun, M.; Liu, Y.; He, G.; Yan, Y. A Soluble and Highly Conductive Ionomer for High-Performance Hydroxide Exchange Membrane Fuel Cells. *Angew. Chemie - Int. Ed.* **2009**, *48* (35), 6499–6502.

(18) Alexandratos, S. D. Ion-Exchange Resins: A Retrospective from Industrial and Engineering Chemistry Research. *Ind. Eng. Chem. Res.* **2009**, *48*, 388–398.

(19) Wang, J.; Li, S.; Zhang, S. Novel Hydroxide-Conducting Polyelectrolyte Composed of an Poly(arylene Ether Sulfone) Containing Pendant Quaternary Guanidinium Groups for Alkaline Fuel Cell Applications. *Macromolecules* **2010**, *43* (8), 3890–3896.

(20) Tanaka, M.; Koike, M.; Miyatake, K.; Watanabe, M. Synthesis and Properties of Anion Conductive Ionomers Containing Fluorenyl Groups for Alkaline Fuel Cell Applications. *Polym. Chem.* **2011**, *2* (1), 99.

(21) Chen, D.; Hickner, M. a. Degradation of Imidazolium- and Quaternary Ammonium-Functionalized Poly ( Fl Uorenyl Ether Ketone Sulfone ) Anion Exchange Membranes. **2012**.

(22) Wang, J.; Zhao, Z.; Gong, F.; Li, S.; Zhang, S. Synthesis of Soluble Poly(arylene Ether Sulfone) Ionomers with Pendant Quaternary Ammonium Groups for Anion Exchange Membranes. *Macromolecules* **2009**, *42* (22), 8711–8717.

(23) Rao, A. H. N.; Kim, H.-J.; Nam, S.; Kim, T.-H. Cardo Poly(arylene Ether Sulfone) Block Copolymers with Pendant Imidazolium Side Chains as Novel Anion Exchange Membranes for Direct Methanol Alkaline Fuel Cell. *Polymer (Guildf).* **2013**, *54* (26), 6918–6928.

(24) Mohanty, A. D.; Lee, Y.; Zhu, L.; Hickner, M. a.; Bae, C. Anion Exchange Fuel Cell Membranes Prepared from C − H Borylation and Suzuki Coupling Reactions. **2014**.

(25) Yan, J.; Hickner, M. a. Anion Exchange Membranes by Bromination of Benzylmethyl-Containing Poly(sulfone)s. *Macromolecules* **2010**, *43* (5), 2349–2356.

(26) Li, N.; Zhang, Q.; Wang, C.; Lee, Y. M.; Guiver, M. D. Phenyltrimethylammonium Functionalized Polysulfone Anion Exchange Membranes. *Macromolecules* **2012**, *45* (5), 2411–2419.

(27) Lin, B.; Qiu, L.; Qiu, B.; Peng, Y.; Yan, F. A Soluble and Conductive Polyfluorene Ionomer with Pendant Imidazolium Groups for Alkaline Fuel Cell Applications. *Macromolecules* **2011**, *44* (24), 9642–9649.

(28) Kostalik, H. a.; Clark, T. J.; Robertson, N. J.; Mutolo, P. F.; Longo, J. M.; Abruña, H. D.; Coates, G. W. Solvent Processable Tetraalkylammonium-Functionalized Polyethylene for Use as an Alkaline Anion Exchange Membrane. *Macromolecules* **2010**, *43* (17), 7147–7150.

(29) Hibbs, M. R.; Fujimoto, C. H.; Cornelius, C. J. Synthesis and Characterization of Poly(phenylene)-Based Anion Exchange Membranes for Alkaline Fuel Cells. *Macromolecules* **2009**, *42* (21), 8316–8321.

(30) Ran, J.; Wu, L.; Varcoe, J. R.; Ong, A. L.; Poynton, S. D.; Xu, T. Development of Imidazolium-Type Alkaline Anion Exchange Membranes for Fuel Cell Application. *J. Memb. Sci.* **2012**, *415-416*, 242–249.

(31) Luo, Y.; Guo, J.; Wang, C.; Chu, D. Quaternized Poly(methyl Methacrylate-Co-Butyl Acrylate-Co-Vinylbenzyl Chloride) Membrane for Alkaline Fuel Cells. *J. Power Sources* **2010**, *195* (12), 3765–3771.

(32) Thomas, O. D.; Soo, K. J. W. Y.; Peckham, T. J.; Kulkarni, M. P.; Holdcroft, S. A Stable Hydroxide-Conducting Polymer. *J. Am. Chem. Soc.* **2012**, *134* (26), 10753–10756.

(33) Han, J.; Peng, H.; Pan, J.; Wei, L.; Li, G.; Chen, C.; Xiao, L.; Lu, J.; Zhuang, L. Highly Stable Alkaline Polymer Electrolyte Based on a Poly(ether Ether Ketone) Backbone. *ACS Appl. Mater. Interfaces* **2013**, *5* (24), 13405–13411.

(34) Zha, Y.; Disabb-Miller, M. L.; Johnson, Z. D.; Hickner, M. a.; Tew, G. N. Metal-Cation-Based Anion Exchange Membranes. *J. Am. Chem. Soc.* **2012**, *134* (10), 4493–4496.

(35) Clark, T. J.; Robertson, N. J.; Kostalik, H. a.; Lobkovsky, E. B.; Mutolo, P. F.; Abruña, H. D.; Coates, G. W. A Ring-Opening Metathesis Polymerization Route to Alkaline Anion Exchange Membranes: Development of Hydroxide-Conducting Thin Films from an Ammonium-Functionalized Monomer. *J. Am. Chem. Soc.* **2009**, *131* (36), 12888–12889.

(36) Robertson, N. J.; Kostalik, H. a T.; Clark, T. J.; Mutolo, P. F.; Abruna, H. D.; Coates, G. W. Tunable High Performance Cross-Linked Alkaline Anion Exchange Membranes for Fuel Cell Applications. *J. Am. Chem. Soc.* **2010**, *132* (10), 3400–3404.

(37) Gu, S.; Cai, R.; Yan, Y. Self-Crosslinking for Dimensionally Stable and Solvent-Resistant Quaternary Phosphonium Based Hydroxide Exchange Membranes. *Chem. Commun. (Camb).* **2011**, *47* (10), 2856–2858.

(38) Lin, B.; Dong, H.; Li, Y.; Si, Z.; Gu, F.; Yan, F. Alkaline Stable C2-Substituted Imidazolium-Based Anion-Exchange Membranes. *Chem. Mater.* **2013**, *25* (9), 1858–1867.

(39) Wilson, M. S.; Gottesfeld, S. Thin-Film Catalyst Layers for Polymer Electrolyte Fuel Cell Electrodes. *J. Appl. Electrochem.* **1992**, *22* (1), 1–7.

(40) Disabb-Miller, M. L.; Johnson, Z. D.; Hickner, M. a. Ion Motion in Anion and Proton-Conducting Triblock Copolymers. *Macromolecules* **2013**, *46* (3), 949–956.

(41) Ye, Y.; Sharick, S.; Davis, E. M.; Winey, K. I.; Elabd, Y. a. High Hydroxide Conductivity in Polymerized Ionic Liquid Block Copolymers. *ACS Macro Lett.* **2013**, *2* (7), 575–580.

(42) Tanaka, M.; Fukasawa, K.; Nishino, E.; Yamaguchi, S.; Yamada, K.; Tanaka, H.; Bae, B.; Miyatake, K.; Watanabe, M. Anion Conductive Block Poly(arylene Ether)s: Synthesis, Properties, and Application in Alkaline Fuel Cells. *J. Am. Chem. Soc.* **2011**, *133* (27), 10646–10654.

(43) Rozendal, R. a.; Hamelers, H. V. M.; Molenkamp, R. J.; Buisman, C. J. N. Performance of Single Chamber Biocatalyzed Electrolysis with Different Types of Ion Exchange Membranes. *Water Res.* **2007**, *41* (9), 1984–1994.

(44) Li, X.; Zhang, H. H.; Mai, Z.; Vankelecom, I. Ion Exchange Membranes for Vanadium Redox Flow Battery (VRB) Applications. *Energy & Environmental Science*. 2011, pp 1147–1160.

(45) Shannon, M. a; Bohn, P. W.; Elimelech, M.; Georgiadis, J. G.; Mariñas, B. J.; Mayes, A. M. Science and Technology for Water Purification in the Coming Decades. *Nature* **2008**, *452* (7185), 301–310.

(46) Manning, G. S. The Molecular Theory of Polyelectrolyte Solutions with Applications to the Electrostatic Properties of Polynucleotides. *Q. Rev. Biophys.* **1978**, *11* (2), 179–246.

(47) Dobrynin, A. V.; Rubinstein, M. Theory of Polyelectrolytes in Solutions and at Surfaces. *Prog. Polym. Sci.* **2005**, *30* (11), 1049–1118.

(48) Lvov, Y.; Antipov, A. a.; Mamedov, A.; Möhwald, H.; Sukhorukov, G. B. Urease Encapsulation in Nanoorganized Microshells. *Nano Lett.* **2001**, *1* (3), 125–128.

(49) Stuart, M. a C.; Huck, W. T. S.; Genzer, J.; Müller, M.; Ober, C.; Stamm, M.; Sukhorukov, G. B.; Szleifer, I.; Tsukruk, V. V; Urban, M.; Winnik, F.; Zauscher, S.; Luzinov, I.; Minko, S. Emerging Applications of Stimuli-Responsive Polymer Materials. *Nat. Mater.* **2010**, *9* (2), 101–113.

(50) Qiu, Y.; Park, K. Environment-Sensitive Hydrogels for Drug Delivery. *Adv. Drug Deliv. Rev.* **2012**, *64* (SUPPL.), 49–60.

(51) Leong, M. F.; Toh, J. K. C.; Du, C.; Narayanan, K.; Lu, H. F.; Lim, T. C.; Wan, A. C. a; Ying, J. Y. Patterned Prevascularised Tissue Constructs by Assembly of Polyelectrolyte Hydrogel Fibres. *Nat. Commun.* **2013**, *4* (May), 2353.

(52) Park, M. R.; Seo, B. B.; Song, S. C. Dual Ionic Interaction System Based on Polyelectrolyte Complex and Ionic, Injectable, and Thermosensitive Hydrogel for Sustained Release of Human Growth Hormone. *Biomaterials* **2013**, *34* (4), 1327–1336.

(53) Kwon, H. J.; Osada, Y.; Gong, J. P. Polyelectrolyte Gels-Fundamentals and Applications. *Polym. J.* **2006**, *38* (12), 1211–1219.

(54) Kreuer, K.-D.; Portale, G. A Critical Revision of the Nano-Morphology of Proton Conducting Ionomers and Polyelectrolytes for Fuel Cell Applications. *Adv. Funct. Mater.* **2013**, *23* (43), 5390–5397.

(55) Peckham, T. J.; Holdcroft, S. Structure-Morphology-Property Relationships of Non-Perfluorinated Proton-Conducting Membranes. *Adv. Mater.* **2010**, *22* (42), 4667–4690.

(56) Tsai, T. H.; Maes, A. M.; Vandiver, M. A.; Versek, C.; Seifert, S.; Tuominen, M.; Liberatore, M. W.; Herring, A. M.; Coughlin, E. B. Synthesis and Structure-Conductivity Relationship of Polystyrene-Block- Poly(vinyl Benzyl Trimethylammonium) for Alkaline Anion Exchange Membrane Fuel Cells. *J. Polym. Sci. Part B Polym. Phys.* **2013**, *51* (24), 1751–1760.

(57) ten Brummelhuis, N.; Weck, M. Orthogonal Multifunctionalization of Random and Alternating Copolymers. *ACS Macro Lett.* **2012**, *1* (10), 1216–1218.

(58) Chen, M.; Häussler, M.; Moad, G.; Rizzardo, E. Block Copolymers Containing Organic Semiconductor Segments by RAFT Polymerization. *Org. Biomol. Chem.* **2011**, *9* (17), 6111–6119.

(59) Kreuer, K. D. On the Development of Proton Conducting Polymer Membranes for Hydrogen and Methanol Fuel Cells. *J. Memb. Sci.* **2001**, *185* (1), 29–39.

(60) Li, J.; Park, J. K.; Moore, R. B.; Madsen, L. a. Linear Coupling of Alignment with Transport in a Polymer Electrolyte Membrane. *Nat. Mater.* **2011**, *10* (7), 507–511.

(61) Chen, C.; Tse, Y.-L. S.; Lindberg, G. E.; Knight, C.; Voth, G. A. Hydroxide Solvation and Transport in Anion Exchange Membranes. *J. Am. Chem. Soc.* **2016**, *138* (3), 991–1000.

(62) Ye, Y.; Choi, J. H.; Winey, K. I.; Elabd, Y. a. Polymerized Ionic Liquid Block and Random Copolymers: Effect of Weak Microphase Separation on Ion Transport. *Macromolecules* **2012**, *45* (17), 7027–7035.

(63) Noto, V. Di; Giffin, G. A.; Vezzu, K.; Nawn, G.; Bertasi, F.; Tsai, T.; Maes, A. M.; Seifert, S.; Coughlin, E. B.; Herring, A. M. Interplay between Solid State Transitions{,} Conductivity Mechanisms{,} and Electrical Relaxations in a [PVBTMA] [Br]-B-PMB Diblock Copolymer Membrane for Electrochemical Applications. *Phys. Chem. Chem. Phys.* **2015**, *17* (46), 31125–31139.

(64) Mohanty, A. D.; Bae, C. Mechanistic Analysis of Ammonium Cation Stability for Alkaline Exchange Membrane Fuel Cells. *J. Mater. Chem. A* **2014**, *2* (41), 17314–17320.

(65) Price, S. C.; Ren, X.; Jackson, A. C.; Ye, Y.; Elabd, Y. a; Beyer, F. L. Bicontinuous Alkaline Fuel Cell Membranes from Strongly Self- Segregating Block Copolymers. **2013**.

(66) Liu, Z.; Zhu, X.; Wang, G.; Hou, X.; Liu, D. Novel Crosslinked Alkaline Exchange Membranes Based on Poly(phthalazinone Ether Ketone) for Anion Exchange Membrane Fuel Cell Applications. *J. Polym. Sci. Part B Polym. Phys.* **2013**, *51* (22), 1632–1638.

(67) Qiu, B.; Lin, B.; Qiu, L.; Yan, F. Alkaline Imidazolium- and Quaternary Ammonium-Functionalized Anion Exchange Membranes for Alkaline Fuel Cell Applications. *J. Mater. Chem.* **2012**, *22* (3), 1040.

(68) Park, J. S.; Park, S. H.; Yim, S. D.; Yoon, Y. G.; Lee, W. Y.; Kim, C. S. Performance of Solid Alkaline Fuel Cells Employing Anion-Exchange Membranes. *J. Power Sources* **2008**, *178* (2), 620–626.

(69) Gu, F.; Dong, H.; Li, Y.; Si, Z.; Yan, F. Highly Stable N3-Substituted Imidazolium-Based Alkaline Anion Exchange Membranes: Experimental Studies and Theoretical Calculations. *Macromolecules* **2014**, *47* (1), 208–216.

(70) Li, Q.; Liu, L.; Miao, Q.; Jin, B.; Bai, R. Hydroxide-Conducting Polymer Electrolyte Membranes from Aromatic ABA Triblock Copolymers. *Polym. Chem.* **2014**, *5* (7), 2208.

(71) Ran, J.; Wu, L.; Xu, T. Enhancement of Hydroxide Conduction by Self-Assembly in Anion Conductive Comb-Shaped Copolymers. *Polym. Chem.* **2013**, *4* (207890), 4612–4620.

(72) Li, X.; Yu, Y.; Liu, Q.; Meng, Y. Synthesis and Properties of Anion Conductive Multiblock Copolymers Containing Tetraphenyl Methane Moieties for Fuel Cell Application. *J. Memb. Sci.* **2013**, *436*, 202–212.

(73) Moad, G.; Rizzardo, E.; Thang, S. H. Living Radical Polymerization by the RAFT Process. *Australian Journal of Chemistry*. 2005, pp 379–410.

(74) Moad, G.; Rizzardo, E.; Thang, S. H. Living Radical Polymerization by the RAFT Process A Second Update. *Aust. J. Chem.* **2009**, *62* (11), 1402–1472.

(75) Mayadunne, R. T. a; Jeffery, J.; Moad, G.; Rizzardo, E. Living Free Radical Polymerization with Reversible Addition-Fragmentation Chain Transfer ( RAFT Polymerization ): Approaches to Star Polymers. *Macromolecules* **2003**, *36*, 1505–1513.

(76) Abreu, C. M. R.; Mendonça, P. V.; Serra, A. C.; Coelho, J. F. J.; Popov, A. V.; Gryn'ova, G.; Coote, M. L.; Guliashvili, T. Reversible Addition-Fragmentation Chain Transfer Polymerization of Vinyl Chloride. *Macromolecules* **2012**, *45* (5), 2200–2208.

(77) Jitchum, V.; Perrier, S. Living Radical Polymerization of Isoprene via the RAFT Process. *Macromolecules* **2007**, *40* (5), 1408–1412.

(78) Perrier, S.; Takolpuckdee, P. Macromolecular Design via Reversible Addition-Fragmentation Chain Transfer (RAFT)/xanthates (MADIX) Polymerization. *J. Polym. Sci. Part A Polym. Chem.* **2005**, *43* (22), 5347–5393.

(79) Mai, Y.; Eisenberg, A. Self-Assembly of Block Copolymers. *Chem. Soc. Rev.* **2012**, *41* (18), 5969.

(80) Cochran, E. W.; Garcia-Cervera, C. J.; Fredrickson, G. H. Stability of the Gyroid Phase in Diblock Copolymers at Strong Segregation. *Macromolecules* **2006**, *39* (7), 2449–2451.

(81) Vavasour, J. D.; Whitmore, M. D. Self-Consistent Field Theory of Block Copolymers with Conformational Asymmetry. *Macromolecules* **1993**, *26* (25), 7070–7075.

(82) Tang, J.; Jiang, Y.; Zhang, X.; Yan, D.; Chen, J. Z. Y. Phase Diagram of Rod–Coil Diblock Copolymer Melts. *Macromolecules* **2015**, acs.macromol.5b02235.

(83) Matsen, M. W. Effect of Architecture on the Phase Behavior of AB-Type Block Copolymer Melts. *Macromolecules* **2012**, *45* (4), 2161–2165.

(84) Shi, W.; Lynd, N. a.; Montarnal, D.; Luo, Y.; Fredrickson, G. H.; Kramer, E. J.; Ntaras, C.; Avgeropoulos, A.; Hexemer, A. Toward Strong Thermoplastic Elastomers with Asymmetric Miktoarm Block Copolymer Architectures. *Macromolecules* **2014**, *47* (6), 2037–2043.

(85) Asai, Y.; Yamada, K.; Yamada, M.; Takano, A.; Matsushita, Y. Formation of Tetragonally-Packed Rectangular Cylinders from ABC Block Terpolymer Blends. *ACS Macro Lett.* **2014**, *3* (2), 166–169.

(86) Sing, C.; Zwanikken, J.; Cruz, M. D. La. Electrostatic Control of Block Copolymer Morphology. *Nat. Mater.* **2014**, *13* (7), 694–698.

(87) Bose, S.; Kuila, T.; Nguyen, T. X. H.; Kim, N. H.; Lau, K.; Lee, J. H. Polymer Membranes for High Temperature Proton Exchange Membrane Fuel Cell: Recent Advances and Challenges. *Prog. Polym. Sci.* **2011**, *36* (6), 813–843.

(88) Zhang, F.; Zhang, H.; Qu, C. Imidazolium Functionalized Polysulfone Anion Exchange Membrane for Fuel Cell Application. *J. Mater. Chem.* **2011**, *21* (34), 12744.

(89) Deavin, O. I.; Murphy, S.; Ong, A. L.; Poynton, S. D.; Zeng, R.; Herman, H.; Varcoe, J. R. Anion-Exchange Membranes for Alkaline Polymer Electrolyte Fuel Cells: Comparison of Pendent Benzyltrimethylammonium- and Benzylmethylimidazolium-Head-Groups. *Energy Environ. Sci.* **2012**, *5* (9), 8584.

(90) Yang, Y.; Wang, J.; Zheng, J.; Li, S.; Zhang, S. A Stable Anion Exchange Membrane Based on Imidazolium Salt for Alkaline Fuel Cell. *J. Memb. Sci.* **2014**, *467*, 48–55.

(91) Weiber, E. A.; Jannasch, P. Polysulfones with Highly Localized Imidazolium Groups for Anion Exchange Membranes. *J. Memb. Sci.* **2015**, *481*, 164–171.

(92) Zhang, B.; Gu, S.; Wang, J.; Liu, Y.; Herring, A. M.; Yan, Y. Tertiary Sulfonium as a Cationic Functional Group for Hydroxide Exchange Membranes. *RSC Adv.* **2012**, *2* (33), 12683–12685.

(93) Janarthanan, R.; Horan, J. L.; Caire, B. R.; Ziegler, Z. C.; Yang, Y.; Zuo, X.; Liberatore, M. W.; Hibbs, M. R.; Herring, A. M. Understanding Anion Transport in an Aminated Trimethyl Polyphenylene with High Anionic Conductivity. *J. Polym. Sci. Part B Polym. Phys.* **2013**, *51* (24), 1743–1750.

(94) Li, Y.; Xu, T.; Gong, M. Fundamental Studies of a New Series of Anion Exchange Membranes: Membranes Prepared from Bromomethylated poly(2,6-Dimethyl-1,4-Phenylene Oxide) (BPPO) and Pyridine. *J. Memb. Sci.* **2006**, *279* (1-2), 200–208.

(95) Li, N.; Leng, Y.; Hickner, M. a.; Wang, C. Y. Highly Stable, Anion Conductive, Comb-Shaped Copolymers for Alkaline Fuel Cells. *J. Am. Chem. Soc.* **2013**, *135* (27), 10124–10133.

(96) Li, N.; Yan, T.; Li, Z.; Thurn-Albrecht, T.; Binder, W. H. Comb-Shaped Polymers to Enhance Hydroxide Transport in Anion Exchange Membranes. *Energy Environ. Sci.* **2012**, *5* (7), 7888.

(97) Gu, S.; Skovgard, J.; Yan, Y. S. Engineering the van Der Waals Interaction in Cross-Linking-Free Hydroxide Exchange Membranes for Low Swelling and High Conductivity. *ChemSusChem* **2012**, *5* (5), 843–848.

(98) Liu, Y.; Zhang, B.; Kinsinger, C. L.; Yang, Y.; Seifert, S.; Yan, Y.; Mark Maupin, C.; Liberatore, M. W.; Herring, A. M. Anion Exchange Membranes Composed of a poly(2,6-Dimethyl-1,4-Phenylene Oxide) Random Copolymer Functionalized with a Bulky Phosphonium Cation. *J. Memb. Sci.* **2016**, *506*, 50–59.

(99) Ye, Y.; Elabd, Y. a. Relative Chemical Stability of Imidazolium-Based Alkaline Anion Exchange Polymerized Ionic Liquids. *Macromolecules* **2011**, *44* (21), 8494–8503.

(100) Stokes, K. K.; Orlicki, J. a.; Beyer, F. L. RAFT Polymerization and Thermal Behavior of Trimethylphosphonium Polystyrenes for Anion Exchange Membranes. *Polym. Chem.* **2011**, *2* (1), 80.

(101) Ye, Y.; Stokes, K. K.; Beyer, F. L.; Elabd, Y. a. Development of Phosphonium-Based Bicarbonate Anion Exchange Polymer Membranes. *J. Memb. Sci.* **2013**, *443*, 93–99.

(102) Robertson, N. J.; Iv, H. a K.; Clark, T. J.; Mutolo, P. F.; Coates, G. W. Tunable High Performance Cross-Linked Alkaline Anion Exchange Membranes for Fuel Cell Applications. **2010**, No. 13, 3400–3404.

(103) Xiong, Y.; Fang, J.; Zeng, Q. H.; Liu, Q. L. Preparation and Characterization of Cross-Linked Quaternized Poly(vinyl Alcohol) Membranes for Anion Exchange Membrane Fuel Cells. *J. Memb. Sci.* **2008**, *311* (1-2), 319–325.

(104) Pan, J.; Chen, C.; Zhuang, L.; Lu, J. Designing Advanced Alkaline Polymer Electrolytes for Fuel Cell Applications. *Acc. Chem. Res.* **2012**, *45* (3), 473–481.

(105) Qiu, B.; Lin, B.; Si, Z.; Qiu, L.; Chu, F.; Zhao, J.; Yan, F. Bis-Imidazolium-Based Anion-Exchange Membranes for Alkaline Fuel Cells. *J. Power Sources* **2012**, *217*, 329–335.

(106) Ding, J.; Chuy, C.; Holdcroft, S. A Self-Organized Network of Nanochannels Enhances Ion Conductivity through Polymer Films. *Chem. Mater.* **2001**, *13* (7), 2231–2233.

(107) Tsang, E. M. W.; Zhang, Z.; Shi, Z.; Soboleva, T.; Holdcroft, S. Considerations of Macromolecular Structure in the Design of Proton Conducting Polymer Membranes : Graft versus Diblock Polyelectrolytes Considerations of Macromolecular Structure in the Design of Proton Conducting Polymer Membranes : Graft versus Diblock . **2007**, 15106–15107.

(108) Park, D. Y.; Kohl, P. A.; Beckham, H. W. Anion-Conductive Multiblock Aromatic Copolymer Membranes: Structure-Property Relationships. *J. Phys. Chem. C* **2013**, *117* (30), 15468–15477.

(109) Li, X.; Liu, Q.; Yu, Y.; Meng, Y. Synthesis and Properties of Multiblock Ionomers Containing Densely Functionalized Hydrophilic Blocks for Anion Exchange Membranes. *J. Memb. Sci.* **2014**, *467*, 1–12.

(110) Li, Y.; Liu, Y.; Savage, A. M.; Beyer, F. L.; Seifert, S.; Herring, A. M.; Knauss, D. M. Polyethylene-Based Block Copolymers for Anion Exchange Membranes. *Macromolecules* **2015**, *48* (18), 6523–6533.

(111) Mohanty, A. D.; Ryu, C. Y.; Kim, Y. S.; Bae, C. Stable Elastomeric Anion Exchange Membranes Based on Quaternary Ammonium-Tethered Polystyrene-B-Poly(ethylene-Co-Butylene)-B-Polystyrene Triblock Copolymers. *Macromolecules* **2015**, *48* (19), 7085–7095.

(112) Yang, Y.; Knauss, D. M. Poly(2,6-Dimethyl-1,4-Phenylene Oxide)-B-Poly(vinylbenzyltrimethylammonium) Diblock Copolymers for Highly Conductive Anion Exchange Membranes. *Macromolecules* **2015**, *48* (13), 4471–4480.

(113) Weber, R. L.; Ye, Y.; Schmitt, A. L.; Banik, S. M.; Elabd, Y. a.; Mahanthappa, M. K. Effect of Nanoscale Morphology on the Conductivity of Polymerized Ionic Liquid Block Copolymers. *Macromolecules* **2011**, *44* (14), 5727–5735.

(114) Sudre, G.; Inceoglu, S.; Cotanda, P.; Balsara, N. P. Influence of Bound Ion on the Morphology and Conductivity of Anion-Conducting Block Copolymers. *Macromolecules* **2013**, *46* (4), 1519–1527.

(115) Cotanda, P.; Sudre, G.; Modestino, M. A.; Chen, X. C.; Balsara, N. P. High Anion Conductivity and Low Water Uptake of Phosphonium Containing Diblock Copolymer Membranes. *Macromolecules* **2014**, *47* (21), 7540–7547.

(116) Jiang, Y.; Freyer, J. L.; Cotanda, P.; Brucks, S. D.; Killops, K. L.; Bandar, J. S.; Torsitano, C.; Balsara, N. P.; Lambert, T. H.; Campos, L. M. The Evolution of Cyclopropenium Ions into Functional Polyelectrolytes. *Nat. Commun.* **2015**, *6*, 5950.

(117) Tsai, T.-H.; Maes, A. M.; Vandiver, M. A.; Versek, C.; Seifert, S.; Tuominen, M.; Liberatore, M. W.; Herring, A. M.; Coughlin, E. B. Synthesis and Structure–conductivity Relationship of Polystyrene-Block-Poly(vinyl Benzyl Trimethylammonium) for Alkaline Anion Exchange Membrane Fuel Cells. *J. Polym. Sci. Part B Polym. Phys.* **2013**, *51* (24), 1751–1760.

(118) Kim, S. Y.; Yoon, E.; Joo, T.; Park, M. J. Morphology and Conductivity in Ionic Liquid Incorporated Sulfonated Block Copolymers. *Macromolecules* **2011**, *44* (13), 5289–5298.

(119) Young, W. S.; Epps, T. H. Ionic Conductivities of Block Copolymer Electrolytes with Various Conducting Pathways: Sample Preparation and Processing Considerations. *Macromolecules* **2012**, *45* (11), 4689–4697.

(120) Wanakule, N. S.; Virgili, J. M.; Teran, A. a.; Wang, Z. G.; Balsara, N. P. Thermodynamic Properties of Block Copolymer Electrolytes Containing Imidazolium and Lithium Salts. *Macromolecules* **2010**, *43* (19), 8282–8289.

(121) Teran, A. A.; Balsara, N. P. Thermodynamics of Block Copolymers with and without Salt. *J. Phys. Chem. B* **2014**, *118* (1), 4–17.

(122) Naidu, S.; Ahn, H.; Gong, J.; Kim, B.; Ryu, D. Y. Phase Behavior and Ionic Conductivity of Lithium Perchlorate-Doped Polystyrene-B-poly(2-Vinylpyridine) Copolymer. *Macromolecules* **2011**, *44* (15), 6085–6093.

(123) Pyun, J.; Matyjaszewski, K.; Wu, J.; Kim, G.-M.; Chun, S. B.; Mather, P. T. ABA Triblock Copolymers Containing Polyhedral Oligomeric Silsesquioxane Pendant Groups: Synthesis and Unique Properties. *Polymer (Guildf).* **2003**, *44* (9), 2739–2750.

(124) Xiong, L.; Manthiram, a. High Performance Membrane-Electrode Assemblies with Ultra-Low Pt Loading for Proton Exchange Membrane Fuel Cells. *Electrochim. Acta* **2005**, *50* (16-17), 3200–3204.

(125) Elabd, Y. a.; Hickner, M. a. Block Copolymers for Fuel Cells. *Macromolecules* **2011**, *44* (1), 1–11.

(126) Choi, J. H.; Willis, C. L.; Winey, K. I. Structure-Property Relationship in Sulfonated Pentablock Copolymers. *J. Memb. Sci.* **2012**, *394-395*, 169–174.

(127) Li, Q.; Jensen, J. O.; Savinell, R. F.; Bjerrum, N. J. High Temperature Proton Exchange Membranes Based on Polybenzimidazoles for Fuel Cells. *Prog. Polym. Sci.* **2009**, *34* (5), 449–477.

(128) Womble, C. T.; Coates, G. W.; Matyjaszewski, K.; Noonan, K. J. T. Tetrakis(dialkylamino)phosphonium Polyelectrolytes Prepared by Reversible Addition–Fragmentation Chain Transfer Polymerization. *ACS Macro Lett.* **2016**, *5* (2), 253–257.

(129) Cheng, S.; Beyer, F. L.; Mather, B. D.; Moore, R. B.; Long, T. E. Phosphonium-Containing ABA Triblock Copolymers: Controlled Free Radical Polymerization of Phosphonium Ionic Liquids. *Macromolecules* **2011**, *44* (16), 6509–6517.

(130) Gu, S.; Cai, R.; Luo, T.; Jensen, K.; Contreras, C. Quaternary Phosphonium Based Polymers as Hydroxide Exchange Membranes. *Chem. Sustain.* **2010**, *3*, 555–558.

(131) Degani, I.; Fochi, R.; Gatti, A.; Regondi, V. Phase-Transfer Synthesis of Symmetrical and Unsymmetrical Dialkyl Trithiocarbonates. *Synthesis (Stuttg).* **1986**, *1986* (11), 894–899.

(132) Bowes, A.; Mcleary, J. B.; Sanderson, R. D. AB and ABA Type Butyl Acrylate and Styrene Block Copolymers via RAFT-Mediated Miniemulsion Polymerization. *J. Polym. Sci. Part A Polym. Chem.* **2007**, *45* (4), 588–604.

(133) Vandiver, M. A.; Horan, J. L.; Yang, Y.; Tansey, E. T.; Seifert, S.; Liberatore, M. W.; Herring, A. M. Synthesis and Characterization of Perfluoro Quaternary Ammonium Anion Exchange Membranes. *J. Polym. Sci. Part B Polym. Phys.* **2013**, *51* (24), 1761–1769.

(134) Keddie, D. J. A Guide to the Synthesis of Block Copolymers Using Reversible-Addition Fragmentation Chain Transfer (RAFT) Polymerization. *Chem. Soc. Rev.* **2013**, *43* (2), 496–505.

(135) Germack, D. S.; Wooley, K. L. Isoprene Polymerization via Reversible Addition Fragmentation Chain Transfer Polymerization. *J. Polym. Sci. Part A Polym. Chem.* **2007**, *45* (17), 4100–4108.

(136) Germack, D. S.; Wooley, K. L. RAFT-Based Synthesis and Characterization of ABC versus ACB Triblock Copolymers Containing Tert-Butyl Acrylate, Isoprene, and Styrene Blocks. *Macromol. Chem. Phys.* **2007**, *208* (23), 2481–2491.

(137) Harrisson, S.; Couvreur, P.; Nicolas, J. SG1 Nitroxide-Mediated Polymerization of Isoprene: Alkoxyamine Structure/control Relationship and ??,??-Chain-End Functionalization. *Macromolecules* **2011**, *44* (23), 9230–9238.

(138) Chen, J. T.; Thomas, E. L.; Ober, C. K.; Mao, G. -p. Self-Assembled Smectic Phases in Rod-Coil Block Copolymers. *Science (80-. ).* **1996**, *273* (5273), 343–346.

(139) Wang, J. Y.; Chen, W.; Roy, C.; Sievert, J. D.; Russell, T. P. Influence of Ionic Complexes on Phase Behavior of Polystyrene-B-Poly(methyl Methacrylate) Copolymers. *Macromolecules* **2008**, *41* (3), 963–969.

(140) Young, W. S.; Epps, T. H. Salt Doping in PEO-Containing Block Copolymers: Counterion and Concentration Effects. *Macromolecules* **2009**, *42* (7), 2672–2678.

(141) Park, M. J.; Balsara, N. P. Phase Behavior of Symmetric Sulfonated Block Copolymers. *Macromolecules* **2008**, *41* (10), 3678–3687.

(142) Diddens, D.; Heuer, A.; Borodin, O. Understanding the Lithium Transport within a Rouse-Based Model for a PEO/LiTFSI Polymer Electrolyte. *Macromolecules* **2010**, *43* (4), 2028–2036.

(143) Chen, H.; Choi, J. H.; Cruz, D. S. D. La; Winey, K. I.; Elabd, Y. a. Polymerized Ionic Liquids: The Effect of Random Copolymer Composition on Ion Conduction. *Macromolecules* **2009**, *42* (13), 4809–4816.

(144) Lee, M.; Choi, U. H.; Colby, R. H.; Gibson, H. W. Ion Conduction in Imidazolium Acrylate Ionic Liquids and Their Polymers. *Chem. Mater.* **2010**, *22* (21), 5814–5822.

(145) Weber, R. L.; Ye, Y.; Banik, S. M.; Elabd, Y. a.; Hickner, M. a.; Mahanthappa, M. K. Thermal and Ion Transport Properties of Hydrophilic and Hydrophobic Polymerized Styrenic Imidazolium Ionic Liquids. *J. Polym. Sci. Part B Polym. Phys.* **2011**, *49* (18), 1287–1296.

(146) Gwee, L.; Choi, J.-H.; Winey, K. I.; Elabd, Y. A. Block Copolymer/ionic Liquid Films: The Effect of Ionic Liquid Composition on Morphology and Ion Conduction. *Polymer (Guildf).* **2010**, *51* (Copyright (C) 2014 American Chemical Society (ACS). All Rights Reserved.), 5516–5524.

(147) Schulze, M. W.; McIntosh, L. D.; Hillmyer, M. a.; Lodge, T. P. High-Modulus, High-Conductivity Nanostructured Polymer Electrolyte Membranes via Polymerization-Induced Phase Separation. *Nano Lett.* **2014**, *14* (1), 122–126.

(148) Kuan, W.-F.; Remy, R.; Mackay, M. E.; Epps, III, T. H. Controlled Ionic Conductivity via Tapered Block Polymer Electrolytes. *RSC Adv.* **2015**, *5* (17), 12597–12604.

(149) Robitaille, C. D.; Fauteux, D. Phase Diagrams and Conductivity Characterization of Some PEO - LiX Electrolytes. *J. Electrochem. Soc.* **1986**, *133* (2 ), 315–325.

(150) Liu, Y.; Wang, J.; Yang, Y.; Brenner, T. M.; Seifert, S.; Yan, Y.; Liberatore, M. W.; Herring, A. M. Anion Transport in a Chemically Stable, Sterically Bulky α-C Modified Imidazolium Functionalized Anion Exchange Membrane. *J. Phys. Chem. C* **2014**, *118* (28), 15136–15145.

(151) Beers, K. M.; Wong, D. T.; Jackson, A. J.; Wang, X.; Pople, J. A.; Hexemer, A.; Balsara, N. P. Effect of Crystallization on Proton Transport in Model Polymer Electrolyte Membranes. *Macromolecules* **2014**, *47* (13), 4330–4336.

(152) Schrock, R. Living Ring-Opening Metathesis Polymerization Catalyzed by Well-Characterized Transition-Metal Alkylidene Complexes. *Acc. Chem. Res.* **1990**, *23*, 158–165.

(153) Nguyen, S. B. T.; Johnson, L. K.; Grubbs, R. H. Ring-Opening Metathesis Polymerization (ROMP) of Norbornene by a Group VIII Carbene Complex in Protic Media. *J. Am. …* **1992**, *114* (8), 3974–3975.

(154) Bielawski, C. W.; Grubbs, R. H. Living Ring-Opening Metathesis Polymerization. *Prog. Polym. Sci.* **2007**, *32* (1), 1–29.

(155) Hillmyer, M. A.; Laredo, W. R.; Grubbs, R. H. Ring-Opening Metathesis Polymerization of Functionalized Cyclooctenes by a Ruthenium-Based Metathesis Catalyst. *Macromolecules* **1995**, *28* (18), 6311–6316.

(156) Rosebrugh, L. E.; Marx, V. M.; Keitz, B. K.; Grubbs, R. H. Synthesis of Highly Cis, Syndiotactic Polymers via Ring-Opening Metathesis Polymerization Using Ruthenium Metathesis Catalysts. *J. Am. Chem. Soc.* **2013**, *135* (27), 10032–10035.

(157) Vougioukalakis, G. C.; Grubbs, R. H. Ruthenium-Based Heterocyclic Carbene-Coordinated Olefin Metathesis Catalysts. *Chem. Rev.* **2010**, *110* (3), 1746–1787.

(158) Choi, T. L.; Grubbs, R. H. Controlled Living Ring-Opening-Metathesis Polymerization by a Fast-Initiating Ruthenium Catalyst. *Angew. Chemie - Int. Ed.* **2003**, *42* (15), 1743–1746.

(159) Lozano, A. M.; Bajek, A.; Monsaert, S.; Drozdak, R.; Verpoort, F. Secondary Metathesis with Grubbs Type Catalysts: In the 1,4-Polybutadiene System. *Chim. Oggi* **2009**, *27* (3), 20–23.

(160) Chatterjee, A. K.; Choi, T. L.; Sanders, D. P.; Grubbs, R. H. A General Model for Selectivity in Olefin Cross Metathesis. *J. Am. Chem. Soc.* **2003**, *125* (37), 11360–11370.

(161) Kobayashi, S.; Pitet, L. M.; Hillmyer, M. a. Regio- and Stereoselective Ring-Opening Metathesis Polymerization of 3-Substituted Cyclooctenes. *J. Am. Chem. Soc.* **2011**, *133* (15), 5794–5797.

(162) Bielawski, C. W.; Grubbs, R. H. Highly Efficient Ring-Opening Metathesis Polymerization (ROMP) Using New Ruthenium Catalysts Containing N-Heterocyclic Carbene Ligands. *Angew. Chemie - Int. Ed.* **2000**, *39* (16), 2903–2906.

(163) Coca, S.; Paik, H.; Matyjaszewski, K. Block Copolymers by Transformation of "Living" Ring-Opening Metathesis Polymerization into Controlled/"Living" Atom Transfer Radical Polymerization. *Macromolecules* **1997**, *30* (21), 6513–6516.

(164) Mathers, R. T.; McMahon, K. C.; Damodaran, K.; Retarides, C. J.; Kelley, D. J. Ring-Opening Metathesis Polymerizations in D-Limonene: A Renewable Polymerization Solvent and Chain Transfer Agent for the Synthesis of Alkene Macromonomers. *Macromolecules* **2006**, *39* (26), 8982–8986.

(165) Madkour, A. E.; Koch, A. H. R.; Lienkamp, K.; Tew, G. N. End-Functionalized ROMP Polymers for Biomedical Applications. *Macromolecules* **2010**, *43* (10), 4557–4561.

(166) Bielawski, C. W.; Morita, T.; Grubbs, R. H. Synthesis of ABA Triblock Copolymers via a Tandem Ring-Opening Metathesis Polymerization: Atom Transfer Radical Polymerization Approach. *Macromolecules* **2000**, *33* (3), 678–680.

(167) Nagarkar, A. A.; Kilbinger, A. F. M. Catalytic Living Ring-Opening Metathesis Polymerization. *Nat. Chem.* **2015**, *7* (9), 718–723.

(168) Pitet, L. M.; Chamberlain, B. M.; Hauser, A. W.; Hillmyer, M. a. Synthesis of Linear, H-Shaped, and Arachnearm Block Copolymers by Tandem Ring-Opening Polymerizations. *Macromolecules* **2010**, *43* (19), 8018–8025.

(169) Mahanthappa, M. K.; Bates, F. S.; Hillmyer, M. a. Synthesis of ABA Triblock Copolymers by a Tandem ROMP-RAFT Strategy. *Macromolecules* **2005**, *38* (19), 7890–7894.

(170) Banik, S. M.; Monnot, B. L.; Weber, R. L.; Mahanthappa, M. K. ROMP-CT/NMP Synthesis of Multiblock Copolymers Containing Linear Poly(ethylene) Segments. *Macromolecules* **2011**, *44* (18), 7141–7148.

(171) Widin, J. M.; Schmitt, A. K.; Im, K.; Schmitt, A. L.; Mahanthappa, M. K. Polydispersity-Induced Stabilization of a Disordered Bicontinuous Morphology in ABA Triblock Copolymers. *Macromolecules* **2010**, *43* (19), 7913–7915.

(172) Widin, J. M.; Schmitt, A. K.; Schmitt, A. L.; Im, K.; Mahanthappa, M. K. Unexpected Consequences of Block Polydispersity on the Self-Assembly of ABA Triblock Copolymers. *J. Am. Chem. Soc.* **2012**, *134* (8), 3834–3844.

(173) Li, Y.; Qian, H. J.; Lu, Z. Y.; Shi, A. C. Enhancing Composition Window of Bicontinuous Structures by Designed Polydispersity Distribution of ABA Triblock Copolymers. *Polym. (United Kingdom)* **2013**, *54* (22), 6253–6260.

(174) Ruzette, A. V.; Tencé-Girault, S.; Leibler, L.; Chauvin, F.; Bertin, D.; Guerret, O.; Gérard, P. Molecular Disorder and Mesoscopic Order in Polydisperse Acrylic Block Copolymers Prepared by Controlled Radical Polymerization. *Macromolecules* **2006**, *39* (17), 5804–5814.

(175) Cooke, D. M.; Shi, A. C. Effects of Polydispersity on Phase Behavior of Diblock Copolymers. *Macromolecules* **2006**, *39* (19), 6661–6671.

(176) Pitet, L. M.; Hillmyer, M. A. Combining Ring-Opening Metathesis Polymerization and Cyclic Ester Ring-Opening Polymerization to Form ABA Triblock Copolymers from 1,5-Cyclooctadiene and D, L-Lactide. *Macromolecules* **2009**, *42* (11), 3674–3680.

(177) Noro, A.; Iinuma, M.; Suzuki, J.; Takano, A.; Matsushita, Y. Effect of Composition Distribution on Microphase-Separated Structure from BAB Triblock Copolymers. *Macromolecules* **2004**, *37* (10), 3804–3808.

(178) Schmitt, A. L.; Mahanthappa, M. K. Polydispersity-Driven Shift in the Lamellar Mesophase Composition Window of PEO-PB-PEO Triblock Copolymers. *Soft Matter* **2012**, *8* (7), 2294.

(179) Han, H.; Chen, F.; Yu, J.; Dang, J.; Ma, Z.; Zhang, Y.; Xie, M. Ring-Opening Metathesis Polymerization of Functionalized Cyclooctene by a Ruthenium-Based Catalyst in Ionic Liquid. *J. Polym. Sci. Part A Polym. Chem.* **2007**, *45* (17), 3986–3993.

(180) Caire, B. R.; Vandiver, M. A.; Liberatore, M. W. Mechanical Testing of Small, Thin Samples in a Humidity-Controlled Oven. *Rheol. Acta* **2015**, *54* (4), 253–261.

(181) Hillmyer, M. A.; Nguyen, S. T.; Grubbs, R. H. Utility of a Ruthenium Metathesis Catalyst for the Preparation of End-Functionalized Polybutadiene. *Macromolecules* **1997**, *30* (4), 718–721.

(182) Cheng, C.; Khoshdel, E.; Wooley, K. L. One-Pot Tandem Synthesis of a Core-Shell Brush Copolymer from Small Molecule Reactants by Ring-Opening Metathesis and Reversible Addition-Fragmentation Chain Transfer (co)polymerizations. *Macromolecules* **2007**, *40* (7), 2289–2292.

(183) Patton, D. L.; Advincula, R. C. A Versatile Synthetic Route to Macromonomers via RAFT Polymerization. *Macromolecules* **2006**, *39* (25), 8674–8683.

(184) Sutthasupa, S.; Shiotsuki, M.; Sanda, F. Recent Advances in Ring-Opening Metathesis Polymerization, and Application to Synthesis of Functional Materials. *Polym. J.* **2010**, *42* (12), 905–915.

(185) Shi, H.; Shi, D.; Yao, Z.; Luan, S.; Jin, J.; Zhao, J.; Yang, H.; Stagnaro, P.; Yin, J. Synthesis of Amphiphilic Poly(cyclooctene)-Graft-Poly(ethylene Glycol) copolymersviaROMP and Its Surface Properties. *Polym. Chem.* **2011**, *2* (3), 679–684.

(186) Walker, R.; Conrad, R. M.; Grubbs, R. H. The Living ROMP of Trans-Cyclooctene. *Macromolecules* **2009**, *42* (3), 599–605.

(187) Chen, X. C.; Wong, D. T.; Yakovlev, S.; Beers, K. M.; Downing, K. H.; Balsara, N. P. Effect of Morphology of Nanoscale Hydrated Channels on Proton Conductivity in Block Copolymer Electrolyte Membranes. *Nano Lett.* **2014**, *14* (7), 4058–4064.

(188) SHULL, K. R.; WINEY, K. I. HOMOPOLYMER DISTRIBUTIONS IN LAMELLAR COPOLYMER HOMOPOLYMER BLENDS. *Macromolecules* **1992**, *25* (10), 2637–2644.

(189) Winey, K. I.; Thomas, E. L.; Fetters, L. J. Swelling of Lamellar Diblock Copolymer by Homopolymer: Influences of Homopolymer Concentration and Molecular Weight. *Macromolecules* **1991**, *24* (23), 6182–6188.

(190) Chen, X. C.; Yang, H.; Green, P. F. Tethered-Polymer Structures in Thin Film Polymer Melts. *Macromolecules* **2011**, *44* (14), 5758–5763.

(191) Chen, X. C.; Yang, H.; Green, P. F. Micellar Formation and Organization in Thin Film Polymer Blends. *Macromolecules* **2012**, *45* (9), 3993–4000.

(192) Semenov, A. N. Theory of Block Copolymer Interfaces in the Strong Segregation Limit. *Macromolecules* **1993**, *26*, 6617–6621.

(193) Evans, C. M.; Sanoja, G. E.; Popere, B. C.; Segalman, R. A. Anhydrous Proton Transport in Polymerized Ionic Liquid Block Copolymers: Roles of Block Length, Ionic Content, and Confinement. *Macromolecules* **2016**, *49* (1), 395–404.

(194) Lewandowski, C. M.; Co-investigator, N.; Lewandowski, C. M. Interplay between Solid State Transitions, Conductivity Mechanisms, and Electrical Relaxations in a [PVBTMA][Br]-B-PMB Diblock Copolymer Membrane for Electrochemical Applications. *PCCP* **2015**, *1*, 1689–1699.

(195) Sethuraman, V.; Pryamitsyn, V.; Ganesan, V. Influence of Molecular Weight and Degree of Segregation on Local Segmental Dynamics of Ordered Block Copolymers. *J. Polym. Sci. Part B Polym. Phys.* **2016**, n/a – n/a.

(196) Sharick, S.; Koski, J.; Riggleman, R. A.; Winey, K. I. Isolating the Effect of Molecular Weight on Ion Transport of Non-Ionic Diblock Copolymer/Ionic Liquid Mixtures. *Macromolecules* **2016**.

(197) Lynd, N. A.; Oyerokun, F. T.; O'Donoghue, D. L.; Handlin, D. L.; Fredrickson, G. H. Design of Soft and Strong Thermoplastic Elastomers Based on Nonlinear Block Copolymer Architectures Using Self-Consistent-Field Theory. *Macromolecules* **2010**, *43* (7), 3479–3486.

(198) Bates, F. S.; Fredrickson, G. H. Block Copolymer Thermodynamics: Theory and Experiment. *Annu. Rev. Phys. Chem.* **1990**, *41* (1), 525–557.

(199) Bates, F. S.; Fredrickson, G. H. Block Copolymers—Designer Soft Materials. *Phys. Today* **1999**, *52* (2), 32.

(200) Matsen, M. W.; Thompson, R. B. Equilibrium Behavior of Symmetric ABA Triblock Copolymer Melts. *J. Chem. Phys.* **1999**, *111* (15), 7139.

(201) Matsen, M. W. Equilibrium Behavior of Asymmetric ABA Triblock Copolymer Melts. *J. Chem. Phys.* **2000**, *113* (13), 5539–5544.

(202) Xie, N.; Li, W.; Qiu, F.; Shi, A. σ Phase Formed in Conformationally Asymmetric AB-Type Block Copolymers. **2014**.

(203) Thomas, E. L.; Alward, D. B.; Kinning, D. J.; Martin, D. C.; Handlin, D. L.; Fetters, L. J. Ordered Bicontinuous Double-Diamond Structure of Star Block Copolymers: A New Equilibrium Microdomain Morphology. *Macromolecules* **1986**, *19* (8), 2197–2202.

(204) Matsen, M.; Schick, M. Microphase Separation in Starblock Copolymer Melts. *Macromolecules* **1994**, *27*, 6761–6767.

(205) Koo, K.; Ahn, H.; Kim, S.-W.; Ryu, D. Y.; Russell, T. P. Directed Self-Assembly of Block Copolymers in the Extreme: Guiding Microdomains from the Small to the Large. *Soft Matter* **2013**, *9* (38), 9059.

(206) Jeong, S. J.; Moon, H. S.; Shin, J.; Kim, B. H.; Shin, D. O.; Kim, J. Y.; Lee, Y. H.; Kim, J. U.; Kim, S. O. One-Dimensional Metal Nanowire Assembly via Block Copolymer Soft Graphoepitaxy. *Nano Lett.* **2010**, *10* (9), 3500–3505.

(207) Thurn-Albrecht, T.; Schotter, J.; Kästle, G. a; Emley, N.; Shibauchi, T.; Krusin-Elbaum, L.; Guarini, K.; Black, C. T.; Tuominen, M. T.; Russell, T. P. Ultrahigh-Density Nanowire Arrays Grown in Self-Assembled Diblock Copolymer Templates. *Science* **2000**, *290* (5499), 2126–2129.

(208) Liu, G.; Wu, Y.; Lin, Y. M.; Farmer, D. B.; Ott, J. A.; Bruley, J.; Grill, A.; Avouris, P.; Pfeiffer, D.; Balandin, A. A.; Dimitrakopoulos, C. Epitaxial Graphene Nanoribbon Array Fabrication Using BCP-Assisted Nanolithography. *ACS Nano* **2012**, *6* (8), 6786–6792.

(209) Ruiz, R.; Kang, H. M.; Detcheverry, F. A.; Dobisz, E.; Kercher, D. S.; Albrecht, T. R.; de Pablo, J. J.; Nealey, P. F. Density Multiplication and Improved Lithography by Directed Block Copolymer Assembly. *Science (80-. ).* **2008**, *321* (5891), 936–939.

(210) Moad, G.; Chong, Y. K.; Postma, A.; Rizzardo, E.; Thang, S. H. Advances in RAFT Polymerization: The Synthesis of Polymers with Defined End-Groups. *Polymer (Guildf).* **2005**, *46* (19 SPEC. ISS.), 8458–8468.

(211) Tong, J. D.; Jerôme, R. Synthesis of Poly(methyl Methacrylate)-B-Poly(n-Butyl Acrylate)-B- Poly(methyl Methacrylate) Triblocks and Their Potential as Thermoplastic Elastomers. *Polymer (Guildf).* **2000**, *41* (7), 2499–2510.

(212) Goldman, E.; Ragle, J. L. Complex of Pyridine with Chloroform: Deuterium Nuclear Quadrupole Coupling. *J. Phys. Chem.* **1986**, *90* (24), 6440–6446.

(213) Sun, Z.; Chen, Z.; Zhang, W.; Choi, J.; Huang, C.; Jeong, G.; Coughlin, E. B.; Hsu, Y.; Yang, X.; Lee, K. Y.; Kuo, D. S.; Xiao, S.; Russell, T. P. Directed Self-Assembly of Poly(2-Vinylpyridine)-B-Polystyrene-B-poly(2-Vinylpyridine) Triblock Copolymer with Sub-15 Nm Spacing Line Patterns Using a Nanoimprinted Photoresist Template. *Adv. Mater.* **2015**, *27* (29), 4364–4370.

(214) Tirumala, V. R.; Daga, V.; Bosse, A. W.; Romang, A.; Ilavsky, J.; Lin, E. K.; Watkins, J. J. Well-Ordered Polymer Melts with 5 Nm Lamellar Domains from Blends of a Disordered Block Copolymer and a Selectively Associating Homopolymer of Low or High Molar Mass. *Macromolecules* **2008**, *41* (21), 7978–7985.

(215) Tirumala, V. R.; Romang, A.; Agarwal, S.; Lin, E. K.; Watkins, J. J. Well Ordered Polymer Melts from Blends of Disordered Triblock Copolymer Surfactants and Functional Homopolymers. *Adv. Mater.* **2008**, *20* (9), 1603–1608.

(216) Nakamura, I.; Wang, Z. G. Thermodynamics of Salt-Doped Block Copolymers. *ACS Macro Lett.* **2014**, *3* (8), 708–711.

(217) Leibler, L. Theory of Microphase Separation in Block Copolymers. *Macromolecules* **1980**, *13* (10), 1602–1617.

(218) Maher, M. J.; Bates, C. M.; Blachut, G.; Sirard, S.; Self, J. L.; Carlson, M. C.; Dean, L. M.; Cushen, J. D.; Durand, W. J.; Hayes, C. O.; Ellison, C. J.; Willson, C. G. Interfacial Design for Block Copolymer Thin Films. *Chem. Mater.* **2014**, *26* (3), 1471–1479.

(219) Bates, C. M.; Seshimo, T.; Maher, M. J.; Durand, W. J.; Cushen, J. D.; Dean, L. M.; Blachut, G.; Ellison, C. J.; Willson, C. G. Polarity-Switching Top Coats Enable Orientation of Sub-10-Nm Block Copolymer Domains. *Science (80-. ).* **2012**, *338* (6108), 775–779.

(220) Maher, M. J.; Rettner, C. T.; Bates, C. M.; Blachut, G.; Carlson, M. C.; Durand, W. J.; Ellison, C. J.; Sanders, D. P.; Cheng, J. Y.; Willson, C. G. Directed Self-Assembly of Silicon-Containing Block Copolymer Thin Films. *ACS Appl. Mater. Interfaces* **2015**, *7* (5), 3323–3328.

(221) Hawker, C. J.; Russell, T. P. Block Copolymer Lithography: Merging “Bottom-Up” with “Top-Down” Processes. *MRS Bull.* **2005**, *30* (12), 952–966.

(222) Kim, S.; Bates, C. M.; Thio, A.; Cushen, J. D.; Ellison, C. J.; Willson, C. G.; Bates, F. S. Consequences of Surface Neutralization in Diblock Copolymer Thin Films. *ACS Nano* **2013**, *7* (11), 9905–9919.

(223) Gu, W.; Hong, S. W.; Russell, T. P. Orienting Block Copolymer Microdomains with Block Copolymer Brushes. *ACS Nano* **2012**, *6* (11), 10250–10257.

(224) She, M. S.; Lo, T. Y.; Ho, R. M. Long-Range Ordering of Block Copolymer Cylinders Driven by Combining Thermal Annealing and Substrate Functionalization. *ACS Nano* **2013**, *7* (3), 2000–2011.

(225) Ji, S.; Liu, G.; Zheng, F.; Craig, G. S. W.; Himpsel, F. J.; Nealey, P. F. Preparation of Neutral Wetting Brushes for Block Copolymer Films from Homopolymer Blends. *Adv. Mater.* **2008**, *20* (16), 3054–3060.

(226) Huang, E.; Pruzinsky, S.; Russell, T. P.; Mays, J.; Hawker, C. J. Neutrality Conditions for Block Copolymer Systems on Random Copolymer Brush Surfaces. *Macromolecules* **1999**, *32* (16), 5299–5303.

(227) Sinturel, C.; Vayer, M.; Morris, M.; Hillmyer, M. a. Solvent Vapor Annealing of Block Polymer Thin Films. *Macromolecules* **2013**, *46* (14), 5399–5415.

(228) Albert, J. N. L.; Epps, T. H. Self-Assembly of Block Copolymer Thin Films. *Materials Today*. 2010, pp 24–33.

(229) Jung, Y. S.; Ross, C. A. Solvent-Vapor-Induced Tunability of Self-Assembled Block Copolymer Patterns. *Adv. Mater.* **2009**, *21* (24), 2540–2545.

(230) Yanagi, H.; Fukuta, K. Anion Exchange Membrane and Ionomer for Alkaline Membrane Fuel Cells (AMFCs). *ECS Trans.* **2008**, *16* (2), 257–262.

(231) Varcoe, J. R.; Slade, R. C. T.; Lam How Yee, E. An Alkaline Polymer Electrochemical Interface: A Breakthrough in Application of Alkaline Anion-Exchange Membranes in Fuel Cells. *Chem. Commun. (Camb).* **2006**, No. 13, 1428–1429.

(232) Verma, A.; Basu, S. Direct Alkaline Fuel Cell for Multiple Liquid Fuels: Anode Electrode Studies. *J. Power Sources* **2007**, *174* (1), 180–185.

(233) Xiao, S.; Yang, X.; Steiner, P.; Hsu, Y.; Lee, K.; Wago, K.; Kuo, D. Servo-Integrated Patterned Media by Hybrid Directed Self-Assembly. *ACS Nano* **2014**, *8* (11), 11854–11859.

(234) Ruiz, R.; Dobisz, E.; Albrecht, T. R. Rectangular Patterns Using Block Copolymer Directed Assembly for High Bit Aspect Ratio Patterned Media. *ACS Nano* **2011**, *5* (1), 79–84.

(235) McMurray, R. J.; Gadegaard, N.; Tsimbouri, P. M.; Burgess, K. V; McNamara, L. E.; Tare, R.; Murawski, K.; Kingham, E.; Oreffo, R. O.; Dalby, M. J. Nanoscale Surfaces for the Long-Term Maintenance of Mesenchymal Stem Cell Phenotype and Multipotency. *Nat Mater* **2011**, *10* (8), 637–644.

(236) Chen, C. S.; Mrksich, M.; Huang, S.; Whitesides, G. M.; Ingber, D. E. Geometric Control of Cell Life and Death. *Science* **1997**, *276* (5317), 1425–1428.

(237) Choi, H. K.; Gwyther, J.; Manners, I.; Ross, C. A. Square Arrays of Holes and Dots Patterned from a Linear ABC Triblock Terpolymer. *ACS Nano* **2012**, *6* (9), 8342–8348.

(238) Tsai, H.; Pitera, J. W.; Miyazoe, H.; Bangsaruntip, S.; Engelmann, S. U.; Liu, C. C.; Cheng, J. Y.; Bucchignano, J. J.; Klaus, D. P.; Joseph, E. A.; Sanders, D. P.; Colburn, M. E.; Guillorn, M. A. Two-Dimensional Pattern Formation Using Graphoepitaxy of PS-B-PMMA Block Copolymers for Advanced FinFET Device and Circuit Fabrication. *ACS Nano* **2014**, *8* (5), 5227–5232.

(239) Barnes, W. L.; Dereux, A.; Ebbesen, T. W. Surface Plasmon Subwavelength Optics. *Nature* **2003**, *424* (6950), 824–830.

(240) Tang, C.; Tracz, A.; Kruk, M.; Zhang, R.; Smilgies, D. M.; Matyjaszewski, K.; Kowalewski, T. Long-Range Ordered Thin Films of Block Copolymers Prepared by Zone-Casting and Their Thermal Conversion into Ordered Nanostructured Carbon. *J. Am. Chem. Soc.* **2005**, *127* (19), 6918–6919.

(241) Angelescu, D. E.; Waller, J. H.; Adamson, D. H.; Register, R. A.; Chaikin, P. M. Enhanced Order of Block Copolymer Cylinders in Single-Layer Films Using a Sweeping Solidification Front. *Adv. Mater.* **2007**, *19* (18), 2687–2690.

(242) Onses, M. S.; Song, C.; Williamson, L.; Sutanto, E.; Ferreira, P. M.; Alleyne, A. G.; Nealey, P. F.; Ahn, H.; Rogers, J. A. Hierarchical Patterns of Three-Dimensional Block-Copolymer Films Formed by Electrohydrodynamic Jet Printing and Self-Assembly. *Nat. Nanotechnol.* **2013**, *8* (9), 667–675.

(243) Berry, B. C.; Bosse, A. W.; Douglas, J. F.; Jones, R. L.; Karim, A. Orientational Order in Block Copolymer Films Zone Annealed below the Order-Disorder Transition Temperature. *Nano Lett.* **2007**, *7* (9), 2789–2794.

(244) Seppala, J. E.; Lewis, R. L.; Epps, T. H. Spatial and Orientation Control of Cylindrical Nanostructures in ABA Triblock Copolymer Thin Films by Raster Solvent Vapor Annealing. *ACS Nano* **2012**, *6* (11), 9855–9862.

(245) Kellogg, G. J.; Walton, D. G.; Mayes, A. M.; Lambooy, P.; Russell, T. P.; Gallagher, P. D.; Satija, S. K. Observed Surface Energy Effects in Confined Diblock Copolymers. *Phys. Rev. Lett.* **1996**, *76* (14), 2503–2506.

(246) Park, C.; Yoon, J.; Thomas, E. L. Enabling Nanotechnology with Self Assembled Block Copolymer Patterns. *Polymer*. 2003, pp 6725–6760.

(247) Park, S. H.; Shin, D. O.; Kim, B. H.; Yoon, D. K.; Kim, K.; Lee, S. Y.; Oh, S.-H.; Choi, S.-W.; Jeon, S. C.; Kim, S. O. Block Copolymer Multiple Patterning Integrated with Conventional ArF Lithography. *Soft Matter* **2010**, *6* (1), 120–125.

(248) Liu, G.; Thomas, C. S.; Craig, G. S. W.; Nealey, P. F. Integration of Density Multiplication in the Formation of Device-Oriented Structures by Directed Assembly of Block Copolymer-Homopolymer Blends. *Adv. Funct. Mater.* **2010**, *20* (8), 1251–1257.

(249) Kim, S. O.; Solak, H. H.; Stoykovich, M. P.; Ferrier, N. J.; De Pablo, J. J.; Nealey, P. F. Epitaxial Self-Assembly of Block Copolymers on Lithographically Defined Nanopatterned Substrates. *Nature* **2003**, *424* (6947), 411–414.

(250) Park, C.; Cheng, J. Y.; Fasolka, M. J.; Mayes, A. M.; Ross, C. A.; Thomas, E. L.; De Rosa, C. Double Textured Cylindrical Block Copolymer Domains via Directional Solidification on a Topographically Patterned Substrate. *Appl. Phys. Lett.* **2001**, *79* (6), 848–850.

(251) Segalman R.A. Patterning with Block Copolymer Thin Films. *Mater. Sci. Eng. R Reports* **2005**, *48* (6), 191–226.

(252) Luo, M.; Seppala, J. E.; Albert, J. N. L.; Lewis, R. L.; Mahadevapuram, N.; Stein, G. E.; Epps, T. H. Manipulating Nanoscale Morphologies in Cylinder-Forming Poly(styrene- B -Isoprene- B -Styrene) Thin Films Using Film Thickness and Substrate Surface Chemistry Gradients. *Macromolecules* **2013**, *46* (5), 1803–1811.

(253) Bang, J.; Bae, J.; L??wenhielm, P.; Spiessberger, C.; Given-Beck, S. A.; Russell, T. P.; Hawker, C. J. Facile Routes to Patterned Surface Neutralization Layers for Block Copolymer Lithography. *Adv. Mater.* **2007**, *19* (24), 4552–4557.

(254) Han, E.; In, I.; Park, S. M.; La, Y. H.; Wang, Y.; Nealey, P. F.; Gopalan, P. Photopatternable Imaging Layers for Controlling Block Copolymer Microdomain Orientation. *Adv. Mater.* **2007**, *19* (24), 4448–4452.

(255) Maher, M. J.; Bates, C. M.; Blachut, G.; Carlson, M. C.; Self, J. L.; Janes, D. W.; Durand, W. J.; Lane, A. P.; Ellison, C. J.; Willson, C. G. Photopatternable Interfaces for Block Copolymer Lithography. *ACS Macro Lett.* **2014**, *3* (8), 824–828.

(256) Yao, L.; Watkins, J. J. Photoinduced Disorder in Strongly Segregated Block Copolymer Composite Films for Hierarchical Pattern Formation. *ACS Nano* **2013**, *7* (2), 1513–1523.

(257) Tran, H.; Ronaldson, K.; Bailey, N. A.; Lynd, N. A.; Killops, K. L.; Vunjak-novakovic, G.; Campos, L. M. Hierarchically Ordered Nanopatterns for Spatial Control of Biomolecules. **2014**, 11846–11853.

(258) Bosworth, J. K.; Black, C. T.; Ober, C. K. Selective Area Control of Self-Assembled Pattern Architecture Using a Lithographically Patternable Block Copolymer. *ACS Nano* **2009**, *3* (7), 1761–1766.

(259) Isono, T.; Otsuka, I.; Kondo, Y.; Halila, S.; Fort, S.; Rochas, C.; Satoh, T.; Borsali, R.; Kakuchi, T. Sub-10 Nm Nano-Organization in AB2- and AB3-Type Miktoarm Star Copolymers Consisting of Maltoheptaose and Polycaprolactone. *Macromolecules* **2013**, *46* (4), 1461–1469.

(260) Barltrop, J. A.; Plant, P. J.; Schofield, P. Photosensitive Protective Groups. *Chem. Commun. (London)* **1966**, No. 22, 822–823.

(261) Zhao, H.; Gu, W.; Sterner, E.; Russell, T. P.; Coughlin, E. B.; Theato, P. Highly Ordered Nanoporous Thin Films from Photocleavable Block Copolymers. *Macromolecules* **2011**, *44* (16), 6433–6440.

(262) Zhao, H.; Sterner, E. S.; Coughlin, E. B.; Theato, P. O-Nitrobenzyl Alcohol Derivatives: Opportunities in Polymer and Materials Science. *Macromolecules* **2012**, *45* (4), 1723–1736.

(263) Lü, S.; Li, B.; Ni, B.; Sun, Z.; Liu, M.; Wang, Q. Thermoresponsive Injectable Hydrogel for Three-Dimensional Cell Culture: Chondroitin Sulfate Bioconjugated with poly(N-Isopropylacrylamide) Synthesized by RAFT Polymerization. *Soft Matter* **2011**, *7* (22), 10763.

(264) Schumers, J.-M.; Gohy, J.-F.; Fustin, C.-A. A Versatile Strategy for the Synthesis of Block Copolymers Bearing a Photocleavable Junction. *Polym. Chem.* **2010**, *1* (2), 161.

(265) Gu, W.; Zhao, H.; Wei, Q.; Coughlin, E. B.; Theato, P.; Russell, T. P. Line Patterns from Cylinder-Forming Photocleavable Block Copolymers. *Adv. Mater.* **2013**, *25* (34), 4690–4695.

(266) Urbas, A.; Sharp, R.; Fink, Y.; Thomas, E. L.; Xenidou, M.; Fetters, L. J. Tunable Block Copolymer/homopolymer Photonic Crystals. *Adv. Mater.* **2000**, *12* (11), 812–814.

(267) Shi, W.; Li, W.; Delaney, K. T.; Fredrickson, G. H.; Kramer, E. J.; Ntaras, C.; Avgeropoulos, A.; Lynd, N. A. Morphology Re-Entry in Asymmetric PS-PI-PS' Triblock Copolymer and PS Homopolymer Blends. *J. Polym. Sci. Part B Polym. Phys.* **2016**, *54* (2), 169–179.

(268) Zhou, H.; Johnson, J. A. Photo-Controlled Growth of Telechelic Polymers and End-Linked Polymer Gels. *Angew. Chemie - Int. Ed.* **2013**, *52* (8), 2235–2238.

(269) Chen, M.; Johnson, J. a. Improving Photo-Controlled Living Radical Polymerization from Trithiocarbonates through the Use of Continuous-Flow Techniques. *Chem. Commun.* **2015**, *51*, 6742–6745.

(270) Hill, M. R.; Carmean, R. N.; Sumerlin, B. S. Expanding the Scope of RAFT Polymerization: Recent Advances and New Horizons. *Macromolecules* **2015**, *48* (16), 5459–5469.

(271) Moad, G.; Rizzardo, E.; Thang, S. H. End-Functional Polymers, Thiocarbonylthio Group Removal/transformation and Reversible Addition-Fragmentation-Chain Transfer (RAFT) Polymerization. *Polym. Int.* **2011**, *60* (1), 9–25.

(272) Wu, Y.; Zhou, Y.; Zhu, J.; Zhang, W.; Pan, X.; Zhang, Z.; Zhu, X. Fast Conversion of Terminal Thiocarbonylthio Group of RAFT Polymer to "Clickable" Thiol Group via the Versatile Sodium Azide. *Polym. Chem.* **2014**, ASAP.

(273) Le Neindre, M.; Magny, B.; NicolaÿR. Evaluation of Thiocarbonyl and Thioester Moieties as Thiol Protecting Groups for Controlled Radical Polymerization. *Polym. Chem.* **2013**, *4* (22), 5577.

(274) Schmid, C.; Falkenhagen, J.; Beskers, T. F.; Nguyen, L. T. T.; Wilhelm, M.; Du Prez, F. E.; Barner-Kowollik, C. Multi-Block Polyurethanes via RAFT End-Group Switching and Their Characterization by Advanced Hyphenated Techniques. *Macromolecules* **2012**, *45* (16), 6353–6362.

(275) Keddie, D. J.; Moad, G.; Rizzardo, E.; Thang, S. H. RAFT Agent Design and Synthesis. *Macromolecules* **2012**, *45* (13), 5321–5342.

(276) Bathfield, M.; D'Agosto, F.; Spitz, R.; Charreyre, M. T.; Delair, T. Versatile Precursors of Functional RAFT Agents. Application to the Synthesis of Bio-Related End-Functionalized Polymers. *J. Am. Chem. Soc.* **2006**, *128* (8), 2546–2547.

(277) Pan, G.; Zhang, Y.; Ma, Y.; Li, C.; Zhang, H. Efficient One-Pot Synthesis of Water-Compatible Molecularly Imprinted Polymer Microspheres by Facile RAFT Precipitation Polymerization. *Angew. Chemie Int. Ed.* **2011**, *50* (49), 11731–11734.

(278) Sudo, A.; Hamaguchi, T.; Aoyagi, N.; Endo, T. RAFT-Approach to Well-Defined Telechelic Vinyl Polymers with Hydroxyl Terminals as Polymeric Diol-Type Building Blocks for Polyurethanes. *J. Polym. Sci. Part A Polym. Chem.* **2013**, *51* (2), 318–326.

(279) Zhou, G.; Harruna, I. I. Synthesis and Characterization of RAFT Polymerization. *Society* **2005**, No. Ii, 4114–4123.

(280) Jiang, K.; Ye, C.; Zhang, P.; Wang, X.; Zhao, Y. One-Pot Controlled Synthesis of Homopolymers and Diblock Copolymers Grafted Graphene Oxide Using Couplable RAFT Agents. *Macromolecules* **2012**, *45* (3), 1346–1355.

(281) Ohno, K.; Ma, Y.; Huang, Y.; Mori, C.; Yahata, Y.; Tsujii, Y.; Maschmeyer, T.; Moraes, J.; Perrier, S. Surface-Initiated Reversible Addition–Fragmentation Chain Transfer (RAFT) Polymerization from Fine Particles Functionalized with Trithiocarbonates. *Macromolecules* **2011**, *44* (22), 8944–8953.

(282) You, Y.; Zhou, Q.; Manickam, D. S.; Wan, L.; Mao, G.; Oupicky, D. Dually Responsive Multiblock Copolymers via Reversible Addition-Fragmentation Chain Transfer Polymerization : Synthesis of Temperature- and Redox-Responsive Copolymers of Poly ( N-Isopropylacrylamide ) and Poly ( 2- ( Dimethylamino ) Ethyl Methacrylate ). *Macromolecules* **2007**, *40*, 8617–8624.

(283) Wang, S.; Vajjala Kesava, S.; Gomez, E. D.; Robertson, M. L. Sustainable Thermoplastic Elastomers Derived from Fatty Acids. *Macromolecules* **2013**, *46* (18), 7202–7212.

(284) He, T.; Zheng, G.; Pan, C. Synthesis of Cyclic Polymers and Block Copolymers by Monomer Insertion into Cyclic Initiator by a Radical Mechanism. *Macromolecules* **2003**, *36* (100 mL), 5960–5966.

(285) O'Reilly, R. K.; Hansell, C. Mild and Facile Synthesis of Multi-Functional RAFT Chain Transfer Agents. *Polymers (Basel).* **2009**, *1* (1), 3–15.

(286) Chaffey-millar, H.; Stenzel, M. H.; Davis, T. P.; Coote, M. L.; Barner-kowollik, C. Design Criteria for Star Polymer Formation Processes via Living Free Radical Polymerization. *Macromolecules* **2006**, *39*, 6406–6419.

(287) Carter, S.; Hunt, B.; Rimmer, S. Highly Branched Poly( N -Isopropylacrylamide)s with Imidazole End Groups Prepared by Radical Polymerization in the Presence of a Styryl Monomer Containing a Dithioester Group. *Macromolecules* **2005**, *38* (11), 4595–4603.

(288) Päch, M.; Zehm, D.; Lange, M.; Dambowsky, I.; Weiss, J.; Laschewsky, A. Universal Polymer Analysis by 1H NMR Using Complementary Trimethylsilyl End Groups. *J. Am. Chem. Soc.* **2010**, *132* (25), 8757–8765.

(289) Skey, J.; O'Reilly, R. K. Facile One Pot Synthesis of a Range of Reversible Addition-Fragmentation Chain Transfer (RAFT) Agents. *Chem. Commun. (Camb).* **2008**, No. 35, 4183–4185.

(290) Robin, M. P.; Jones, M. W.; Haddleton, D. M.; O'Reilly, R. K. Dibromomaleimide End Functional Polymers by RAFT Polymerization without the Need of Protecting Groups. *ACS Macro Lett.* **2012**, *1* (1), 222–226.

(291) Robin, M. P.; Wilson, P.; Mabire, A. B.; Kiviaho, J. K.; Raymond, J. E.; Haddleton, D. M.; O'Reilly, R. K. Conjugation-Induced Fluorescent Labeling of Proteins and Polymers Using Dithiomaleimides. *J. Am. Chem. Soc.* **2013**, *135* (8), 2875–2878.

(292) Binauld, S.; Delafresnaye, L.; Charleux, B.; D'Agosto, F.; Lansalot, M. Emulsion Polymerization of Vinyl Acetate in the Presence of Different Hydrophilic Polymers Obtained by RAFT/MADIX. *Macromolecules* **2014**, *47* (10), 3461–3472.

(293) Oehlenschlaeger, K. K.; Guimard, N. K.; Brandt, J.; Mueller, J. O.; Lin, C. Y.; Hilf, S.; Lederer, A.; Coote, M. L.; Schmidt, F. G.; Barner-Kowollik, C. Fast and Catalyst-Free Hetero-Diels-Alder Chemistry for on Demand Cyclable Bonding/debonding Materials. *Polym. Chem.* **2013**, *4* (16), 4348–4355.

(294) Zhang, L.; Cool, L. R.; Wesdemiotis, C.; Weiss, R. a.; Cavicchi, K. a. Syntheses of Quaternary Ammonium-Containing, Trithiocarbonate RAFT Agents and Hemi-Telechelic Cationomers. *Polym. Chem.* **2014**, *5* (4), 1180–1190.

(295) Zhang, L.; Tang, Q.; Weiss, R. A.; Cavicchi, K. A. Synthesis and Characterization of Quaternary Phosphonium-Containing{,} Trithiocarbonate RAFT Agents. *Polym. Chem.* **2014**, *5* (18), 5492–5500.

(296) Baussard, J. F.; Habib-Jiwan, J. L.; Laschewsky, A.; Mertoglu, M.; Storsberg, J. New Chain Transfer Agents for Reversible Addition-Fragmentation Chain Transfer (RAFT) Polymerisation in Aqueous Solution. *Polymer (Guildf).* **2004**, *45* (11), 3615–3626.

(297) Moughton, A. O.; O'Reilly, R. K. Thermally Induced Micelle to Vesicle Morphology Transition for a Charged Chain End Diblock Copolymer. *Chem. Commun. (Camb).* **2010**, *46* (7), 1091–1093.

(298) Doncom, K. E. B.; Willcock, H.; O'Reilly, R. K. The pH Induced Vesicle to Micelle Morphology Transition of a THP-Protected Polymer. *J. Polym. Sci. Part A Polym. Chem.* **2014**, *52* (21), 3026–3031.

(299) Stamenović, M. M.; Espeel, P.; Camp, W. Van; Du Prez, F. E. Norbornenyl-Based RAFT Agents for the Preparation of Functional Polymers via Thiol-Ene Chemistry. *Macromolecules* **2011**, *44* (14), 5619–5630.

(300) van Strijdonck, G.; van Haare, J.; J. M. Honen, P.; van den Schoor, R.; C. Feiters, M.; van der Linden, J.; J. Steggerda, J.; J. M. Nolte, R. Cyclotriveratrylene Models for [4Fe-4S] Proteins: 3[ratio]1 Subsite Differentiation and Modulation of the Redox Potential. *J. Chem. Soc.{,} Dalt. Trans.* **1997**, No. 3, 449–462.

(301) Claire F. Hansell Milan M. Stamenovic, Ian A. Barker, Andrew P. Dove, Filip E. Du Prez, Rachel K. O'Reilly, P. E.; Hansell, C. F.; Espeel, P.; Stamenovic, M. M.; Barker, I. a; Dove, A. P.; Du Prez, F. E.; O'Reilly, R. K. Additive-Free Clicking for Polymer Functionalization and Coupling by Tetrazine-Norbornene Chemistry. *J. Am. Chem. Soc.* **2011**, *133* (35), 13828–13831.

(302) Moad, G.; Chong, Y. K.; Mulder, R.; Rizzardo, E.; Thang, S. H. New Features of the Mechanism of RAFT Polymerization. In *Controlled/Living Radical Polymerization: Progress in RAFT, DT, NMP & OMRP*; pp 3–18.

(303) Zard, S. Z. On the Trail of Xanthates: Some New Chemistry from an Old Functional Group. *Angew. Chem. Int. Ed.* **1997**, *36*, 672.

(304) Quiclet-Sire, B.; Zard, S. Z. Powerful Carbon - Carbon Bond Forming Reactions Based on a Novel Radical Exchange Process. *Chem. - A Eur. J.* **2006**, *12* (23), 6002–6016.

(305) McLeary, J. B.; Calitz, F. M.; McKenzie, J. M.; Tonge, M. P.; Sanderson, R. D.; Klumperman, B. Beyond Inhibition: A 1H NMR Investigation of the Early Kinetics of RAFT-Mediated Polymerization with the Same Initiating and Leaving Groups. *Macromolecules* **2004**, *37* (7), 2383–2394.

(306) McLeary, J. B.; McKenzie, J. M.; Tonge, M. P.; Sanderson, R. D.; Klumperman, B. Initialisation in RAFT-Mediated Polymerisation of Methyl Acrylate. *Chem. Commun. (Camb).* **2004**, *6* (17), 1950–1951.

(307) Chen, M.; Ghiggino, K. P.; Rizzardo, E.; Thang, S. H.; Wilson, G. J. Controlled Synthesis of Luminescent Polymers Using a Bis-Dithiobenzoate RAFT Agent. *Chem. Commun. (Camb).* **2008**, No. 9, 1112–1114.

(308) Chen, M.; Ghiggino, K. P.; Mau, A. W. H.; Rizzardo, E.; Sasse, W. H. F.; Thang, S. H.; Wilson, G. J. Synthesis of Functionalized RAFT Agents for Light Harvesting Macromolecules. *Macromolecules* **2004**, *37* (15), 5479–5481.

(309) Tanaka, S.; Nishida, H.; Endo, T. Miscibility of Polystyrene with One Hydroxystyrene Chain End into Poly ( Butyl Methacrylate ) Miscibility of Polystyrene with One Hydroxystyrene Chain End into Poly ( Butyl Methacrylate ). **2009**, *26*, 293–298.

(310) Houshyar, S.; Keddie, D. J.; Moad, G.; Mulder, R. J.; Saubern, S.; Tsanaktsidis, J. The Scope for Synthesis of Macro-RAFT Agents by Sequential Insertion of Single Monomer Units. *Polym. Chem.* **2012**, *3* (7), 1879.

(311) François, A.; Laroche, A.; Pinaud, N.; Salmon, L.; Ruiz, J.; Robert, J.; Astruc, D. Encapsulation of Docetaxel into PEGylated Gold Nanoparticles for Vectorization to Cancer Cells. *ChemMedChem* **2011**, *6* (11), 2003–2008.

(312) Bouhadir, G.; Legrand, N.; Quiclet-Sire, B.; Zard, S. Z. A New Practical Synthesis of Tertiary S-Alkyl Dithiocarbonates and Related Derivatives. *Tetrahedron Lett.* **1999**, *40* (2), 277–280.

(313) Thang, S. H.; Chong, B. Y. K.; Mayadunne, R. T. A.; Moad, G.; Rizzardo, E. A Novel Synthesis of Functional Dithioesters, Dithiocarbamates, Xanthates and Trithiocarbonates. *Tetrahedron Lett.* **1999**, *40* (12), 2435–2438.

(314) Kubowicz, S.; Baussard, J.-F.; Lutz, J.-F.; Thünemann, A. F.; von Berlepsch, H.; Laschewsky, A. Multicompartment Micelles Formed by Self-Assembly of Linear ABC Triblock Copolymers in Aqueous Medium. *Angew. Chemie Int. Ed.* **2005**, *44* (33), 5262–5265.

(315) Akeroyd, N.; Pfukwa, R.; Klumperman, B. Triazole-Based Leaving Group for RAFT-Mediated Polymerization Synthesized via the Cu-Mediated Huisgen 1,3-Dipolar Cycloaddition Reaction. *Macromolecules* **2009**, *42* (8), 3014–3018.

(316) Simms, R. W.; Davis, T. P.; Cunningham, M. F. Xanthate-Mediated Living Radical Polymerization of Vinyl Acetate in Miniemulsion. *Macromol. Rapid Commun.* **2005**, *26* (8), 592–596.

(317) Stenzel, M. H.; Cummins, L.; Roberts, G. E.; Davis, T. P.; Vana, P.; Barner-Kowollik, C. Xanthate Mediated Living Polymerization of Vinyl Acetate: A Systematic Variation in MADIX/RAFT Agent Structure. *Macromol. Chem. Phys.* **2003**, *204* (9), 1160–1168.

(318) Bernard, J.; Favier, A.; Zhang, L.; Nilasaroya, A.; Davis, T. P.; Barner-Kowollik, C.; Stenzel, M. H. Poly(vinyl Ester) Star Polymers via Xanthate-Mediated Living Radical Polymerization: From Poly(vinyl Alcohol) to Glycopolymer Stars. *Macromolecules* **2005**, *38* (13), 5475–5484.

(319) Skrabania, K.; Li, W.; Laschewsky, A. Synthesis of Double-Hydrophilic BAB Triblock Copolymers via RAFT Polymerisation and Their Thermoresponsive Self-Assembly in Water. *Macromol. Chem. Phys.* **2008**, *209* (13), 1389–1403.

(320) You, Y. Z.; Zhou, Q. H.; Manickam, D. S.; Wan, L.; Mao, G. Z.; Oupický, D. Dually Responsive Multiblock Copolymers via Reversible Addition- Fragmentation Chain Transfer Polymerization: Synthesis of Temperature- and Redox-Responsive Copolymers of poly(N-Isopropylacrylamide) and poly(2-(dimethylamino)ethyl Methacrylate). *Macromolecules* **2007**, *40* (24), 8617–8624.

(321) Skrabania, K.; Miasnikova, A.; Bivigou-Koumba, A. M.; Zehm, D.; Laschewsky, A. Examining the UV-Vis Absorption of RAFT Chain Transfer Agents and Their Use for Polymer Analysis. *Polym. Chem.* **2011**, *2* (9), 2074.

(322) Save, M.; Manguian, M.; Chassenieux, C.; Charleux, B. Synthesis by RAFT of Amphiphilic Block and Comblike Cationic Copolymers and Their Use in Emulsion Polymerization for the Electrosteric Stabilization of Latexes. *Macromolecules* **2005**, *38* (2), 280–289.

(323) Doak, K. W. Copolymerization. XV.1 Copolymerization of Acetylene Derivatives with Olefins. Retardation by Radicals from Acetylenes. *J. Am. Chem. Soc.* **1950**, *72* (10), 4681–4686.

(324) Elyashiv-Barad, S.; Greinert, N.; Sen, A. Copolymerization of Methyl Acrylate with Norbornene Derivatives by Atom Transfer Radical Polymerization. *Macromolecules* **2002**, *35* (19), 7521–7526.

(325) Ihara, E.; Honjyo, S.; Kobayashi, K.; Ishii, S.; Itoh, T.; Inoue, K.; Momose, H.; Nodono, M. Radical Copolymerization of Methyl 2-Norbornene-2-Carboxylate and 2-Phenyl-2-Norbornene with Styrene, Alkyl Acrylate, and Methyl Methacrylate: Facile Incorporation of Norbornane Framework into Polymer Main Chain and Its Effect on Glass Transition Temperat. *Polymer (Guildf).* **2010**, *51* (2), 397–402.

(326) Vandenbergh, J.; Junkers, T. Alpha and Omega: Importance of the Nonliving Chain End in Raft Multiblock Copolymerization. *Macromolecules* **2014**, *47* (15), 5051–5059.

(327) Teo, Y. C.; Xia, Y. Importance of Macromonomer Quality in the Ring-Opening Metathesis Polymerization of Macromonomers. *Macromolecules* **2015**, *48* (16), 5656–5662.

(328) Si, Z.; Qiu, L.; Dong, H.; Gu, F.; Li, Y.; Yan, F. Effects of Substituents and Substitution Positions on Alkaline Stability of Imidazolium Cations and Their Corresponding Anion-Exchange Membranes. *ACS Appl. Mater. Interfaces* **2014**, *6* (6), 4346–4355.

(329) Lin, B.; Chu, F.; Ren, Y.; Jia, B.; Yuan, N.; Shang, H.; Feng, T.; Zhu, Y.; Ding, J. Alkaline Stable C2-Substituted Imidazolium-Based Cross-Linked Anion Exchange Membranes for Alkaline Fuel Cell Applications. *J. Power Sources* **2014**, *266*, 186–192.

(330) Benoit, D.; Harth, E.; Fox, P.; Waymouth, R. M.; Hawker, C. J. Accurate Structural Control and Block Formation in the Living Polymerization of 1,3-Dienes by Nitroxide-Mediated Procedures. *Macromolecules* **2000**, *33* (2), 363–370.

(331) Hawker, C. J.; Bosman, A. W.; Harth, E. New Polymer Synthesis by Nitroxide Mediated Living Radical Polymerizations. *Chem. Rev.* **2001**, *101* (12), 3661–3688.

(332) Jana, N. K.; Verkade, J. G. Phase-Vanishing Methodology for Efficient Bromination, Alkylation, Epoxidation, and Oxidation Reactions of Organic Substrates. *Org. Lett.* **2003**, *5* (21), 3787–3790.

(333) Porto, R. S.; Vasconcellos, M. L. A. A.; Ventura, E.; Coelho, F. Diastereoselective Epoxidation of Allylic Diols Derived from Baylis-Hillman Adducts. *Synthesis (Stuttg).* **2005**, No. 14, 2297–2306.

(334) Klukovich, H. M.; Kean, Z. S.; Ramirez, A. L. B.; Lenhardt, J. M.; Lin, J.; Hu, X.; Craig, S. L. Tension Trapping of Carbonyl Ylides Facilitated by a Change in Polymer Backbone. *J. Am. Chem. Soc.* **2012**, *134* (23), 9577–9580.

(335) Bunton, C. A.; Foroudian, H. J.; Kumar, A. Sulfide Oxidation and Oxidative Hydrolysis of Thioesters by Peroxymonosulfate Ion. *J. Chem. Soc. Perkin Trans. 2* **1995**, No. 1, 33.

(336) Di Noto, V.; Fontanella, J. J.; Wintersgill, M. C.; Giffin, G. A.; Vezzù, K.; Piga, M.; Negro, E. Pressure, Temperature, and Dew Point Broadband Electrical Spectroscopy (PTD-BES) for the Investigation of Membranes for PEMFCs▲. *Fuel Cells* **2013**, *13* (1), 48–57.

(337) Piccolo, M.; Giffin, G. A.; Vezzù, K.; Bertasi, F.; Alotto, P.; Guarnieri, M.; Dinoto, V. Molecular Relaxations in Magnesium Polymer Electrolytes via GHz Broadband Electrical Spectroscopy. *ChemSusChem* **2013**, *6* (11), 2157–2160.

(338) Giffin, G. A.; Haugen, G. M.; Hamrock, S. J.; Di Noto, V. Interplay between Structure and Relaxations in Perfluorosulfonic Acid Proton Conducting Membranes. *J. Am. Chem. Soc.* **2013**, *135* (2), 822–834.

(339) Di Noto, V.; Piga, M.; Giffin, G. A.; Vezz??, K.; Zawodzinski, T. A. Interplay between Mechanical, Electrical, and Thermal Relaxations in Nanocomposite Proton Conducting Membranes Based on Nafion and a [(ZrO 2)??(Ta2O5)0.119] Core-Shell Nanofiller. *J. Am. Chem. Soc.* **2012**, *134* (46), 19099–19107.

(340) Bellin, I.; Kelch, S.; Langer, R.; Lendlein, a. Polymeric Triple-Shape Materials. *Proc. Natl. Acad. Sci. U. S. A.* **2006**, *103* (48), 18043–18047.

(341) Behl, M.; Bellin, I.; Kelch, S.; Wagermaier, W.; Lendlein, A. One-Step Process for Creating Triple-Shape Capability of AB Polymer Networks. *Adv. Funct. Mater.* **2009**, *19* (1), 102–108.

(342) Luo, Y.; Guo, Y.; Gao, X.; Li, B. G.; Xie, T. A General Approach towards Thermoplastic Multishape-Memory Polymers via Sequence Structure Design. *Adv. Mater.* **2013**, *25* (5), 743–748.

(343) Xie, T. Tunable Polymer Multi-Shape Memory Effect. *Nature* **2010**, *464* (7286), 267–270.

(344) Kohlmeyer, R. R.; Lor, M.; Chen, J. Remote, Local, and Chemical Programming of Healable Multishape Memory Polymer Nanocomposites. *Nano Lett.* **2012**, *12* (6), 2757–2762.

(345) Beers, K. M.; Yakovlev, S.; Jackson, A.; Wang, X.; Hexemer, A.; Downing, K. H.; Balsara, N. P. Absence of Schroeder's Paradox in a Nanostructured Block Copolymer Electrolyte Membrane. *J. Phys. Chem. B* **2014**, *118* (24), 6785–6791.

(346) Park, M. J.; Downing, K. H.; Jackson, A.; Gomez, E. D.; Minor, A. M.; Cookson, D.; Weber, A. Z.; Balsara, N. P. Increased Water Retention in Polymer Electrolyte Membranes at Elevated Temperatures Assisted by Capillary Condensation. *Nano Lett.* **2007**, *7* (11), 3547–3552.

(347) Hart, K. E.; Abbott, L. J.; L??sal, M.; Colina, C. M. Morphology and Molecular Bridging in Comb- and Star-Shaped Diblock Copolymers. *J. Chem. Phys.* **2014**, *141* (20).

(348) Moilanen, D. E.; Spry, D. B.; Fayer, M. D. Water Dynamics and Proton Transfer in Nafion Fuel Cell Membranes. *Langmuir* **2008**, *24* (8), 3690–3698.

(349) Bothe, M.; Schmidt-Naake, G. An Improved Catalytic Method for Alkoxyamine Synthesis - Functionalized and Biradical Initiators for Nitroxide-Mediated Radical Polymerization. *Macromol. Rapid Commun.* **2003**, *24* (10), 609–613.

(350) Miura, Y.; Yoshida, Y. Synthesis of Six-Arm Star Polymer by Nitroxide-Mediated "Living" Radical Polymerization. *Polym. J.* **2002**, *34* (10), 748–754.

(351) Nicolas, J.; Guillaneuf, Y.; Lefay, C.; Bertin, D.; Gigmes, D.; Charleux, B. Nitroxide-Mediated Polymerization. *Prog. Polym. Sci.* **2013**, *38* (1), 63–235.

(352) Jung, Y. S.; Ross, C. A. Orientation-Controlled Self-Assembled Nanolithography Using a Polystyrene - Polydimethylsiloxane Block Copolymer. *Nano Lett.* **2007**, *7* (7), 2046–2050.

(353) Tegou, E.; Bellas, V.; Gogolides, E.; Argitis, P.; Eon, D.; Cartry, G.; Cardinaud, C. Polyhedral Oligomeric Silsesquioxane (POSS) Based Resists: Material Design Challenges and Lithographic Evaluation at 157 Nm. *Chem. Mater.* **2004**, *16* (13), 2567–2577.

(354) Hirai, T.; Leolukman, M.; Liu, C. C.; Han, E.; Kim, Y. J.; Ishida, Y.; Hayakawa, T.; Kakimoto, M. A.; Nealey, P. F.; Gopalan, P. One-Step Direct-Patterning Template Utilizing Self-Assembly of POSS-Containing Block Copolymers. *Adv. Mater.* **2009**, *21* (43), 4334–4338.

(355) Anastasiadis, S. H.; Russell, T. P.; Satija, S. K.; Majkrzak, C. F. The Morphology of Symmetric Diblock Copolymers as Revealed by Neutron Reflectivity. *J. Chem. Phys.* **1990**, *92* (9), 5677–5691.

(356) Singh, M.; Odusanya, O.; Wilmes, G. M.; Eitouni, H. B.; Gomez, E. D.; Patel, a J.; Chen, V. L.; Park, M. J.; Fragouli, P.; Iatrou, H.; Hadjichristidis, N.; Cookson, D.; Balsara, N. P. Effect of Molecular Weight on the Mechanical and Electrical Properties of Block Copolymer Electrolytes. *Macromolecules* **2007**, *40* (13), 4578–4585.

(357) Yuan, R.; Teran, A. A.; Gurevitch, I.; Mullin, S. A.; Wanakule, N. S.; Balsara, N. P. Ionic Conductivity of Low Molecular Weight Block Copolymer Electrolytes. *Macromolecules* **2013**, *46* (3), 914–921.

(358) Panday, A.; Mullin, S.; Gomez, E. D.; Wanakule, N.; Chen, V. L.; Hexemer, A.; Pople, J.; Balsara, N. P. Effect of Molecular Weight and Salt Concentration on Conductivity of Block Copolymer Electrolytes. *Macromolecules* **2009**, *42* (13), 4632–4637.

(359) Gomez, E. D.; Panday, A.; Feng, E. H.; Chen, V.; Stone, G. M.; Minor, A. M.; Kisielowski, C.; Downing, K. H.; Borodin, O.; Smith, G. D.; Balsara, N. P. Effect of Ion Distribution on Conductivity of Block Copolymer Electrolytes. *Nano Lett.* **2009**, *9* (3), 1212–1216.

(360) Ganesan, V.; Pyramitsyn, V.; Bertoni, C.; Shah, M. Mechanisms Underlying Ion Transport in Lamellar Block Copolymer Membranes. *ACS Macro Lett.* **2012**, *1* (4), 513–518.

(361) Borodin, O.; Smith, G. D. Mechanism of Ion Transport in Amorphous Poly(ethylene oxide)/LiTFSI from Molecular Dynamics Simulations. *Macromolecules* **2006**, *39* (4), 1620–1629.

(362) Schneider, Y.; Modestino, M. A.; McCulloch, B. L.; Hoarfrost, M. L.; Hess, R. W.; Segalman, R. A. Ionic Conduction in Nanostructured Membranes Based on Polymerized Protic Ionic Liquids. *Macromolecules* **2013**, *46* (4), 1543–1548.

(363) McLeod, D. C.; Tsarevsky, N. V. Atom Transfer Radical Polymerization of an Epoxide-Containing Monomer, 4-Vinylphenyloxirane, Employing Low Concentration of Catalyst: Synthesis of Linear and Star-Shaped Macromolecules. *Polym. Int.* **2014**, *63* (5), 868–875.

(364) McLeod, D. C.; Tsarevsky, N. V. Well-Defined Epoxide-Containing Styrenic Polymers and Their Functionalization with Alcohols. *J. Polym. Sci. Part A Polym. Chem.* **2016**, *54* (8), 1132–1144.

(365) Jones, R. G.; Yoon, S.; Nagasaki, Y. Facile Synthesis of Epoxystyrene and Its Copolymerisations with Styrene by Living Free Radical and Atom Transfer Radical Strategies. *Polymer (Guildf).* **1999**, *40* (9), 2411–2418.